MEASUREMENT OF THE DIFFERENTIAL ANGULAR DISTRIBUTION OF THE W BOSON PRODUCED IN ASSOCIATION WITH JETS IN PROTON-ANTIPROTON COLLISIONS AT $\sqrt{s} = 1.8$ TeV

BY

JOHN STROLOGAS

Diploma, University of Athens, 1994
M.S., University of Illinois at Urbana-Champaign, 2002

THESIS

Submitted in partial fulfillment of the requirements
for the degree of Doctor of Philosophy in Physics
in the Graduate College of the
University of Illinois at Urbana-Champaign, 2002

Urbana, Illinois

Abstract

The full differential cross section of the W boson produced in a proton-antiproton collider can be written as a sum of nine terms. Each term is a product of an analytical expression of the azimuthal and polar angles (ϕ and θ) of the charged lepton from the W decay measured in the W-rest frame (leptonic part) times a helicity cross section (hadronic part). By dividing the helicity cross sections by the full unpolarized cross section we end up with eight angular coefficients (A_0–A_7), which describe the W decay distribution. At low W transverse momentum, only one of the angular coefficients is non-zero. In order to study all the coefficients, we need to study the production of the W at high transverse momentum, in association with the production of jets that balance this transverse momentum.

In this thesis we present the first measurement of the A_2 and A_3 angular coefficients, for four ranges of the W transverse momentum p_T^W. We performed the analysis on CDF Run Ia and Run Ib $W \to e\nu_e$ data (integrated luminosity of 110 pb^{-1}) and $W \to \mu\nu_\mu$ data (integrated luminosity of 107 pb^{-1}) with the requirement for the existence of at least one jet passing the CDF jet requirements. We directly measure the ϕ angle of the charged lepton in the Collins-Soper W rest-frame. In this frame, ϕ is exactly known, in spite of our ignorance of the longitudinal momentum of the decay neutrino. Moreover, the W-mass systematic uncertainty on the measured azimuthal angle is negligible. We extract measurements for the electron and muon channel W decays, and the statistical combination of the two.

We also present the Standard Model prediction for the W angular coefficients A_i as a function of p_T^W, using a W+jet Monte Carlo event generator, which includes gluon loops. The prediction for three of the angular coefficients (A_1, A_4 and A_6) is presented for the first time.

To my Parents and Sister, for all their love and support.

Acknowledgments

This thesis would not have been possible without the genuine interest, valuable suggestions, and continuous support from my advisor Professor Steven Errede. My collaboration with Steve was harmonious and I enjoyed our conversations on physics and other intellectual topics. I really hope that our partnership continues after my graduation.

During my graduate career at the University of Illinois and CDF experiment at Fermilab, I enjoyed collaborating with Len Christofek on physical analysis, Lee Holloway, Rob Roser, Bob Downing, Vaidas Simaitis, Kevin Lannon and Nathan Eddy on hardware and with Prem Singh and George Velev on software. It was a real pleasure working with them. I would like to especially thank Len for our very interesting conversations, his interest in my work and his willingness to help me with my analysis.

I would also like to thank the support staff at the High Energy group at the University of Illinois. David Lesny, our system administrator, managed a reliable computational environment with a plurality of hardware and software resources. Most of the times I was pushing the system to its limits, but users like me are the reason Moore's law is still valid. Tom Shaw, Donna Guzy, Shirley Rothermel, and Joyce Ruch made sure all financial, travel, and bureaucratic issues were taken care of. In this exceptional setting, I was able to concentrate only on physics.

My graduate education at Illinois was a unique experience. The academic environment in Urbana encourages students to enrich their curriculum with courses and research in other fields of study. I benefited from courses in both the Physics Department and Department of Electrical Engineering. I would like to thank the instructors of all the classes I took. For my Master research in Electrical Engineering

I was fortunate to work with Prof. Karl Hess, a remarkable scientist and a great person. I am indebted to the administration of the Departments of Physics and ECE, especially the Associate Heads Jack Mochel, Jim Wolfe, and Alan Nathan (Physics) and William Perkins (ECE), for their advises and directions. Their open-door policy encourages graduate students to discuss and solve any problems they might have.

I would also like to thank the theorists who influenced my work, mainly K. Hagiwara, K. Hikasa and N. Kai (for their "T-odd/P-odd" paper [20] and for suggesting the measurement of the NLO angular coefficients), E. Mirkes (for his work on the extraction of the Standard Model prediction for the W angular coefficients [19, 21]), U. Baur (for checking my theoretical paper), W. Giele (for explaining DYRAD and providing support for the software) and T. Stelzer (for helping me write my own event generator). Many thanks to Scott Willenbrock for being a great teacher of particle physics and for his interest in my phenomenological work.

The CDF experiment is a large collaboration of hundreds of physicists from tens of institutions. All of them contributed, through detector hardware and software, in the collection of the data I used for my analysis. The collaboration comments were also invaluable. I really appreciated the interest Willis Sakumoto and Pierre Savard (the conveners of the CDF top/electroweak group) and Doug Benjamin showed on my analysis. The feedback from the CDF group and especially from the godparent committee (David Waters, Evi Halkiadaki and Bob Wagner) was priceless.

Finally, nothing could be possible without the emotional support I received from my family and friends. A Ph.D. in high-energy physics is a tremendous task, and the people close to me always helped me to maintain a minimal balance in my life. I thank them all from the bottom of my heart.

This thesis was supported in part by the Unites States Department of Energy under grant `DE-FG02-91ER-40677`.

Table of Contents

List of Tables

List of Figures

Chapter 1

Introduction

1.1 Understanding the World

Humankind has always possessed the desire to understand its environment. From the very early years, humans realized that they are physically weak compared to their natural competitors, and a way to survive was to decipher the world around them, analyze reality and rationally solve their problems using their mental superiority. This struggle for survival in an unfavorable environment is a possible source of the natural inquisitiveness of people and a motive behind their quest for the full understanding of the world.

1.2 The Early Greek Science

The most reasonable way for people to comprehend the whole is to understand its parts. The first Greek Philosophers, the physical philosophers (6^{th} century BC), tried to explain the origins of the world based on few material constituents and their properties [1]. They were the first physicists, because they deviated from the mythological interpretation of reality as they were naturally explaining the creation and the future collapse of the world. Thales of Miletus upheld that everything had come out of water, Anaximander of Miletus that the *apeiron* (infinity) and its qualities (cold and hot) generated the cosmos. Anaximenes of Miletus declared that the air is the origin of the world and expressed the first physical conservation law: nothing can come out of nothing and what we observe are different manifestations of the

same quality. This statement could be the discovery of the concept of *energy* as a physical quantity that is always conserved. Parmenides of Elea posed one of the first difficult physical problems: how could motion exist? Something cannot move into something that exists because the latter has to stop existing. Heracletus, on the other hand, believed that everything is in motion and that fire is the generative of the universe. Empedocles of Acragas declared that there are four material elements (*roots of everything*) and two forces (*love* and *hate*). The elements come together and mix through love, and separate from each other through hate. This could be the considered as the first physical theory that explicitly includes both matter and interactions. Anaxagoras of Clazomenae believed that everything is made of infinitely small parts that are mechanically mixed in different ways to produce our world. That was the start of the atomic theory. Major is the contribution of the atomist Leucippus of Miletus who found a solution to Parmenides problem. He arrived at the conclusion that there are two fundamental principles in the physical world, the empty space and the filled space which consists of atoms. The word atom comes from the greek word "atomo" which means indivisible. Hence the ancient Greek atom was in fact an "elementary particle". Democritus of Abdera tried to explain every phenomenon using these elementary particles. He even explained colors as sharp atoms hitting the eye like needles. This could be viewed as the first suggestion that light consists of particles; the photons.

As it is understood from the above, the Greeks were able to develop physical theories that could not be disproved, due to the lack of relevant experiments. The conflict between the theories, which led to magnificent results, was always at the theoretical and logical level. As mentioned above, the Parmenides argument of non-motion led to the discovery of empty space. Parmenides' friend Zeno of Elea had developed many paradoxes, like the well known one about Achilles and the turtle, which are based on the conflict between the discrete and the continuum. This conflict was resolved with the discovery of the limiting processes of differential and integral calculus by Archimedes [2]. The continuous motion of the particles was not illogical any more.

The first attempt to quantify the physical knowledge came from Pythagoras of

Samos. His doctrine was that "all things are numbers". He described the motion of celestial bodies, the harmonics of a string and its melody and arrived at important geometrical discoveries using numbers. One of his followers, Hippasus of Metapontum, discovered the irrational numbers in 450 BC. Aristotle summarized the physical knowledge of Ancient Greece in many of his books and his view of the Universe as homocentric imperfect terrestrial and perfect celestial spheres survived for more than 1,500 years.

1.3 The Birth of the Atomic Science

Inevitably, the philosophers of Ancient Greece could not proceed further in their pursuit for understanding the basic elements of nature, without experimental data and a complete quantitative establishment of the physical science. Humanity had to wait for thousands of years for these conditions to be satisfied. Scientists first learned how bodies move and interact through gravitational and electromagnetic forces, how light behaves and then they were ready to start probing into the matter using their technology. By the end of the nineteenth century, physicists were comfortable with Newton's concept of force, the Lagrange and Hamilton formalism of mechanics, and the understanding of the electromagnetic waves. However they needed quantum physics, relativity, and their combination (field theory) to proceed. And of course, without experimental observations nothing is possible.

Until 1897 scientists believed that the world was constructed by atoms not much different than the ones described by the Atomic Philosophers. They thought of them as indivisible spherical objects that come in different kinds and construct all matter both terrestrial and celestial. In 1869 chemist Mendeleev arranged all known elements in a table, based on their atomic weight, and the assumption was made that all atoms were fundamentally unique.

The discovery of radioactivity by Henri Becquerel in 1896 signaled the start of a new era. Experiments by Marie and Pierre Curie and Ernest Rutherford showed that there exist three kinds of radiation: α (helium nuclei, the result of strong interactions in the nucleus), β (electrons and positrons from the weak interactions in the nucleus)

and γ (the result of electromagnetic interactions in the nucleus). Of course, when α, β and γ radiation were discovered, their true nature was not understood.

The discovery of the first elementary particle came in 1897, when Joseph John Thompson discovered the electron using a cathode ray tube. He also suggested that electrons are the building blocks of the atom. In his theory, often called "raisin cake model", the electrons were embedded in a cloud of massless positive charge, to construct the neutral atom.

In 1900, Max Planck explained the black body radiation by quantizing the radiative energy. Unlike the Greeks, who had to solve the paradox of the continuum, the physicists of the early 20^{th} century had to understand quantization. In 1905, Einstein explained the photoelectric effect by using the quantization of light. That same year Einstein wrote his first paper on relativity, the proper theory to describe subatomic particles moving at high speeds comparable to the speed of light. In 1908, Rutherford and Geiger realized that the α particles were actually Helium nuclei (He^{++}).

The discovery of the nucleus by Rutherford in 1911 was the first demonstration of how angular distributions of particles and differential cross sections could be used to extract important physical information. By studying the angular distribution of α particles after being scattered by gold atoms, he came to the conclusion that the scattering of the α particles in big angles could not be explained, unless all the positive charge of the atom is concentrated in the center and its mass is considerably greater than that of an α particle.

In 1913, Niels Bohr developed a theory to explain the frequency of the spectral lines. In his theory, electrons rotate around the nucleus and the only way to make the system stable was to quantize the angular momentum. That same year Geiger and Marsden verified the Rutherford hypothesis.

Rutherford made another big discovery in 1918, when he realized that the Hydrogen nucleus is an elementary particle present in all nuclei. He named it *proton* which means "first" in greek. It was the first subnuclear particle discovered. In 1923, Compton experimentally verified that the photon is a particle.

Bose, Einstein, de Broglie, Schrödinger, Heisenberg, Bohr and Born are among the theorists who contributed to the formation of quantum mechanics, which reached its

final firm theoretical basis after the operator algebra formalism of John von Neumann in 1932. That same year James Chadwick discovered the neutron.

1.4 Particle Physics: Towards the Theory of Everything

Immediately after the realization that nuclei were made of protons and neutrons, it was understood that there is a separate interaction binding the protons together. It was named *strong* interaction, because it had to be stronger than the electrical repulsion between the protons. Similarly, as soon as the beta decay was viewed as the result of the decay of a neutron, the weak interactions were introduced to explain this process. As a result, physicists concluded that there were four interactions in nature: the electromagnetic, the weak, the strong and the gravitational interaction. The particles that interact weakly and (if they are charged) electromagnetically were named *leptons* (from the greek "leptos" meaning light or weak) and the particles that also interact strongly were named "hadrons" (from the greek "hadros" meaning heavy or strong).

On the theoretical front, Dirac arrived at the equation of motion for the electron in 1930. He predicted the existence of the electron's antiparticle to explain the negative energy solutions of his equation. The Dirac equation described all particles with spin equal to 1/2 and associated an antiparticle to each one. That first antiparticle to be observed was the antiparticle of the electron (the *positron*) discovered in the cosmic rays by Carl Anderson in 1932 [3].

In 1930, Wolfgang Pauli suggested that the missing energy in the beta decays is actually carried by a new neutral particle. Enrico Fermi named this particle *neutrino*, because it is a neutral lepton. According to Fermi's theory of weak interactions, formulated in 1934, the neutrino interacts only weakly.

Until 1933, the physical world at the lowest scale was very simple and understandable. There were only five elementary particles: the photon, the electron, the proton, the neutron and the neutrino. The whole world was constructed by these particles, as they were interacting through the four interactions. The cosmic rays, dramatically changed this picture. In 1937, Anderson and Nedermeyer discovered the muons [4],

and in 1947, Powell *et al.* discovered the pions. Both types of particles were charged and were detected in cosmic radiation, coming from galactic and extragalactic sources. In fact the muons and pions are part of the secondary cosmic radiation, which is produced via the interaction of the primary cosmic radiation – mainly protons – with the atmosphere. While the existence of the pions, as the supposed mediators of the strong interactions, was predicted by Yukawa in 1935, the muons were the first particles which did not have any particular reason to exist and no theory predicted them. The muons are 200 times heavier than the electrons, they are members of the second generation of leptons, and their existence puzzled the scientists, because – just like the leptons of the third generation – they do not construct the material world around us. Physicists, almost immediately realized that a neutrino must exist to be associated with this newly discovered charged lepton. In 1953 the electron neutrino was discovered by Reines and Cowan, and in 1962 the muon neutrino by Lederman, Schartz and Steinberg. The antiproton, the antiparticle of the proton predicted by the Dirac equation, was discovered in 1955 by Chamberlain, Segre, Wiegard and Ypsilantis [5]. Meanwhile, the Quantum theory of the electromagnetic interactions (Quantum Electrodynamics, or QED) was introduced by Feynman, Schwinger, and Tomonaga, in 1948.

The surprise of the discovery of a second family of leptons was not the only one. As the energies of the accelerators in the US and Europe were continuously increasing, new particles, that did not fit in the established workframe of the time, were discovered. Between 1947 and 1953 new particles were created in the laboratory, that had the strange properties of being produced in association, decaying always separately and living longer than expected. These particles were produced via strong interactions and decayed through weak interactions and they were attributed the quantum number of strangeness; a quantum number that was conserved in strong interactions but violated in weak interactions. Such particles are the kaons (K^+, K^-, K^0, $\bar{K^0}$), which are mesons (boson (integer spin) hadrons) and the baryons (fermion (half-integer spin) hadrons) Σ^+, Σ^+, Σ^0, Λ^0, Ω^-, Ξ^- and Ξ^0 and their excitations. Later on, the $\rho^{\pm}$, ρ^0, ϕ^0, ω^0 and η^0 mesons were discovered and more particles were being discovered every year. There was a chaos of over 150 hadrons that had to be

put in order.

It was more than obvious that the hadrons were composite particles. Zweig and Gell-Mann introduced the theory of *quarks* in 1964, and Feynman introduced the more general notion of partons. According to the original quark model, only three types of quarks (fermion elementary particles interacting through all interactions) were sufficient to describe the hadrons discovered by 1964. They were named u, d and s (*up*, *down* and *strange*). The quantum number that was given to them was named "color" and had to have three different values (due to the fact that, for example, $\Delta^{++} = uuu$ and $\Omega^- = sss$ and no three fermions can be in the same state unless they have three different extra quantum numbers, according to the Pauli exclusion principle for fermions), as Han and Greenberg noticed in 1965. Finally, in order not to increase the number of all particles by a factor of three, it was explicitly stated that only "white" or "color-neutral" states can be found free in nature. This also explained why the quarks could not be seen in the laboratory. They were always bound in the hadrons. The way to construct white particles is to combine all three colors of three valence quarks or three valence antiquarks (baryons) or combine a valence quark with a valence antiquark of the opposite color (mesons). The most common baryons are the protons and neutrons. In addition, in every hadron there exists a "sea" of virtual quarks and antiquarks, which are pair-produced from (and annihilated to) gluons. This theory of strong interactions (Quantum Chromodynamics or QCD) established an order in the original anarchy of the hadrons.

The statement that a fourth quark has to exist for symmetry reasons, since there were two pairs of leptons at the time, was first made by Bjorken and Glashow in 1964. In 1970 Glashow, Iliopoulos and Maiani established the prediction on more theoretical grounds showing that this fourth quark could explain the absence of flavor changing neutral currents in weak interactions.[†] A Brookhaven National Laboratory group (lead by S. Ting [6]) and a joint Stanford Linear Accelerator Center (SLAC)-Lawrence Berkeley Laboratory group (lead by B. Richter [7]) independently discovered this fourth quark (named *charm*, c) in 1974, as the $J/\psi = c\bar{c}$ meson materialization. Later also "naked charm" (only one c or $\bar{c}$ in the hadron) was detected. The symmetry was

[†]See Appendix A for more details.

again established. There were two families of leptons and two families of quarks.

In 1975, a third charged lepton was discovered by Perl *et al.* at SLAC [8], called the τ lepton, which was almost 3500 times heavier than the electron. Thus, an associated neutrino and a third generation of quarks were also expected. In 1977, Lederman *et al.* discovered the Υ particle [9] and the *bottom* (or *beautiful*) quark b ($\Upsilon = b\bar{b}$) at Fermilab in Illinois, USA. Later on, more excitations of Υ as well as "naked beauty" (only one b or $\bar{b}$ quark in the hadrons) were discovered.

The carriers of the strong interactions are eight gluons, that carry a combination of color and anticolor and couple the quarks together. An interesting feature of the strong interactions is the fact that they are weak if the interacting particles are close to each other, leading to quarks that are almost free inside the hadrons; a phenomenon called "asymptotic freedom". On the other hand, the strength of the strong interactions increases rapidly as the distance between the quarks increases, leading to the "infrared slavery"; the quarks cannot exist in free states. If a quark is knocked outside a hadron, its interaction strength with the rest of hadron increases continuously, until the potential energy is greater than that of a quark-antiquark pair production created from the vacuum. This way quark-antiquark pairs are continuously produced and a jet of hadrons is created. The first hadronic jets as a result of quark and gluon emission were observed at TASSO and JADE experiments in electron-positron collisions at DESY laboratory in Hamburg, Germany, in 1979. This was the first experimental evidence of the correctness of QCD.

The carriers of the weak interactions (the W^+, W^- and Z bosons), unlike the gluons, are massive and directly detectable. They were described by the Standard Model of Glashow, Salam and Weinberg in 1968. This model, as discussed in Appendix A, unified the weak and electromagnetic interactions into an electroweak theory. The intermediate (or vector) bosons acquired their mass through the Higgs mechanism, invented in 1964. The vector bosons were discovered by the UA1 and UA2 experiments at CERN laboratory in Geneva, Switzerland in 1983 [10, 11]. This was a triumph of the human civilization.

The sixth quark (*top* quark), the partner of b quark, was discovered in 1995, by the CDF and D0 experiments at Fermilab [12, 13] in the form of $t\bar{t}$ production in

proton-antiproton collisions at $\sqrt{s} = 1.8$ TeV.[†] No top meson was observed, since the lifetime of the top quark is much smaller than its hadronization time. As a result, the top quark decays before it actually creates a meson. Its mass is exceptionally high, about 176 GeV[‡], close to the mass of a gold atom!

The sixth lepton, the tau neutrino, was directly observed in the production of tau leptons as a kink of their decay in emulsion, by the DONUT experiment at Fermilab, in 2001 [14]. There exist good theoretical reasons enforcing the common belief that there are only three generations of quarks and leptons.

1.4.1 The Overall Picture

A formal synopsis of the Standard Model from basic principles to the calculation of cross sections associated with this dissertation can be found in Appendix A. It is understandable that we have not yet arrived at the final theory to describe the building blocks of the world and the interactions between them. Although our theory is very successful so far, it is actually an effective field theory, valid at energies achieved by our accelerators, but invalid at the Planck scale (energy equal to 10^{19} GeV or, equivalently, distance equal to 10^{-33} cm), where gravity has the same order of magnitude as any other interaction. Another problem of our current theory is that it contains 19 free parameters, the values of which are not derived from any theory, but rather established solely by experimental measurements. In this section, we summarize the reality, as it is observed by experiment and explained by theory.

In nature we have three kinds of elementary particles: The leptons (which interact electroweakly), the quarks (which interact both electroweakly and strongly) and the gauge bosons which mediate these fermionic interactions. The photons transmit the electromagnetic interaction, the weak bosons ($W^{\pm}$ and Z) carry the weak interactions and the gluons the strong.

The Lagrangians associated with each interaction is invariant under certain gauge symmetries. The $U(1)$ group describes the electromagnetic interactions, the $SU(2)$

[†]The quantity s is one of the Mandelstam variables, equal to the square of the sum of the energies of the colliding particles.

[‡]In accordance with the $\hbar = c = 1$ convention, in this thesis eV is the abbreviation for eV/c if used as the unit of momentum, and eV/c^2 if used as the unit of mass, where c is the speed of light.

The elementary particles					
Family	Particle	Charge	Mass (MeV)	Spin	Interactions
Leptons	e	-1	0.511	1/2	EM and weak
	μ	-1	105.66	1/2	EM and weak
	τ	-1	1777	1/2	EM and weak
	ν_e	0	$< 3 \cdot 10^{-6}$	1/2	Weak
	ν_μ	0	< 0.19	1/2	Weak
	ν_τ	0	< 18.2	1/2	Weak
Quarks	u	$+2/3$	1.5-4.5	1/2	EM, weak and strong
	d	$-1/3$	5.0-8.5	1/2	EM, weak and strong
	s	$-1/3$	80-155	1/2	EM, weak and strong
	c	$+2/3$	1000-1400	1/2	EM, weak and strong
	b	$-1/3$	4000-4500	1/2	EM, weak and strong
	t	$+2/3$	174000	1/2	EM, weak and strong
Gauge bosons	$W^\pm$	± 1	$80.40 \cdot 10^3$	1	EM and weak
	Z	0	$91.18 \cdot 10^3$	1	Weak
	g	0	0	1	Strong
	γ	0	0	1	EM

Table 1.1 The elementary particles

the weak interactions and the $SU(3)$ the strong interactions. The weak bosons and the gluons are unique because they interact with themselves, due to the non-abelian nature of $SU(2)$ and $SU(3)$. There are also discrete symmetries: *Charge* conjugation ($q \to -q$ transformation of charge), *Parity* transformation ($\boldsymbol{r} \to -\boldsymbol{r}$ transformation of the spatial coordinates),and *Time* reversal ($t \to -t$ transformation of time), or C, P, T. Physicists originally thought that these three symmetries and their combinations always conserved. As experiment proved, The weak interactions violate the C and P symmetry and there is also a CP violation at least in the K^0 weak decay [15].

With the exception of the photons, neutrinos and gluons, all particles are massive and interact gravitationally. This interaction is extremely weak compared to the other ones. The Standard Model does not currently include a quantum theory of gravity. Table 1.1 summarizes the properties of the known elementary particles and associated quantum numbers. There is evidence of neutrino oscillations [16], which means that the neutrinos could be massive.

The leptons can exist in free states, whereas the infrared slavery of the QCD interactions forces quarks to be bound together to form the hadrons. Hadrons could

have three valence quarks (baryons) or a pair of valence quark and antiquark (mesons). In either case, the hadrons also include a sea of quarks, antiquarks, and gluons. There is a rich spectroscopy of hadrons due to the many possible combinations of quarks and antiquarks and the existence of excited states.

One of the big questions of modern physics is the origin of mass. The Unified electroweak model incorporates the SU(2) symmetry for the left-handed fields and the U(1) for hypercharge (a function of charge and the third projection of isospin). This model preassumes massless fermions, because any mass terms would not be invariant under SU(2). The mass of the fermions is generated by a process called *the Higgs mechanism*. A doublet of scalar fields is introduced and its self-interactions provide a mechanism for spontaneous symmetry breaking, causing the generation of mass terms. One could argue that the generation of mass is explained, but the value of the particles masses is not fully understood. The Yukawa couplings of the Higgs field to the fermions are the new introduced parameters that determine the masses and have to be deciphered. Although the Higgs particle has not been discovered yet, the mechanism of mass production associated with it is attractive, because it explains a basic property of the particles without destroying the elegant theory we use to describe them.

Along with the quest for the Higgs, there are many other theories or extensions of the current theory that try to solve fundamental questions. The Grand Unified Theories (GUT), for example, are designed to unify all interactions. This unification of interactions is considered to be a fundamental truth of nature. There is no reason for the particles not to be assigned a single property and interact accordingly. Even if this unification is broken in our world as we understand it, we would expect it to be valid in higher energies. The Standard Model is based on the successful unification of the Electromagnetic and Weak Interactions (Weinberg, Salam and Glashow model), but it does not incorporate the strong interactions in the same picture yet. The Grand Unifying Theories try to make this unification a reality, by introducing new higher symmetries. As a side-effect, they also predict the existence of extra gauge particles and phenomena such as the proton decay. One of the theories that has attracted a lot of attention is Supersymmetry (SUSY), which assigns a supersymmetric partner

to every existing known particle (the supersymmetric partners of bosons are fermions and vise versa), and also assigns fermionic space dimensions to the existing bosonic space dimensions. SUSY solves the naturalness problem: in the Standard Model the Higgs' mass has to be fine-tuned, which is unnatural. It also unifies the particle interactions, incorporates the gravitational interaction and solves the gauge hierarchy problem (why the Standard Model scale of $\sim$ 100 GeV is so much smaller than the Planck scale of 10^{19} GeV).

On earth we do not usually encounter many of the elementary or composite particles, unless we are near an accelerator or nuclear reactor. All ordinary matter is constructed from protons, neutrons and electrons. Radioactivity also produces positrons and gamma rays. Cosmic rays that primarily consist of protons reach earth mainly in the form of muons (from the pion decays) or electrons and positrons (from the muon decays). Many neutrinos also reach earth, as the decay products of cosmic rays or directly from the center of our Sun. All other particles do not exist naturally around us. If one wants to systematically study all particles one has to artificially generate them in the laboratory. Most of the particles were common when the universe was young, before the creation of matter as we know it. These particles are still produced in specific locations of the universe, where high energy conditions exist, for example the center of stars or super-nova explosions. There are also astronomical bodies, such as the neutron stars, which consist of only elementary particles in a form of a plasma, possible including hyperons (hadrons heavier than the proton and neutron).

1.5 About this Thesis

As we have already mentioned, many important discoveries in particle physics came from the study of the angular distribution of particles in space. The discovery of the nucleus, the discovery of parity violation in weak interactions [17], and the measurement of the spin of the W [11] are few examples of how the study of differential cross sections and angular distributions of particles may affect our understanding of the microcosm.

After the discovery of the W boson, most scientists worked hard on measuring

its mass and Breit-Wigner width as accurately as possible. Its total hadron collider production cross section was also measured, some times as a function of its transverse momentum. However, there were no systematic attempts to study the W helicity and its full differential cross section at a collider, with the exception of the indirect measurement of α_2 (defined in Equation (2.17)) by the $D0$ experiment at Fermilab [18].

There are several reasons that motivate us to pursue the study of the angular distribution of the leptons from the W decay [19]. This study enables us, in principle, to measure the angular coefficients and helicity cross sections of the W boson and compare our results with the ones predicted by the Standard Model or any other model. The angular coefficients A_5, A_6 and A_7 are P-odd and T-odd [20] (their sign flips under Parity or Time reversal transformation), and they could be associated with possible CP violation in W production and decay. In addition, the measurement of the angular decay distribution of leptons provides constraints on the parton distribution functions [21]. Once the helicity cross sections are established for standard W, we can use the same analysis to determine the couplings of possible heavier charged weak bosons, since the next-to-leading order terms depend less on the normalization and factorization scales [21]. The measurement of the lepton distributions in nucleon-nucleon scattering [22] appears to disagree with the QCD improved parton model, so it is interesting to test whether the W angular distribution at the Tevatron follows the theoretical predictions. Finally the angular coefficients of the W and corresponding helicity cross sections have not been measured before (with the exception of A_0 indirectly measured by the D0 experiment) and it is worthwhile to experimentally establish the complete differential cross section of the W boson. This study is physically rich, combining the electroweak physics with QCD and the polarization of the W.

The main difficulty in the study of the angular distribution of the W is that it cannot be fully reconstructed, due to our ignorance of the longitudinal momentum of the neutrino. For example nobody had ever tried to directly measure the azimuthal angle of the charged lepton in the W rest frame, because it is not possible to boost to the W rest frame, if we do not completely reconstruct the W. In this thesis we attack

the problem of measuring the full differential cross section and angular distribution of the W which is related to its helicity cross sections and its polarization. We manage to measure for the first time two of the five leading order angular coefficients related to the azimuthal angle of the charged lepton in the W rest frame. We also extract the Standard Model prediction for all the angular coefficients, using a Monte Carlo (MC) generator of W+jet up to second order in perturbative QCD. Three of these Standard Model angular coefficients have not been presented before.

Chapter 2

Theory of W Angular Distribution

2.1 Review of the Theory of W Production at a Hadron Collider

The simplest case of W boson production in high energy proton-antiproton collisions is the zero transverse momentum production. Because the colliding partons probably have a small net transverse momentum, the W will also have a small transverse momentum which can nevertheless be neglected. The tree-level Feynman diagram describing this process is shown in Figure 2.1. The quarks a and b are valence or sea quarks originated from the proton and the antiproton, while the produced W decays leptonically into a charged lepton and its antineutrino. The differential cross section for this tree level $W^{\pm}$ production follows the Drell-Yan distribution $(1 \mp \cos\theta)^2$ [25], if only valence quarks contribute, where θ is the azimuthal angle of the charged lepton from the W decay in the W's center of mass frame and the positive z-axis has the direction of the proton in the laboratory frame. The Drell-Yan process describes the production of a vector boson from a collision of two quarks; quark-gluon interactions are not included.

The differential cross section becomes much more complicated, when the transverse momentum of the W is non-negligible. This is the case, when the W is produced in association with a jet of hadrons. The jet is the result of the hadronization of a parton coming out of the interaction point. The Feynman diagram for this process can be seen in Figure 2.2. Here, c is an outgoing gluon or quark producing a jet of hadrons. The diagrams in the interaction blob is not explicitly shown, because there

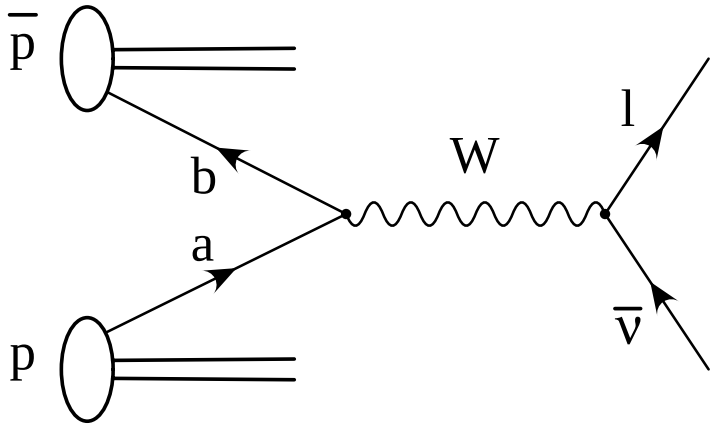

Figure 2.1 W production at tree level and low p_T at a $p\bar{p}$ collider.

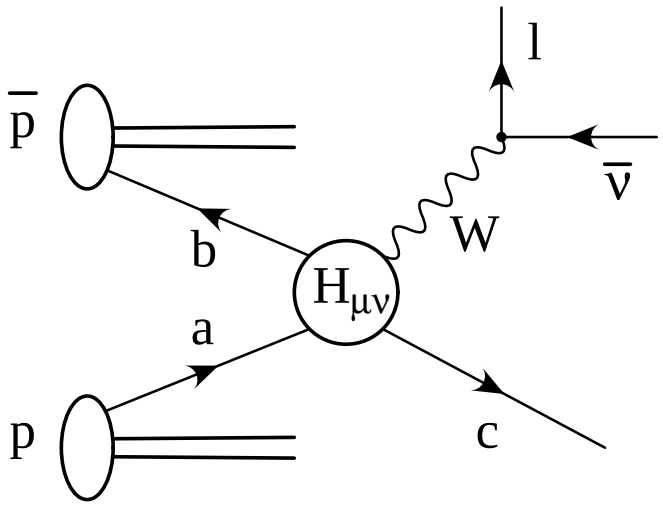

Figure 2.2 W production in association with a jet at high p_T at a $p\bar{p}$ collider.

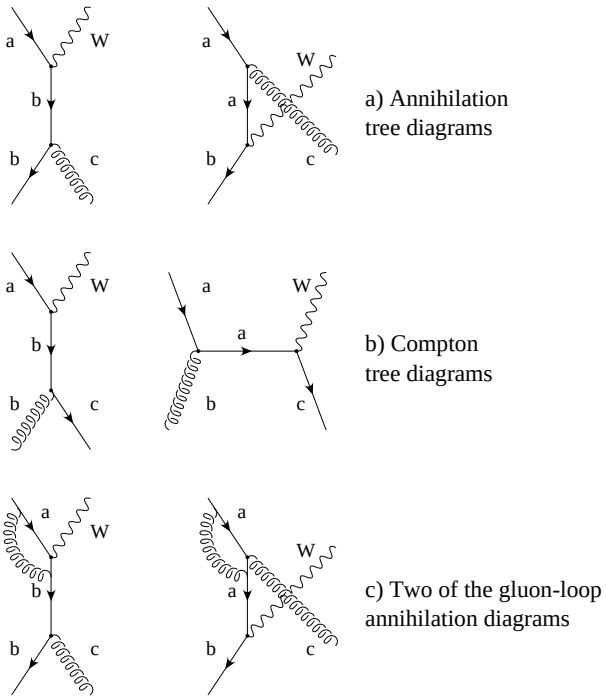

Figure 2.3 Feynman Diagrams for the W+1jet production.

are many processes that can contribute to the interaction with the same incoming and outgoing particles. The most common higher-order process is the quark-antiquark annihilation with an outgoing gluon jet. The tree level annihilation Feynman diagrams are shown in Figure 2.3a.

The quark-gluon interactions cannot be neglected in W+jet production. In fact, the interaction of the quark from one nucleon with a gluon from the other results in Compton Feynman diagrams with a quark propagator. The tree level Compton diagrams can be seen in Figure 2.3b. In that case, the jet comes from the hadronization of a quark. The interaction blob can also include second order Compton or Annihilation diagrams (with the appearance of a gluon loop) as shown in Figure 2.3c.

We will systematically [26] study the interaction of Figure 2.2. Two incoming partons a and b (4-momenta p_1 and p_2) collide and produce an outgoing W (4-momentum q) which decays into a charged lepton (4-momentum k_1) and its antineutrino (4-momentum k_2), and an outgoing parton c (4-momentum $p_1 + p_2 - q$) which hadronizes into a jet. The interaction may include Compton or Annihilation diagrams at any

QCD order of perturbation. It is common to use the following kinematic variables:

$$P = p_1 + p_2$$
$$p = p_1 - p_2$$
$$q = k_1 + k_2$$
$$k = k_1 - k_2$$

Using Equation (A.73) the *partonic cross section* for the colliding partons a and b becomes

$$\frac{d\hat{\sigma}_{ab}}{d(p_T^W)^2 dy d\Omega} = K_{ab}^W L_{\mu\nu} H_{ab}^{\mu\nu}, \tag{2.1}$$

where p_T^W is the transverse momentum of the W, Ω is the solid angle of the charged lepton in the W rest frame and y is the rapidity of the W corresponding to its energy and longitudinal momentum. y is defined as

$$y = \frac{1}{2}\ln(\frac{E^W + p_z^W}{E^W - p_z^W}), \tag{2.2}$$

where E^W is the energy and p_z^W is the longitudinal momentum of the W boson in the laboratory frame. K_{ab}^W is a constant that contains the electroweak and strong couplings, phase space factors, spin average factors, the gauge boson propagator, the mass scale of the interaction and the renormalization scale of the subprocess. $L_{\mu\nu}$ and $H_{ab}^{\mu\nu}$ are the leptonic and hadronic tensors respectively, related to the spinors of the interacting particles and the kind of interaction. After summing over all the spin states of the leptons, according to Equation (A.74), the leptonic tensor is given by

$$L_{\mu\nu}(q,k) = g_{\mu\nu} - \frac{q_\mu q_\nu}{q^2} - \frac{k_\mu k_\nu}{k^2}. \tag{2.3}$$

The form of the hadronic tensor is more complicated than the tree level one presented in Appendix A (Equation (A.75)), and it is related to the processes that are hidden in the blob of Figure 2.2. For a model-independent description of the hadronic tensor, we need to construct it out of $g^{\mu\nu}$, p, P and q. We will only keep the symmetric terms in the hadronic tensor, since it is going to be contracted with the symmetric

leptonic tensor (see Equation (2.3)). In any case, the hadronic tensor needs to be orthogonal to q^μ ($q^\mu H_{\mu\nu} = H_{\mu\nu} q_\nu = 0$). Hence, we construct the tensor out of the tilded quantities $\tilde{g}^{\mu\nu}$, $\tilde{p}$, $\tilde{P}$ and $\tilde{q}$, where $\tilde{g}^{\mu\nu} = g^{\mu\nu} - q^\mu q^\nu / q^2$ and $\tilde{p}_\mu = p_\mu - pq/Q^2 q_\mu$, with similar relations for $\tilde{P}$ and $\tilde{q}$. So we can write

$$H_{\mu\nu}(p, P, q) = \sum_i H_i' P_i^{\mu\nu}, \tag{2.4}$$

where $P_i^{\mu\nu}(\tilde{p}, \tilde{P}, \tilde{q})$ are the *projection operators* and $H_i'(s, M^2, qp, qP)$ are the *invariant structure functions* which depend on the invariant variables s, M^2, qp, qP ($s = -P^2$, $M^2 = -q^2$, $pP = kq = 0$).

Using Equations (2.1), (2.3) and (2.4) we get

$$\frac{d\hat{\sigma}_{ab}}{d(p_T^W)^2 dy d\Omega} = \frac{d\hat{\sigma}_{ab}}{d(p_T^W)^2 dy d\theta_1 d\theta_2 d\phi} = \sum_i H_i' F_i(\theta_1, \theta_2, \phi), \tag{2.5}$$

where F_i are functions of θ_1 and θ_2 (the polar angles of the two leptons) and ϕ (the angle between the lepton production planes), measured in the hadrons center of mass. There is a problem in the formula above: the hadronic and leptonic degrees of freedom are not manifestly separated. For fixed arguments of the structure functions (hadronic variables) only two of the θ_1, θ_2, ϕ are independent. To solve this problem we introduce the *helicity amplitudes* $H_{ab}^{\sigma\sigma'}$ defined as

$$H_{ab}^{\sigma\sigma'}(s, M^2, qp, qP) = \epsilon_\mu(\sigma) H_{ab}^{\mu\nu}(p, P, q) \epsilon_\nu^*(\sigma'), \tag{2.6}$$

where $\epsilon_\mu(\sigma)$ are the polarization vectors for the gauge boson in its rest frame. For the Collins-Soper frame W rest frame [27], the W polarization vectors are $\epsilon_\mu(\pm) = \frac{1}{2}\sqrt{2}(0; \pm 1, -i, 0)$ and $\epsilon_\mu(0) = (0; 0, 0, 1)$. We are now able to define the *helicity structure functions* H_α which are linear combinations of the helicity amplitudes, or equivalently, the space components of the hadronic tensor.

$$H_\alpha = f_1(H_{ab}^{\sigma\sigma'}) = f_2(H_{ab}^{ij}), \quad i, j = 1, 2, 3. \tag{2.7}$$

The number of non-zero helicity structure functions depends on the intermediate

states we allow in the blob of Figure 2.2. For only tree level W production with no jet, there are two of them (H_{-1} and H_4). For tree level production of a W with an outgoing parton (jet) we have six helicity structure functions ($H_{-1} - H_4$). If we include second order (i.e., a gluon loop) processes, then there are nine helicity structure functions which contribute to the total cross section. These helicity structure functions are [21]

$$\begin{aligned}
H_{-1} &\equiv H^{00} + H^{++} + H^{--} = H_{11} + H_{22} + H_{33} \\
H_0 &\equiv H^{00} = H_{33} \\
H_1 &\equiv \frac{1}{4}(H^{+0} + H^{0+} - H^{-0} - H^{0-}) = -\frac{1}{2\sqrt{2}}(H_{31} + H_{13}) \\
H_2 &\equiv \frac{1}{2}(H^{+-} + H^{-+}) = \frac{1}{2}(H_{22} - H_{11}) \\
H_3 &\equiv \frac{1}{4}(H^{+0} + H^{0+} + H^{-0} + H^{0-}) = -\frac{i}{2\sqrt{2}}(H_{23} - H_{32}) \\
H_4 &\equiv H^{++} - H^{--} = -i(H_{12} - H_{21}) \\
H_5 &\equiv -\frac{i}{2}(H^{+-} - H^{-+}) = -\frac{1}{2}(H_{21} + H_{12}) \\
H_6 &\equiv -\frac{i}{4}(H^{+0} - H^{0+} + H^{-0} - H^{0-}) = -\frac{1}{2\sqrt{2}}(H_{23} + H_{32}) \\
H_7 &\equiv -\frac{i}{4}(H^{+0} - H^{0+} - H^{-0} + H^{0-}) = -\frac{i}{2\sqrt{2}}(H_{31} - H_{13}).
\end{aligned}$$

We have nine Equations with nine unknowns (the space components of the hadronic tensors). The helicity structure functions of the equation above are defined so that if we solve for the $H_{\mu\nu}$ and replace in Equation (2.1) we get the following expression for the cross section at the parton level:

$$\begin{aligned}
\frac{d\hat{\sigma}_{ab}}{d(p_T^W)^2 dy d\Omega} &= K_{ab}^W L_{\mu\nu} H_{ab}^{\mu\nu} = \sum_{\alpha=-1}^{7} g_\alpha(\theta,\phi) K_{ab}^W H_\alpha(p_T^W, y) \\
&= \sum_{\alpha=-1}^{7} \frac{3}{16\pi} g_\alpha(\theta,\phi) \frac{d\hat{\sigma}_{ab}^\alpha}{d(p_T^W)^2 dy}, \qquad (2.8)
\end{aligned}$$

where

$$\frac{d\hat{\sigma}_{ab}^\alpha}{d(p_T^W)^2 dy} = \frac{16\pi}{3} K_{ab}^W H_\alpha(p_T^W, y) \qquad (2.9)$$

are the *partonic helicity cross sections*, θ and ϕ give us the direction of the charged lepton in the Collins-Soper W rest frame, p_T^W and y are directly related to the hadronic variables and the $g_a(\theta,\phi)$ functions are

$$\begin{aligned}
g_{-1}(\theta,\phi) &= 1+\cos^2\theta \\
g_0(\theta,\phi) &= 1-3\cos^2\theta \\
g_1(\theta,\phi) &= 2\sqrt{2}\sin 2\theta\cos\phi \\
g_2(\theta,\phi) &= 2\sin^2\theta\cos 2\phi \\
g_3(\theta,\phi) &= 4\sqrt{2}\sin\theta\cos\phi \\
g_4(\theta,\phi) &= 2\cos\theta \\
g_5(\theta,\phi) &= 2\sin^2\theta\sin 2\phi \\
g_6(\theta,\phi) &= 2\sqrt{2}\sin 2\theta\sin\phi \\
g_7(\theta,\phi) &= 4\sqrt{2}\sin\theta\sin\phi. \qquad (2.10)
\end{aligned}$$

In order to get the total *hadronic cross section*, we have to convolute the partonic cross section with the parton distribution functions f_a and f_b and sum over all processes

$$\frac{d\sigma}{d(p_T^W)^2 dy d\Omega} = \sum_{a,b}\int dx_1 dx_2 f_a(x_1,M^2) f_b(x_2,M^2)\frac{d\hat{\sigma}_{ab}}{d(p_T^W)^2 dy d\Omega}, \qquad (2.11)$$

where x_1 and x_2 are the momentum fractions of the partons a and b inside the proton and the antiproton. We can also write the expression above as

$$\frac{d\sigma}{d(p_T^W)^2 dy d\Omega} = \sum_{\alpha=-1}^{7}\frac{3}{16\pi}g_\alpha(\theta,\phi)\frac{d\sigma^\alpha}{d(p_T^W)^2 dy}, \qquad (2.12)$$

where

$$\frac{d\sigma^\alpha}{d(p_T^W)^2 dy} = \sum_{a,b}\int dx_1 dx_2 f_a(x_1,M^2) f_b(x_2,M^2)\frac{d\hat{\sigma}^\alpha_{ab}}{d(p_T^W)^2 dy} \qquad (2.13)$$

are the *hadronic helicity cross sections*.

We now define the *standard angular coefficients*

$$\begin{aligned}
A_0 &= 2\frac{d\sigma^0}{d\sigma^{-1}}, \qquad A_1 = 2\sqrt{2}\frac{d\sigma^1}{d\sigma^{-1}}, \quad A_2 = 4\frac{d\sigma^2}{d\sigma^{-1}}, \\
A_3 &= 4\sqrt{2}\frac{d\sigma^3}{d\sigma^{-1}}, \quad A_4 = 2\frac{d\sigma^4}{d\sigma^{-1}}, \qquad A_5 = 2\frac{d\sigma^5}{d\sigma^{-1}}, \\
A_6 &= 2\sqrt{2}\frac{d\sigma^6}{d\sigma^{-1}}, \quad A_7 = 4\sqrt{2}\frac{d\sigma^7}{d\sigma^{-1}}.
\end{aligned} \tag{2.14}$$

Using the angular coefficients of Equations (2.14) and the g_a functions of Equations (2.10) along with Equation (2.12), we get the following standard expression for the total hadronic cross section of the W:

$$\begin{aligned}
\frac{d\sigma}{d(p_T^W)^2 dy d\cos\theta d\phi} &= \frac{3}{16\pi}\frac{d\sigma^{-1}}{d(p_T^W)^2 dy}[(1+\cos^2\theta) \\
&+ \frac{1}{2}A_0(1-3\cos^2\theta) + A_1\sin 2\theta\cos\phi \\
&+ \frac{1}{2}A_2\sin^2\theta\cos 2\phi + A_3\sin\theta\cos\phi \\
&+ A_4\cos\theta + A_5\sin^2\theta\sin 2\phi \\
&+ A_6\sin 2\theta\sin\phi + A_7\sin\theta\sin\phi].
\end{aligned} \tag{2.15}$$

In contrast to Equation (2.5), the dependence of the hadronic cross section on the leptonic variables θ and ϕ is completely manifest in Equation (2.15) and the dependence on the hadronic variables $(p_T^W)^2$ and y is completely hidden inside the angular coefficients. This allows us to treat the problem in a model-independent manner since all the hadronic physics is described implicitly by the helicity structure functions and it is decoupled from the well understood lepton physics.

If the W is produced with no transverse momentum, it is polarized along the beam axis, due to the $V-A$ nature of the weak interactions and Helicity conservation. In that case, A_4 is the only non-zero coefficient. If only valence quarks contributed to the $W^{\pm}$ production, A_4 would equal ∓ 2, and the angular distribution (2.15) would be proportional to $(1\mp\cos\theta)^2$, a result that was verified by the UA1 experiment [11].

If the W is produced with non-negligible transverse momentum balanced by the associative production of jets, the rest of the angular coefficients ($A_{i\neq 4}$) are non-zero and the cross section depends on the azimuthal angle ϕ as well. The last three angular coefficients (A_5, A_6, and A_7) are non-zero, only if gluon loops are present in the production of the W. Therefore, in order to study all the angular coefficients and associated helicity cross sections of the W in a hadron collider, we have to consider the production of the W with QCD effects up to order α_s^2.[†]

It is common to integrate Equation (2.15) over one of the angles, in order to get simpler relations, which are also easier to study experimentally. Equation (2.15) is also usually integrated over the rapidity y of the W, which is not determined experimentally, leading to the study of the y-integrated angular coefficients. If we integrate Equation (2.15) over ϕ and y, we get

$$\frac{d\sigma}{d(p_T^W)^2 d\cos\theta} = C(1 + \alpha_1 \cos\theta + \alpha_2 \cos^2\theta) \tag{2.16}$$

where

$$C = \frac{3}{8}\frac{d\sigma}{d(p_T^W)^2}[1 + \frac{A_0}{2}], \quad \alpha_1 = \frac{2A_4}{2 + A_0}, \quad \alpha_2 = \frac{2 - 3A_0}{2 + A_0} \tag{2.17}$$

If we integrate Equation (2.15) over $\cos\theta$ and y, we get

$$\frac{d\sigma}{d(p_T^W)^2 d\phi} = C'(1 + \beta_1 \cos\phi + \beta_2 \cos 2\phi + \beta_3 \sin\phi + \beta_4 \sin 2\phi) \tag{2.18}$$

where

$$C' = \frac{1}{2\pi}\frac{d\sigma}{d(p_T^W)^2}, \quad \beta_1 = \frac{3\pi}{16}A_3, \quad \beta_2 = \frac{A_2}{4}$$
$$\beta_3 = \frac{3\pi}{16}A_7, \quad \beta_4 = \frac{A_5}{2} \tag{2.19}$$

Finally, if we integrate Equation (2.15) over $\cos\theta$, ϕ, and y, we get

$$\int \frac{d\sigma}{d(p_T^W)^2 d\cos\theta d\phi} d\cos\theta d\phi = \frac{d\sigma^{-1}}{d(p_T^W)^2}. \tag{2.20}$$

[†] $\alpha_s \equiv g_s/4\pi$ is the strong coupling constant. For a definition of g_s, see Section A.4.

We conclude that the cross section on the right-hand side of Equation (2.20) is the *unpolarized total cross section*.

2.2 Standard Model Prediction for the W Angular Coefficients

In this section, we derive the Standard Model prediction for the W angular coefficients. Three of these coefficients (A_1, A_4 and A_6) are presented for the first time.

If we define Equation (2.15) to describe the W^- production, this equation has to be CP-transformed, to describe the W^+ bosons. Parity transformation does not affect the y-integrated angular coefficients studied in this thesis, but it does change the sign of some of the $g_i(\cos\theta, \phi)$ functions. In the Collins-Soper frame, parity transformation of the W takes θ to $\pi - \theta$ and leaves ϕ unchanged, hence the $g_{1,4,6}(\cos\theta, \phi)$ are parity-odd. If we CP transform both the incoming and outgoing particles, then we also transform the Collins-Soper frame. In that case, the A_i angular coefficients and the g_i functions are the same for both charges of the W bosons, as expected from CP conservation. On the other hand, if we keep the Collins-Soper frame unchanged, based on the proton direction in the laboratory, then we have to multiply the coefficients A_1, A_4, and A_6 in Equation (2.15) by (-1), to correctly describe the W^+ bosons. In this thesis we keep the colliding proton-antiproton system and the definition of the Collins-Soper frame fixed, and we study the angular coefficients and helicity cross sections for the W^- bosons. To increase the statistics of our samples, we CP transform the W^+ bosons and we include them in our sample.

We generate W+jet events up to order α_s^2, including up to one gluon loop, at $\sqrt{s} =$ 1.8 TeV, using the DYRAD Monte Carlo event generator [28] described in Chapter 5. We measure the θ and ϕ angles of the charged lepton in the Collins-Soper (CS) W rest frame, shown in Figure 2.4. The CS frame is the rest frame of the W, where the z-axis bisects the angle between the proton momentum ($\vec{p}_{\rm CS}$) and the opposite of the antiproton momentum ($-\vec{\bar{p}}_{\rm CS}$). The CS frame is unique, in the sense that the ϕ and $|\cos\theta|$ of the charged lepton are known, even though the longitudinal momentum of the neutrino ($\vec{p}_z^{\,\nu}$) is not measurable.

The signs of the angular coefficients depend on the orientation of the Collins-Soper

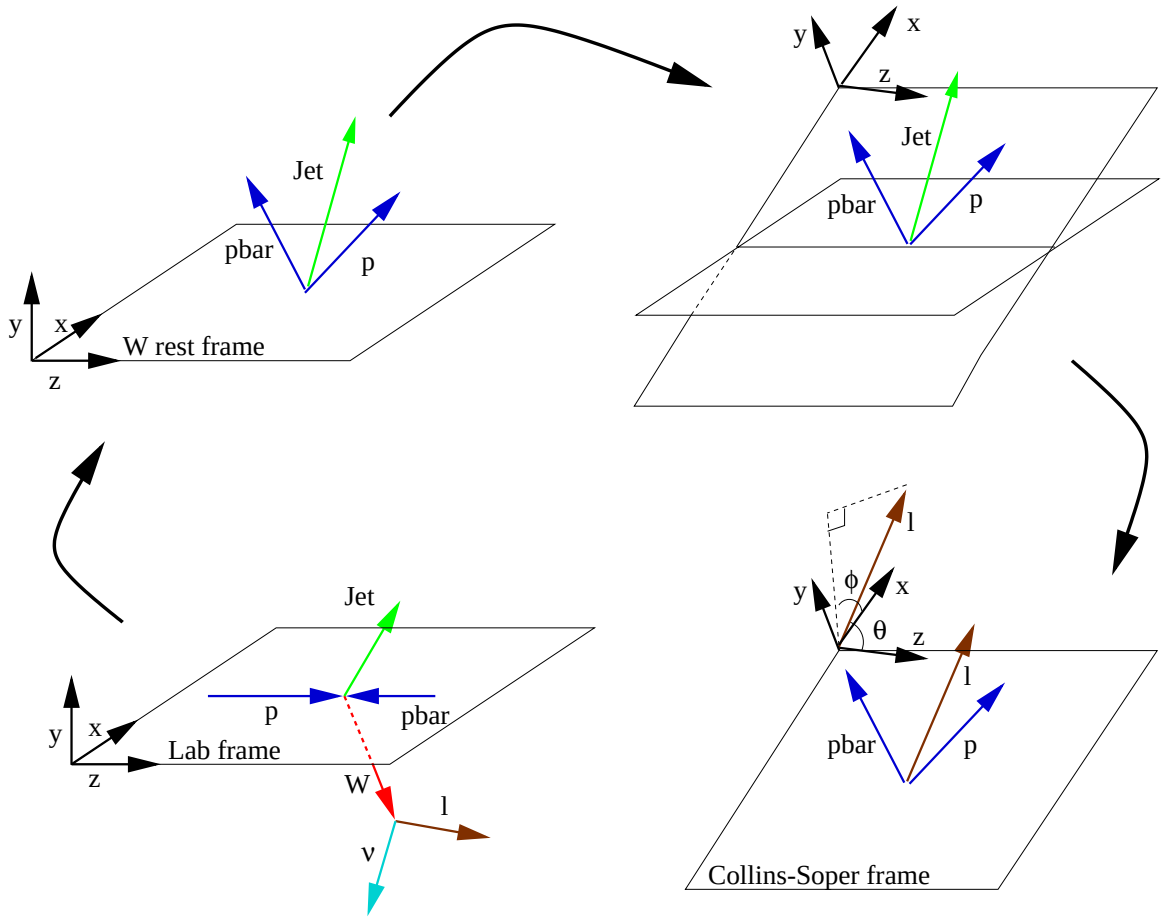

Figure 2.4 Going from the lab frame to the Collins-Soper frame. First, we boost to the W rest-frame, then we rotate the $x-z$ plane so it coincides with the $\vec{p}-\vec{\bar{p}}$ plane. Finally, we rotate the frame around the y-axis so the z-axis bisects the angle between $\vec{p}$ and $-\vec{\bar{p}}$). The positive y-axis is selected to have the same direction as $\vec{p}_{\rm CS} \times \vec{\bar{p}}_{\rm CS}$.

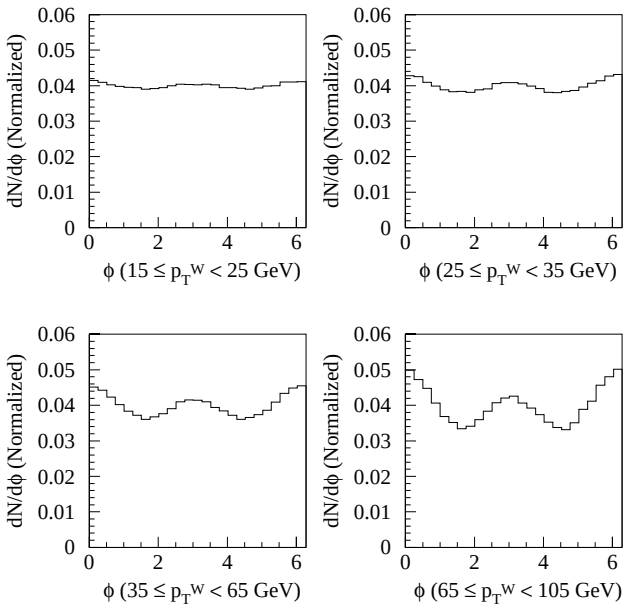

Figure 2.5 The Standard Model distributions of the Collins-Soper azimuthal angle of the charged lepton from W+jet events, for four p_T^W regions.

x and y axes. We define the x and y axes so that the $x-z$ plane coincides with the $\vec{p}_{\rm CS}-\vec{\bar{p}}_{\rm CS}$ plane and the positive y-axis has the same direction as $\vec{p}_{\rm CS}\times\vec{\bar{p}}_{\rm CS}$. The set of transformations we perform to the laboratory 4-momenta in order to go to the Collins-Soper frame are:

- Boost along the laboratory z-axis, so that the W has zero longitudinal momentum,
- Boost along the direction of the transverse momentum of the W, so that the W is at rest,
- Rotation about the z-axis, so that the proton momentum lies on the $x-z$ plane,
- Rotation about the y-axis, so that the proton momentum lies along the positive z-axis,
- Rotation about the y-axis, so that the z-axis bisects the proton momentum and the opposite of the antiproton momentum.

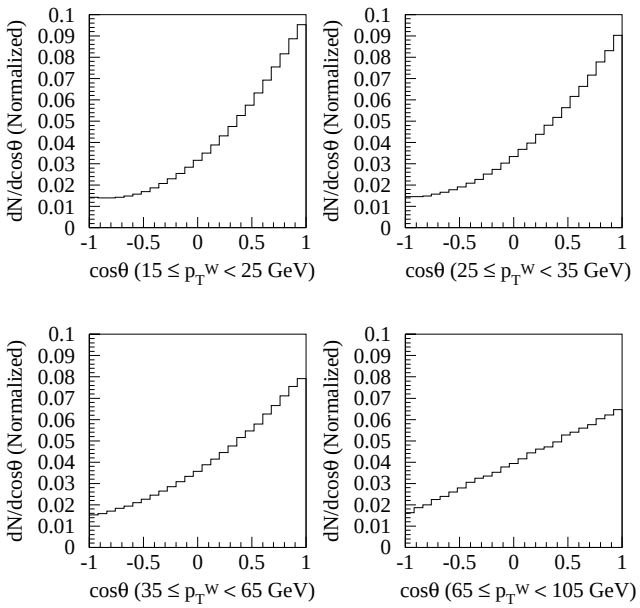

Figure 2.6 The Standard Model distributions of the cosine of the Collins-Soper polar angle of the charged lepton from W+jet events, for four p_T^W regions.

The SM distributions of ϕ and $\cos\theta$ for four p_T^W bins (15–25, 25–35, 35–65 and 65–105 GeV) can be seen in Figures 2.5 and 2.6 respectively. We note that at low transverse momentum of the W, the ϕ-distribution is almost flat, whereas the θ-distribution follows the $(1+\cos\theta)^2$ law. At the fourth p_T^W bin, there is a strong ϕ dependence of the cross section, and the θ distribution is almost a straight line (the $|\cos\theta|$ distribution is flat). There is a correlation between $\cos\theta$ and M_T^W, with the low $\cos\theta$ corresponding to low M_T^W events, as seen in Figure B.4 of Appendix B.

To calculate the angular coefficients from the angles of the charged lepton, we use the method of moments. First, we define the *moment* of the function $m(\theta,\phi)$ as

$$< m(\theta,\phi) >= \frac{\int\int d\sigma(p_T^W, y, \theta, \phi) m(\theta,\phi) d\cos\theta d\phi}{\int\int d\sigma(p_T^W, y, \theta, \phi) d\cos\theta d\phi}. \tag{2.21}$$

We can easily prove that

$$< m_0 > \equiv < \frac{1}{2}(1 - 3\cos^2\theta) >= \frac{3}{20}(A_0 - \frac{2}{3})$$

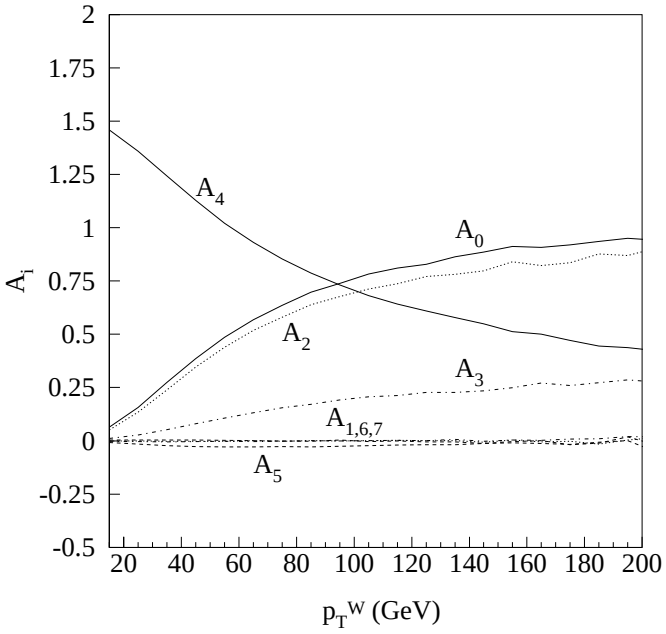

Figure 2.7 The W angular coefficients up to order α_s^2.

$$
\begin{aligned}
< m_1 > &\equiv < \sin 2\theta \cos\phi >= \frac{1}{5} A_1 \\
< m_2 > &\equiv < \sin^2\theta \cos 2\phi >= \frac{1}{10} A_2 \\
< m_3 > &\equiv < \sin\theta \cos\phi >= \frac{1}{4} A_3 \\
< m_4 > &\equiv < \cos\theta >= \frac{1}{4} A_4 \\
< m_5 > &\equiv < \sin^2\theta \sin 2\phi >= \frac{1}{5} A_5 \\
< m_6 > &\equiv < \sin 2\theta \sin\phi >= \frac{1}{5} A_6 \\
< m_7 > &\equiv < \sin\theta \sin\phi >= \frac{1}{4} A_7
\end{aligned}
\tag{2.22}
$$

For a set of discrete data from a Monte Carlo event generator, we replace the integrals of Equation (2.21) by sums and the cross section values by the weights w_i of the events. The moments become

$$
< m(\theta,\phi) >= \frac{\sum_{i=1}^{N} m(\theta_i,\phi_i) w_i}{\sum_{i=1}^{N} w_i} \tag{2.23}
$$

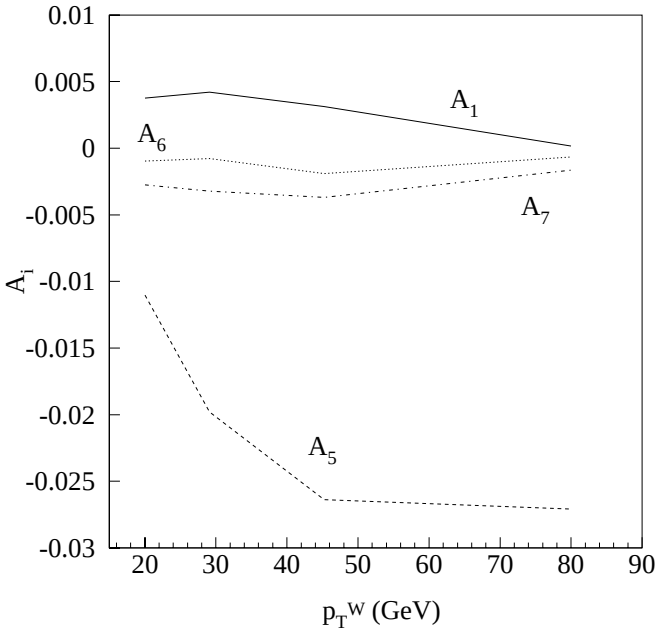

Figure 2.8 A_1 and the NLO angular coefficients A_5, A_6, and A_7 for the production of the W up to order α_s^2.

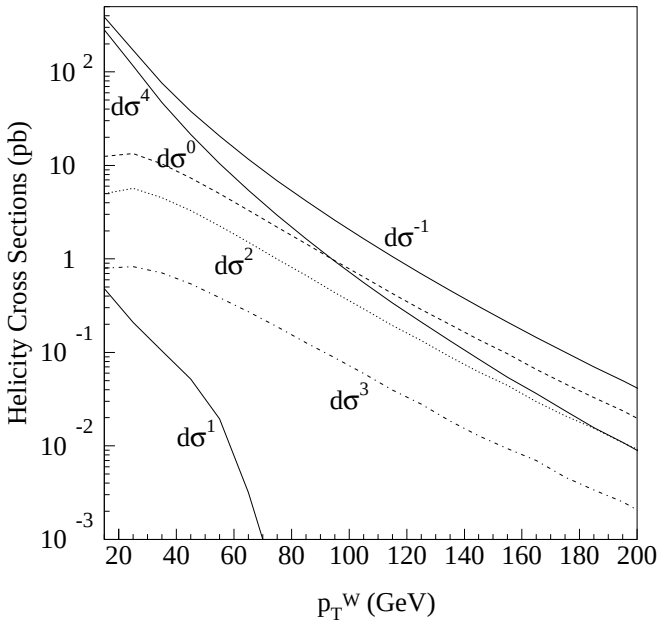

Figure 2.9 The W helicity cross sections up to order α_s^2.

If we solve Equations (2.22) for the angular coefficients and substitute the moments with the discrete expressions of Equations (2.23), we extract the Standard Model prediction. Ignoring the W rapidity, we actually calculate the y-integrated angular coefficients, which are now functions only of p_T^W. The results are presented in Figure 2.7. There are infrared and colinear singularities associated with the theoretical calculation for $p_T^W < 10$ GeV, and this determines the minimum of the p_T^W-axis. The maximum of the axis is determined by statistics.

We notice that A_4 is the only surviving coefficient at low p_T^W values, as expected. It is also the only one that decreases as the p_T^W increases. A_1, although it is a leading-order coefficient, is much smaller than $A_{0,2,3,4}$ and comparable to the next-to-leading order ones $A_{5,6,7}$. The coefficients A_0 and A_2 would be exactly equal if gluon loops were not included. At order α_s^2, A_0 is consistently greater than A_2. To better measure A_1 and $A_{5,6,7}$ we use the four p_T^W bins, to improve the statistics. The result is shown in Figure 2.8. Using Equations (2.14) that directly connect the angular coefficients with the Helicity cross sections of the W, extracting the unpolarized cross section of the W as a function of p_T^W at the generator level, and using our measurement of the angular coefficients, we arrive in the Standard Model prediction for the W helicity cross sections at $\sqrt{s} = 1.8$ TeV, as shown in Figure 2.9.

Chapter 3

The CDF Experiment

3.1 The Tevatron Collider at Fermilab

The Fermilab Tevatron collider, located close to Chicago in the state of Illinois, is currently the most powerful particle accelerator in the world, accelerating protons and antiprotons up to an energy of 0.9 TeV or equivalently 1.8 TeV in the center of mass of the colliding particles. The reason antiprotons are used, although their production, cooling and storage is involved, is the higher production rates for many processes that are present in a proton-antiproton collider at about 2 TeV. At higher energies this advantage diminishes, so the future Large Hadron Collider (LHC) at CERN will be a proton-proton collider (to operate at 14 TeV in the center of mass). Another advantage of a proton-antiproton collider is that the same sets of magnets can be used to control the trajectory of both particles of opposite charge moving in opposite directions. Figure 3.1 illustrates the Fermilab Accelerator System. We describe here the Accelerator system used for collider Run Ia (1992-1993) and Run Ib (1994-1995).

The protons are accelerated in many stages. We start with gaseous Hydrogen which is injected into the ion magnetron source and it is negatively ionized. The H^- ions are extracted from the source at 18-20 KeV, and the beam has a current of 50-55 mA. One bottle of Hydrogen can supply protons for a period of 4–6 months. A 90° bending magnet is used to compensate for the large asymmetry in the two transverse axes and to obtain an almost circular beam. The beam is electrostatically accelerated by a 3-staged diode-capacitor voltage multiplier, called the *Cockcroft-*

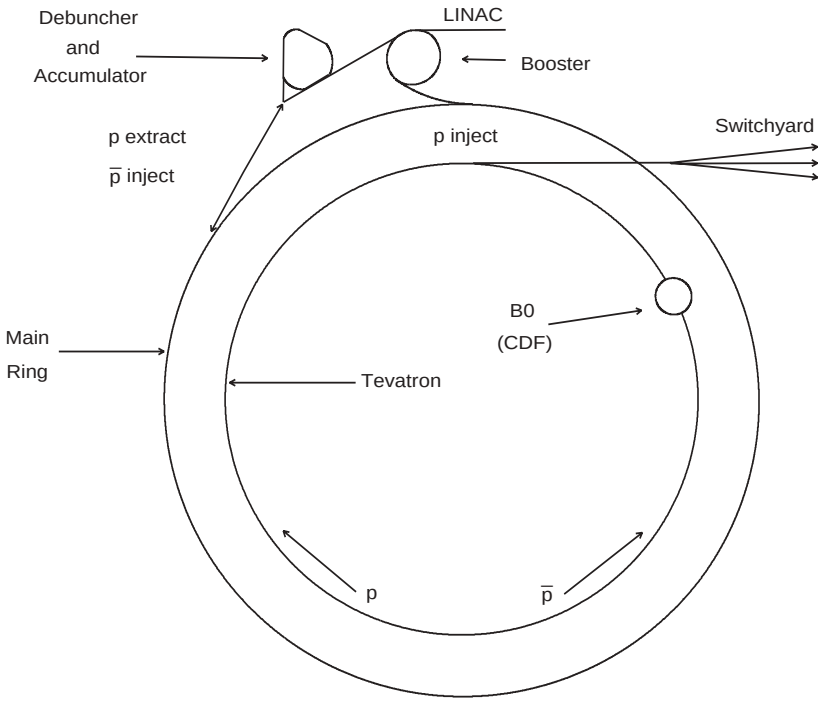

Figure 3.1 The Fermilab Accelerator System. The picture is not in scale and the Main Ring and Tevatron share the same tunnel.

Walton preaccelerator, to 750 KeV.

Subsequently the ion beam is transmitted to a 150 m long linear accelerator (*Alvarez Linac*) [29, 30, 31, 32] consisting of a series of drift tubes with 201.25 MHz radio-frequency (RF) AC voltage. The lengths of the drift tubes gradually increase as the H^- are accelerated, so that the anions are always in the tubes when the direction of the electric field is opposite to the acceleration direction, and they are accelerated only when they are in the gaps between the tubes and the electric field has the forward direction. RF cavities are used because they operate in only one frequency (the frequency of the standing wave defined by the cavities geometry) while all other noise frequencies are rejected.

Until 1993 (Run Ia) the Linac consisted of nine 201.25 MHz drift tubes and the final energy of the ion beam was 200 MeV. After 1993 (Run Ib), only the first five 201.25 MHz drift tubes are used (old part of the Linac) and accelerate the beam to 116 MeV. After passing a 4 meter radio-frequency transition section, which matches the 201.25 MHz old part of the Linac with the new 805 MHz one, the ions are accelerated to 400 MeV by a series of seven 805 MHz side-coupled cavity structures. The higher frequency allows higher accelerating gradients (average axial field became $E_0 = 8$ MV/m, three times better than the drift tubes one). The frequency is limited by the probability of appearance of sparks and is given by the formula

$$f = 1.643 E_k^2 e^{-8.5/E_k}, \tag{3.1}$$

where E_k is the conventional Kilpatrick limit on the surface field to avoid sparking and $1.643E_k$ is the maximum surface field. The old part of the Linac is powered by triodes and the new one by klystrons. The H^- beam passes through a carbon foil which removes the electrons leaving protons at 400 MeV. The energy upgrade of the Linac led to increased proton brightness intensity delivered to the rest of the accelerating system, reduced the beam emittance degradation in the 8 GeV Booster accelerator following the Linac and increased the total intensity of the antiprotons. A typical Linac pulse is 40 μs wide and includes 4,000 bunches and 6 trillion protons in total. A bunch is a collection of particles that are collectively handled by the

accelerating, cooling or storing systems. The horizontal emittance of the linac beam is 6π mm-mrad and the vertical emittance is 5π mm-mrad for ions at 400 MeV. The emittance ϵ of a beam is defined as

$$\epsilon = \sqrt{\sigma_y^2 \sigma_{y'}^2 - \sigma_{yy'}^2}, \tag{3.2}$$

where y is one of the transverse space coordinates (horizontal x pointing outwards, or vertical z pointing upwards), y' is the space coordinate differentiated with respect to s (the space coordinate along the beam direction), σ_y and $\sigma_{y'}$ are the RMS beam widths corresponding to y and y' ($\sigma_y = \sqrt{\langle y^2 \rangle}$, $\sigma_{y'} = \sqrt{\langle y'^2 \rangle}$), and $\sigma_{yy'}$ is the correlation between them ($\sigma_{yy'} = \langle y \cdot y' \rangle$). There is a horizontal and vertical emittance and their values are a measure of the transverse size of the beam. The Linac beam has a peak current of 45 mA and its transfer to Booster accelerator is 98% efficient.

The next acceleration stage is the Booster [38, 39, 33], an alternating circular synchrotron, 500 feet in diameter, which accelerates the protons through 17 RF cavities up to an energy of 8 GeV in 0.0333 seconds. In that interval the beam goes around the Booster 16,000 times. Because the circumference of the Booster is only 2.2 μs long, the Linac beam must be wrapped around the Booster many times. The synchrotrons have two kinds of magnets: dipoles for bending the beam and quadrupoles for focusing. Because the quadrupole magnets focus in one direction and defocus in the orthogonal direction, alternate focusing and defocusing magnets are used (by continuously reversing the magnets polarity), so that stability is achieved overall in both directions. This method is called *strong focusing*. In the Booster, the bending and focusing functions are combined in the same conventional magnets made of copper water-cooled coils. Ninety six such magnets are used. Unlike the Linac, the synchrotron-accelerated particles pass many times through the same RF cavities and magnets, so the radio-frequencies and magnetic fields must increase with time and be synchronized with the beam acceleration, hence the term synchrotron. Seventeen RF cavities of frequency ranging from 30 to 53 Hz are employed. Increasing the magnetic field allows us to keep the particles in the same circular orbit. The protons in a synchrotron-accelerated bunch participate in transverse oscillations, called *betatron*

oscillations, which are originated from small divergences of the originally injected beam, small asymmetries in the magnet alignments and other deviations. The protons also undergo longitudinal oscillations called *synchrotron oscillations*, which are due to the fact that some particles are slightly faster or slightly slower than the center of the bunch, which is in synchronous phase. Fortunately, the RF system is such that the faster particles receive a smaller RF kick and the slower ones a larger RF kick and the dynamic stability is achieved through synchrotron oscillations. The particles oscillate around the equilibrium point within the bunch. The nominal Booster horizontal and vertical tunes (number of betatron oscillations during one revolution) are 6.7 and 6.8 and the synchrotron tune (number of synchrotron oscillations during one revolution) is $\nu_s = 0.075$. The transition gamma of the booster is $\gamma_t = 5.445$ and the harmonic number of the ring is $h = 84$. The transition gamma times mc gives us the momentum for isochronous revolution of a particle. If $p > \gamma_t mc$, the particle will have revolution period shorter than that of a synchronous particle, whereas the opposite is true for a particle with $p < \gamma_t mc$. The harmonic number times the revolution frequency defines the RF frequency of the cavities. The harmonic number $h = 84$ means that the Booster RF must sweep from 30 to 53 MHz during the 33.3 msec acceleration interval. The Booster loads 9–13 pulses (bunches) of 8 GeV protons beam into the Main Ring.

The Main Ring [29, 33, 34, 35, 36, 37] is a synchrotron with a radius of one kilometer, and 1011 conventional magnets: 771 Dipoles for bending and 240 Quadrupoles for focusing. There are also two overpasses to accommodate the experimental areas of the CDF and D0 detectors, making the Main Ring one of the truly non-planar accelerators in the world. The Main Ring accelerates the protons and the antiprotons through two separate RF systems of eight cavities each. The RF frequency is controlled by feedback control systems as the protons and antiprotons are accelerated to 150 GeV, which is the energy of the beams at the time they are injected to the Tevatron accelerator. The final frequency of the cavities is 53 MHz, with a harmonic number $h = 1113$. The Main Ring also produces the 120 GeV proton beam used for the production of antiprotons. The particle bunches are combined into a single high intensity bunch before being injected to the Tevatron; this process is called *bunch*

coalescing. This is done with two RF bunch phase space rotations before extraction: the first one is to lower the beam energy spread and it takes place in normal Main Ring RF bucket ($h = 1113$, $f = 53$ MHz) with some additional linearizing ($h = 2226$, $f = 106$ MHz). The second rotation is for a quarter of a synchrotron period in a low frequency bucket ($h = 53$, $f = 2.5$ MHz), with some additional linearizing ($h = 106$, $f = 5$ MHz). This rotated ensemble of bunches is then recaptured in a single bucket ($h = 1113$, $f = 53$ MHz) and injected into the Tevatron. Note that all (h, f) combinations of the RF systems, correspond to the same rotational frequency of the protons in the Main Ring, which is 47.6 KHz for protons having speed almost equal to the speed of light. The efficiency of the coalescing process is a function of both the initial and longitudinal emittances of the individual bunches and the RF voltages available for the $h = 53$ bunch rotation (and its $h = 106$ linearization). This is the reason why the $h = 53$ and $h = 106$ RF voltages were increased in RunIb by a factor of 2.5. The whole procedure is repeated six times, to produce the six proton and six antiproton bunches in the Tevatron.

We now discuss the production and acceleration of the antiprotons. To produce them, we first accelerate about 80 bunches of protons of intensity 3×10^{12} to 120 GeV in the Main Ring. The protons are extracted and transported to a target area where they collide with a nickel target every 1.5 sec (Figure 3.2). Antiprotons along with many other secondary particles are produced. About 10^6 protons are needed for the production of one anitproton. The antiprotons are focused with a lithium lens and they are separated from the rest of the particles with a pulsed magnet. Since the initial Main Ring protons were bunched, the antiproton beam will also be bunched. The antiprotons are produces with energy of about 8 GeV.

Subsequently the antiprotons are transferred to the Debuncher [40, 41], a synchrotron accelerator, where the bunches of antiprotons are reduced in size through *betatron stochastic cooling* (damping of transverse motion) and *momentum cooling* (reduction of longitudinal momentum spread). The latter is achieved with the use of RF bunch rotation and adiabatic debunching. The reduction of the pulses momentum and the limitation of the betatron oscillations are combined with adiabatic debunching to improve the transfer to the Accumulator (the next antiproton beam

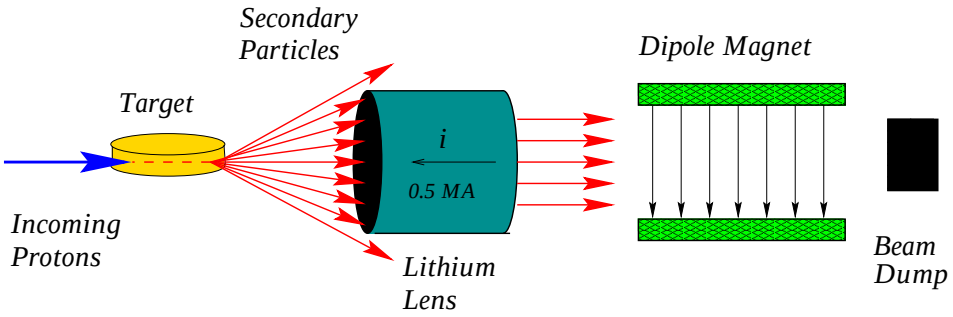

Figure 3.2 The antiprotons are produced by the collision of a 120 GeV proton beam with a nickel target. The resulting antiprotons are focused by the lithium lens and separated by a dipole magnet.

stage) because of the limited momentum aperture of the Accumulator at injection.

The stochastic cooling increases the phase space density of the beam, provides low emittance (maximum luminosity), makes space for more particles in the same ring, preserves the beam quality, and creates almost monoenergetic beams. The Debuncher has a triangle shape with rounded corners and it is divided to 6 sectors of 19 Quadrupole and 11 Dipole magnets each. Correction dipoles and sextupoles are also included in the lattice. There are three straight sections (low dispersion parts) and three arcs (high dispersion parts). Dispersion increases in the arcs because of the bending magnets that have different effects on the particles, depending on the particles position within the beam and their momentum. The stochastic cooling is achieved with the feedback technique using pairs of pickup electrodes which sense the position of the particle, and "kickers" which apply electric force to limit the betatron transverse oscillation of the particle. The cooling kickers, the extraction kickers, the septum, and Schottky pickups are located at the straight sections of the Booster. The pickups and kickers must be an odd multiple of $\pi/2$ apart in betatron phase and far enough so that a chord drawn across the ring is significantly shorter than the signal.

For debunching the beam, the large energy spread and the narrow time spread are exchanged for narrow energy spread and large time spread. This action corresponds to a rotation of the beam in $x-x'$ phase space. It is done based on the fact that the faster antiprotons are decelerated and the slow ones are accelerated by the Debuncher's RF cavities. There are three RF systems. The DRF-1 system (53.1 MHz, $h = 90$) is used to perform six bunch rotations and adiabatic debunching, since initially the 8

GeV antiprotons retain the bunch structure of the 120 GeV protons that created them. The circumference of the Debuncher is 7.1% larger that of the Accumulator. To fit the antiproton beam into the Accumulator, a gap has to be created by the DRF-2 system (2.36 MHz, $h = 4$), which creates a barrier bucket that excludes some of the particles. Actually the phase of the RF wave is shifted by 180 degrees, so that the higher momentum particles are accelerated upon entering the barrier region, whereas the lower momentum particles are decelerated and separated by the rest of the beam. The DRF-3 is only used for accelerator studies. The antiprotons stay in the Debuncher for 1.5 sec, during which the emittance of the beam reduces from 17π mm-mrad to 4π mm-mrad. They are transferred to the Accumulator just before another beam of antiprotons arrive from the target. There are about $6 - 9 \times 10^7$ antiprotons in the output beam fed to the Accumulator.

The main purpose of the Accumulator [40, 42, 43, 44] is to store the antiprotons for several hours or days, until the desirable intensity is achieved. Successive Debuncher antiproton pulses are stacked together. The Accumulator consists of three RF systems responsible for moving the antiprotons from the injected orbit to the center of the Accumulator beam pipe (the *core*), capturing a proton of the core and moving it towards the injection point and bunching the beam during extraction. There are also three cooling systems: *momentum cooling* (reduces the longitudinal energy spread with pickups at the high dispersion area), *betatron cooling* (reduces the transverse spread due to betatron oscillations with pickups at the low dispersion area) and *core/tail cooling*. Dipole, quadrupole and other correction magnets are also included.

Initially, the injection kickers put the injected antiprotons onto the injection closed orbit, which is 80 mm to the outside of the central orbit. The kicker is located in a high dispersion region causing the higher energy injected beam to be displaced to the outside of the Accumulator. After the antiprotons are injected, the shutter opens and the first RF system, the ARF-1 (52.8 MHz, $h = 84$), captures the incoming beam at injection orbit, adiabatically bunches it into 84 bunches, decelerates it by approximately 60 MeV to the edge of the stack tail (deposition orbit), adiabatically debunches the beam and then adiabatically turns off. This process takes 430 ms. After that, the stack tail momentum cooling system acts on the antiprotons and

decelerates them by 150 MeV to move them 63 mm closer to the core. This process takes 30 minutes. During stacking six stochastic cooling systems act on the beam. The 2–4 GHz and 4–8 GHz core momentum cooling systems control the momentum spread and keep the antiprotons from hitting the low momentum aperture and allow a denser bunch. The 2–4 GHz and 4–8 GHz core horizontal and vertical betatron cooling systems keep the transverse emittances minimized. The GHz frequencies, mentioned above, refer to the Traveling Wave Tubes that amplify the pickup signals by 30–60 db over a bandwidth of microwave frequencies. The cooling rate is proportional to the bandwidth of the system. A typical horizontal emittance is 0.9π mm-mrad, a typical vertical emittance is 0.6π mm-rad, and a typical momentum width is 2.5 MeV. A common problem that introduces instabilities is the existence of trapped positive ions. The ARF-2 is used for stabilizing RF to minimize the number of trapped ions in the Accumulator, by weakly bunching the beam. This frees the trapped positive ions from their potential traps.

The stacking process lasts for hours or days until the desired intensity is achieved. When the antiprotons reach a satisfactory number (around 10^{12} particles), they are ready to start being extracted with the use of the ARF systems. The ARF-2 (1.26 MHz, $h = 2$) system is used to unstack beam from the core during collider operation. The ARF-3 (1.26 MHz, $h = 2$) is used to narrow bunches to 210 ns on the extraction orbit. Finally, the ARF-1 is energized, the antiprotons are rebunched into 11 bunches separated by 19 ns, the extraction kicker shutter closes, and the kicker is fired. The antiproton beam passes through the Lambertson[†] and is extracted to the transfer line that leads to the Main Ring.

The 11 bunches of the antiprotons are accelerated to 150 GeV in the Main Ring and coalesced into one bunch. This process is repeated six times to produce six antiproton bunches in the Tevatron. Waiting 40–120 seconds before each Accumulator antiproton extraction allows the core to cool down to smaller emittances in all three dimensions. The emittance of the 6^{th} extracted antiproton beam is typically 10% smaller than the 1^{st} extraction.

The final stage of the proton and antiproton acceleration is the Tevatron [45, 46,

[†]A Lambertson magnet has a field-free area, through which the beam normally passes, and a dipole magnetic-field area, through which the particles are forced to pass at extraction mode.

47, 48, 29, 35], the world's first superconducting synchrotron and currently highest energy accelerator. It shares the same tunnel as the Main Ring. Its 1000 superconducting magnets can reach magnetic fields of 4.2 Tesla, which allows the acceleration of the protons up to 980 GeV. The magnets are made of niobium-titanium alloy wires and the current reaches the 4000 Amperes at 980 GeV. Liquid helium is used to keep the magnets cold. This cryogenic cooling system is the largest in the world. It is able to supply 1000 liters per hour and to keep the temperature at 4.6 K. The Tevatron is loaded with six proton bunches and six antiproton bunches, which are injected onto electrostatically separated orbits. Strong focusing low-beta quadrupoles either side of each interaction region squeeze down the beam spot size and the beams are then brought into collisions at the center of the CDF detector.

The Tevatron luminosity L is defined as

$$L = \frac{f n_b N_p N_{\bar{p}}}{2\pi\sqrt{\sigma_p^2 + \sigma_{\bar{p}}^2}} F(\frac{\sigma_\ell}{\beta}), \tag{3.3}$$

where f is the revolution frequency, n_b is the number of bunches per beam (six), N_p and $N_{\bar{p}}$ are the number of protons and antiprotons in each bunch respectively, σ_p and $\sigma_{\bar{p}}$ are the proton and antiproton transverse beam sizes at interaction point respectively, F is a form factor that depends on the length of the bunches (σ_ℓ) and the beta function (β) at the interaction point (often denoted β^*). The beta function describes the amplitude of the betatron oscillations and is a measure of the transverse beam size. The actual relation is

$$\sigma(s) = \sqrt{\epsilon\beta(s)}, \tag{3.4}$$

where ϵ is the emittance, and s is the position along the Tevatron beam pipe. If we multiply the luminosity by the cross section of a particular particle process (defined by A.56), we obtain the rate at which this process will be produced at the Tevatron.

From the discussion above, we understand that the luminosity at the Tevatron is proportional to the product of the phase space density of the proton bunches and the number of antiprotons in the collider for a particular store. The number of antiprotons is determined by the antiproton production rate, the typical store duration, and

the transmission efficiency from the Accumulator to the low-beta quadruple in the Tevatron. Typical antiproton store lengths are 11 hours, average antiproton production rate is 3×10^{10} $\bar{p}$/h (Run Ia) and 4.5×10^{10} $\bar{p}$/h (Run Ib), and the antiproton transmission efficiency is 70%. A typical number of antiprotons per bunch is 3×10^{10} (Run Ia) and 6.5×10^{10} (Run Ib), and a typical number of protons per bunch is 12×10^{10} (Run Ia) and 22×10^{10} (Run Ib). The proton emittance is 20π mm-mrad (Run Ia) and 22π mm-mrad (Run Ib), and the antiproton emittance is 12π mm-mrad (Run Ia) and 14π mm-mrad (Run Ib). These values lead to a typical instantaneous luminosity of $0.5 \times 10^{31}\text{cm}^{-2}\text{s}^{-1}$ (Run Ia) and $2 \times 10^{31}\text{cm}^{-2}\text{s}^{-1}$ (Run Ib). The bunch length is 55 cm, the bunch spacing is 3 μm, and the beta at the interaction point is 35 cm.

The total integrated luminosity delivered by the Tevatron in Run I was 150 pb^{-1}. Due to finite overall data taking efficiency, the integrated luminosity seen by CDF was 110 pb^{-1} (20 pb^{-1} in Run Ia and 90 pb^{-1} in Run Ib). The reasons for the increase in the number of antiprotons in Run Ib are the increase by 50% of the number of protons targeted for antiproton production and the improvement by a factor of three of the antiproton stacking rate. The acceleration of particles in the Tevatron is slow (30 seconds in collider mode), thus no feedback is needed. The Tevatron accelerates the protons and the antiprotons to their final energy of 900 GeV, which was the reliable operational energy during the Run I. The six bunches in the Tevatron would normally lead to 12 collisions per revolution. To prevent collisions where no detectors exist, electrostatic separators are used to provide two-dimensional helical orbits and allow bunch crossings only at the two detector locations. There is one bunch crossing every 3.5 μs.

The Fermilab accelerator system has been upgraded for the Run II. The goals are the increase of the luminosity by a factor of 10 (over the original $10^{31}\text{cm}^{-2}\text{s}^{-1}$) and the increase of the energy of the proton and antiproton beams to 1 TeV. In 1999, the Main Injector [29, 49, 50] was commissioned to replace the Main Ring. It is a rapid cycling proton synchrotron, 3.3 km in circumference, consisting of 344 dipole magnets, and 80 quadrupole magnets. The Main Injector has larger aperture than the Main Ring and its goal is to deliver 36 bunches of protons and 36 bunches of antiprotons

in the Tevatron. A new 8 GeV storage Ring, the Recycler [51, 52], is installed in the same tunnel as the Main Injector, and makes use of 45 strontium ferrite permanent low-field dipole magnets. Its purpose is to recover antiprotons from the end of stores so they can be used again. In Run I, more than half of the antiprotons remained at the end of the collider stores and one would like to reuse them.

The Run II Tevatron [29] will initially accelerate 36 particle bunches per beam with a minimum spacing of 392 ns, to be followed by the operation at 108 bunches per beam and a minimum spacing of 132 ns. To achieve these goals a proton density is chosen that produces an antiproton beam-beam tune shift close to maximum. It is also essential to have the Accumulator deliver the maximum number of antiprotons. The Run II Accumulator lattice [53] and its stack-tail system are upgraded. There is also an improvement of the pickup and kicker systems of the Debuncher, the operation of which will be dynamically varied based on the transverse beam size. The energy upgrade of the Tevatron accelerator to 1 TeV per beam (2 TeV in the center of mass of the system) will be achieved by identifying inadequately performing magnets, and by either replacing them or decreasing their temperature by proper cryogenic manipulation.

3.2 The Collider Detector at Fermilab

3.2.1 Overview

The Collider Detector at Fermilab (CDF) is a general purpose detector of charged leptons, jets of hadrons, and photons [54]. The W and Z bosons are detected through their leptonic decay products, and the transverse momentum of the neutrinos is estimated from the missing transverse energy of the events ($\not\!\!E_T$). Individual charged mesons and baryons are also routinely detected.

The z-axis of the detector coincides with the direction of the proton beam and defines the polar angle θ of the laboratory frame. The x-axis is horizontal pointing outwards, and the y-axis is vertical pointing upwards. The high energy collisions occurring at the center of the detector produce particles that are uniformly distributed

in azimuthal angle ϕ, and in *rapidity* y. The rapidity of a particle is defined as

$$y \equiv \frac{1}{2}\ln(\frac{E+p_z}{E-p_z}), \tag{3.5}$$

where E is the energy of the particle and p_z its longitudinal momentum. We use the rapidity because all the high energy events are boosted and y is additive quantity under relativistic boosts. For high energy interactions and not very massive particles, the rapidity can be approximated by the *pseudorapidity* η, given by

$$\eta \equiv -\ln[\tan(\theta/2)]. \tag{3.6}$$

The detector η and the azimuthal angle ϕ are used to specify detector areas of CDF. The detector η is defined with respect to the nominal center of the CDF detector. When we describe regions of the CDF detector, we will refer to the detector pseudorapidity. For the physics analysis, we use the physical pseudorapidity of the particles, defined with respect to the vertex of the event. Other useful quantities used to describe the operation of the detector and the data selection, are the transverse momentum of a particle $p_T = p\sin\theta$ (where p is the total momentum of the particle), the transverse energy of a particle $E_T = E\sin\theta$ (where E is the energy of the particle), and the missing transverse energy of the events

$$\not\!\!\vec{E}_T = \sum_i E_T^i \hat{n}_i, \tag{3.7}$$

where the sum is over all the energy clusters, E_T^i is the transverse energy of cluster i, and $\hat{n}_i$ is the unit vector pointing to the cluster i. Equation (3.7) is actually a fast crude calculation of the missing transverse energy, used by the trigger system of the detector. We will present a more accurate calculation in Chapter 4.

The CDF detector consists of a central detector covering the absolute η-region $0 < |\eta| < 1.1$, a plug detector covering the absolute η-region $1.1 < |\eta| < 2.4$ and a forward/backward detector covering the absolute η-region $2.4 < |\eta| < 4.2$ The central detector is made up of the solenoid magnet, steel yoke, central tracking chamber, electromagnetic calorimeter, hadron calorimeter and muon chambers. The plug de-

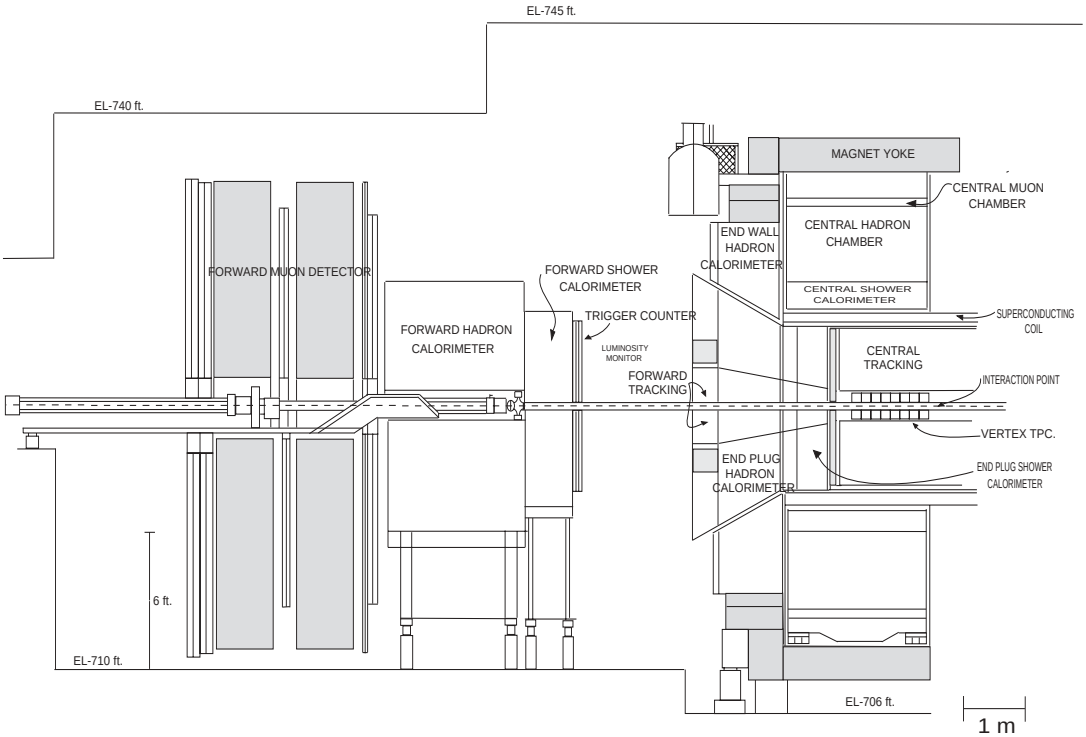

Figure 3.3 The CDF detector at Fermilab. The central, plug and forward regions are shown.

tector consists of electromagnetic and hadron calorimeters. The forward/backward detector consists of time-of-flight counters (for luminosity monitoring), electromagnetic, hadron calorimeters and muon chambers. At the center of the detector, there exists a vertex detector, enclosing a silicon vertex detector. A schematic of the CDF detector can be seen in Figure 3.3. The location of the main subdetectors in η is shown in Figure 3.4. In this section we will describe these subdetectors of the CDF system.

3.2.2 The Tracking System

The tracking system of the detector consists of the silicon vertex detector, the vertex detector and the central tracking chamber and it is immersed in a magnetic field of 1.4 Tesla and longitudinal direction along the positive z axis. The magnetic field is produced by a superconducting solenoid of length 4.8 m and radius 1.5 m. The

Figure 3.4 A quadrant of the CDF detector at Fermilab. The main subdetectors and their respective η locations are shown.

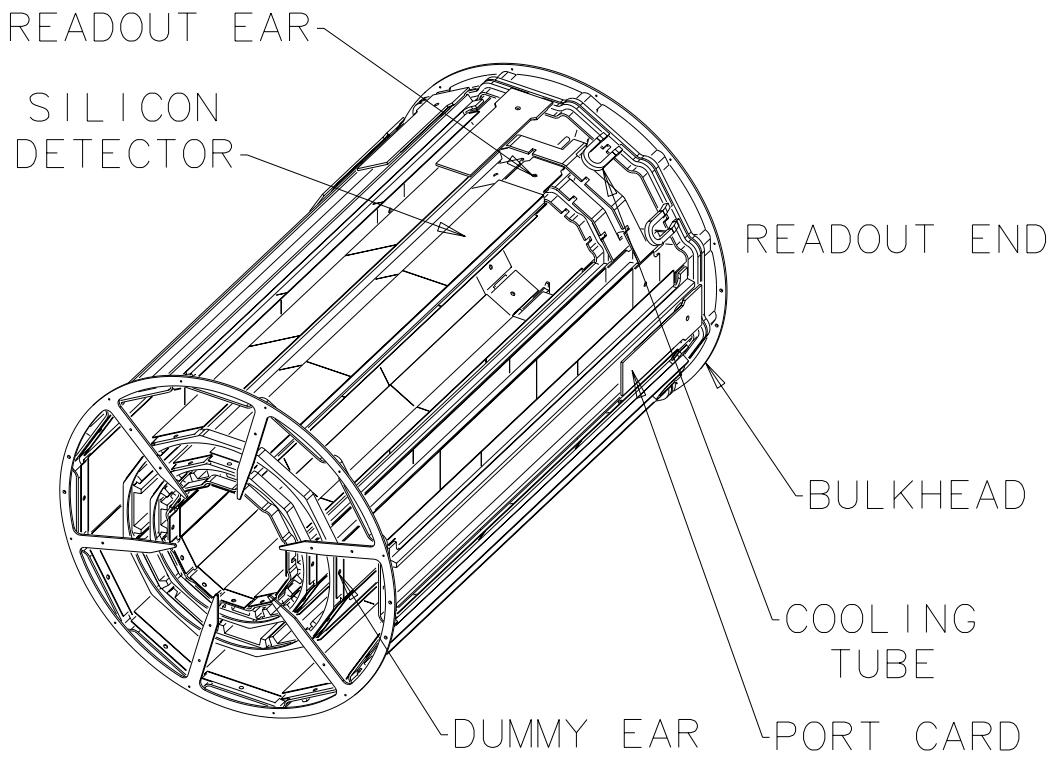

Figure 3.5 A Silicon Vertex Detector (SVX) barrel.

coils are made of an alluminum-stabilized niobium-titanium alloy. The combined momentum resolution of the tracking system is $\delta p_T/p_T = \sqrt{(0.0009 p_T)^2 + (0.0066)^2}$, where p_T is the transverse momentum in GeV. In the following, we describe the subdetectors of the tracking system.

The Silicon Vertex Detector (SVX)

The SVX [55] is a four-layer silicon micro-strip vertex detector located immediately outside the beampipe. It is used to find secondary vertices and to provide the impact parameter of tracks in the transverse $r-\phi$ plane. This is important for tagging long-lived heavy flavors produced in the $p\bar{p}$ collisions. In Run Ib a radiation harder version of the detector (SVX′ [56]) was developed[†].

The active area of the SVX consists of two back-to-back cylindrical modules that

[†]Unless otherwise stated, when we mention SVX, we also refer to SVX′

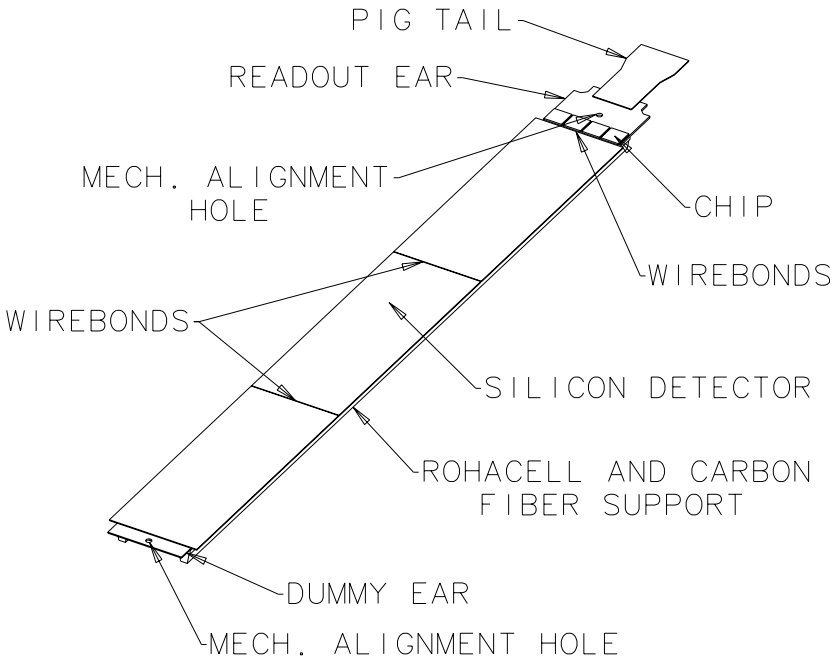

Figure 3.6 The SVX ladder consists of three silicon strip detectors.

cover a region of 51 cm. The SVX consists of four radial layers of 8.5 cm long silicon strip detectors, which are arranged as a twelve-sided barrel at each radial direction. An SVX barrel can be seen in Figure 3.5. The radii of the four layers are 3.0 cm, 4.3 cm, 5.7 cm, and 7.9 cm. (the first layer radius of SVX′ is 2.9 cm). The strips on the inner three layers have 60 μm pitch, whereas the pitch is 55 μm for the outermost layer.

The silicon strip detectors are single sided (n-type substrate with p-type silicon strips one one side), and they are connected in groups of three called *ladders*. Overall, there are 96 ladders (12 faces $\times$ 4 layers $\times$ 2 ends). The ladders are tilted by 3° with respect to the radial direction, to increase the overlap between adjacent faces. At one end of the ladder there is a board, called *ear*, which contains the readout chips for the ladder, as well as some of the bus circuitry. When a particle passes through the fiducial region of the silicon strip detector, it deposits energy that moves electrons from the valence band to the contaction band of the silicon, with the subsequent creation of holes in the valence band. The detection of the electron-hole pairs leads to the detection of the position the particle passed through. Due to the low energy needed for the creation of an electron-hole pair in silicon (of the order of 1 eV), the

SVX efficiency is greater than 99%.

Figure 3.6 shows an SVX ladder. There are 128 channels per chip, 46,080 individual readout channels, and the power dissipation is 175 mW. In order to process the signals, a Very Large Scale Integrated (VLSI) circuit is developed that amplifies, samples, sparsifies, and multiplexes data from the SVX. This way, the amount of electronics needed is limited. The detector is operated in sparce mode to read out only channels whose signal is above a hardware threshold. The readout time is 2.7 μs (2.1 μs for SVX$'$).

Particles traversing the active regions of the detector will pass an average of 3% of radiation length, so the effect of the SVX on the rest of the CDF detector is minimal. The radiation length (X_0) is defined as the distance an electron travels in a material, before it loses $1/e$ of its energy. Careful consideration for the radiation levels the SVX experiences has been taken. The impact parameter resolution of the SVX is $\sigma_d = (13 + 40/p_T)$ μm, where p_T is the transverse momentum of the track in GeV, and the average position resolution is 12 μm. The resolution is very satisfactory, compared to the size of the B-meson track of $c\tau_B = 430\mu$m before its decay.

The Vertex Detector (VTX)

The VTX [57] is located outside the SVX and it is a vertex drift chamber that provides tracking information in the $(r - z)$ space, up to a radius of 22 cm and pseudorapidity of $|\eta| \leq 3.5$. It is used for the measurement of the z-position of the primary vertex. It also provides event topologies for $3.5^\circ \leq \theta \leq 176.5^\circ$, identifies multiple interactions, detects conversions, and provides intermediate angle tracking, essential for electron/pion separation. It is composed of 28 octagonal time projection chambers surrounding the beam pipe and mounted end-to-end along the beam direction. Figure 3.7 shows the cross section of a VTX module. As a particle passes through, it generates electrons through ionization and excitation of the atoms of the gas in the chambers. From the drift times of the produced electrons, as they move towards the sense wires, we are able to reconstruct the track of the particle.

The 28 modules are separated into two halves, to reduce the drift time of the electrons produced in the gas as they pass the fiducial volume of the VTX, so that

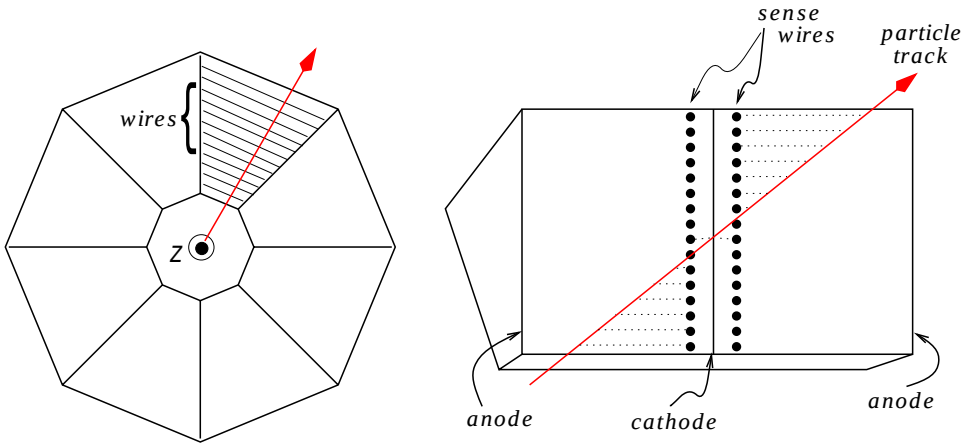

Figure 3.7 The Vertex Detector (VTX) cross section.

it is shorter than the time between bunch crossings (3.5 μs). Adjacent modules are rotated 15 degrees with respect to each-other in ϕ, to eliminate inefficiencies near their boundaries. Each octant consists of a cathode grid, a plane of field shaping wires, a plane of sense wires, and a resistive ink cathode plane. The materials are chosen with emphasis towards low mass and long radiation length. (Kapton film, Rohacell foam, epoxy-fiber, glass and graphite fiber). The gas in the chambers is 50%-50% argon-ethane. There are 16 sense wires per octant at low $|z|$ positions and 24 sense wires at the modules which are located at higher $|z|$. The signals from the wires pass through an Amplifier-Shaper-Discriminator (ASD) and a Time-to-Digital Converter (TDC) and provide drift time information useful for the $r-z$ reconstruction of the track. Track segments in the VTX are intercepted with the beam axis to reconstruct the primary vertex. Special correction is needed to remove the leading-electrons effect which can cause shifts in track position. The resolution of the measurement of the z position of the vertex is 2 mm.

The Central Tracking Chamber (CTC)

Surrounding the SVX and the VTX is the Central Tracking Chamber [58], a large cylindrical drift chamber with excellent spatial and momentum resolution (200 μm and $dp_T/p_T^2 = 0.002$ to 0.004 respectively) used for the measurements of the track parameters of isolated particles with high transverse momentum p_T. This information, when combined with calorimeter data, is critical to the identification of high

momentum leptons, especially muons. The CTC is also used for the measurement of high-p_T particles in jet cores and the measurement of track parameters at angles below 30° with respect to beam direction. It is additionally used for the identification of cracks in the calorimetry or muon chambers, for the identification of secondary vertices in cooperation with the vertex detectors, and for matching the tracks with shower centroids in the calorimeters (important for particle identification and removal of pion backgrounds). Finally, the CTC is used for many detector studies, such as studying the calorimeter response as a function of the position and momentum of the particles.

The CTC is 3.2 m long and covers the pseudorapidity interval $|\eta| \leq 1.0$ and transverse momentum $p_T \geq 0.4$ GeV. It consists of 84 layers of sense wires arranged in five superlayers of *axial wires* and four superlayers of *stereo wires*. The axial superlayers have 12 radially separated layers of sense wires, parallel to the z-axis that measure the $r - \phi$ position of the tracks. The axial superlayers are interleaved with the stereo superlayers, which have six layers of sense wires with a 3° stereo angle with respect to the z-axis and they measure a combination of $r - \phi$ and z information. All sense wires are tilted by 45° with respect to the radial direction, so that the Lorentz angle (the angle of the electron drift direction with respect to the applied electric field) is large and the drift trajectories are approximately azimuthal. In addition, making the Lorentz angle large ensures that the particles produced in the collider will pass close to at least one sense wire. The cross-section of the CTC with its superlayers can be seen in Figure 3.8

Both axial and stereo layers are divided into cells, so that the maximum drift distance is less than 40 mm, corresponding to about 800 ns of drift time. The boundaries of the cells are defined by two planes of *field wires*. The field wire voltages control the strength of the drift field. Between the field wire planes there exists the plane of sense wires. Each sense wire is separated by its neighbor by a *potential wire* that controls the gas gain. Each cell includes a set of 14 special wires to keep the electric field uniform. Typical electric fields are 1350 V/cm.

The inner fiducial radius of the CTC is 309 mm and the outer fiducial radius is 1320 mm. The endplates are made of two-inch-thick aluminum, 30% of which was

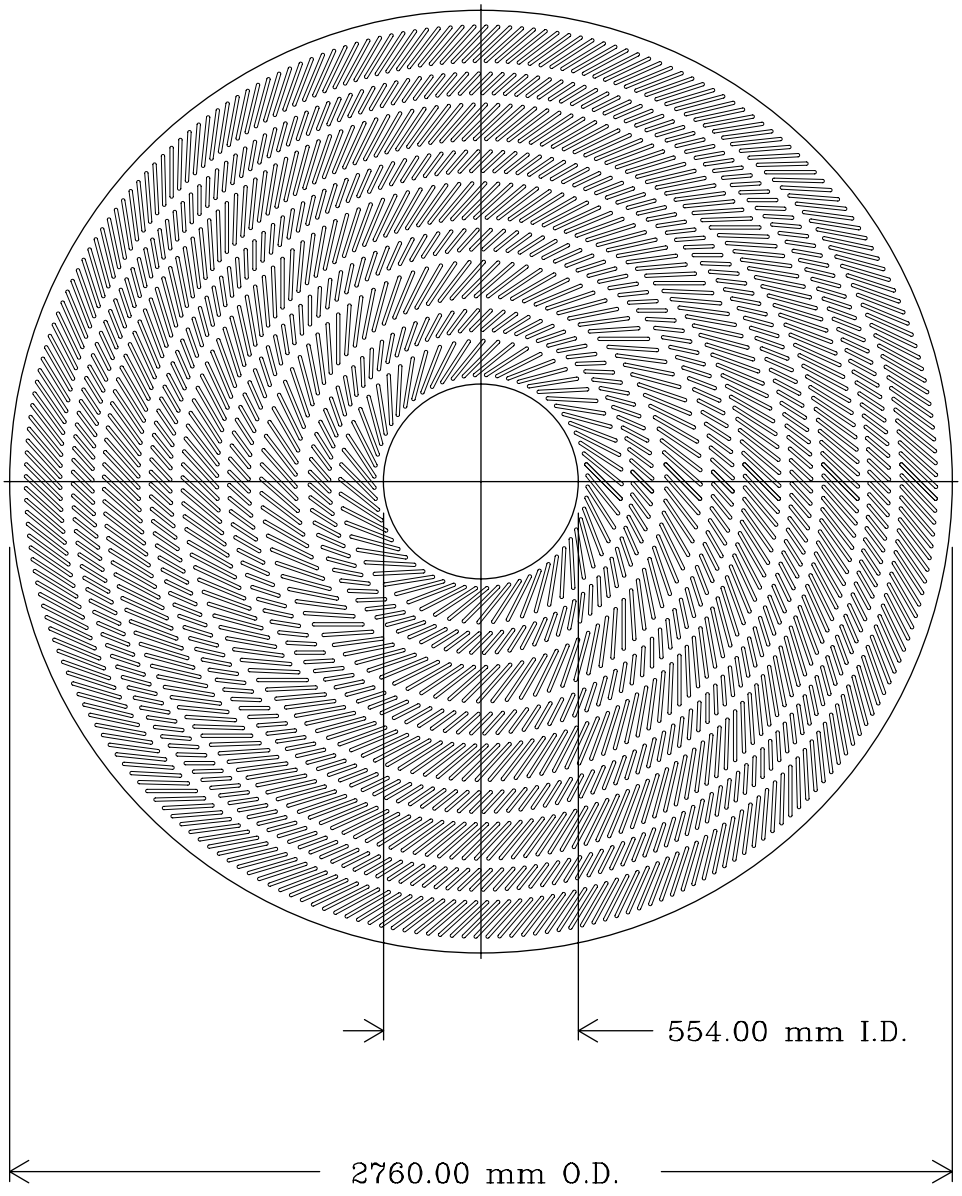

Figure 3.8 The Central Tracking Chamber (CTC) cross section. The 84 layers arranged in five axial and four stereo superlayers.

removed to allow passage of the wires and insulators. The inner support cylinder is made of 2 mm thick carbon fiber reinforced plastic and supports the axial compressive load of 9 tons.

The stereo and axial data are combined to reconstruct the three-dimensional track, important for properly matching the calorimeter and muon chambers information. When a charged particle is produced, it enters the fiducial volume of the CTC, and it follows a curved trajectory because of the magnetic field of 1.4 Tesla. The particle interacts with the gas of the chamber (49.6% argon, 49.6% ethane, 0.8% ethanol), ionizes its molecules, and produces electron-ion pairs, which drift to the cathode and anode wires creating electromagnetic signals on the sense wires along the trajectory. Each sense wire is connected to a preamplifier, which provides fast and low-noise amplification of the signal and eliminates the wire-to-wire cross-talk (caused by the $1/t$ tail in the signal due to the positive ion motion). The preamplified signal is passed through the ASD, where the timing information is extracted, and consequently through a multiple-hit TDC. For Run I, the TDC had to have a resolution better than 1 ns and a range of about 1 μs to accommodate at least eight hits per wire per event. Each signal corresponds to a point in the space and by fitting these points we get the curvature and the momentum of the particle. Practically the momentum of the particle is constrained from an extra point, the interaction vertex. This final momentum is called *beam constrained momentum*.

3.2.3 The Calorimetry system

Central Electromagnetic Calorimeter (CEM)

The Central Electromagnetic Calorimeter [59] detects electrons and photons and measures their energy. While other particles that interact electromagnetically may also deposit some of their energy in the CEM, electrons and photons deposit almost all of their energy in the calorimeter. The CEM consists of 31 layers of 5 mm thick SCSN-38 polystyrene scintillator interleaved with 30 layers of 1/8 inch lead, clad on both sides with 0.015 inch aluminum; the CEM total thickness is 18 radiation lengths (32 cm), to make sure that 99.7% of the electrons energy will be deposited. In order to maintain

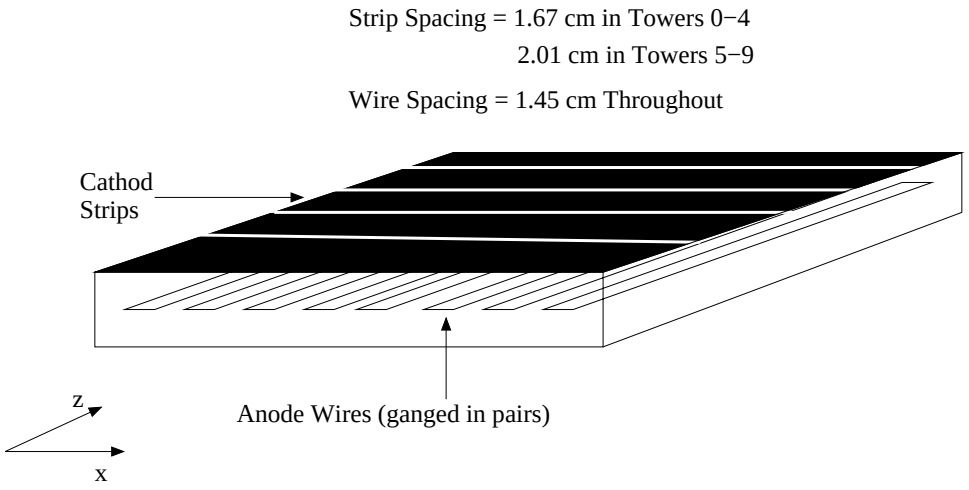

Figure 3.9 A portion of the Central Electromagnetic Strip Chamber.

a constant radiation length thickness as polar angle varies, acrylic is used instead of lead in certain layers. A proportional strip chamber (Central Electromagnetic Strip chamber, or CES) is inserted between the 8^{th} lead layer and the 8^{th} scintillator layer, at the depth corresponding to maximum average transverse shower development (5.9 X_0 within the calorimeter, or 184 cm from the beam line). The strip chambers are small drift chambers consisting of wires and strips used to determine the shower position and transverse development of the cascade by measuring the charge deposition on them. The wire signals give us the ϕ position and the strip signals the z shower position. The shower topology information allows us to distinguish an electron or a photon from a light hadron (π or K) or muon signals that may also shower in the calorimeter, since the transverse development of the showers is different for these particles. The position resolution of the CES is 2 mm in both transverse directions for 50 GeV electrons and 3 mm for 10 GeV electrons. Figure 3.9 shows a cell of the CES.

The whole central electromagnetic calorimeter consists of 48 modules. Each one of them is segmented into 10 projective towers of 0.1 unit in η and 15° in ϕ pointing to the nominal interaction point at the center of the detector. The 48 modules are arranged into 24 east wedges and 24 south wedges, each wedge covering 15° in ϕ. A CEM module can be seen in Figure 3.10.

The photons and electrons interact with the lead layers and produce electrons

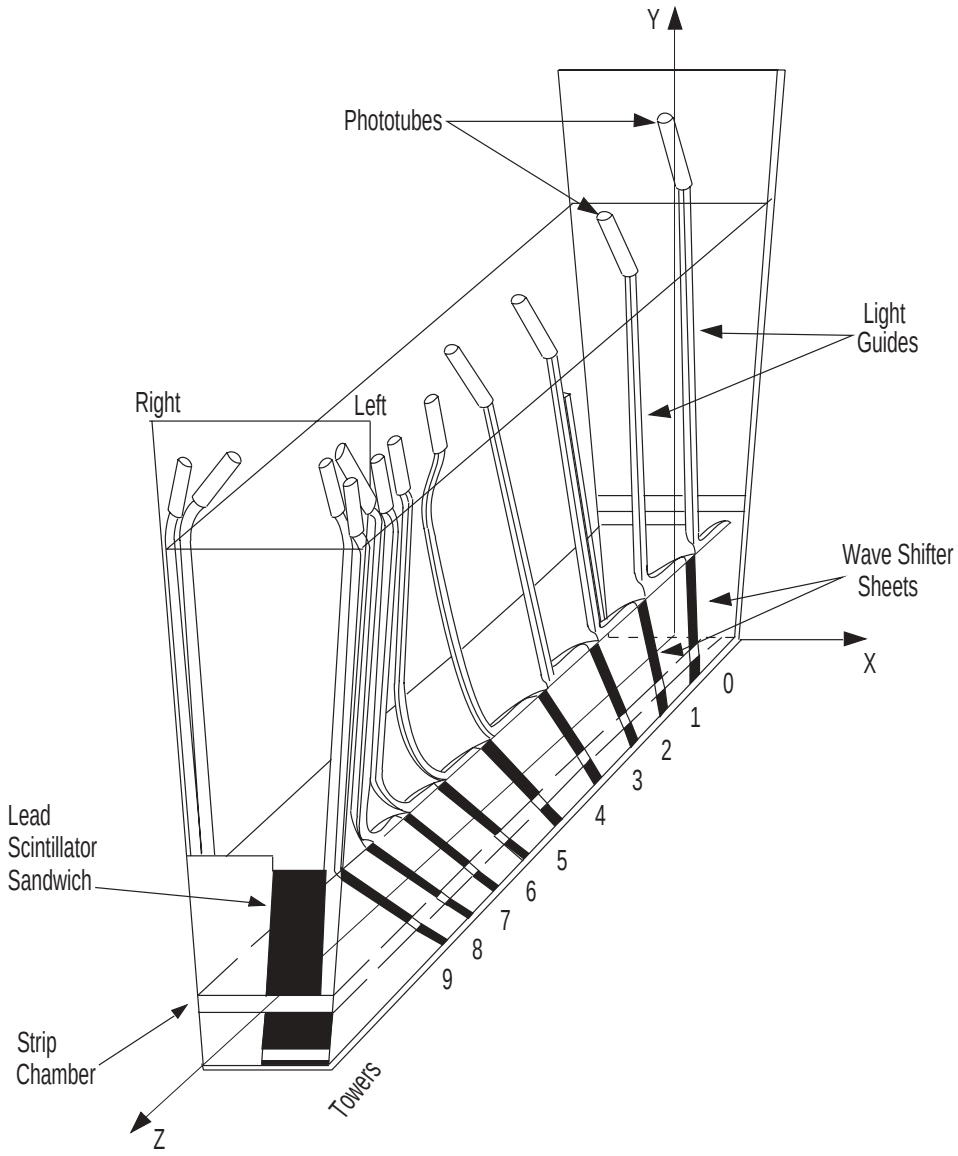

Figure 3.10 One of the 48 wedges of the electromagnetic calorimeter. The ten $(\Delta\phi, \eta) = (15^\circ, 0.1)$ projective towers are shown.

(through mainly pair production) and photons (through mainly bremsstrahlung). The new photons and electrons also interact with the lead layers producing more electrons and photons and finally, a electromagnetic shower is created. Lead was chosen to be the interaction material because of the small radiation length $X_0[gr/cm^2] \approx A/Z$ (the energy deposited by an electron due to bremsstrahlung is $dE/dx = E/X_0$ and we want it to be as large as possible). As the energy of the shower decreases, the particles lose their energy due to mainly ionization, instead of radiation. The scintillators interact with the electrons (mainly) and photons and transform their energy into blue light. The light is collected in 3 mm thick UVA acrylic doped with 30 ppm Y7. Two waveshifters redirect the light through lightguides to the photomultiplier tubes (PMTs). Without any corrections, the light output from individual waveshifters varies from point to point as much as 45% due to internal reflection and different transmission through the waveshifters. This problem is solved by eliminating reflection, by controlling the thickness of the waveshifter material with laser cutting, and by limiting other non-uniformities.

The PMTs are 1.5 inches in diameter, they have a bialkali photocathode and ten stages of amplification. They detect the green light emitted by the waveshifters and output electrical signals used for the measurement of the energy of the initial particle. Their gain is 4×10^5 for a high voltage of 1700 V and a full scale output pulse is 1200 pC. Since there are 48 modules of 10 towers each and 2 PMTs per tower, 960 photomultiplier tubes are needed. Actually four of these PMTs are not installed, since they correspond to the two chimney towers that were removed to make space for the cryogenic plumbing needed for the superconduction solenoid magnet.

The CEM covers the pseudorapidity region $|\eta| \leq 1.1$ and it has an average energy resolution $\delta E_T/E_T = \sqrt{(13.5\%/\sqrt{E_T})^2 + (2\%)^2}$, where E_T is the transverse energy of the detected particle in GeV. The position resolution is 2 mm at 50 GeV.

Plug Electromagnetic Calorimeter (PEM)

The PEM [60] consists of two cylindrical modules covering both ends of the 3 m in diameter and 5 m long solenoid. The modules have an outer diameter of 280 cm and depth of 53 cm. The total coverage in pseudorapidity is $1.1 \leq |\eta| \leq 2.4$. At

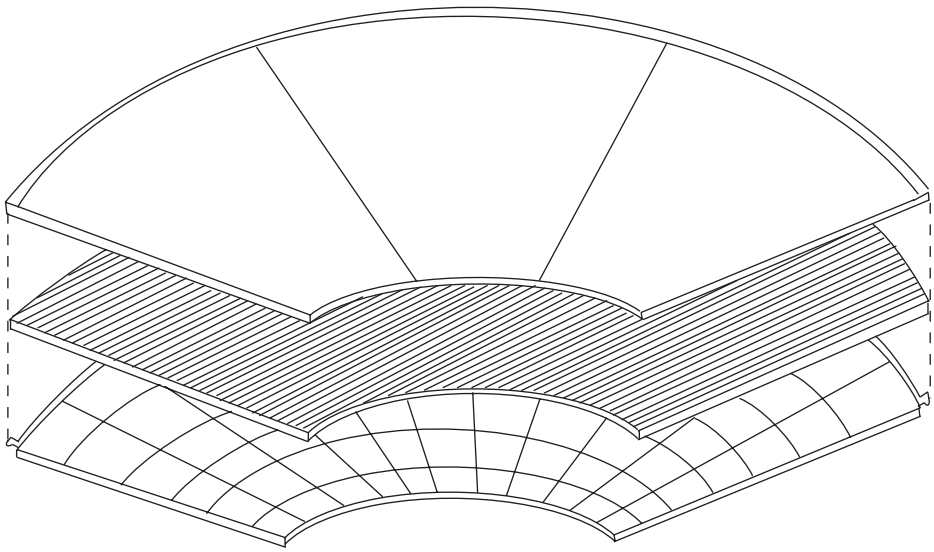

Figure 3.11 A quadrant of the Plug electromagnetic calorimeter. The pad and wire layers are shown.

high pseudorapidity areas, a fine lateral segmentation of the detector is needed. If scintillator had been used as the interacting material, many hot/dead spots would have been created. For this reason, gas proportional chambers were used instead of scintillator.

One PEM module consists of four quadrants ($\Delta\phi = 90^\circ$) of 34 layers of proportional tubes. The tubes are made of contactive plastic, their cross-section is 7 mm by 7 mm and the anode in their middle is made of gold-plated tungsten. They are interleaved with 2.7 mm thick lead absorber. The contactive plastic has high resistivity and enables us to pick up the signals caused by the electromagnetic avalanche, utilizing the pads and strips etched on printed circuit boards. The patterns of pads and strips gives us the (η, ϕ, z) segmentation of the calorimeter. The strips are segmented four to five times finer than the pads, in order to provide high resolution around the shower maximum for pion background rejection. A quadrant of the Plug Electromagnetic Calorimeter can be seen in Figure 3.11.

The signals from the tubes pass through a charge integrating amplifier. The analog output (maximum 2.5 V for a 500 pC input) is digitized by a 16-bit ADC.

There are 8,720 PEM channels overall. The ϕ resolution from the strips is 0.1°, while the θ resolution from 0.04° to 0.06°. This corresponds to 2 mm by 2 mm position resolution. The signal from the interaction of the electrons and photons with the gas (50%-50% argon-ethane with a little ethyl alcohol) is proportional to their energy.

The energy resolution is given by the empirical formula $\sigma_E/E = 30\%\sqrt{L/E}$, where L is the thickness of each layer in radiation lengths, with a constant term of 2% added in quadrature. The average energy resolution is $\sigma_E/E = \sqrt{(28\%/\sqrt{E})^2 + (2\%)^2}$, where E is the energy in GeV. Given the high energies of the electrons and photons which reach the plug electromagnetic calorimeter, the resolution above is comparable to the central electromagnetic calorimeter.

Forward Electromagnetic Calorimeter (FEM)

The Forward Electromagnetic Calorimeter [61] consists of two modules covering the pseudorapidity region $2.4 \leq |\eta| \leq 4.2$. They are located 6.5 m away from the interaction point and they enclose the beam pipe. Each calorimeter is 3 m long on side and 1 m deep and it consists of 30 sampling layers of cathode pads, 80% radiation lengths thick lead sheets (radiating medium), and gas proportional tubes. The tubes are constructed of aluminum and fiberglass. The cathode pad geometry is etched on three fiberglass panels. A FEM proportional tube is shown in Figure 3.12. There are 1440 pads per layer and 5760 towers in total. Each pad covers 0.1 units in pseudorapidity and five degrees in azimuthal angle. The gas is 50%-50% argone-ethane with an addition of isopropand to prevent glow discharges. The nominal high voltage value is 1900 V resulting to a gain of 5000.

The signal from the cathode pads is transferred to a low-noise charge integrator and subsequently to a sample-and-hold system (for high rate environment) and an ADC. The energy resolution is $\sigma_E/E = \sqrt{(25\%/\sqrt{E})^2 + (2\%)^2}$, where E is the energy in GeV, and the position resolution varies from 1 mm to 4 mm, depending on the location.

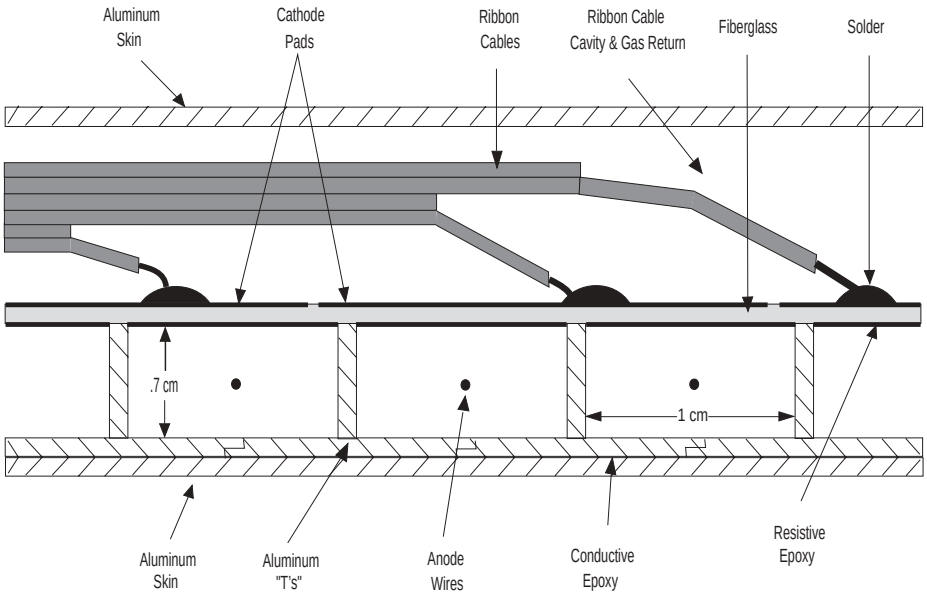

Figure 3.12 A proportional tube of the Forward Electromagnetic Calorimeter.

Central Hadronic Calorimeter (CHA) and Endwall Hadron Calorimeter (WHA)

The hadrons produced in the CDF detector deposit energy in the hadron calorimeter [62], whereas the electrons and photons do not often reach the hadron calorimeter's material, since their shower is almost completely absorbed in the electromagnetic calorimeter. Hadron–electron/photon identification is the reason why the electromagnetic calorimeter is closer to the interaction point than the hadron calorimeter. The hadron interactions with the calorimeter's material are much more complicated than the electromagnetic interactions of the electrons and photons in the electromagnetic calorimeter and they produce a hadronic shower. The CHA covers the pseudorapidity region $0 \leq |\eta| \leq 0.9$ and the WHA covers the $0.7 \leq |\eta| \leq 1.3$. There are 48 wedges of 2.5 cm sampling for the CHA and 48 wedges of 5.0 cm sampling for the WHA. Each CHA wedge is divided into eight projective towers, and each WHA wedge is divided into six projective towers. Each tower covers approximately 0.1 unit of pseudorapidity and 15° in ϕ.

The hadronic calorimeters consist of layers of steel (interacting material) interleaved with layers of scintillator (signal collector material). There are 32 layers in

the CHA and 15 layers in WHA. The scintillator used is PMMA plastic doped with 8% napthalene, 1% butyl-PBD and 0.01% POPOP (1 cm thick). Three main interactions lead to a hadronic shower: the hadron production, the nuclear deexcitation and the pion/muon decays. These strong and electroweak interactions cannot be analytically described, so they are properly simulated. The hadronic absorption length is $\lambda[gr/cm^2] \approx 35A^{1/3}$, therefore steel was chosen as the interaction material. The hadronic absorption length λ is defined as the distance a pion travels in a material, before it loses $1/e$ of its energy. The length of the hadron calorimeter was chosen to be 4.7λ to make sure that almost all the energy of the shower is absorbed. The light output from the scintillator is collected by waveshifters and is transferred to 12-staged photomultiplier tubes. There are 1344 PMTs overall; 768 for the CHA and 576 for the WHA. Anode signals are digitized by a 16-bit ADC with full scale of 750 pC. The arrival time of the signals is digitized by a 16-bit TDC with full scale of 3.2 μs. The calibration of the hadron calorimeters is done with laser systems and radioactive sources. Twelve of the towers are totally in the CHA, six are in WHA, and six are shared.

The energy resolution of the central and wall hadron calorimeters is $\sigma_E/E = \sqrt{(50\%/\sqrt{E})^2 + (3\%)^2}$, where E is the hadron energy in GeV, but this degrades at hadron energies higher than 50 GeV. The spatial resolution is 10 cm by 5 cm.

Plug Hadronic Calorimeter (PHA)

The Plug Hadronic Calorimeter is located behind the Plug Electromagnetic Calorimeter and has the same segmentation with it. It consists of 20 layers of proportional tubes interleaved with 5.1 cm thick steel. The pseudorapidity coverage is $1.32 < |\eta| < 2.4$, the position resolution is 2 cm by 2 cm, and the energy resolution is $130\%/\sqrt{E_T} + (4\%)^2$, where E_T is the transverse energy in GeV. The hadrons interact with the steel and a hadronic shower is developed. The produced particles interact with the gas of the proportional tubes and their energy is measured. Unlike the CHA and WHA, scintillator could not have been used as the signal collectors in PHA, due to the high rates of particles per unit volume of the plug detectors.

Forward Hadronic Calorimeter (FHA)

The FHA [63] is designed to detect energy and position of hadrons in the pseudorapidity region of $2.2 \leq |\eta| \leq 4.2$, through their interaction with the gas of ionization chambers. There are two modules at both ends of the detector along the z-axis. Each module is segmented into four independent sections made of 27 steel plates interleaved with 27 ionization chambers. The cathode surface of each ionization chamber is segmented into 20 bins of $\Delta\eta = 0.1$ and 18 bins of $\Delta\phi = 5^\circ$, for a total of 360 pads per chamber. The cathode pads at fixed (η, ϕ) locations form a projective tower and their signals are summed up to give the charge signal for that tower. This signal is digitized by the ADC. In addition to providing the charge information, the sense wires form six sections of wires per chamber and their signals are used for monitoring the performance of the calorimeter, and for studying the longitudinal development of showers. The energy precision of the calorimeter is $\sigma_E/E = \sqrt{(130\%/\sqrt{E})^2 + (4\%)^2}$, where E is the energy of the traversing particle in GeV. The spatial resolution is 3 cm by 3 cm.

3.2.4 The Muon System

The muon chambers [64] are the outermost part of the detector, because the high energy muons are able to pass through the rest of the detector without losing much of their energy. The central muon system is capable of detecting muons with transverse momentum $p_T \geq 1.4$ GeV and pseudorapidity $|\eta| < 1.0$, through their interaction with the gas and subsequent drift of the produced electrons towards the anode wires. The detection of high-p_T muons is very important because their most probable source is a vector boson decay. There are three central muon detectors, the central muon chambers (CMU) covering the $|\eta|$-region from 0 to 0.6, the central muon upgrade chambers covering the same $|\eta|$-region as the CMU, and the central muon extension chambers (CMX), covering the $|\eta|$-region from 0.6 to 1. The ϕ coverage is not complete: 84% of the solid angle for $|\eta| < 0.6$ is covered by CMU, 63% by CMP, and 53% by both. Figure 3.13 shows the coverage of the central muon detectors in the $(\eta - \phi)$ space. At the high pseudorapidity region, there exists a forward muon system.

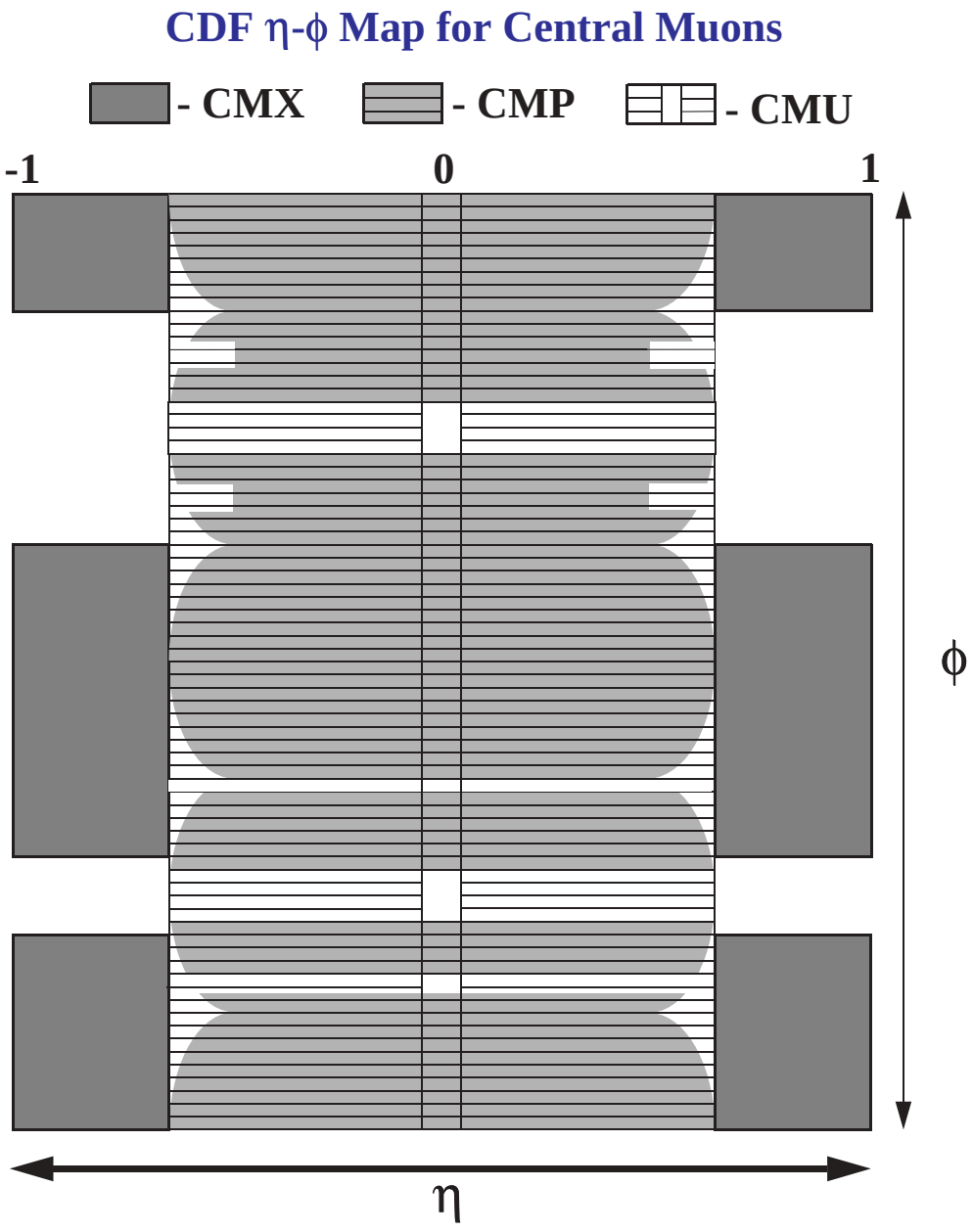

Figure 3.13 The Muon coverage of the central muon system (CMU, CMP and CMX).

Central Muon Chambers (CMU)

The CMU system is located 35 m from the interaction point, and it is segmented in ϕ into 24 east and 24 west 15°-wedges, which fit into the top of each central calorimeter wedge. Each wedge contains three muon chambers and each muon chamber consists of four layers of four rectangular drift cells. A stainless steel sense wire with a resistance of 0.4 Ωmm^{-1} and diameter of 50 μm is located in the center of each cell. Four sense wires, one from each layer, make up a muon tower. The sense wires from alternating layers are offset with each other. By comparing the drift times for alternating layers, we resolve the ambiguity of which side of the sense wires the muon passed. To reduce the number of electronics and to read out the signals only from one side of the chambers, each sense wire is connected at its end to a sense wire in the same layer which is separated from the first by an intervening cell. Figure 3.14 shows a CMU chamber.

The walls of the muon chamber cells are held at -2500 V and the sense wires at +3150 V. Typical electric fields are 100 V/mmm. The gas used is 49.6% argon, 49.6% ethane, 0.8% ethanol. The electric pulse passes through the blocking capacitor of the front-end electronics and subsequently through an Analog-to-Digital converter (ADC) and a TDC. The final output is the charge collected in the ADC and the timing information from the TDC. The position of the track along the sense wire is determined by charge division. The charge collected from the ADCs of two connected wires, when a muon passes through a chamber, is not the same. The difference depends on the position of charge deposition in the z-axis. On the other hand, the time information from the TDC is used to determine the drift-ϕ information and to correct the calculation of the z-position of the muon passage due to the exponential decay of the charged accumulated in the capacitor. Calibration of the chambers is performed using radioactive sources, cosmic rays, and a pion test beam. The drift-ϕ resolution is 250 μm and the z resolution is 1.2 mm. The system is essentially 100% efficient for muons above 3 GeV. The geometric acceptance is limited by the 2.4°-gaps between the CMU wedges.

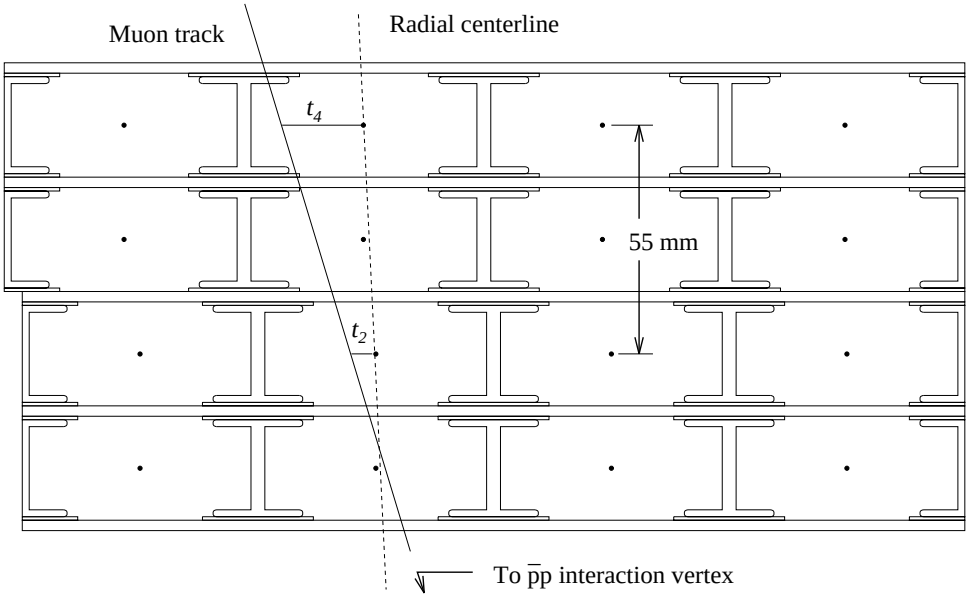

Figure 3.14 A Central Muon Chamber (CMU chamber) consists of 16 drift cells. Four cells in the same radial direction make up a tower. There are three CMU chamber per wedge and 48 wedges in total.

Central Muon Upgrade (CMP)

The CMP chambers are located above the CMU chambers and they were introduced to remove the π punch-through contamination. The three absorption lengths of steel (0.6 m in thickness) between the CMU and CMP chambers absorb any energetic pions that reach the CMU chambers, so they do not reach the CMP chambers. The muons, on the other hand, pass through both detectors and a signal from both CMU and CMP is a confirmation of a true muon passage. The pseudorapidity coverage of the CMP chambers is the same as the CMU ones. The ϕ coverage is not complete, as shown in Figure 3.13.

The CMP muon chambers are drift chambers operating in the limited streamer mode. They are very similar to the CMU, with the exceptions that preamplifiers are included, there is only one anode wire per chamber, and the anode wires are not connected in couples, because the z-information of the CMP chambers is not important. Unlike the CMU chambers which are arranged in towers, the CMP chambers are arranged in stacks, positioned around the detector. The resolution of the chambers in the drift-ϕ direction is 250 μm. Figure 3.15 shows a CMP stack.

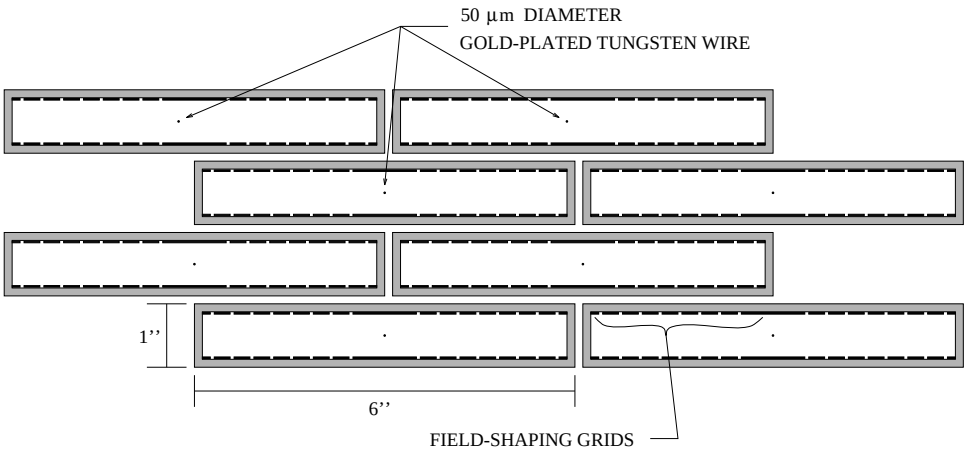

Figure 3.15 A Central Muon Upgrade (CMP) stack.

Central Muon Extension (CMX)

The Central Muon Extension chambers cover the region $0.6 \leq |\eta| \leq 1.0$. These drift chambers are similar to the CMP ones and they are sandwiched between scintillators (CSX). The chambers are arranged in wedges, like the one shown in Figure 3.16. There are gaps in the CMX configuration at $\phi = 90^\circ$ (bottom) due to the collision hall, and at $\phi = 20^\circ$ (top) due to the beam pipe and the solenoid refrigeration.

Depending on the incident angle, particles have to penetrate 6-9 absorption lengths on material to be detected in the CMX. The ϕ information of the muons is measured with a resolution of 250 μm. The CMX chambers were used in the Run Ib to increase the pseudorapidity coverage in the central region.

Forward Muon System (FMU)

At the high pseudorapidity region, there are two muon spectrometers [65]. Each spectrometer contains two 1 m thick, 7.82 m in diameter, 395 ton steel toroids, which are excited by four coils to a magnetic field of 2 T at the inner radius to 1.6 T at the outer radius. Three layers of drift chambers measure the muon trajectories with accuracy of 5° in the ϕ direction and $\sim$ 200 μm in the r direction. Each chamber is composed of two planes of drift cells: 56 *coordinate* cells are closest to the beam and 40 *ambiguity* cells are staggered relative to the coordinate cells to resolve the left-right ambiguity. Each cell contains a 63 μm in diameter anode wire. All cells are graded

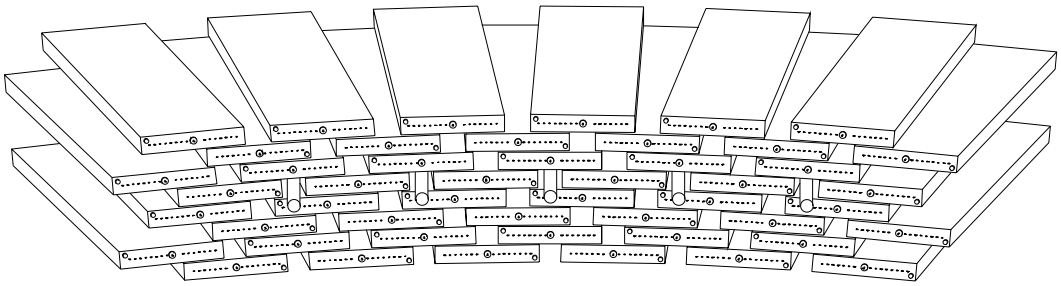

Figure 3.16 A Central Muon Extension (CMX) wedge.

and projective with respect to the nominal interaction point. Position resolution is 130 μm and the gas used is 50%-50% argone-ethane. Two layers of counters made of 13 mm thick 10% naphthalene-doped acrylic scintillator provide trigger information. Signals from the spectrometers pass through a preamplifier, amplifier-discriminator, and a TDC. The momentum resolution is 13% for muons with total momentum greater than 8 GeV.

3.2.5 The Beam-Beam Counters

There is a plane of scintillation counters (beam-beam counters (BBC) [54, 66]) on the front face of each of the forward and backward electromagnetic shower calorimeters, that cover the pseudorapidity region $3.24 \leq |\eta| \leq 5.90$. They provide a minimum-bias trigger, and they also monitor the luminosity. Their timing resolution is 200 ps, hence they provide the best measurement of the interaction time. Because their position resolution is 4 cm, they only provide a crude measurement of the vertex position of the interactions. The minimum-bias trigger requires at least one of the counters in each plane to fire within 15 ns window, centered on the beam crossing time. The rate (number) of coincidences in the BBC counters divided by the effective cross section of the counters gives us the instantaneous (integrated) luminosity.

3.2.6 The Triggers

The event rate at CDF is 286 kHz for one bunch crossing every 3.5 μs. Typical minimum-bias multiplicity is greater than 50 charged particles. Because we are limited by the data recording rate of $\sim$ 10 Hz, we have to select and write on the tape only the interesting events. This is achieved with the CDF three-level trigger system [66]. The most time-consuming process in the data handling is the data readout of the detector components by the data acquisition system, which takes about 1 ms. Readout starts only if Level 2 trigger has been satisfied.

The CDF has a three-level trigger system designed to select events that can contain electrons, muons, jets and missing transverse energy. The first two levels are implemented in hardware, while the third is a software trigger (a version of the offline reconstruction software optimized for speed and implemented by a CPU farm). More than one level is used so that the fast and simple functions are performed at a lower level, where the rate of data is high, and the more complicated and time consuming processes are taking care at the higher level, where the rate of incoming data is considerably decreased. The trigger system of CDF is designed so that the known interesting high energy processes are accepted, without excluding possible new-physics related processes.

Level 1 Trigger

At level 1 decisions on which events will be further considered have to be made in less than 3.5 μm, the time between beam crossings. These decisions are based on

- The sums of the energy from the electromagnetic and hadron calorimeters and the sum of total transverse energy E_T of the event,
- The transverse energy imbalances in the electromagnetic and hadron calorimeters (given by $E_T \cos\phi$ and $E_T \sin\phi$),
- The existence of stiff track in CTC and/or existence of muon candidates in central and forward muon chambers and
- The presence of beam-beam interaction and/or presence of beam-gas interaction

The synchronization of all processes of the trigger system is taken care by the Timing Control. Since speed is an important issue at Level 1, the first steps of the central calorimetry energy summation is performed on analog signals, with the use of operational amplifiers. In the case of Forward and Plug calorimeters the summation is performed by the front-end amplifier cards.

Initially, the signals from two neighboring calorimeter towers are combined to form trigger towers with resolution of $(\eta, \phi) = (0.2, 15^\circ)$. This reduces the number of electronic channels. The signals are then multiplied by a weighted factor, to accommodate tower gain variations, and a bias factor is added, to compensate for calorimeter amplifier pedestals. These functions are performed by the Receive And Weight (RAW) cards. The signals are consecutively passed to the Compare And Sum (CAS) cards, which sum the tower energies that are above a threshold. There are five Electromagnetic Crates and five Hadronic front-end Crates. Each crate has 10 CAS cards and each CAS card has 24 channels. These accommodate 2016 channels from the calorimeters. The crates sum the output signals from the CAS cards. The energy sums at the CAS and Crate levels are analog. The output from the crate summation is digitized by the Fast ADCs on the crates and passed to the Level 1 Sum (Sum of all Crates), for the final – digital – summation. The digital logic used is ECL for speed and compatibility with the FASTBUS backplane. The output sums are $\sum E_T$, $\sum E_T \cos\phi$, and $\sum E_T \sin\phi$ for the electromagnetic and hadronic calorimeters. If the sums are above a threshold, a bit is produced. The sums and the comparison bit are stored in a RAM until next event flushes them out. Information on the comparisons, for 4 different thresholds, is sent to the Fred which will take the final decision for Level 1.

Level 1 trigger also uses information from the BBC counters, which provide a minimum-bias trigger, tag the halo particles, roughly find the interaction point with a precision of 10 cm, and accurately measures the interaction time.

At level 1, electrons are selected by the presence of an electromagnetic trigger-tower with E_T above 6–8 GeV (one trigger tower is two adjacent physical towers in pseudorapidity). Muons are selected by the presence of a track stub in the CMU or CMX, where there is also signal in CMP.

Level 1 delivers a data rate of few KHz to Level 2 trigger. The specific Level 1 trigger requirements for our data sets are presented in Chapter 4.

Level 2 Trigger

The Level 2 trigger system has 20 – 30 microseconds to decide if an event is interesting enough to be recorded. This introduces 10% dead-time for the detector. Level 2 studies the topological features of the transverse energy deposition (clustering of transverse energy in calorimeters) and performs calculations (invariant mass of groups of clusters). It also associates high-p_T tracks with calorimeter clusters and perform first order electron-pion discrimination. The Central Fast Tracker (CFT) is another essential part of the Level 2 trigger. It is a special purpose processor which finds tracks in the CTC that are above a programmable p_T threshold. The Level 1 Muon trigger signals come from the analysis of track segments from central muon systems. Angular cuts are applied in the $r-\phi$ plane that correspond to the p_T threshold. There is also the requirement that the segment should track back to the nominal interaction point.

A list of energy clustering is compiled and passed to a set of programmable processors that make the final decision, which is based on

- The number of energy clusters and their properties (E_T, $E_T \sin\phi$, $E_T \cos\phi$, $\langle\eta\rangle$, σ_η (rms width), $\langle\phi\rangle$, σ_ϕ) and presence of high-p_T tracks,
- The presence and position of track segments in the muon chambers that are associated with high-p_T tracks,
- The total energy and possible transverse energy imbalance in the detector and
- The presence of beam-beam interaction or beam-gas interaction.

At level 2, the CAS energy information from level 1 is loaded to the Cluster Finder, which assigns particular towers to the energy cluster and returns this information to the CAS. This way, the CAS board creates energy sums of individual clusters.

The procedure for finding clusters in the calorimeter starts with the application of an initial high threshold on the RAW card (100 GeV) through the DAC. The threshold

gradually decreases until at one or more calorimeter towers pass the cut; these are the first seeds of the clustering algorithm. A second low threshold (1 GeV) is then applied and the towers which pass this requirement are loaded to the Cluster Finder as low level towers. The process of creating the clusters starts with the seeds, which ask their nearest neighbors that pass the low threshold to turn on. These towers to the same with their nearest neighbors, until no contiguous towers are found. In the process the diagonal neighbors (with different η and ϕ than the requesting towers) are excluded. The energy information of the towers of the cluster is then sent to the CAS to be summed. This process is repeated for all seeds in order to construct all calorimeter clusters. After that, the whole detector is treated as one cluster and the total energy at the towers is summed, to give us an accurate indication of possible missing transverse momentum.

As the clusters are created, the Track Finder is monitoring the Cluster Bus (over which the cluster information is transmitted) and as soon as a bit that corresponds to a high-p_T CTC track is turned on, the momentum information of the particular track is passed to the Timing Control and is to be included in the List of properties of the event.

The Crate Sum at Level 2 is similar to the Level 1 Crate Sum. The difference is that at Level 2 the three analog quantities received from CAS E_T, $E_T \sin\phi$, and $E_T \sin\phi$ correspond to a single calorimeter cluster, and the weighted sums $\sum E_T\eta$ and $\sum E_T\eta^2$ are also produced in Level 2. These five quantities are digitized by a Fast ADC and are sent to the Listmaker, along with the number of calorimeter towers in a cluster.

The Listmaker hardware compiles a list of physical quantities pertinent to the Level 2 Trigger. It outputs three 64-bit words per cluster. The first word contains the electromagnetic E_T, $E_T \sin\phi$, $E_T \sin\phi$, $\langle\eta\rangle$, σ_η, $\langle\phi\rangle$ and σ_ϕ and the second contains the same quantities for the hadronic calorimeters. The third word includes the origin of the cluster, the number of trigger towers, position of the Cluster Finder seeds and, in case there was a high-p_T CTC track associated with the towers, the momentum of the particle. The Listmaker is composed of Sum Boards, Multiplier Boards and RAM Boards. The first two kinds perform the arithmetic operation while the third

one stores the information to be used by the Level 2 processors.

When the interaction between the Cluster Finder and the CAS is over, the muon system takes over the Cluster Bus and transfers the η and ϕ information of muon candidates (which have a high-p_T CTC track associated with the muon chambers) to the Cluster Finder. The CAS, Crate Sum and Listmaker work like before, so the first two words of the muon input to the Level 2 processors will have the electromagnetic and hadronic information associated with the muon and the third one will include the muon momentum.

The Level 2 processors receive the List of three words per calorimeter cluster or track, process the information and make trigger decisions. For example, electron and muon selections are made based on the List information. The results of all the operations are sent to the Fred upon request.

Fred receives up to 12 Level 1 input signals (four bits from the energy sum comparisons and bits from muon logic, track processor, beam-beam counters and silicon counters) and generates a Level 1 accept/reject. If a Level 1 accept is generated, then the Level 2 Processors information is used to generate a Level 2 accept/reject. Fred also serves as the interface between the trigger system and the data acquisition system (DAQ). If a Level 2 accept is generated, the read out of the front-end electronics begins and the trigger information from the Fred is passed to the Level 3 trigger.

The specific Level 2 trigger requirements for our data sets are presented in Chapter 4.

Level 3 Trigger

Unlike Level 1 and Level 2 triggers, the Level 3 trigger is implemented with software. The FASTBUS system is flexible with support for both high and low speed devices.

If an event passes Level 1 and Level 2 triggers, data from the end crates are digitized and read by scanner modules. Each scanner can buffer four events and the buffering is managed by the Trigger Supervisor. When an event is buffered, the Buffer Manager (BFM) is notified. The BFM supervises dataflow from the scanner modules to the host computers. The Event Builder (EVB) reads the buffers and reconstructs complete events. It writes these events into a specified node in the Level 3 processor

farm (Silicon Graphics computers) of thoughput of about 100 events/sec. The EVB reformats scanner data into banks which are organized by detector component.

The Level 3 computers execute FORTRAN filter algorithms and they apply trigger requirements on-line. If the events pass the Level 3 trigger, their banks are stored on magnetic tape. The specific Level 3 trigger requirements for our data sets are presented in Chapter 4.

Chapter 4

Data Selection

The determination of the data sets used in the physical analysis is a crucial task. One wants to apply the proper requirements (cuts) in order to accept the maximum number of signal events and, at the same time, reduce the background as much as possible.

As discussed in the previous chapter, the online data selection takes place in three trigger levels. In this Chapter we describe the specific electron and muon requirements that need to be satisfied at each level of the trigger system. We also present the quality cuts that are applied on the data sets to generate strict inclusive lepton data sets associated with the production and decay of the W boson. Jet cuts are applied to select the W and at-least-one-jet data set (*inclusive* W+jet data sample). As discussed in Chapter 2, we perform our analysis on a high-p_T W data sample containing at least one jet satisfying our selection requirements. This jet balances the W transverse momentum p_T^W and allows us to compare our results to the Standard Model prediction of the angular distribution of the W as a function of the p_T^W. This prediction includes at least one jet, for non-trivial values of the W transverse momentum.

4.1 The Electron Data Sample

4.1.1 The Level 1 Electron Trigger

The electron candidates are required to deposit a minimum energy of 6 GeV (Run Ia) or 8 GeV (Run Ib) in a trigger tower, to be further considered. One trigger tower is the sum of energies of two adjacent (in η) physical towers of the CEM calorimeter.

4.1.2 The Level 2 Electron Trigger

The Level 2 trigger rejects electron candidates if the ratio of the hadronic to electromagnetic energy in the central calorimeter is greater than 0.125.

In Run Ia, the event passes the trigger if the energy cluster in CEM is at least 9 GeV with a seed tower of at least 7 GeV and there exists a matching track in the CFT with $p_T > 9.2$ GeV. It also passes the trigger if there is an isolated cluster in the CEM calorimeter of at least 16 GeV.

In Run Ib, the event passes the trigger if

- the energy cluster in CEM is at least 16 GeV and there exists a matching track in the CFT of $p_T > 12$ GeV (most common trigger), or
- the energy cluster in CEM is at least 8 GeV and there exists a matching track in the CFT of $p_T > 7.5$ GeV, or
- or the energy cluster in CEM is at least 8 GeV and there exists a matching track in the CFT of $p_T > 7.5$ GeV and matching CES hits, or
- there exists an isolated cluster in the CEM calorimeter of at least 16 GeV (with or without CES hits), or
- if there is an isolated cluster in the CEM calorimeter of at least 23 GeV and matching CES hits.

There is an overlap between loose and tight trigger requirements, in order not to bias the data sample at this early stage.

4.1.3 The Level 3 Electron Trigger

At Level 3, the online triggers are a logical "or" of eight central electron triggers [67].

In Run Ia, most of the accepted events pass the trigger requirement that the CEM cluster has $E_T > 18$ GeV and it is associated with a track of $p_T > 13$ GeV. The transverse energy of the cluster is defined as $E_T = E \sin\theta$, where E is the total energy deposited in the CEM calorimeter and θ is the polar angle measured from the event vertex to the centroid of the cluster. An event can also pass the trigger if $E_T > 25$ GeV. Quality cuts check the shape of the electron shower profile and the energy deposition patterns.

In Run Ib, the CEM $E_T > 18$ GeV and CFT $p_T > 13$ GeV requirements are applied, with the addition of a tighter requirement of CEM $E_T > 50$ GeV and CFT $p_T > 25$ GeV.

The offline selection starts with the reconstruction of the electromagnetic clusters, starting with the towers with E_T greater than 3 GeV (seed towers). The towers adjacent to the seed towers are included in the cluster, if their E_T is at least 100 MeV. If the E_T of a newly included tower is greater than the E_T of the seed, it becomes the new seed. In the central region (CEM), which is the one used for this analysis, most of the electromagnetic clusters are contained in one tower. The wider energy deposition covers three towers in η, whereas the development of the shower in more than one tower in ϕ is prohibited by the CEM cracks. The event passes the offline Level 3 trigger if $E_T > 5$ GeV, and the ratio of hadronic to the electromagnetic energy associated with the cluster is less than 0.125

Events that pass the Level 3 triggers constitute an *inclusive high-p_T electron sample*.

4.1.4 The Electron Quality Cuts

To improve the quality of the electron sample, reducing the probability that some of our events are not true $W \to e\nu_e$, we apply the following requirements:

- Good Run requirement.

  Some runs are not acceptable because the beam was not stable or at least one

major part of the detector or the data acquisition systems did not operate properly. These runs are not included in the analysis.

- $|Z_{\rm VTX}| \leq 60$ cm,
  where $Z_{\rm VTX}$ is the event vertex as measured by the VTX. We require the production of the electron to occur within the expected z range of proton-antiproton collisions, to maintain the projective property of the calorimeter towers and to be confident we use the fiducial volume of our detector.

- Fiducial region requirement.
  We apply the geometrical requirement that the electron passes through a part of the CEM calorimeter which functions properly and is well understood. The position of the cluster is determined from the CES strip detector centroid and its local coordinates $(X^{\rm local}_{\rm ces}, Z^{\rm local}_{\rm ces})$ have to be: $|X^{\rm local}_{\rm ces}| \leq 21$ cm and $9.0 \leq |Z^{\rm local}_{\rm ces}| \leq 230$ cm.

- $E_T^{\rm corr} \geq 20$ GeV,
  where $E_T^{\rm corr} \geq 20$ is the transverse energy of the cluster corrected for differences in response, non-linearities, and time-dependent changes. In the rest of this dissertation, when we mention the energy of the electron, we will always refer to the corrected energy of the cluster. The requirement that the transverse energy is high reduces the tau lepton background, where the tau decays to a electron. The electrons originated from tau decays tend to have lower transverse energy, due to the extra neutrinos present in the process. The QCD background is also suppressed in high-E_T electron events.

- $E^{\rm HAD}/E^{\rm EM} \leq 0.055 + 0.00045E$,
  where $E^{\rm HAD}$ is the energy deposited by the electron in the hadronic calorimeter and $E^{\rm EM}$ is the energy deposited in the electromagnetic calorimeter, both in GeV. We do not expect large energy deposition in the hadronic calorimeters by the electron. The energy deposited in the hadronic calorimeter slightly increases with the electrons energy; that is the reason we use the sliding cut. This cut has constant efficiency with electron energy.

- $ISO(0.4) \equiv E_T^{\rm Excess}(\Delta R = 0.4)/E_T^{\rm Cluster} < 0.10$,
  where $E_T^{\rm Excess}(\Delta R = 0.4)$ is the transverse energy in the hadronic and electromagnetic calorimeters in a cone of size $\Delta R = \sqrt{(\Delta\phi)^2 + (\Delta\eta)^2} = 0.4$, with the energy of the electron excluded. The quantity ISO is called *isolation*. This cut rejects the electrons that are not isolated from extra hadronic activity and could be the products of quark semileptonic decays.

- $|\Delta X| < 1.5$ cm and $|\Delta Z| < 3$ cm,
  where ΔX is the difference in the η-ϕ space between the extrapolated CTC track and the CES position of the shower, measured at the CES. ΔZ is the same difference in the z direction. These matching cuts make certain that the electromagnetic cluster position, measured by the CES, corresponds to the track seen in the CTC. This dramatically increases the probability that both signals were caused by the same particle.

- $L_{\rm SHR} \equiv 0.14 \sum_i \frac{E_i^{\rm meas} - E_i^{\rm exp}}{\sqrt{(0.14)^2 E^{\rm meas} + (\Delta E_i^{\rm exp})^2}} < 0.2$,
  where $L_{\rm SHR}$ is the *lateral shower profile*, $E_i^{\rm meas}$ is the energy measured in the i-tower adjacent to the seed tower, and $E_i^{\rm exp}$ is the expectation for the energy in that tower (based on the seed tower energy, the CES position, the event vertex and shower profile parameterization from test beam studies). The quantity $(\Delta E_i^{\rm exp})$ is the uncertainty on the expected energy and $0.14\sqrt{E^{\rm meas}}$ is the uncertainty in the measurement of the cluster energy. The sum is over the two adjacent (in ϕ) towers to the seed tower. From beam studies and Monte Carlo simulation, we know that the $L_{\rm SHR} < 0.2$ cut, nicely separates electrons from other particles that shower in the CEM.

- $0.5 < E/p_T^{\rm BC} < 2$,
  where $p_T^{\rm BC}$ is the *beam-constrained* momentum of the electron. This means that when we use the CTC hit points to determine the momentum, we include the event vertex in the fit. This increases the momentum resolution by a factor of two. In the rest of this dissertation, when we mention the track momentum of the electron, we will always refer to the beam-constrained momentum. About the cut: the high energy electrons have energy which is equal to their momen-

tum. In practice, the energy measured in CEM and the momentum measured in the CTC do not exactly match, because of the limited resolution of the detector, because of bremsstrahlung some electrons experience in the CTC and because of cracks in the electromagnetic calorimeter. Nevertheless, to accept an events, we demand that the ratio of the measured energy of the electron to its momentum to be between 0.5 and 2.

- ($\chi^2_{\rm CES} < 10$).
  The CES strip detector provides us with the transverse development of the electromagnetic shower, when it reaches its expected maximum. The strips measure the shower profile in the z direction and the wires of the CES measure the shower profile in the x direction. By comparing the measured x-shape and z-shape with the expected ones (determined from test-beam studies) we construct the $\chi^2_{\rm str}$ and $\chi^2_{\rm wir}$ chi-squared quantities respectively. We use the average of the two ($\chi^2_{\rm CES}$) and we require it to be less than 10, to make certain that the shower is caused by an electron and not another particle.

- Conversions Removal.
  We remove electrons that come from photon conversion in the material of the inner detector of CDF. A conversion is identified from the reconstruction in the CTC of a low mass (< 1 GeV) electron-positron pair coming from common secondary vertex. Another indication of a photon conversion is the mismatch in the wire hits between the VTX and CTC. If we get more hits in the CTC, a conversion is probable.

The electrons passing these quality cuts are called *golden electrons*. The integrated luminosities for the inclusive electron data sets used in our analysis are $19.64 \pm 0.71 {\rm pb}^{-1}$ (Run Ia) and $90.35 \pm 3.70 {\rm pb}^{-1}$ (Run Ib), for a total luminosity of 110 pb^{-1}.

To define our inclusive W data sample, we need to describe the correct determination of jets and missing E_T. The next two sections address these issues.

4.2 The Construction of Jets

Partons (quarks and gluons) are very frequently produced in hadron collisions. As they move away from their production vertex, the QCD interaction between them continuously increases. When the potential energy between them is larger than the energy required for the production of a quark-antiquark pair out of vacuum, the latter phenomenon takes place. This process is repeated for the resulting new partons and consequently a spray of hadrons (materialization of quarks) is coming out of the interaction point. This avalanche of hadrons is called a *jet*. The direction of motion and energy of the outgoing jet is an indication of the direction and energy of the initial parton.

Frequently, several jets per event are produced in hadron collisions. Hence, we define a *jet clustering* algorithm that properly reconstruct the jets, and separates them or clusters them together, depending on their topology.

The CDF jet clustering algorithm [68] is an iterative cone algorithm. It starts with *seeds* in the electromagnetic and hadron calorimeters (towers with transverse energy greater than 1 GeV). The highest-E_T tower becomes the attraction point and a precluster is constructed by grouping together its adjacent towers within a cone of radius R in η-ϕ space. Next, the E_T-weighted centroid of the precluster is calculated and a new cone of radius R is formed around that centroid. All towers in that cone that have $E_T > 100$ MeV are grouped into a new cluster. The new centroid is calculated and the procedure is repeated until the cluster remains unaltered. The cluster centroids are vector sums of massless four-vectors associated with every tower of the cluster. The magnitude of such a four-vector is equal to the energy deposited and its direction coincides with the outgoing ray connecting the event vertex to the centroid of the tower. There is often an overlap between clusters. The algorithm sums the transverse energies of the overlapping towers and divides the sum by the total transverse energy of the smaller cluster. If the result is greater than 0.75, the two clusters are combined into one. Otherwise, the two clusters remain separate and the overlap towers are assigned to the cluster with the nearest center in η-ϕ space. In both cases, the new centroids are calculated.

The energy of the cluster cannot be associated with the energy of the jet without

corrections. The corrections applied (JTC96S) in the right order are [69]:

- Relative corrections: The calorimeters are not perfect instruments. Their response varies from tower to tower as a function of η of the detector. Also, cracks between the calorimeter modules affect the energy measurement. For these reasons a correction is applied to the raw energy reported by the calorimeter. This correction is detector-η depended and is determined from studies of dijets, with one well measured central jet. The correction is applied to the calorimeter towers, so that the second jet balances the well measured one.

- Extra interactions corrections: In the discussion on jet reconstruction, we made the implicit assumption that there is only one interaction per beam bunch crossing. It is very common that extra proton-antiproton interactions, the number of which is generally proportional to the number of the reconstructed vertices, take place in a bunch crossing and deposit energy in the calorimeters. In order to accurately measure the jet energy, we multiply it with a correction factor, determined from minimum-bias events studies.

- Absolute corrections: Unlike the relative corrections, which depend on the location of the cluster in the calorimeters, the absolute corrections are relevant to the global inefficiencies of the calorimeters, or physical processes (for example, semileptonic decays of the heavy quarks within the jets resulting to neutrinos and muons which deposit little or no energy in the calorimeters). Monte Carlo generators produce and fragment partons that are processed by the CDF detector simulator. The transverse momentum measured by the calorimeters is compared to the actual transverse momentum of the generated particles and the correction factor (as a function of the p_T of the jet) is determined.

- Underlying event corrections: There is an *underlying event* which is not related to the physical processes we study and it is due to the fact that the colliding hadrons consist of many spectator partons which also minimally interact with each other. As a result, there is extra energy in the calorimeters which is not related to the jet-producing outgoing parton. A small E_T value is subtracted from each jet to account for this effect.

- Out of cone corrections: Some of the energy of the jet is deposited outside the clustering cone. This energy is called *out-of-cone* energy and results in an underestimation of the jet energy. One usual source of out-of-cone radiation is the production of soft gluons. To compensate for this effect, we add some energy in the measured amount. The correction is larger for low-p_T jets, which are wider in η-ϕ space and more of their energy lies outside the clustering cone.

After the application of the corrections, we are confident that our measurement of the jet energy is as accurate as possible for the clustering cone chosen. In this analysis, we use a radius of $R = 0.7$ for the clustering cone of jets. For the calculation of the missing transverse energy, described in next section, we use jets of cone radius $R = 0.4$. For the rest of this thesis, all jets have the JTC96S corrections applied.

4.3 The Missing Transverse Energy

Neutrinos produced in the proton-antiproton collisions are not detected by CDF, because they only interact through weak interactions. Since our detector is hermetic in the transverse plane, we can measure any energy imbalance in that plane for each event and associate it with the undetected neutrino. This is the missing transverse energy ($\not\!\!E_T$), widely used in high energy physics analyses. On the other hand, the same cannot be done in the longitudinal direction, due to the particles that are not detected in the beam-line, or at very high pseudorapidities. In the z-direction, we loose a significant number of particles, not just the neutrinos, and therefore the longitudinal missing energy cannot be solely assigned to the neutrinos. As a result, we can only make statements about the transverse properties of the neutrinos.

Equation (3.7), used for the fast estimation of the $\not\!\!E_T$ at the trigger level, is not very accurate in providing us the missing transverse energy because of two reasons: if there are more than one vertices in the event, the $\not\!\!E_T$ could be calculated using the wrong vertex, and, in addition, not all of the towers of the calorimeters have the same response to the deposited energy ([70], [71]). The correct equation is:

$$\vec{\not\!\!E}_T = -\sum(\vec{E}_e + \vec{E}_\gamma + \vec{E}_\mu + \vec{E}_{\rm jet} + K\vec{E}_{\rm uncl}) \tag{4.1}$$

where $\vec{E}_e$ is the electron cluster energy in the electromagnetic calorimeter, $\vec{E}_\gamma$ is any photon energy in the calorimeter, $\vec{E}_\mu$ is the muon energy and $\vec{E}_{\rm jet}$ is the total jet energy calculated in a cone of $\Delta R = 0.4$ and minimum jet E_T of 10 GeV, $\vec{E}_{\rm uncl}$ is the unclustered energy, and K is a scale factor for the unclustered energy correction. Of course, for an electron sample, there are no muons or real photons in the above formula. In the case of the muon sample, there are no electrons or real photons.

We calculate the unclustered energy by summing the energy deposited in all the towers of the calorimeters, if it exceeds the 100 MeV. Because of detector cracks and imperfections, the unclustered energy has to be corrected by the scale factor K. Its value is determined by looking at Z events, where no missing energy is expected and the events have to be balanced. In the above, we have to make sure not to count the electron energy twice; when we calculate the jet energy, we remove the electromagnetic calorimeter clusters that have already been counted as electron clusters.

4.4 The $W \to e\nu_e$ Events Selection

After having defined the $\not\!\!E_T$, we can proceed with the $W \to e\nu_e$ events selection requirements:

- $E_T^e > 20$ GeV.
  The typical W events are associated with large charged lepton transverse energy. Electrons with low E_T could originate from processes other than direct W decays.

- $\not\!\!E_T > 20$ GeV.
  The typical W events are associated with large missing transverse energy.

- $|\eta^e| \leq 1$.
  We concentrate on central electrons, measured in the CEM. Most of the W decays, result in central electrons. In addition, we require the absolute physical pseudorapitity of the electrons to be less than one, since we apply the same requirement to the Monte Carlo sample.

- $M_T^W > 40$ GeV,
  where the transverse mass is defined as $M_T^W = \sqrt{2E_T^e E_T^\nu[1-\cos(\phi_e - \phi_\nu)]}$. The transverse energy E_T^ν of the neutrino equals the missing transverse energy $\not\!\!E_T$ of the event and the azimuthal angles ϕ_e and ϕ_ν of the electron and the neutrino respectively are known, since the momenta of both particles are reconstructed in the transverse plane. The transverse mass cut reduces the $W \to \tau\nu_\tau$ background, where the τ decays to an electron, as we will see in detail in Chapter 6.

- The event should not be consistent with a Z or a one-legged Z.
  The Z particles decay to two electrons, so identifying both of them and verifying that the combined mass of the dielectron is close to the mass of the Z leads to the removal of these events from our sample. One-legged Z bosons are the ones that have only one of their decay leptons (*legs*) detected. The other leg is not observed, because it does not leave a track in the CTC or passes through a non-fiducial part of the detector like the cracks between modules of the electromagnetic calorimeter. These Z bosons look like W bosons, since their signature is a lepton and a missing transverse energy (the energy of the undetected second leg). Using the kinematics of the events, we can remove most of them.

After the application of the above jet cuts, we end up with 73363 inclusive $W \to e\nu_e$events (13290 Run Ia events and 60073 Run Ib events)

4.5 The ($W \to e\nu_e$)+Jet Events Selection

The final step to the creation of the ($W \to e\nu_e$)+jet) data set used in our analysis is the application of the jet requirements. At CDF, a well measured jet has to have:

- $E_T^{\rm jet} \geq 15$ GeV and
- $|\eta^{\rm jet}| < 2.4$ GeV.

In addition, we would like to have a good separation between the electron and the jet in the η-ϕ space. We define this separation as

$$\Delta R_{l-j} = \sqrt{(\Delta\phi)^2 + (\Delta\eta)^2}, \tag{4.2}$$

where $\Delta\phi = \phi^l - \phi^{\rm jet}$ and $\Delta\eta = \eta^l - \eta^{\rm jet}$, the differences between the lepton (electron) and jet positions in the η-ϕ space. We require that

- $\Delta R_{l-j} > 0.7$.
  This cut complements the isolation cut, described in Section 4.1.4.

Finally, we perform our analysis for $p_T^W > 15$ GeV. Our sample would be biased for p_T^W below 15 GeV, because of the jet E_T cut of 15 GeV we impose on the data and because of the approximate balance between the jet and the W. This balance is manifest in our event generator (DYRAD, described in Chapter 5), which sets a cut on the produced jet at 10 GeV. So we impose:

- $p_T^W > 15$ GeV
  This cut complements the isolation cut, described in Section 4.1.4.

After the application of the above jet cuts, we end up with 12817 electron events (2277 Run Ia events and 10540 Run Ib events).

Our analysis is done for four p_T^W bins (15-25 GeV, 25-35 GeV, 35-65 GeV, and 54-105 GeV), because we want to measure the angular coefficients as a function of the transverse momentum of the W. Therefore, we present the Run I W+jet yields for the W decaying to an electron, in Table 4.1

In an angular distribution analysis of the W, it is necessary to choose a charge of the W study, as explained in Section 2.2. We choose to work on W^- and we CP transform all W^+ events to look like W^- eventsThe histograms of Figures 4.1 to 4.6 show the lepton, neutrino, W and jet four-momenta, rapidity, transverse momentum and W transverse mass for our W+jet data set and for the Fast Monte Carlo (FMC) prediction. Plot 4.7 shows the plots for the transverse momentum of the W. The four-momentum of the electron is constructed based on the electron's corrected CEM

Data yields for inclusive ($W \rightarrow e\nu_e$)+jet	
p_T^W (GeV)	Number of electrons
15-25	5166 ± 72
25-35	3601 ± 60
35-65	3285 ± 57
65-105	624 ± 25

Table 4.1 The electron CDF data yields for inclusive W+jet. The uncertainties are only statistical.

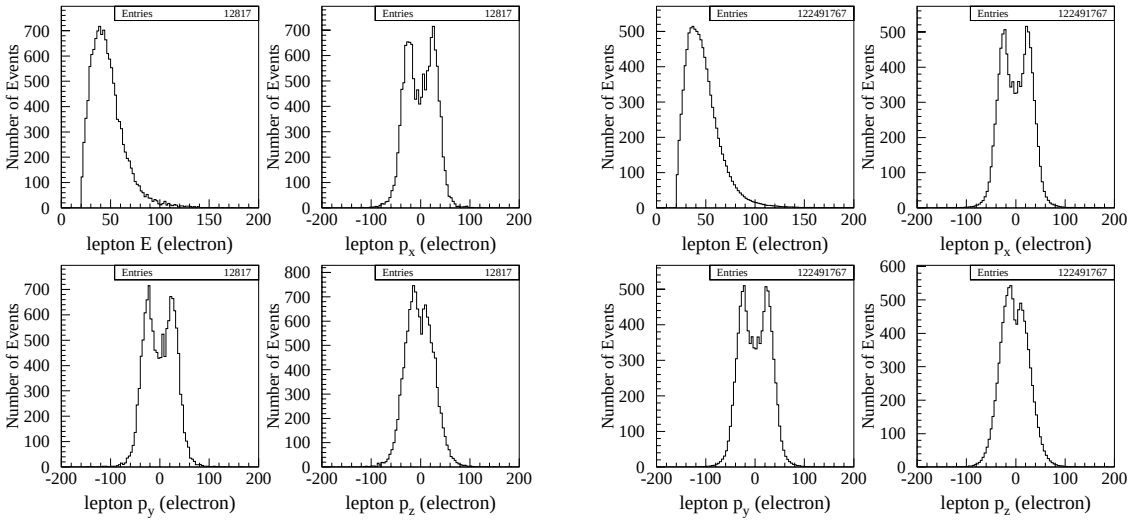

Figure 4.1 Four-momentum of electron for electron data (left) and electron FMC (right) in W^-+jet events. The four-momentum of the electron is constructed based on the electron's corrected CEM energy. The FMC histograms are normalized to the expected yields (no backgrounds are included).

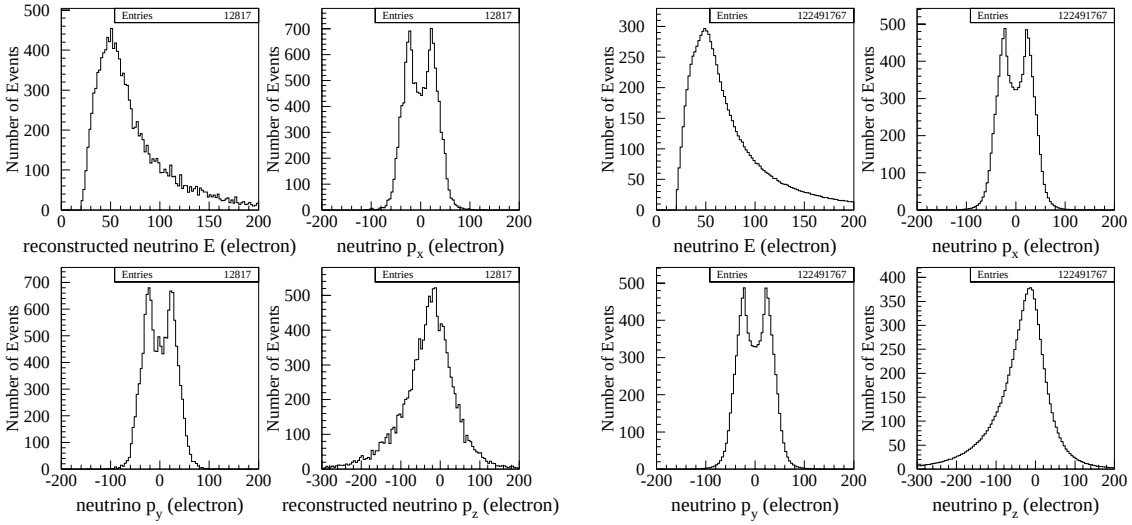

Figure 4.2 Four-momentum of neutrino for electron data (left) and electron FMC (right) in W^-+jet events. The FMC histograms are normalized to the expected yields (no backgrounds are included).

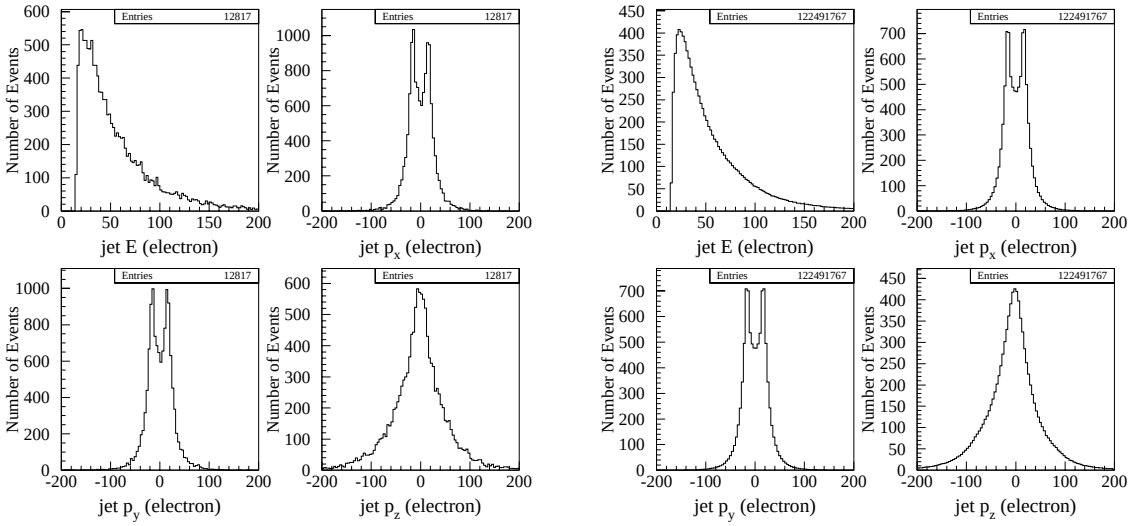

Figure 4.3 Four-momentum of jet for electron data (left) and electron FMC (right) in W^-+jet events. The FMC histograms are normalized to the expected yields (no backgrounds are included).

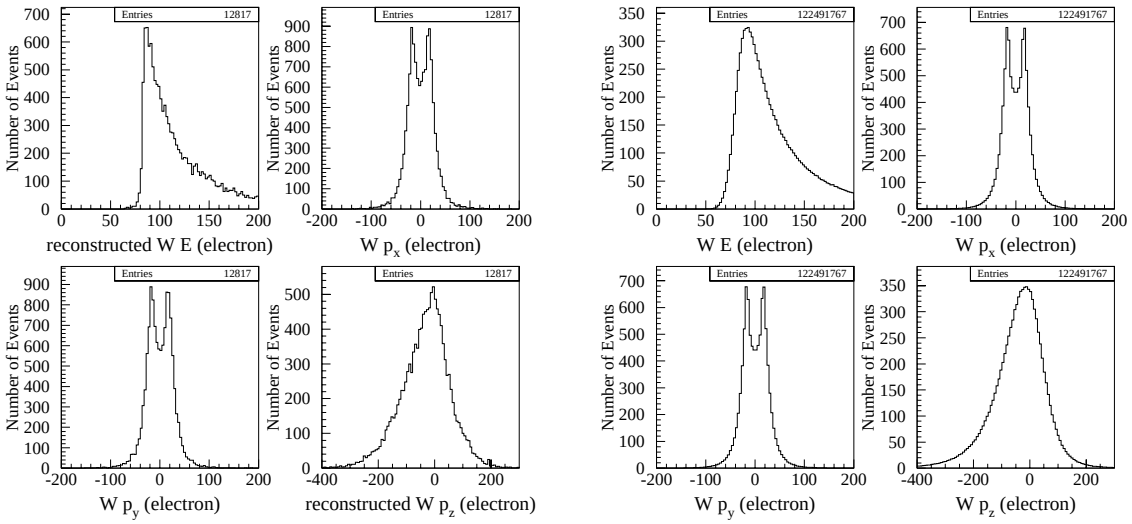

Figure 4.4 Four-momentum of W boson for electron data (left) and electron FMC (right) in W^-+jet events. The FMC histograms are normalized to the expected yields (no backgrounds are included).

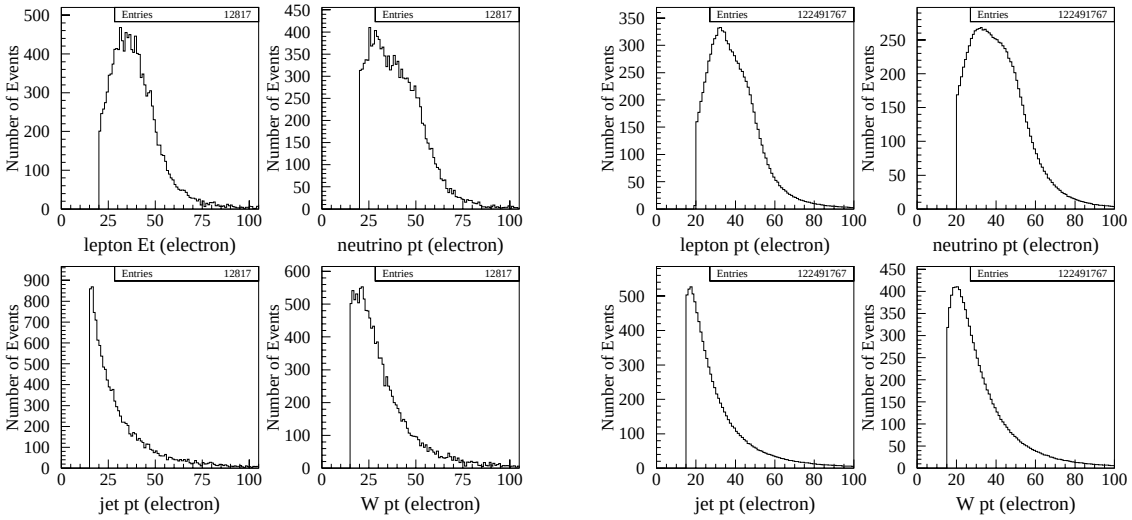

Figure 4.5 Transverse momentum of the particles for electron data (left) and electron FMC (right) in W^-+jet events. The FMC histograms are normalized to the expected yields (no backgrounds are included).

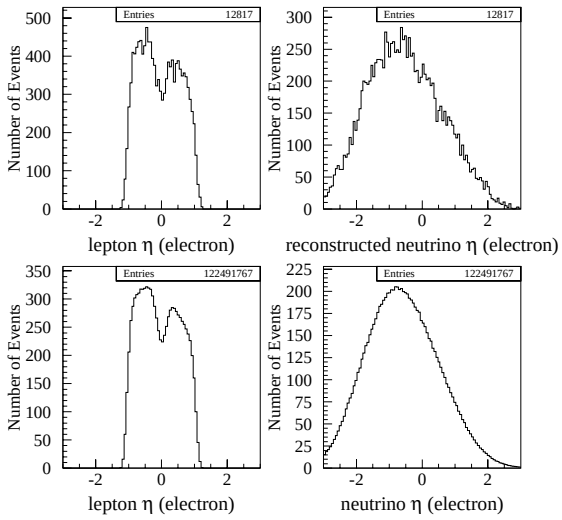

Figure 4.6 Rapidity of the electron and neutrino for the electron data (upper plots) and electron FMC (lower plots) in W^-+jet events. The FMC histograms are normalized to the expected yields (no backgrounds are included).

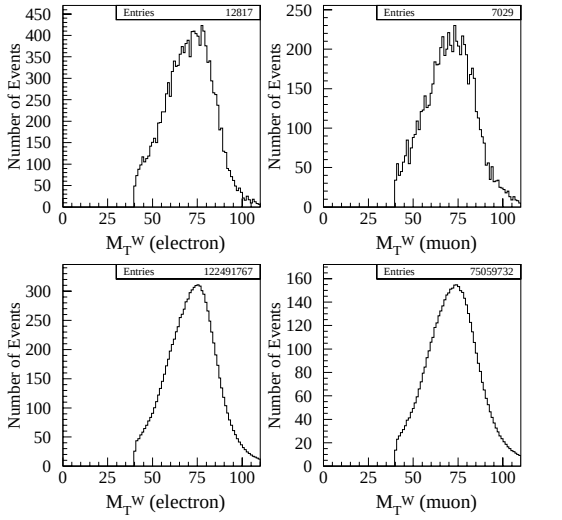

Figure 4.7 Transverse mass of the W for the electron and muon data (upper plots) and the electron and muon FMC (lower plots) in W^-+jet events. The FMC histograms are normalized to the expected yields (no backgrounds are included).

energy (and not its track momentum). The W four-momentum is the sum of the electron and neutrino four-momenta. The FMC is a fast CDF detector simulator which analyzes events produced from the DYRAD W+jet next-to-leading (NLO) event generator. The DYRAD and FMC Monte-Carlos are described in Chapter 5. The FMC events are normalized to the FMC yield predictions and the backgrounds have not been included yet. In the data plots, the longitudinal information for the neutrino and the W is not known but it is reconstructed. The two possible solutions for the longitudinal momentum of the neutrino and the W are constrained by the W mass while the choice of one of the two solutions is made using the phase space of the kinematic variables, which consists of the DYRAD rapidity of the jet, charged lepton, neutrino and the W. More details on this method can be found in Appendix B. We observe good agreement, between the FMC and data plots.

4.6 The Muon Data Sample

4.6.1 The Level 1 Muon Trigger

The Level 1 trigger uses the drift time information from the CMU, CMP, and CMX to reconstruct the momentum of a muon candidate that created a stub in the above muon detectors. This stub momentum is inversely proportional to the drift time difference between anode wires within the muon chambers, as seen in Figure 3.14. The Level 1 requirement is that the stub momentum has to be greater than 6 GeV.

4.6.2 The Level 2 Muon Trigger

The Run Ia Level 2 trigger uses the CFT information on high-p_T tracks. It looks at the $r-\phi$ pattern maps from CTC to the muon chambers and does not reject the muon candidate, if the ϕ angle difference between the CFT extrapolation to the muon chambers and the actual muon stub in the muon chambers is less than 5°. This corresponds to a 9.2 GeV cut on the momentum of the CFT track. The muon stub can be in either CMU and CMP chambers, or only in CMU, or only in CMP. No CMX triggers are accepted in Run Ia.

In Run Ib, the Level 2 trigger requires a stub in CMU only, or CMU+CMP, or CMX with a matching CFT track with momentum greater than 12.5 GeV and a matching window of 5° in ϕ. At this level there are also stricter triggers that require minimum ionization transverse energy in the calorimeter wedge less than 3 GeV for a CMU or CMP stub, and non-zero energy in the calorimeter wedge in front of the muon stub for a CMX stub. Also accepted are the muon candidates that have a muon chamber stub (in the CMU only, or CMP only, or in both CMU and CMP, or in CMX) with the additional requirement of the presence of a jet [67].

4.6.3 The Level 3 Muon Trigger

The Level 3 trigger requires that [67]:

- $p_T^\mu > 18$ GeV,
  where p_T^μ is the CTC momentum of the muon candidate.
- $E^{\rm HAD} < 6$ GeV,
  where $E^{\rm HAD}$ is the energy deposited in the hadronic calorimeter by the muon candidate,
- $|\Delta X_{\rm CMU}| < 5$ cm, $|\Delta X_{\rm CMP}| < 10$ cm, and $|\Delta X_{\rm CMX}| < 10$ cm,
  where $\Delta X_{\rm CMU}$, $\Delta X_{\rm CMP}$, and $\Delta X_{\rm CMX}$ are the differences between the x position of the stub in the muon chambers and the extrapolation of the CTC track to these muon chambers.

These requirements are implemented with online software. If the event passes these cuts, the event is written on tape and a second set of requirements are applied offline:

- $p_T^\mu > 18$ GeV,
- $E^{\rm HAD} < 6$ GeV,
- $E^{\rm EM} < 2$ GeV,
  where $E^{\rm EM}$ is the energy deposited in the electromagnetic calorimeter by the muon candidate,

- $|\Delta X_{\rm CMU}| < 2$ cm, $|\Delta X_{\rm CMP}| < 5$ cm, and $|\Delta X_{\rm CMX}| < 5$ cm.

These cuts are specific to our analysis. The electromagnetic energy cut was not applied from the beginning, in order to avoid biasing data sets useful for other analyses. After Level 3 trigger, we have an *inclusive high-p_T muon sample.*

4.6.4 The Muon Quality Cuts

To make sure we have true muons in our sample and we understand the data well, we include the following requirements in our analysis program:

- Good Run requirement.
  Some runs are not acceptable because the beam was not stable or at least one major part of the detector or the data acquisition systems did not operate properly. These runs are not included in the analysis.

- $|Z_{\rm VTX}| \leq 60$ cm,
  where $Z_{\rm VTX}$ is the event vertex as measured by the VTX. We require the production of the muon to occur within the expected z range of proton-antiproton collisions.

- Fiducial region requirement.
  We apply the geometrical requirement that the muon passes through a part of the detector that functions properly and is well understood.

- $p_T^{\rm BC} \geq 20$ GeV,
  where $p_T^{\rm BC}$ is the beam constrained momentum of the muon. This means that when we use the CTC hit points to determine the momentum, we also include the event vertex in the fit. This increases the momentum resolution by a factor of two. Another correction of the momentum of the muon is the *false curvature* correction i.e., a correction based on the fact that the CTC sense wires are not perfectly aligned. In the rest of this dissertation, when we mention the momentum of the muon, we will always refer to the beam constrained momentum. The requirement that the transverse momentum is high, reduces the tau

background, where the tau decays to a muon. The muons originated from tau decays have lower momentum, due to the extra neutrinos present in the process. The QCD background is also suppressed in high-p_T muon events.

- $E^{\rm HAD} \leq 6$ GeV.
  We do not expect large energy deposition in the hadronic calorimeters by the muon.

- $E^{\rm EM} \leq 2$ GeV.
  We do not expect large energy deposition in the electromagnetic calorimeters by the muon, as it is much heavier than the electron.

- $ISO(0.4) \equiv E^{\rm Excess}_{\Delta R=0.4}/p_T^{\rm BC} < 0.10$,
  where $E^{\rm Excess}$ is the total energy in the calorimeters in a cone of size $\Delta R = \sqrt{(\Delta\phi)^2 + (\Delta\eta)^2} = 0.4$ with the energy of the muon excluded. We stress that the beam constrained momentum is used in the definition of the muon isolation. This cut rejects the muons that are not isolated and could be the products of quark semileptonic decays.

- $|\Delta X_{\rm CMU}| < 2$ cm, $|\Delta X_{\rm CMP}| < 5$ cm, and $|\Delta X_{\rm CMX}| < 5$ cm.
  These matching cuts increase our confidence that the stub detected in the muon chambers and the track seen in the CTC correspond to the same particle. Figure 4.8 illustrates the extrapolation and comparison process. Multiple scattering effects are removed this way.

- Cosmic filter cut.
  We require that the muon is detected within a time window after the proton-antiproton collision. This time correlation considerably reduces the probability that the muon is a cosmic one.

- $|d_0| \leq 0.2$ cm,
  where d_0 is the impact parameter of the muon with respect to the event vertex. This cut makes sure that the muon is close to the event vertex in the $r - \phi$ plane.

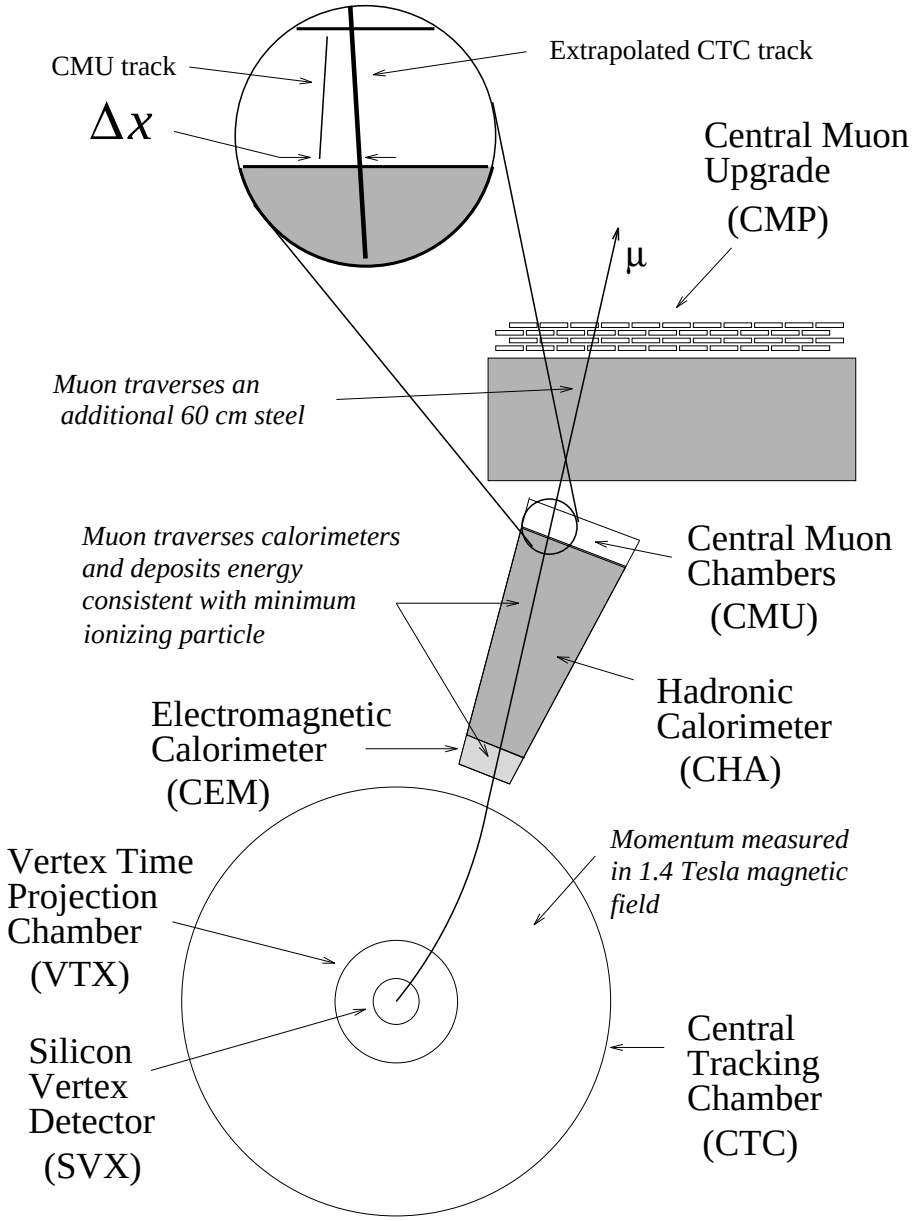

Figure 4.8 The track measured at the CTC is extrapolated to the muon chambers and it has to match well with the muon stab reconstructed at the chambers.

- $|Z_0 - Z_{\rm VTX}| \leq 5$ cm.

  This cut ensures that the muon is close to the event vertex position on the z axis. This cut combined with the impact parameter and the cosmic filter ones ensures us that the muon is spatially correlated to the event vertex and it is not a cosmic muon.

The muons passing these quality cuts are called *golden muons*. The integrated luminosities of Run Ia and Run Ib are: Run Ia (CMUP): 18.33 ± 0.66 pb^{-1}, Run Ia (CMNP): 19.22 ± 0.69 pb^{-1}, Run Ib (CMUP): 88.35 ± 3.62 pb^{-1}, Run Ib (CMNP): 89.20 ± 3.66 pb^{-1}, and Run Ib (CMX): 88.98 ± 3.65 pb^{-1}.[†] The total integrated luminosity is 107 pb^{-1} for the inclusive $W \to \mu\nu_\mu$ Run I events.

4.7 The $W \to \mu\nu_\mu$ Events Selection

- $p_T^\mu > 20$ GeV.

  The typical W events are associated with large charged lepton transverse energy. Muons with low E_T could come from processes other than direct W decays.

- $\not\!\!E_T > 20$ GeV.

  To select W events from the golden muon sample, we have to calculate the $\not\!\!E_T$ that corresponds to the neutrino undetected energy, according to Equation (4.1). In the muon data set case there are no electrons or real photons.

- $M_T^W > 40$ GeV,

  where the transverse mass is defined as $M_T^W = \sqrt{2p_T^\mu E_T^\nu[1 - \cos(\phi_\mu - \phi_\nu)]}$. The transverse momentum E_T^ν of the neutrino equals the missing transverse energy $\not\!\!E_T$ of the event, and the azimuthal angles ϕ_μ and ϕ_ν of the muon and the neutrino in the laboratory frame are known. The momenta of both particles are reconstructible in the transverse plane. The transverse mass cut reduces the $W \to \tau\nu_\tau$ background, where the tau decays to a muon, as we will see in detail in Chapter 6.

[†]CMUP muons pass through both the CMU and CMP chambers, whereas CMNP muons pass only through the CMU and not the CMP chambers.

- The event should not be consistent with a Z or a one-legged Z.

  Z bosons decay to two muons. If they are detected and their combined energy corresponds to the mass of the Z, the events are rejected. Often, one of the muons is not detected, because even though it may be isolated, it passes through a crack of the muon chamber (i.e., it is not fiducial). In that case, we have a one-legged Z, which contributes in the background, because the event looks like a high p_T muon accompanied with missing E_T, just like W event signatures. We can remove plenty of them by studying the topology of the events.

After the application of the above cuts, we arrive to a W inclusive sample with the W decaying to a muon. The total number of events is 38601 (4441 Run Ia CMUP, 955 Run Ia CMNP, 20527 Run Ib CMUP, 3273 Run Ib CMNP and 9405 Run Ib CMX).

4.8 The $(W \rightarrow \mu\nu_\mu)$+Jet Events Selection

The jet requirements for selecting an inclusive $(W \rightarrow \mu\nu_\mu)$+jet data sample are the same as in the electron case:

- $E_T^{\rm jet} \geq 15$ GeV
- $|\eta^{\rm jet}| < 2.4$ GeV
- $\Delta R_{l-j} > 0.7$
- $p_T^W > 15$ GeV

The result is 7029 muon W+jet events (745 Run Ia CMUP, 184 Run Ia CMNP, 3718 Run Ib CMUP, 659 Run Ib CMNP and 1723 Run Ib CMX). The yields for the four p_T bins used in our analysis can be seen in Table 4.2.

Our analysis is done for the W^- boson (we have to choose a charge to perform the helicity analysis). All W^+ in the sample are CP transformed to be treated as W^-. Plots 4.9 to 4.14 show the muon, neutrino, W and jet four-momenta, rapidity, transverse momentum and W transverse mass for our W+jet data set and for the Fast Monte Carlo (FMC) prediction. Plot 4.7 shows the plots for the transverse

Data yields for inclusive ($W \rightarrow \mu\nu_\mu$)+jet	
p_T^W (GeV)	Number of muons
15-25	2821 ± 53
25-35	1869 ± 43
35-65	1880 ± 43
65-105	371 ± 19

Table 4.2 The muon CDF data yields for inclusive W+jet. The uncertainties are only statistical.

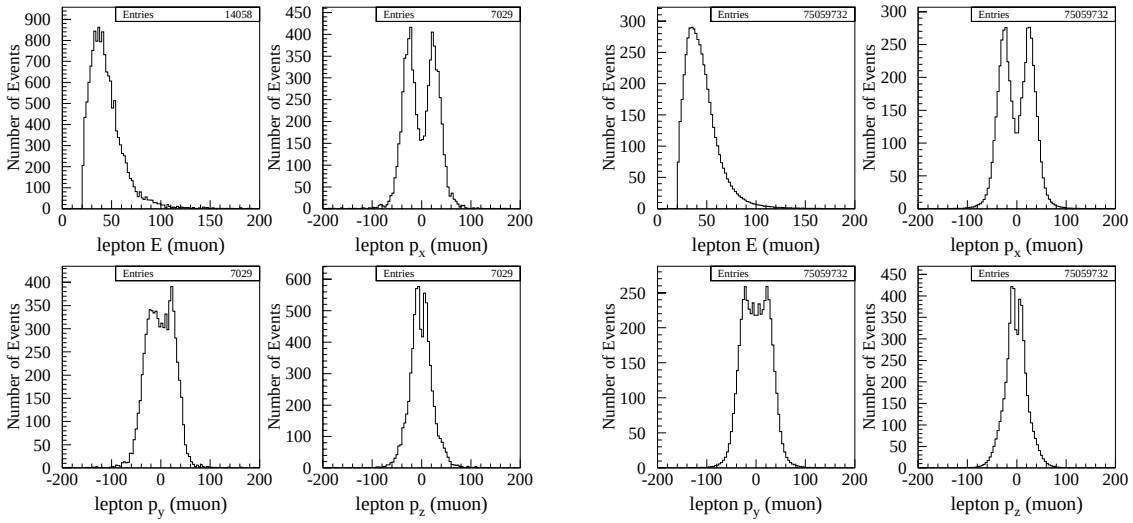

Figure 4.9 Four-momentum of muon for muon data (left) and muon FMC (right) in W^-+jet events. The FMC histograms are normalized to the expected yields (no backgrounds are included).

momentum of the W. The four-momentum of the muon is constructed based on the muon's beam constrained CTC track. The W four-momentum is the sum of the muon and neutrino four-momenta. The experimental longitudinal neutrino and W quantities are reconstructed, as discussed in 4.5. The FMC events are normalized to the FMC yield predictions and the backgrounds have not been included yet.

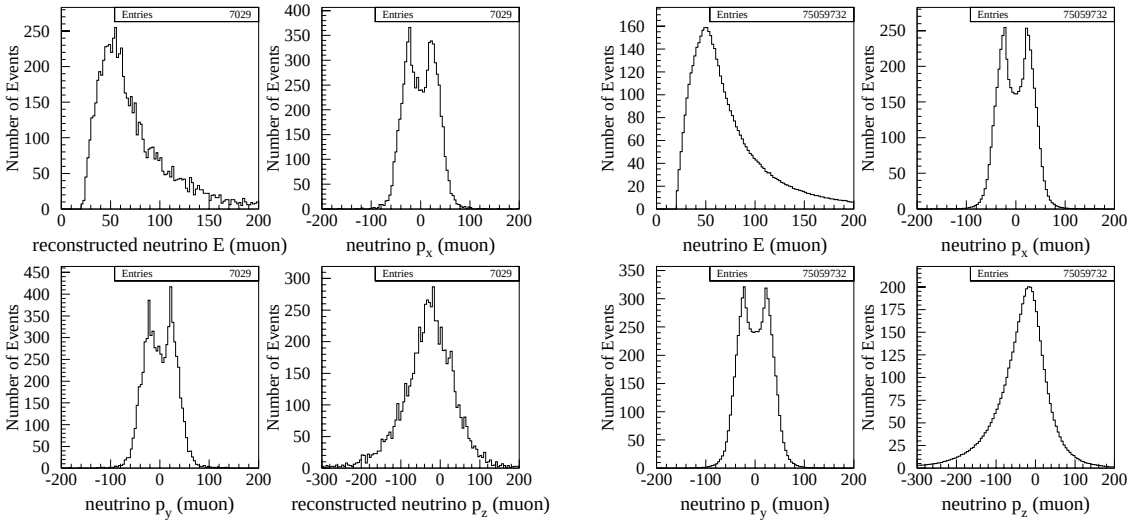

Figure 4.10 Four-momentum of neutrino for muon data (left) and muon FMC (right) in W^-+jet events. The FMC histograms are normalized to the expected yields (no backgrounds are included).

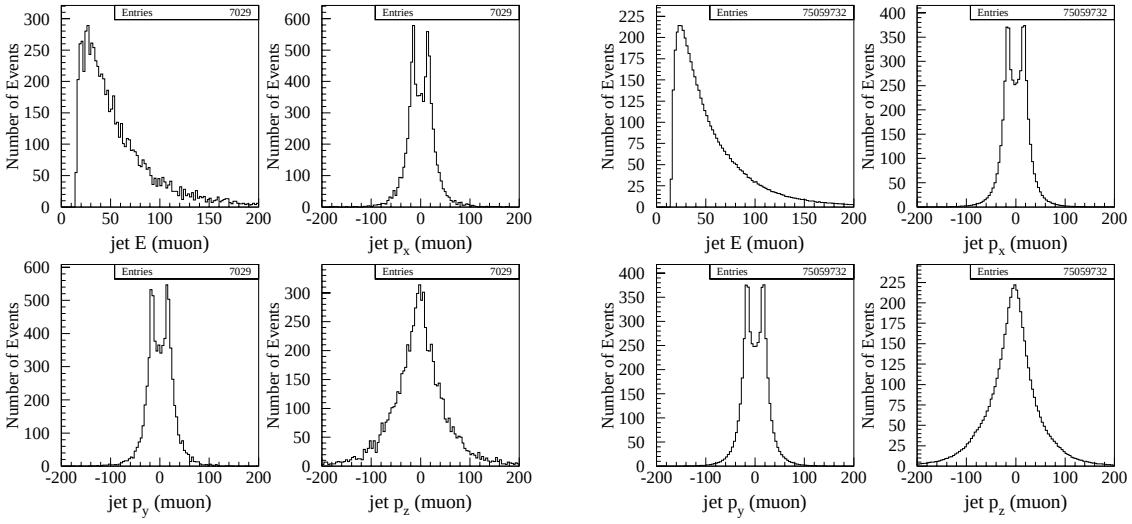

Figure 4.11 Four-momentum of jet for muon data (left) and muon FMC (right) in W^-+jet events. The FMC histograms are normalized to the expected yields (no backgrounds are included).

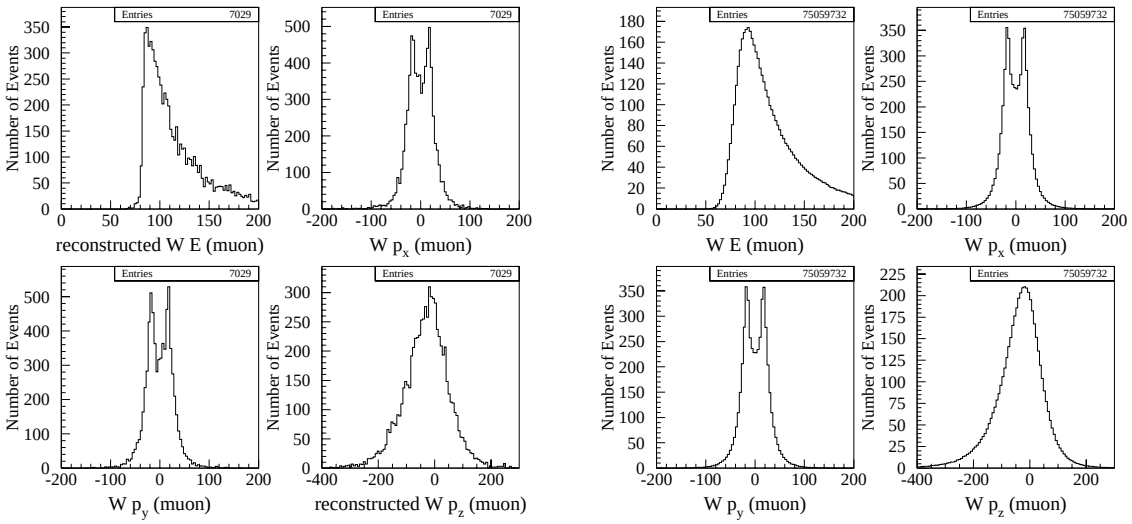

Figure 4.12 Four-momentum of W boson for muon data (left) and muon FMC (right) in W^-+jet events. The FMC histograms are normalized to the expected yields (no backgrounds are included).

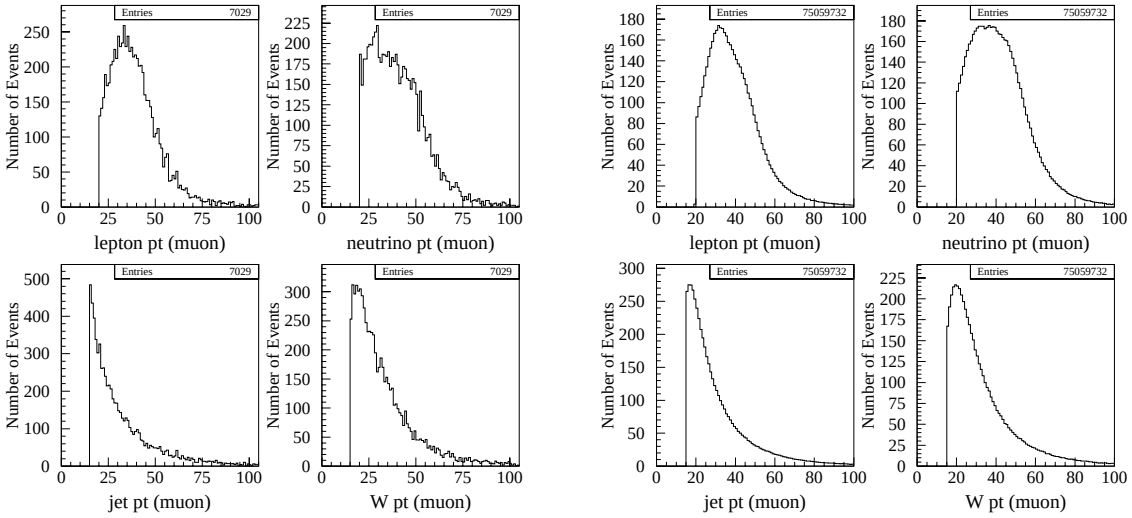

Figure 4.13 Transverse momentum of the particles for muon data (left) and muon FMC (right) in W^-+jet events. The FMC histograms are normalized to the expected yields (no backgrounds are included).

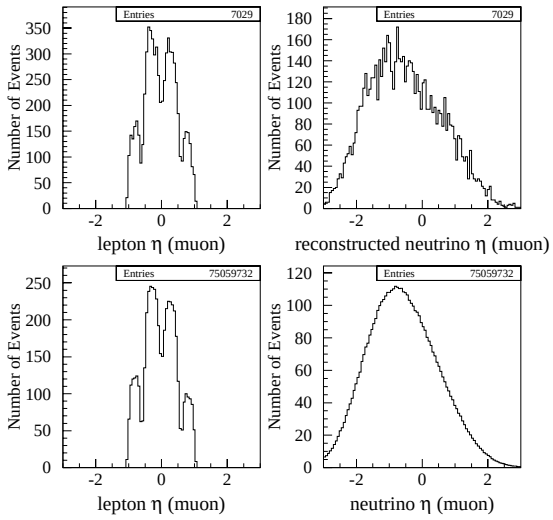

Figure 4.14 Rapidity of the muon and neutrino for the muon data (upper plots) and muon FMC (lower plots) in W^-+jet events. The FMC histograms are normalized to the expected yields (no backgrounds are included).

Chapter 5

Detector Acceptances and Efficiencies

Every particle detector biases the collected data in some manner, due to its limitations in measuring the actual physical processes. It is important to understand these limitations in order to properly reconstruct our expectations of what the detector will see if a particular theory sufficiently reflects reality. If the detector was perfect, we would directly measure the true physical phenomena and we would expect a successful theory to fully describe the detected data without any corrections. In actuality, the combination of reality and detector response gives us what we finally see in an experiment. For a valid theory to agree with our observation, we must properly include the detector limitations (acceptances and efficiencies) in our theoretical predictions.

The *geometrical acceptance* of the detector describes the fraction of events the detector is able to measure, given its geometrical characteristics. Because of the beam-pipe, separation between detector modules and other practical reasons, we cannot have a full coverage detector (i.e., a detector that covers a solid angle of 4π). Every subdetector of the CDF system loses some particles because of the limited geometrical coverage. Given that only the fiducial volume of the detector is used, the actual acceptance of the detector is worse than what is indicated by its geometrical dimensions. The *kinematic acceptance* in our analysis is related to the W events we lose because of the kinematic cuts we apply, namely the demand for a lepton with transverse energy greater than 20 GeV, missing E_T greater than 20 GeV, transverse mass of the W greater than 40 GeV and a jet with transverse energy greater then

15 GeV, absolute pseudorapidity less than 2.4 and $\Delta R_{l-j} > 0.7$. The cuts are used to improve the signal and remove backgrounds, but they inevitably remove some of the signal too. The acceptance is the ratio of the $(W \to e\nu_e)$ or $(W \to \mu\nu_\mu)$ events our detector can accept, to the number of corresponding W events, that are actually produced in the $p\bar{p}$ collisions.

The *relative efficiency* of the detector is related to the physical limitations of the detector to accurately measure a physical quantity of a particle (momentum, energy or position). Because of resolution constraints, there is an uncertainty associated with every measurement we make. As a result, any physical distribution constructed from experimental data is *smeared*, with respect to the actual distribution. The *absolute efficiencies*, on the other hand, are constant and not related to the actual quantity measured. They are mainly trigger efficiencies and particle ID efficiencies. At the trigger level, we apply some fast preliminary cuts to decide which events will prove to be more interesting (Sections 4.1.1–4.1.3 and 4.6.1–4.6.3). Also, the requirements for a golden electron (Section 4.1.4) or a golden muon (Section 4.6.4) further limited our sample. For every trigger and every applied lepton identification (ID) cut, there is an associated efficiency, which gives us the percentage of signal that passes the trigger or cut. The product of all absolute efficiencies gives us the total absolute efficiency, which is the ratio of the number of electrons (muons) that pass the triggers and all cuts and are included in our data sets, to the actual number of electrons (muons) that are produced.

We multiply the acceptances and efficiencies to produce a quantity (*acceptances times efficiencies*) which describes our detector and can be written as a function of any measured quantity. It is determined with the use of experimental data, Monte Carlo data or test-beam data. For our sample, the lepton ID and trigger efficiencies are measured by looking at the second lepton from data of Z decays and by studying random cone distributions in data of leptonic W and Z decays. They are discussed in detail in [67] and [72].

In this Chapter, we will describe the determination of the kinematic and geometrical acceptances and the relative efficiency of the detector system as a function of $(\cos\theta, \phi)$, where θ and ϕ are the polar and azimuthal angles of the charged lepton

in the Collins-Soper (CS) frame of the W respectively.[†] Because the trigger and ID efficiencies are constant, they do not affect the shape of the angular distributions we measure, hence for the rest of this dissertation, we will utilize only the geometrical and kinematic acceptances and relative efficiencies of the detector, the product of which will be denoted $ae(\cos\theta, \phi)$. These acceptances and efficiencies are calculated using the DYRAD event generator, which produces the SM prediction, and the FMC detector simulator, which produces the CDF experimental expectation. We first describe the above simulators.

5.1 The Monte-Carlo Simulators

5.1.1 The DYRAD Event Generator

DYRAD [28] is the W+jet event generator we use to establish the SM prediction. This program simulates the collision of a proton and antiproton at center-of-mass energy equal to 1.8 TeV and the production of a W, that decays leptonically, and up to two final state partons. If there is a gluon loop in the Feynman diagram, there is no more than one outgoing parton. The partons are fragmented into jets and the jet clustering algorithm is the same used by the CDF experiment. So this generator produces W+jet events based on the Standard Model next-to-leading order in perturbative QCD (order α_s^2) calculations.

The matrix elements of the Standard Model calculations and the parton distribution functions (PDF) are explicitly included in the DYRAD program. The differential cross section of the process as a function of the four-vectors of the incoming and outgoing particles is calculated, after all possible subprocesses have been taken into account. A VEGAS adaptive Monte Carlo integrator [73], which incorporates importance sampling, integrates the differential cross section over the whole phase space and generates four-vectors for the outgoing particles. Because of the importance sampling, the four-vectors are randomly selected to more probably lie in the phase-space regions where the differential cross section is higher. As a result, the

[†]See Chapter 2 for a discussion why the CS frame is used.

generator simulates the way nature produces W decays, if the underlying theory is the correct one.

The user of DYRAD can select the PDF, the energy scale of the events, the number of jets (0 or 1) and the order in QCD calculations (0 gluon loop or 1 gluon loop). As we have discussed in Chapter 2, at least one gluon loop is necessary for the theory to be sensitive to the last three P-odd and T-odd angular coefficients, so we run in the 1-loop DYRAD mode. Since we study W+jet, we select the one-jet option. The original PDF we use is the CTEQ4M($\Lambda = 0.3$ GeV), where Λ is the scale of QCD, and the energy scale is equal to the pole mass of the W ($Q^2 = (M_W^{\rm pole})^2$).

We can impose any cuts on the outgoing particles. The calculated cross section and data distributions depend on these cuts. Because in nature there are no cuts, we try to relax most of them, to get the SM unbiased prediction of the angular coefficients and the theoretically expected angle distributions, as presented in Chapter 2. One cut we do impose is on the minimum jet E_T. We require that $E_T^{\rm jet} > 10$ GeV, because the theoretical calculations are unstable and unreliable for small jet transverse energies due to the infrared and collinear divergencies. There is also a cut related to the jet-jet separation, important for the definition of a jet. We use 0.7-cone jets, which equals the cone size used in our data sets. All other kinematic cuts of the jet, charged lepton and neutrino are removed. The cross section for inclusive W+jet calculated up to order α_s^2, with the above minimal cuts, is 722.51 ± 3.89 pb for both signs of W. The DYRAD program generates massless leptons, without any discrimination related to their flavor.

The DYRAD generator assigns a weight on every event produced, and the sum of all weights is proportional to the cross section of the process. For this reason, when we histogram any physical quantity using the DYRAD data, we properly weigh all events. If DYRAD is run in the 1-loop mode, we take into account tree Feynman diagrams with one outgoing parton, *virtual*[†] Feynman diagrams with one gluon loop and an outgoing parton, and *real* Feynman diagrams with two outgoing partons and no gluon loop. The inclusion of the α_s^2 processes introduces negative weights, which cause spikes in the distributions we histogram. In order to have smooth SM distributions

[†] "Real" refers to outgoing particles and "virtual" refers to loops of particles in the Feynman diagrams.

to use for the ae calculation, we have to run for a very big sample of DYRAD events ($\sim$250 million events). To remove most of the remaining spikes, which are caused by few events with very large weights, we set a cut on the maximum value of a weight for a particular event to be accepted.

The DYRAD simulator allows us to establish the SM prediction for the ϕ-distribution of the charged lepton and the predictions for the angular coefficients and helicity cross sections of the W. The expected ϕ and $\cos\theta$ distributions of the decay charged lepton in W+jet events up to order α_s^2 in QCD, for the four p_T^W bins, can be seen in Figure 2.5 and 2.6 respectively. Using DYRAD events we can extract the SM predictions for the angular coefficients up to order α_s^2, using the method of moments. For zero p_T^W we expect a flat ϕ-distribution, whereas the QCD effects at higher p_T^W result in two minima.

Figure 5.1 shows the $\cos\theta$ versus ϕ distribution of the charged lepton from DYRAD data, for four bins of the W p_T. We use 50 bins for the $\cos\theta$ direction and 50 bins for the ϕ direction. These scatter plots are going to be used for the determination of the $ae(\cos\theta, \phi)$.

5.1.2 The FMC Detector Simulator

To obtain the detector response to the actual theoretical distribution, which is what we finally get performing our experiment, we pass the DYRAD-generated events through the FMC program. The FMC (Fast Monte Carlo) is a CDF detector simulator. It analytically includes the detailed geometry of the detector, the detector resolution effects, the luminosities, the geometrical and kinematic acceptances of all subdetectors, the relative efficiencies, and all experimental cuts imposed on the W, leptons, $\not\!\!E_T$, and jets. The effect of the minimum-bias underlying event is also included. We input into the FMC the particle four-vectors and the cross section produced by DYRAD. The FMC uses the known resolutions of all the subdetectors, and accordingly smears the input four-vectors using a Gaussian distribution. Taking into account all the acceptances and efficiencies, it gives us the CDF detector response to the input four-vectors of the particles.

Because the CDF detector in Run Ib is not identical to the Run Ia CDF detector,

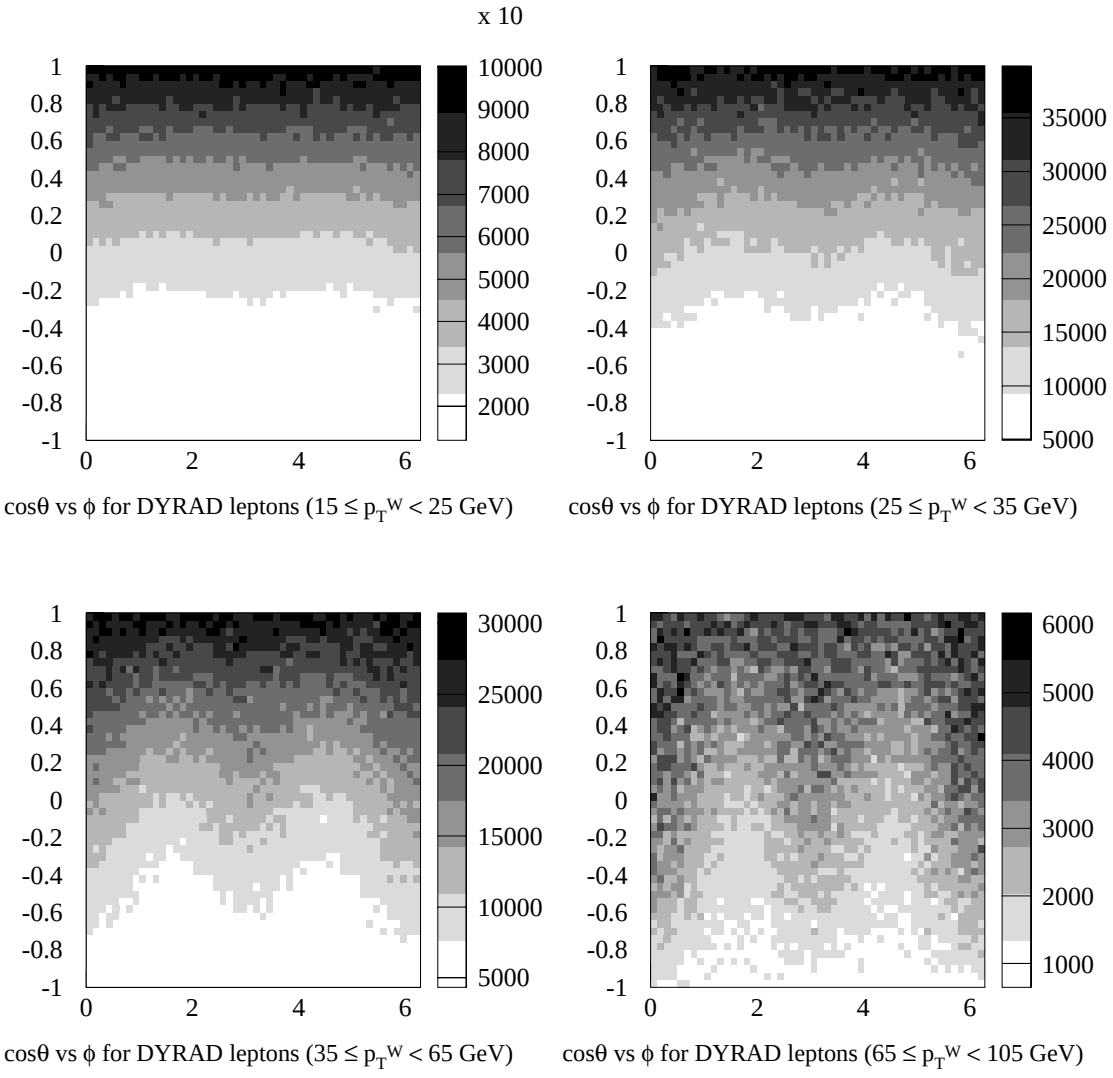

Figure 5.1 The $(\cos\theta, \phi)$ phase space for the four p_T^W bins, for the DYRAD generator.

FMC yields for inclusive W+jet		
p_T^W (GeV)	N_e	N_μ
15-25	3867 ± 137	2027 ± 102
25-35	2632 ± 93	1384 ± 66
35-65	2474 ± 87	1314 ± 67
65-105	518 ± 18	279 ± 14

Table 5.1 The electron and muon FMC yields for inclusive W+jet up to order α_s^2. The backgrounds and the PDF/Q^2 scale systematics are not included.

there are actually two versions of the program for the two runs. In addition, the electrons and muons are naturally treated differently by FMC, unlike DYRAD that produces massless generic high energy leptons. Hence, we run the FMC program four times for each DYRAD input four-vector file: for Run Ia electrons, Run Ib electrons, Run Ia muons, and Run Ib muons. For each run we get a file with the smeared four-vectors, affected by the efficiencies and acceptances, as well as the FMC yields for each relevant region of the detector for the two leptons: Run Ia CEM electrons, RUN Ib CEM electrons, Run Ia CMUP muons, Run Ia CMNP muons, Run Ib CMUP muons, Run Ib CMNP muons, and Run Ib CMX muons (CEM electrons deposit energy in the CEM calorimeter, CMUP muons leave a stub in a CMU and a CMP chamber, CMNP leave a stub in a CMU chamber but not in a CMP chamber, and CMX muons leave a stub in a CMX muon chamber). Table 5.1 shows the yields for the inclusive W+jet next-to-leading order Monte Carlo sample and for the four p_T^W bins. The uncertainties correspond to uncertainties in the integrated luminosities, the cross section, and the acceptance and efficiency of the detector. The observed preliminary deviation of these FMC yields from the data yields of tables 4.1 and 4.2 will be addressed in Section 7.3.8. After the inclusion of the backgrounds and PDF/Q^2 scale systematic uncertainties in the FMC prediction and the jet E_T and jet η systematic uncertainties in the CDF data measurement, the disagreement is less significant. The actual number of W+jet events is not of critical importance for us, because we are interested in the relative yields between different lepton regions (for the calculation of the acceptances and efficiencies (ae)) and in the shape of the angular distributions (for the extraction of the angular coefficients of the W). The absolute yields variations do not affect our analysis. Figures 5.2 and 5.3 show the

FMC ϕ-distributions for the electron and muon data set respectively. Figures 5.4 and 5.5 show the FMC $\cos\theta$-distributions for the electron and muon data set respectively. The plots are normalized to the FMC event yields.

The effects of the acceptances and efficiencies are significant. In the ϕ distributions, instead of two minima we get two maxima; the main reason for this behavior of the data is the charged lepton and neutrino p_T cuts that limit the allowed $(\cos\theta, \phi)$ phase space considerably. The FMC plots are normalized to the FMC yields and the jet cuts of $E_T^{\rm jet} > 15$ GeV and $|\eta_{\rm jet}| < 2.4$ have been applied to the leading jet. All lepton and $\not\!\!E_T$ experimental cuts have been applied to the FMC data as well. These angular distributions provide the theoretical prediction of what the CDF experimental charged lepton angular distributions would be.

Figures 5.6 and 5.7 show the FMC $\cos\theta$ versus ϕ distribution of FMC electrons and muons respectively, for four bins of the W p_T. These two-dimensional scatter plots have a 50×50 binning, and will be used for the determination of the $ae(\cos\theta, \phi)$.

The plots shown in Figures 5.2, 5.4, and 5.6 were generated by combining the respective CEM(Run Ia), CEM(Run Ib) electron plots in the right proportions. Similarly, the plots in Figures 5.3, 5.5, and 5.7 were constructed combining the respective CMUP(Run Ia), CMNP(Run Ia), CMUP(Run Ib), CMNP(Run Ib) and CMX(Run Ib) muon plots in the right proportions. These proportions are given by the FMC yields for each lepton region and CDF run.

5.2 The Determination of Efficiencies and Acceptances

To produce the $ae(\cos\theta, \phi)$, we divide the two-dimensional plots of Figures 5.6 and 5.7 by the two-dimensional plots of Figure 5.1, for the four W p_T bins respectively. The results are the acceptance times efficiency of the detector for electrons and muons from W+jet events, for the $(\cos\theta, \phi)$ phase space and for the four p_T^W bins of interest. They can be seen in Figures 5.8 and 5.9 for electrons and muons respectively. It is important to remove most of the statistical noise in the $ae(\cos\theta, \phi)$ distributions, so that they can be properly used without introducing non existing effects in our

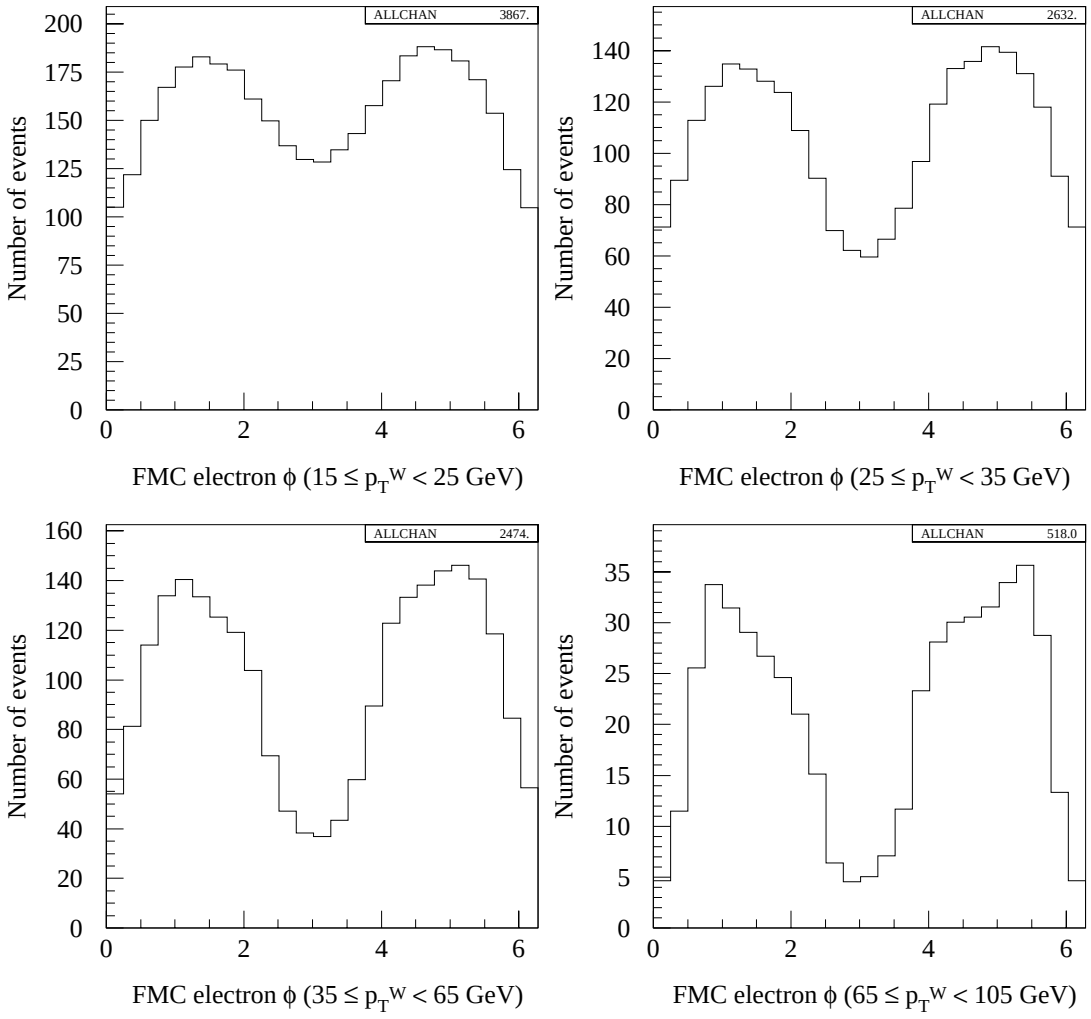

Figure 5.2 Expected experimental (FMC) ϕ distribution of the electron from the decay of the W in W+jet events, up to order α_s^2, for the four p_T^W bins. The plots are normalized to the FMC yields (no backgrounds have been added).

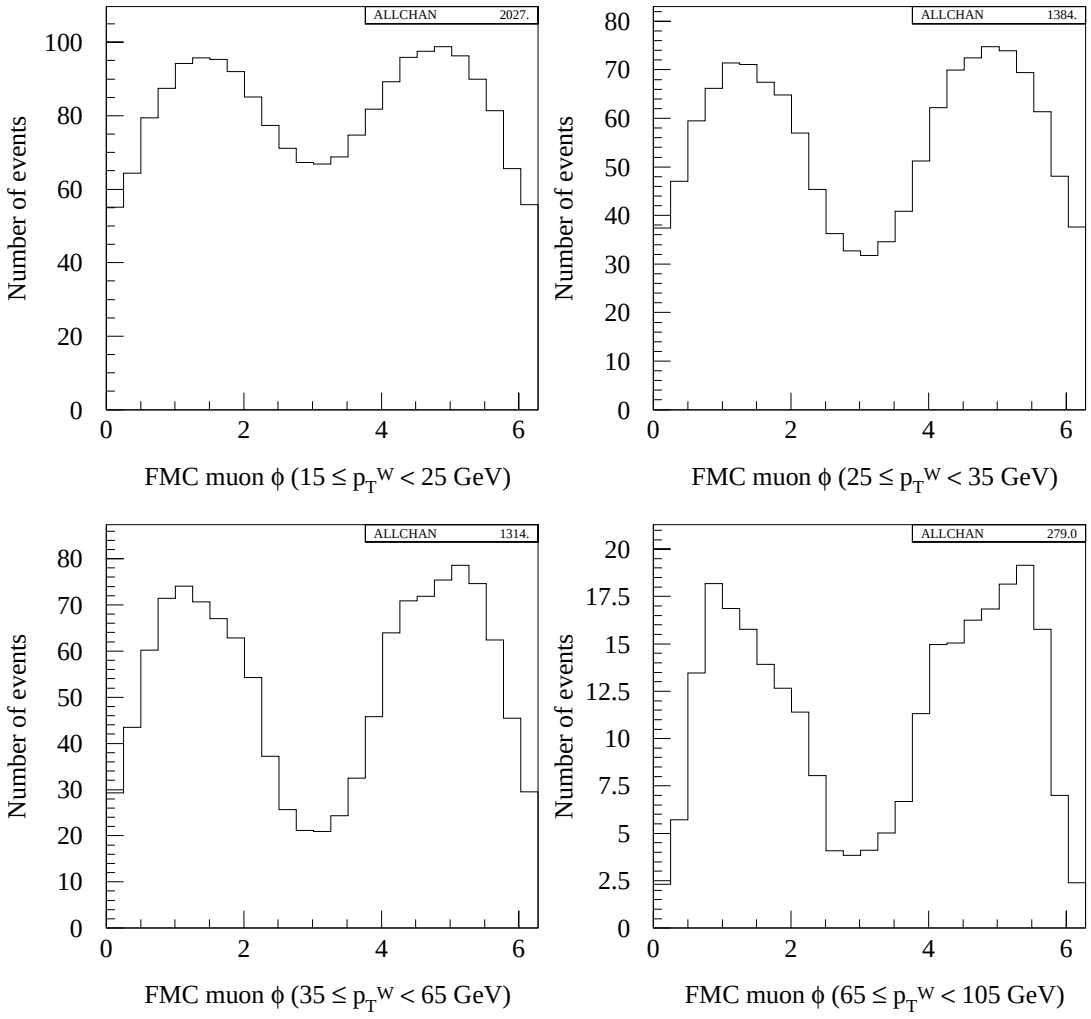

Figure 5.3 Expected experimental (FMC) ϕ distribution of the muon from the decay of the W in W+jet events, up to order α_s^2, for the four p_T^W bins. The plots are normalized to the FMC yields (no backgrounds have been added).

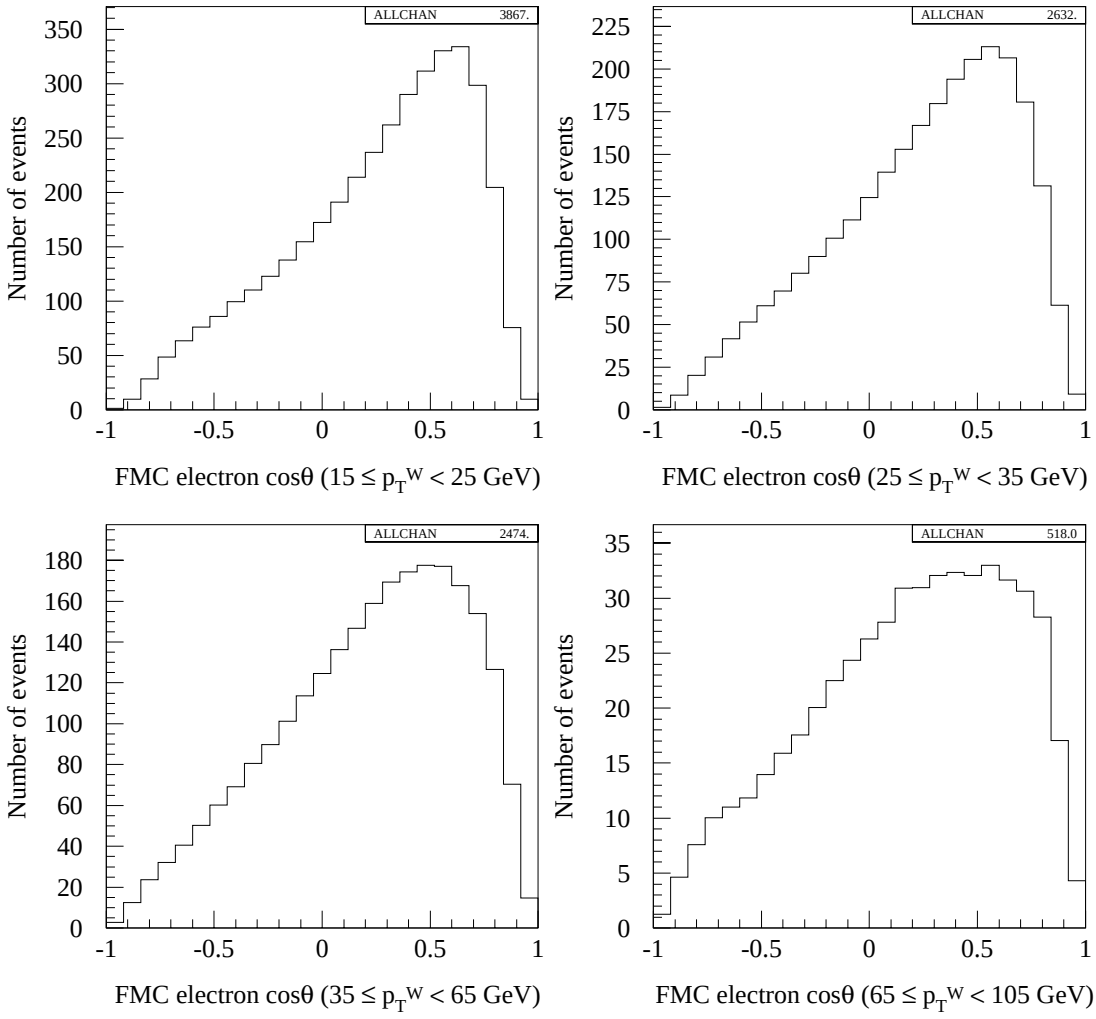

Figure 5.4 Expected experimental (FMC) $\cos\theta$ distribution of the electron from the decay of the W in W+jet events, up to order α_s^2, for the four p_T^W bins. The plots are normalized to the FMC yields (no backgrounds have been added).

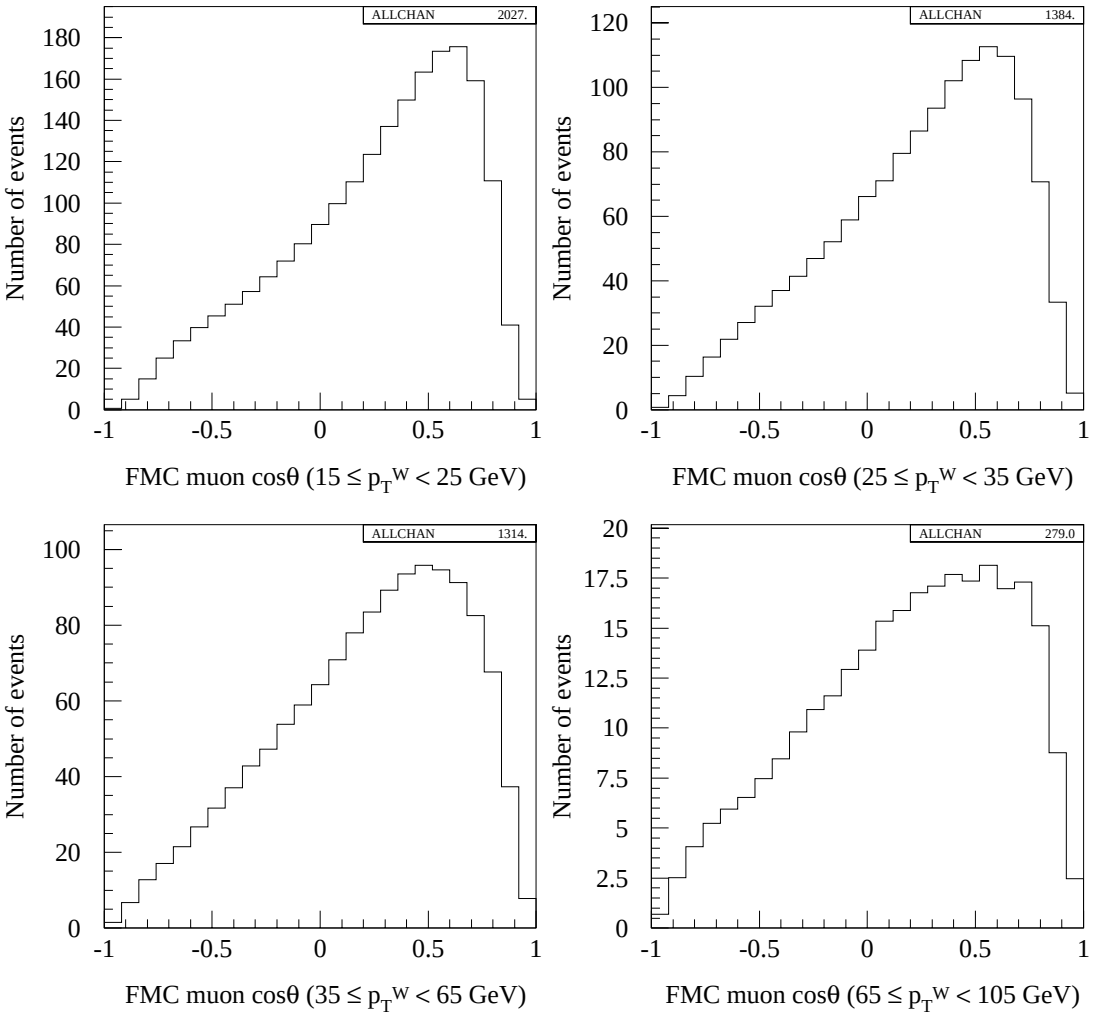

Figure 5.5 Expected experimental (FMC) $\cos\theta$ distribution of the muon from the decay of the W in W+jet events, up to order α_s^2, for the four p_T^W bins. The plots are normalized to the FMC yields (no backgrounds have been added).

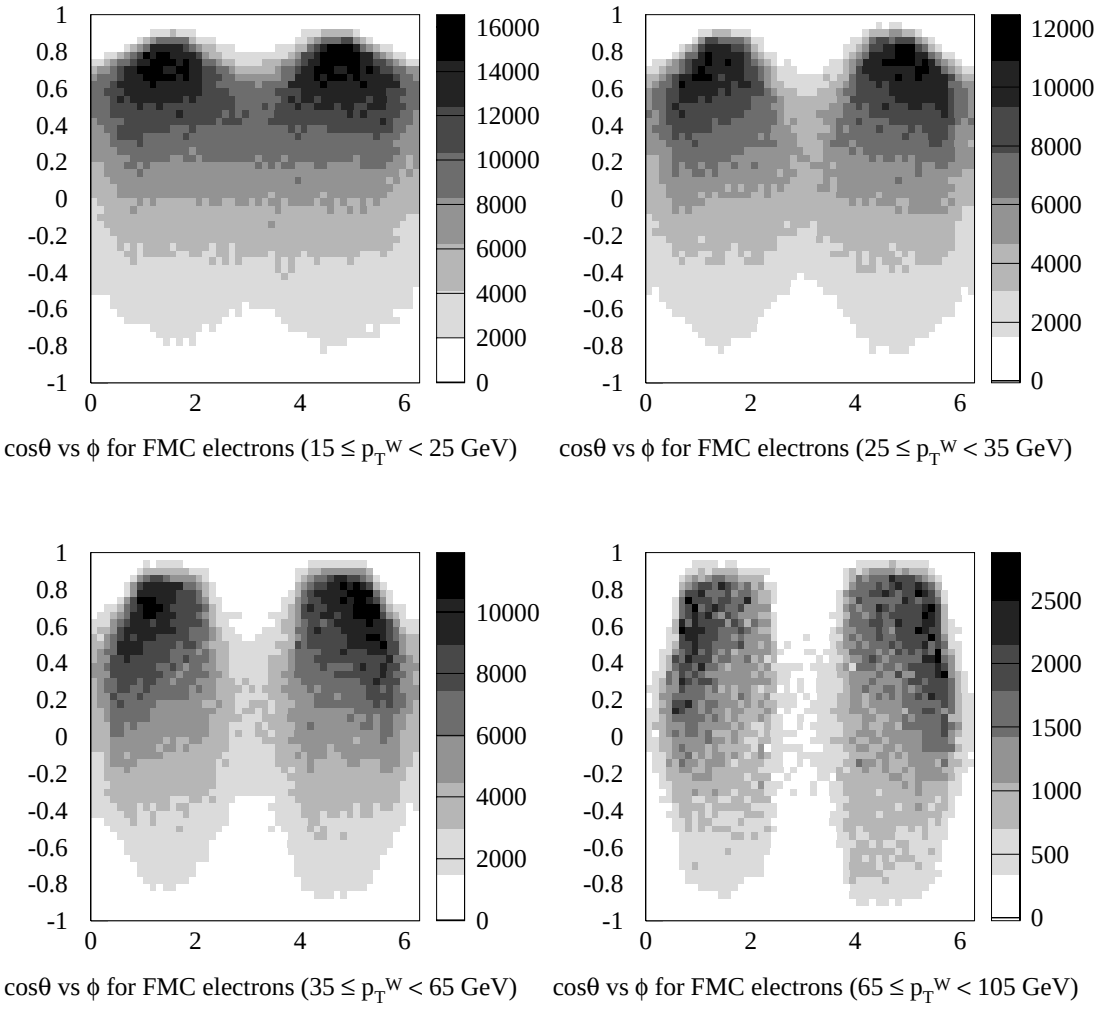

Figure 5.6 The $(\cos\theta, \phi)$ phase space for the four p_T^W bins, for the electron FMC.

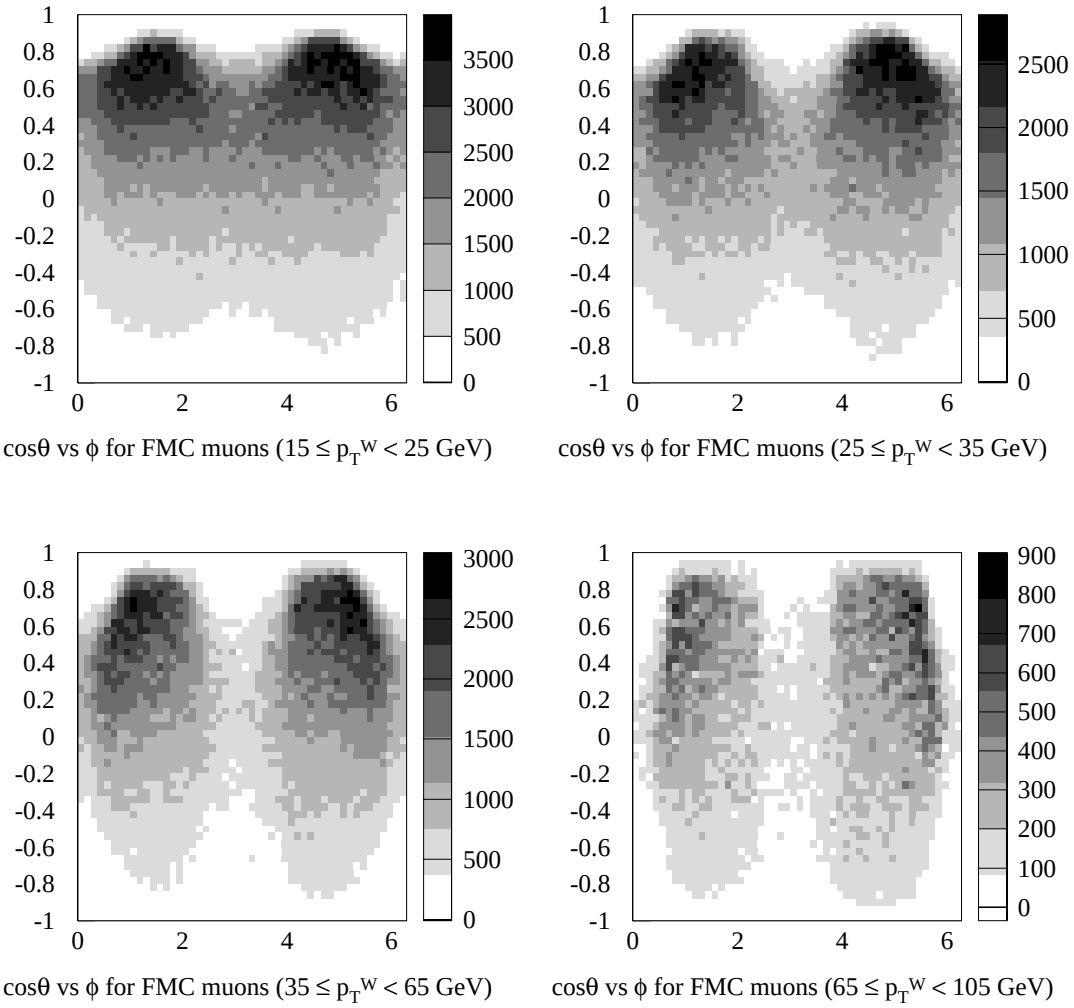

Figure 5.7 The $(\cos\theta, \phi)$ phase space for the four p_T^W bins, for the muon FMC.

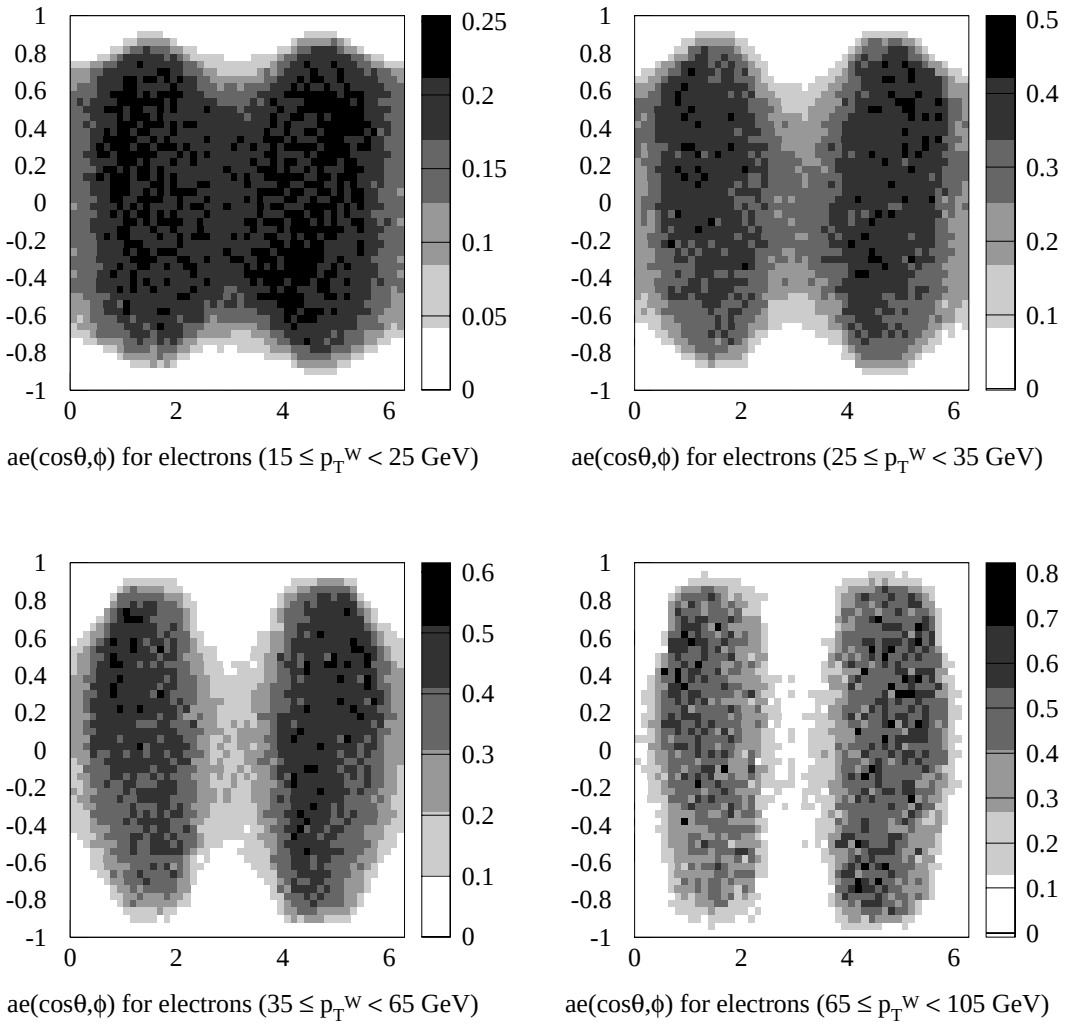

Figure 5.8 Acceptances and efficiencies for the electrons as a function of $\cos\theta$ and ϕ.

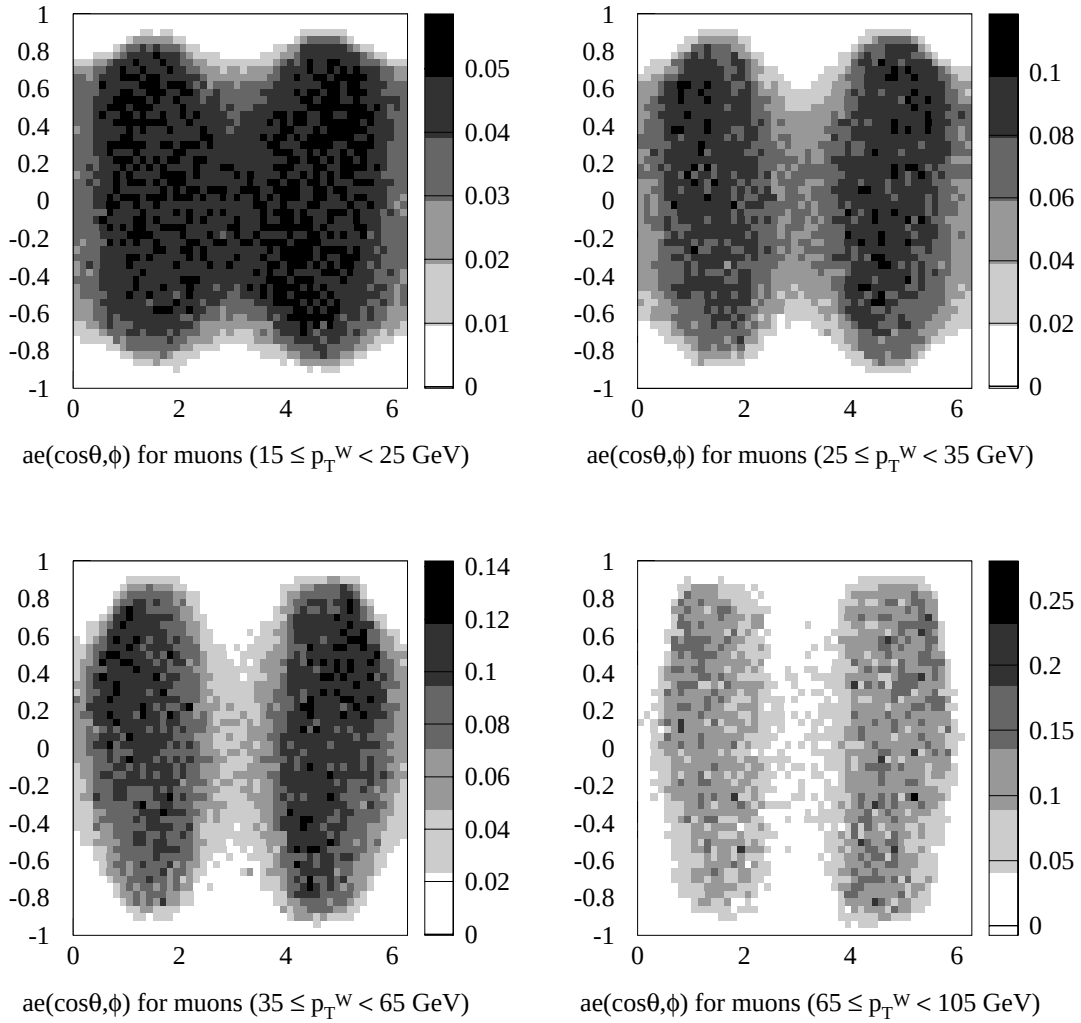

Figure 5.9 Acceptances and efficiencies for the muons as a function of $\cos\theta$ and ϕ.

predictions. For this reason, in our analysis programs, whenever we need the value of $ae(\cos\theta, \phi)$ for a particular pixel of the 50 scatter plot, we actually average over the ae values of that pixel and its first neighboring pixels. All the pixel values are equally weighted.

Chapter 6

Backgrounds

The main sources of background in the $(W \to e\nu)$+jet and $(W \to \mu\nu)$+jet processes are the $(W \to \tau\nu)$+jet events, the Z+jet events [where the Z is misidentified as a W (one-legged Z)], the QCD background of jets misidentified as electrons or muons and passing the rest of the cuts and finally the EM background of $W + \gamma$ events. The latter ones comprises of only few events with run and event numbers same as the $W + \gamma$ events of [67] and we treat them as a systematic error in the measurement. This error is very small (see Section 7.3.4).

Another small background is the top-antitop ($t\bar{t}$) production where one of the produced Ws is decaying leptonically and the other ones result in jets and missing transverse energy. This background is estimated to be about 30 events [69]. Because the distribution is expected to be flat as a function of p_T^W, we expect to have about 3 events in each of the first two bins, 10 events in the third bin and 13 events in the last bin. To demonstrate the insignificance of this background, we performed our analysis including these $t\bar{t}$ background events in several possible shapes. The change in the extracted results was minimal, and always smaller than our systematic and statistical uncertainties. For this reason we ignore the effects of the top quarks in our analysis.

In our analysis we concentrate on the azimuthal angle ϕ of the charged lepton in the Collins-Soper rest frame of the W. Therefore, we study the ϕ distribution of the backgrounds, in addition to the backgrounds event yields.

One-legged Z+jet background				
p_T^W (GeV)	N_e	Fraction	N_μ	Fraction
15-25	47 ± 2	1.22 ± 0.07 %	127 ± 7	6.26 ± 0.47 %
25-35	30 ± 1	1.14 ± 0.05 %	82 ± 4	5.92 ± 0.40 %
35-65	25 ± 1	1.01 ± 0.05 %	72 ± 4	5.48 ± 0.41 %
65-105	5 ± 0	0.96 ± 0.03 %	12 ± 1	4.30 ± 0.42 %

Table 6.1 Monte Carlo background estimation of the number of electron and muon one-legged Z+jet events. The fractions of the backgrounds are calculated with respect to the FMC W+jet events.

6.1 The One-Legged Z Background

To study this background we generate a DYRAD file of Z+jet and we pass it through the FMC Monte Carlo and the subsequent analysis program to see how many Z's are misidentified as W's by having one of their "legs" (decay leptons) be undetected and by satisfying all other kinematic and quality cuts. The DYRAD cross section for the Z+jet up to order α_s^2 is 68.21 ± 0.37 pb [using $Q^2 = (M_W^{\rm pole})^2$, the CTEQ4M($\Lambda = 0.3$ GeV), 0.7-cone jets and no cuts other than the $E_T^j > 10$ GeV cut and all experimental charged lepton, $\not\!\!E_T$ and W cuts]. At the FMC level, we require at least one "good" jet ($E_T^{\rm jet} > 15$ GeV and $|\eta^{\rm jet}| < 2.4$) that also passes the $\Delta R_{l-j} > 0.7$ cut. The result can be seen in Table 6.1. Overall we expect 123 ± 5 electron one-legged-Z+jet and 337 ± 18 muon one-legged-Z+jet passing the W+jet cuts. Comparing these numbers to the FMC yields for W+jet we see that the one-legged-Z+jet background is 1.14% for the electron W+jet and 5.90% for the muon W+jet sample. Figure 6.1 shows the FMC W transverse mass for the W+jet events and for one-legged Z+jet events. To see how this background affects the W+jet lepton ϕ distribution, we plot the ϕ distribution for the leptons coming from one-legged-Zs for the four p_T^W bins (Figures 6.2 and 6.4). Figures 6.3 and 6.5 show the one-legged-Z background overimposed on the FMC signal, for electrons and muons respectively. We see that the same pattern of two maxima at $\frac{\pi}{2}$ and $\frac{3\pi}{2}$ is present. The plots are normalized to the actual expected yields from FMC. We will include the one-legged Z FMC ϕ distribution files into the theoretical prediction of the ϕ distributions, in order to correctly extract the angular coefficients.

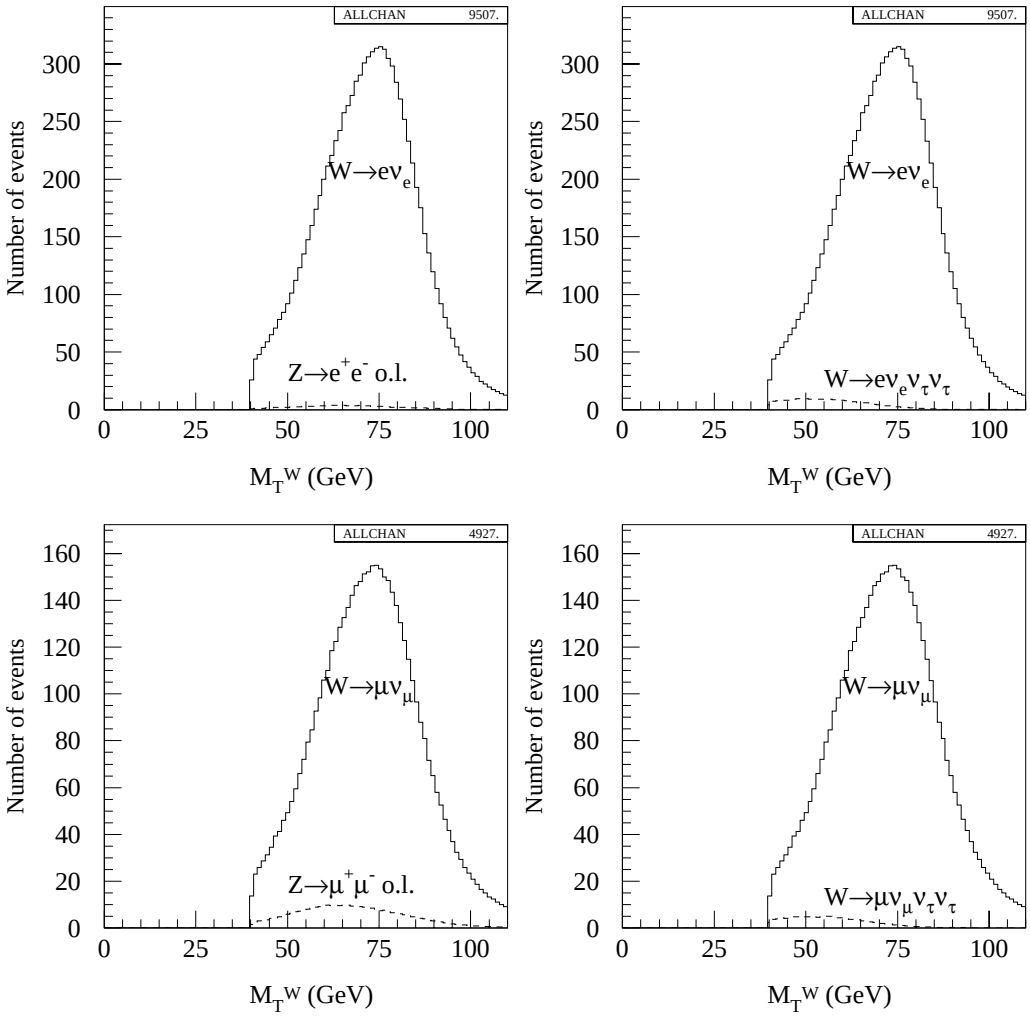

Figure 6.1 The W transverse mass for the W+jet signal and for one-legged Z and tau background for FMC electrons (upper histograms) and FMC muons (lower histograms) normalized to FMC yields.

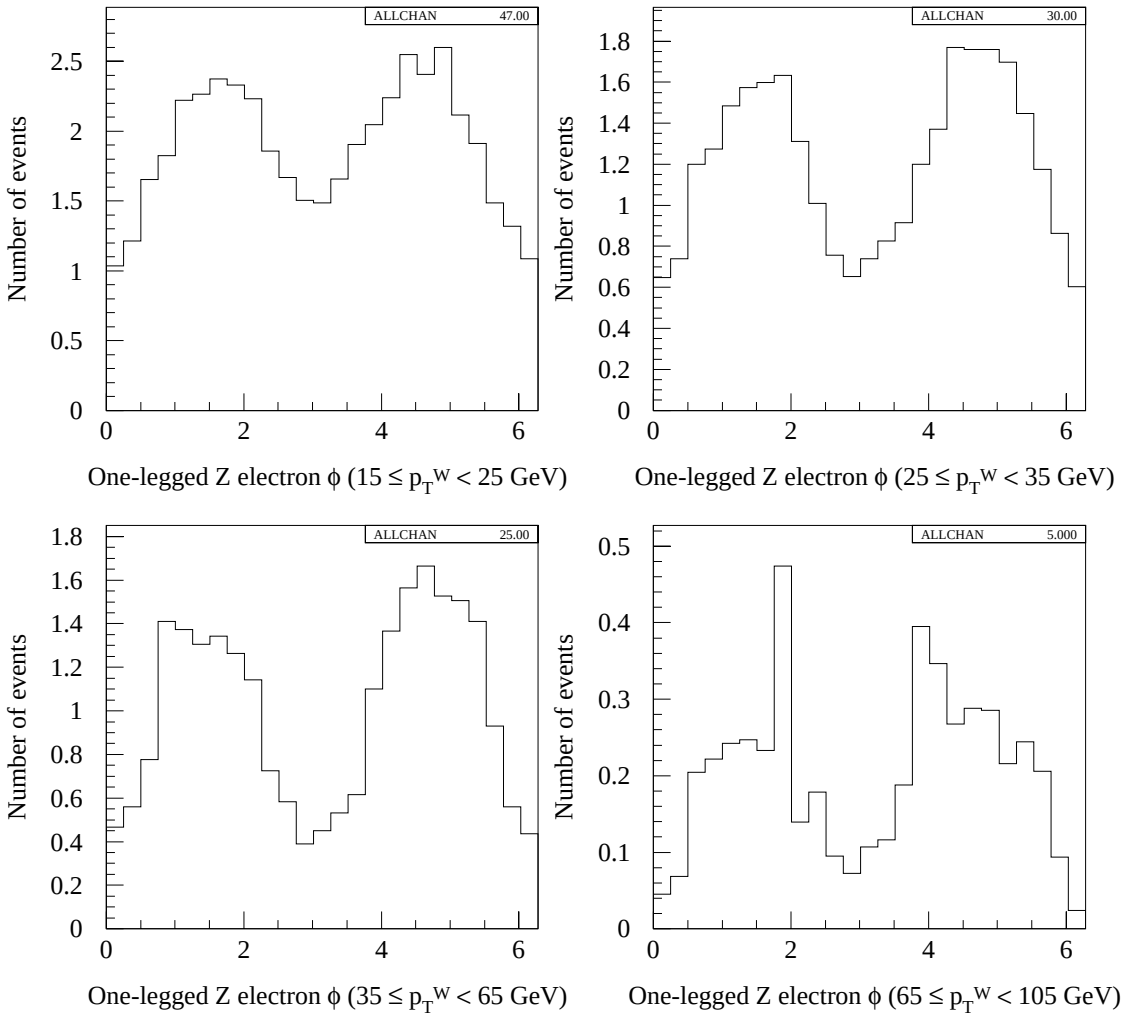

Figure 6.2 Electron ϕ distributions for the four p_T^W bins for the Z+jet FMC events, where one of the Z electron decay products is undetected and the other one passes the detection and analysis requirements. All other experimental cuts are applied. The histograms are normalized to the electron Z+jet FMC yields.

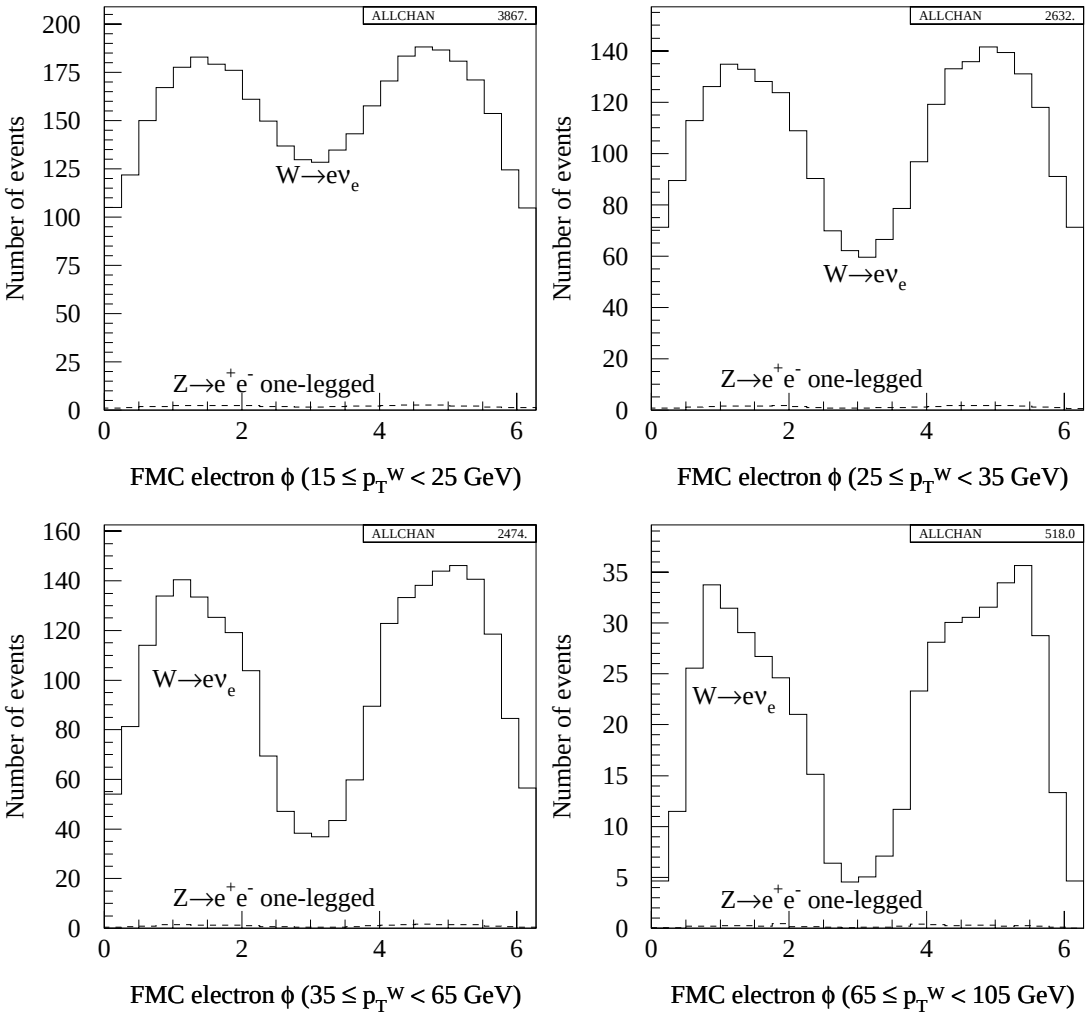

Figure 6.3 Electron ϕ distributions for the four p_T^W bins for electron W+jet FMC events (solid histogram) and for Z+jet FMC events, where one of the Z electron decay products is undetected and the other one passes the detection and analysis requirements (dashed histogram). All other experimental cuts are applied. The histograms are normalized to the electron FMC yields.

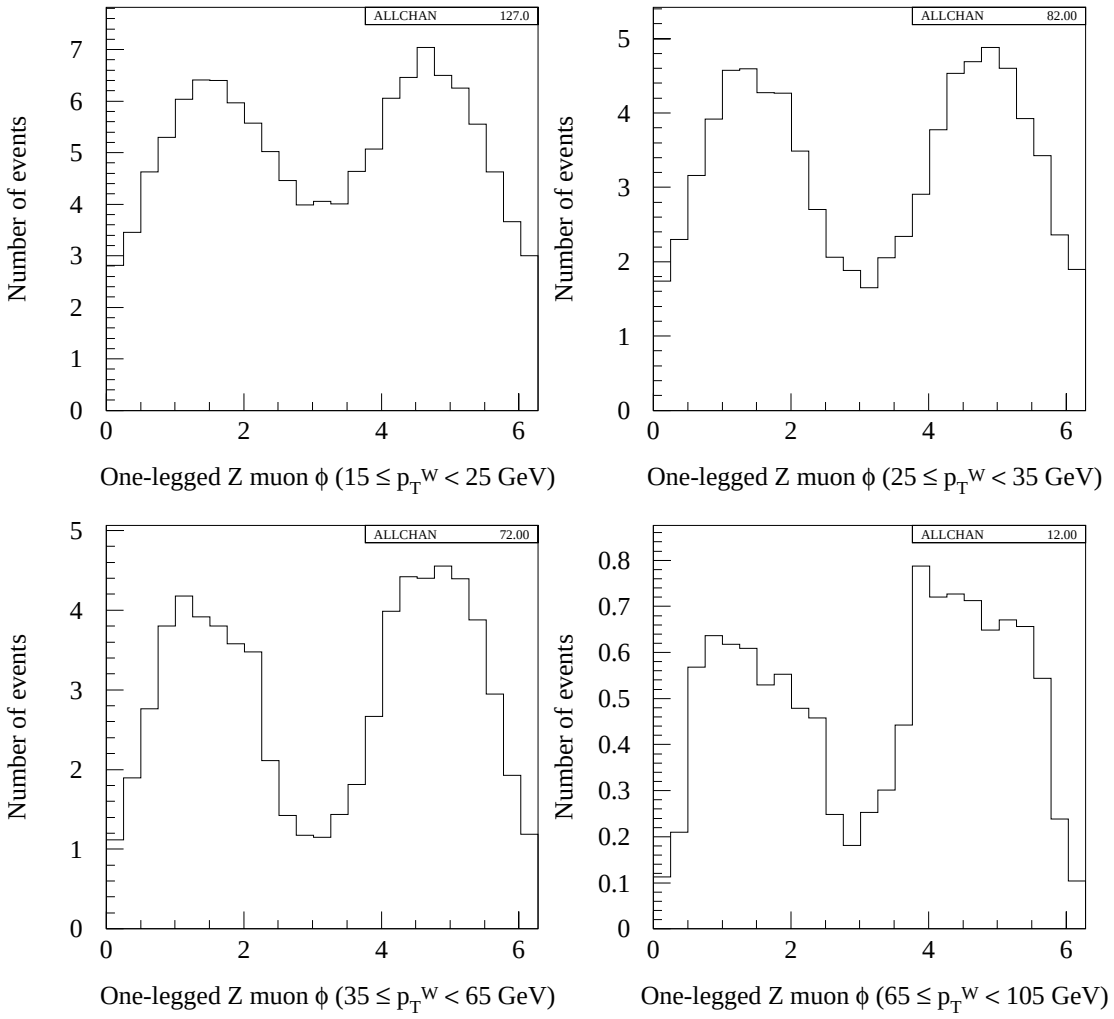

Figure 6.4 Muon ϕ distributions for the four p_T^W bins for the Z+jet FMC events, where one of the Z muon decay products is undetected and the other one passes the detection and analysis requirements. All other experimental cuts are applied. The histograms are normalized to the muon Z+jet FMC yields.

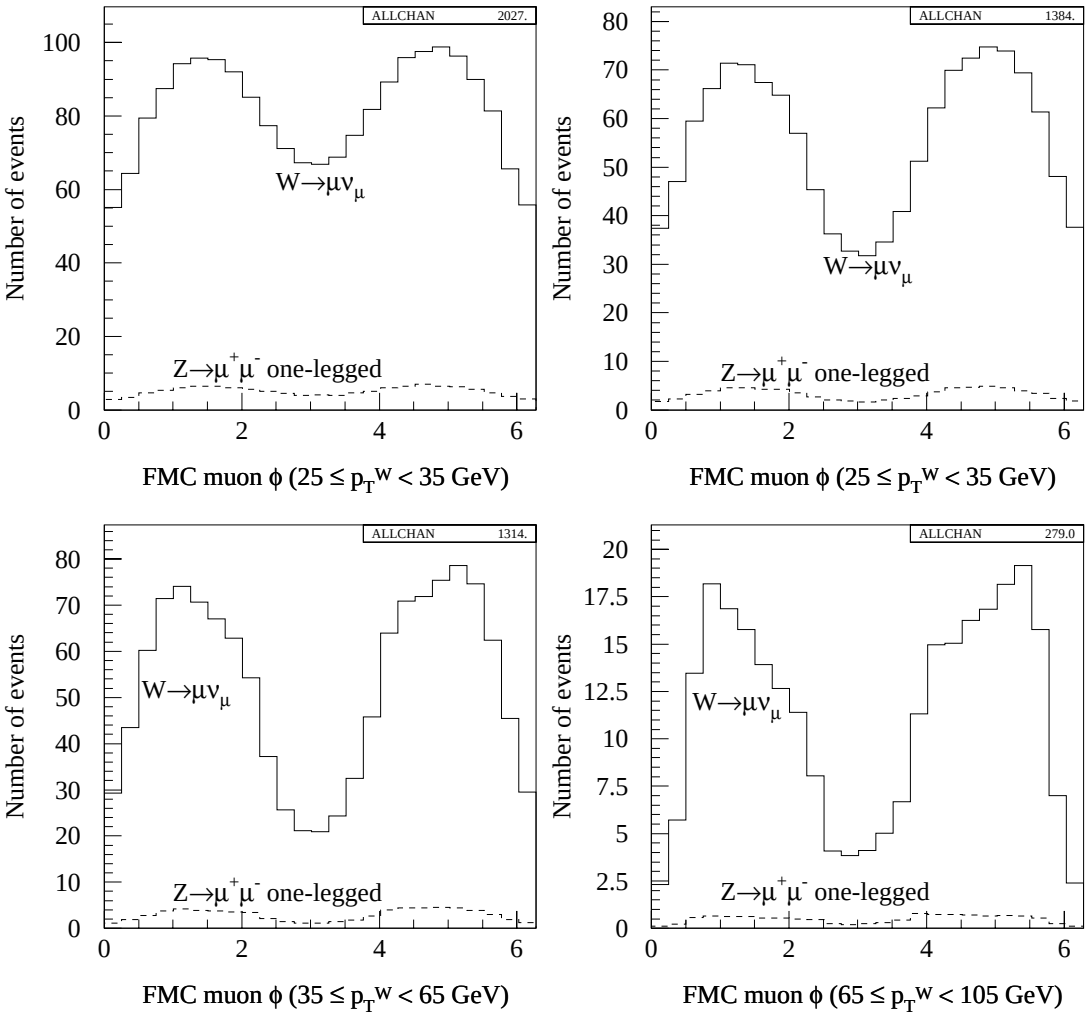

Figure 6.5 Muon ϕ distributions for the four p_T^W bins for muon W+jet FMC events (solid histogram) and for Z+jet FMC events, where one of the Z muon decay products is undetected and the other one passes the detection and analysis requirements (dashed histogram). All other experimental cuts are applied. The histograms are normalized to the muon FMC yields.

6.2 The ($W \rightarrow \tau\nu$)+Jet Background

If the W decays to a τ, the resulting particles are the charged lepton (electron or muon) from the τ decay and three neutrinos (two neutrinos from the τ decay and one neutrino from the W decay). The three neutrinos are observed as a single missing E_T and the signal of one charged lepton along with missing E_T mimics the one of the W direct decay to the charged lepton. There is no similar background from muon decays, because muons rarely decay inside the detector, given their long lifetimes (2.197 μs) and energies (around 40 GeV).

Most of the tau background is removed when we utilize the fact that the charged lepton and missing E_T coming from the τ decay are *soft* (low energy ones). Also the W transverse mass in the τ events is significantly smaller than the one in the electron or muon events. Figures 6.6 and 6.7 show how the SM charged lepton and neutrino E_T and the M_T^W look like for the tau events and the electron/muon events. By applying the p_T cuts for the leptons ($p_T^l > 20$ GeV and $p_T^\nu > 20$ GeV) and the W transverse mass cut ($M_T^W > 40$ GeV) we remove 92% of the tau W+jet events at the DYRAD generator level as shown in these Figures. The remaining background is discussed in the rest of this section.

To study the $W \rightarrow \tau\nu_\tau$ background we start with a tau DYRAD sample and we let the tau decay to an electron or a muon. Then, we vector-sum the three neutrinos resulting from the W and tau decays to form a single missing E_T. Subsequently, we pass the events through the FMC detector simulator to see how many events pass the W+jet cuts after they are weighted by the detector acceptances and efficiencies. The charged lepton, $\not\!\!E_T$, and W quality cuts are also applied. The branching ratio used for the tau decays is 17.83 % for electrons and 17.37 % for muons. At the FMC level, we require at least one "good" jet ($E_T^{\rm jet} > 15$ GeV and $|\eta^{\rm jet}| < 2.4$) that also passes the $\Delta R_{l-j} > 0.7$ cut. The results can be seen in Table 6.2. Overall, we expect 247 ± 9 tau electrons and 130 ± 7 tau muons infiltrated into the W+jet samples. Comparing these numbers to the FMC yields for W+jet we see that the tau background is 2.28% for both the electron and muon W+jet samples. Figure 6.1 shows the FMC W transverse mass for the W+jet events, where the W decays directly to an electron or muon, and

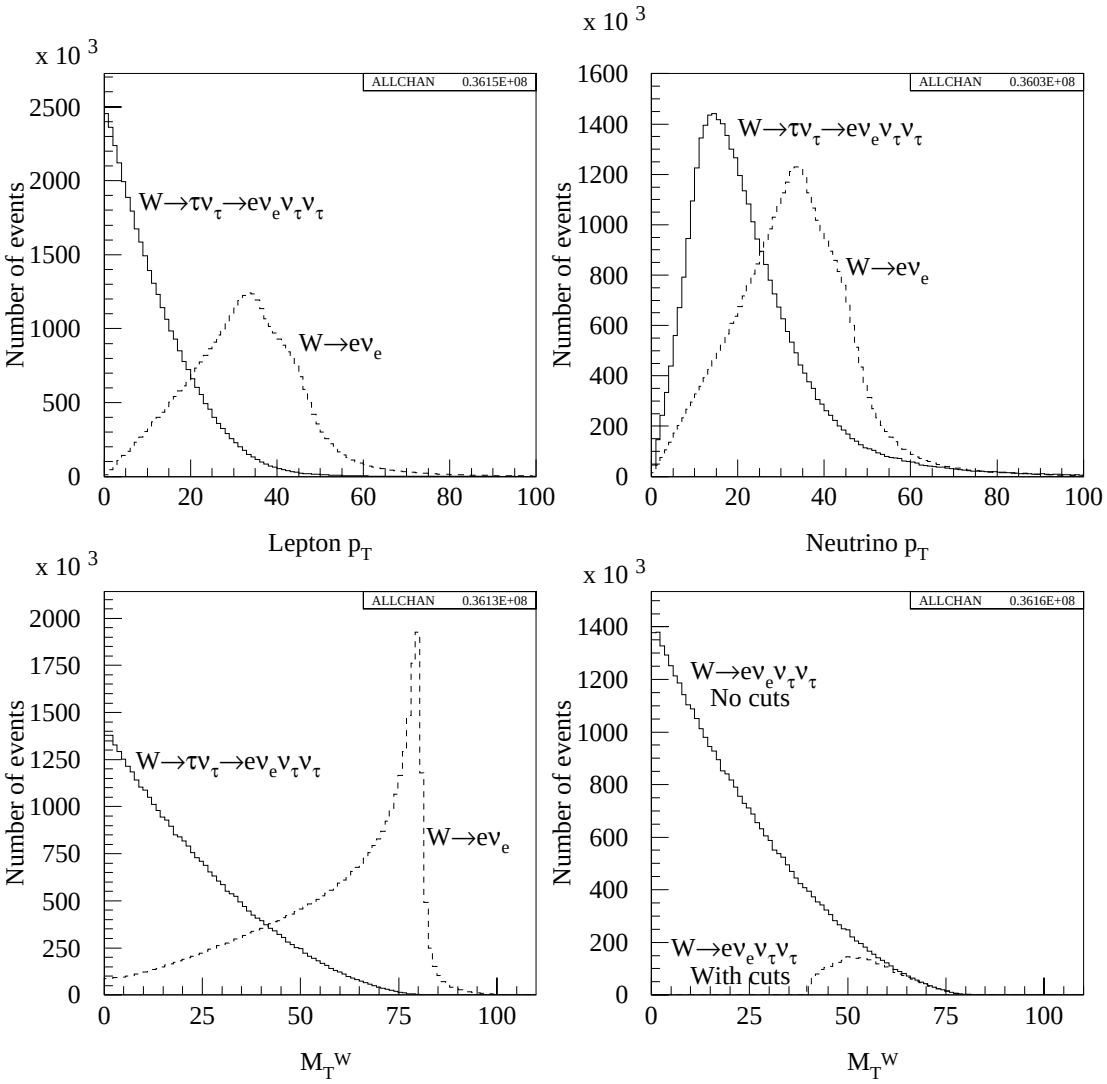

Figure 6.6 Electron and $\not\!\!E_T$ transverse momenta and W transverse mass from the decay of the tau coming from W+jet DYRAD events (solid histogram) superimposed on the transverse momenta and W mass from the direct decay of the W to electrons (dashed histogram). The resulting transverse mass from the tau decay is shown in the lower right plot for all events (solid histogram) and for the ones that remain after the application of the leptons p_T cut of 20 GeV and the transverse mass of 40 GeV (dashed histogram). This way 92% of the tau background is removed.

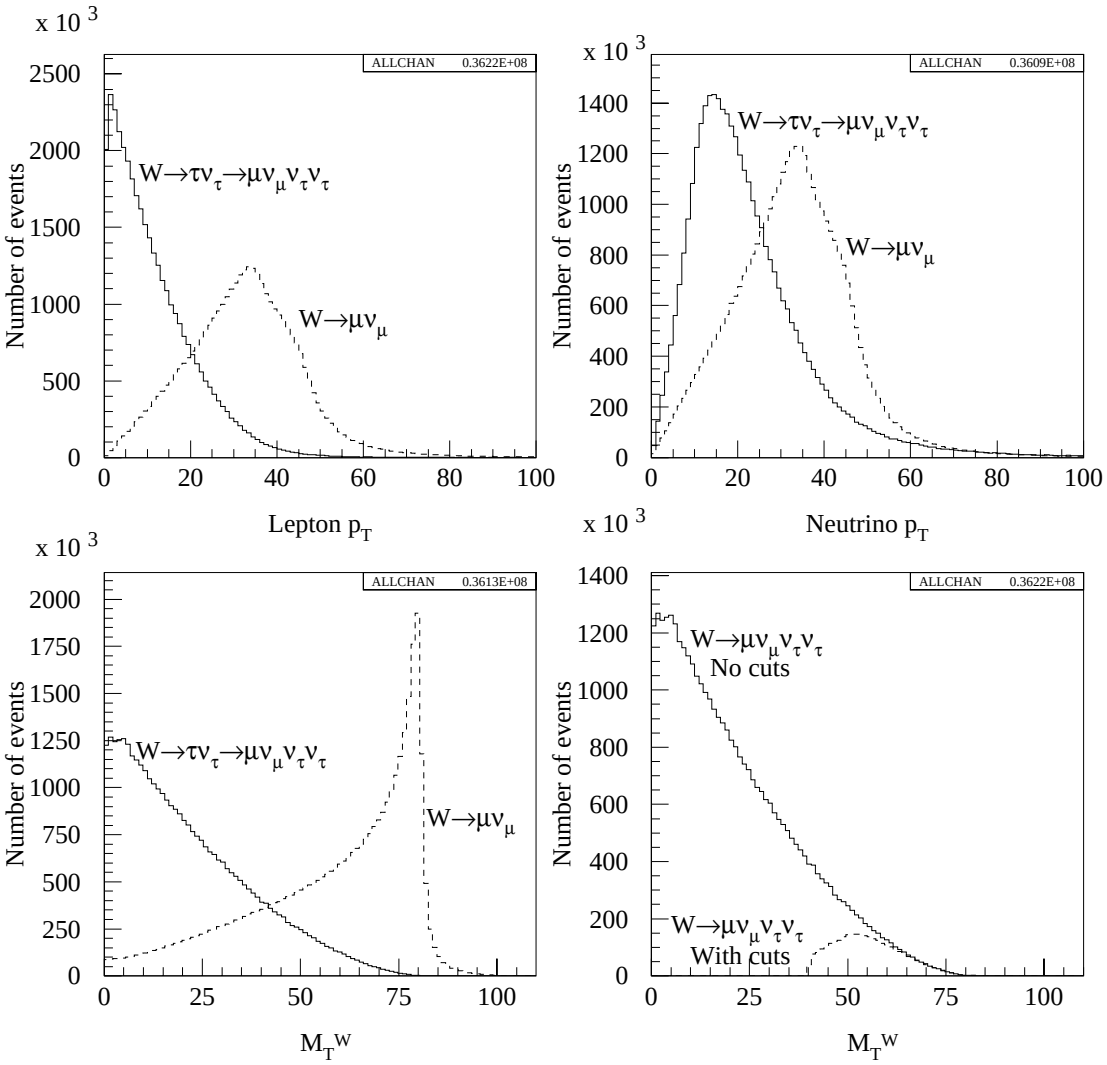

Figure 6.7 Muon and $\not\!\!E_T$ transverse momenta and W transverse mass from the decay of the tau coming from W+jet DYRAD events (solid histogram) superimposed on the transverse momenta and W mass from the direct decay of the W to muons (dashed histogram). The resulting transverse mass from the tau decay is shown in the lower right plot for all events (solid histogram) and for the ones that remain after the application of the leptons p_T cut of 20 GeV and the transverse mass of 40 GeV (dashed histogram). This way 92% of the tau background is removed.

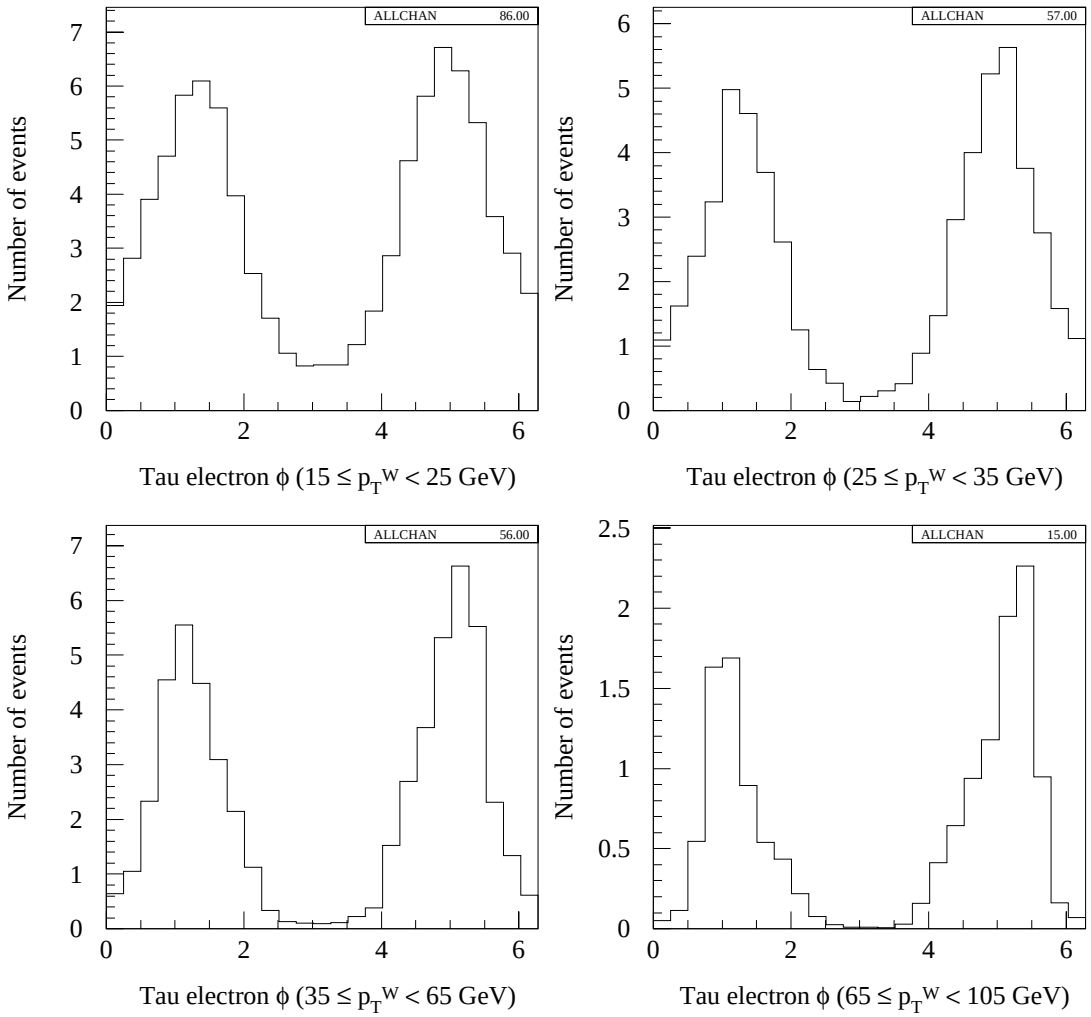

Figure 6.8 Electron ϕ distributions for the four p_T^W bins for the W+jet FMC events, where the W decays to a tau which subsequently decays to an electron passing all kinematic requirements. All other experimental cuts are applied. The histograms are normalized to the FMC yields.

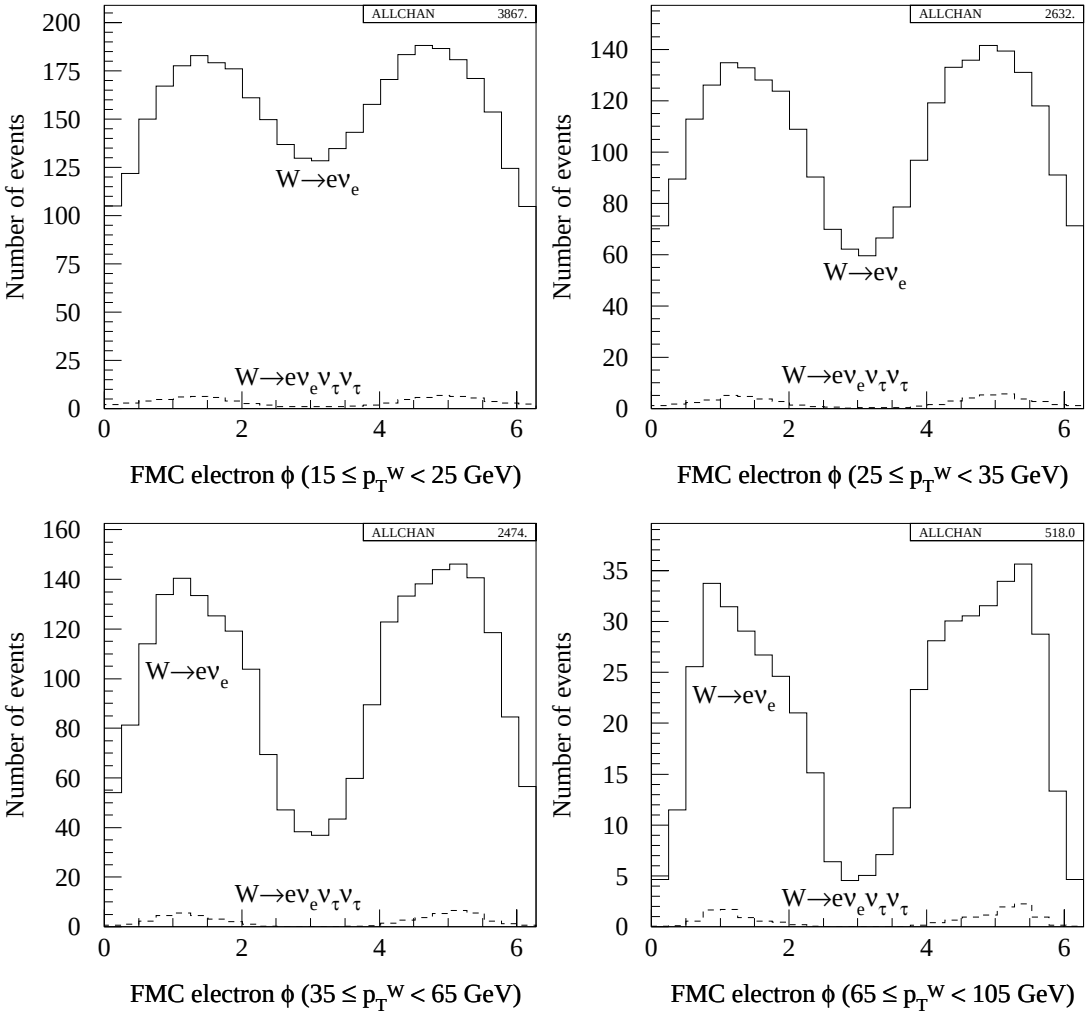

Figure 6.9 Electron ϕ distributions for the four p_T^W bins for electron W+jet FMC events (solid histogram) and for tau W+jet FMC events, where the tau decays to an electron (dashed histogram). All other experimental cuts are applied. The histograms are normalized to the FMC yields.

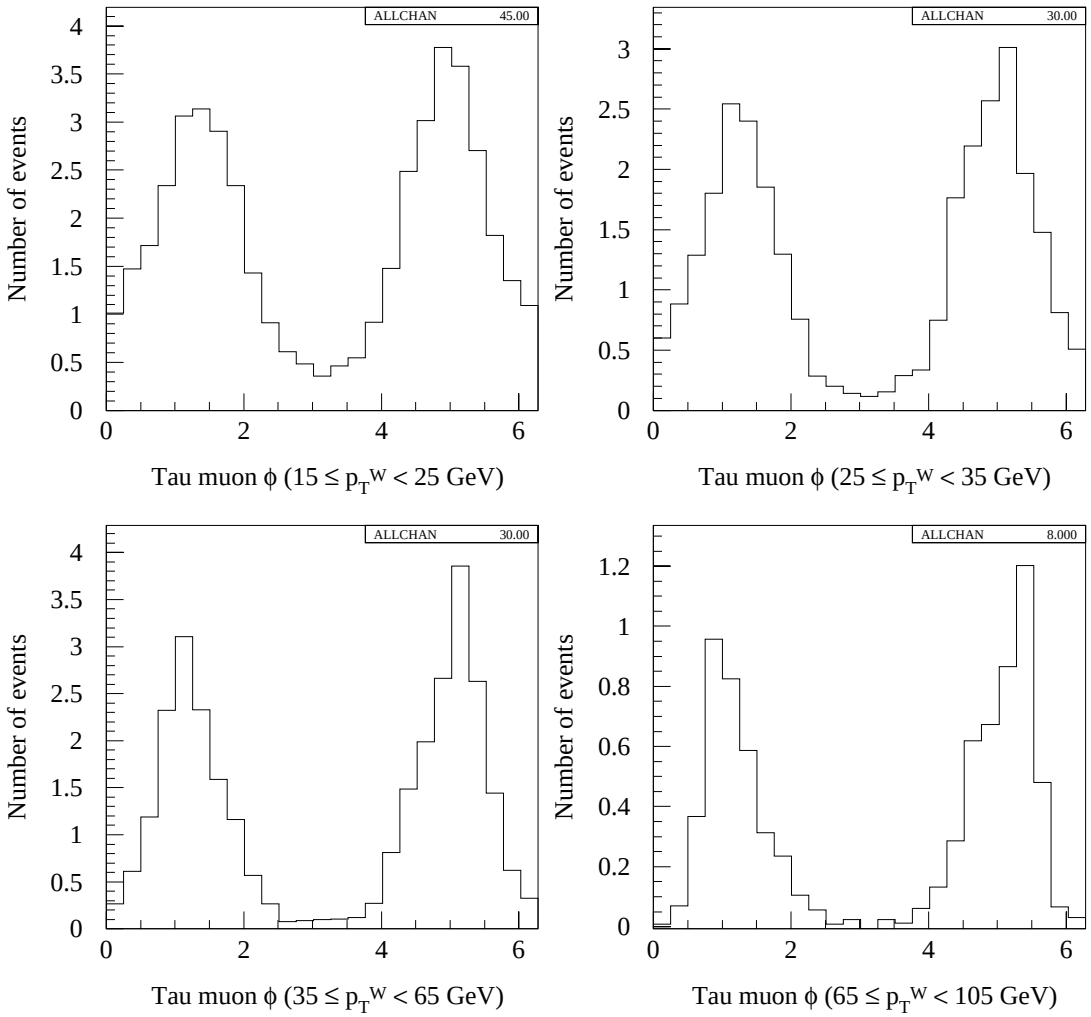

Figure 6.10 Muon ϕ distributions for the four p_T^W bins for the W+jet FMC events, where the W decays to a tau which subsequently decays to a muon passing all kinematic requirements. All other experimental cuts are applied. The histograms are normalized to the FMC yields.

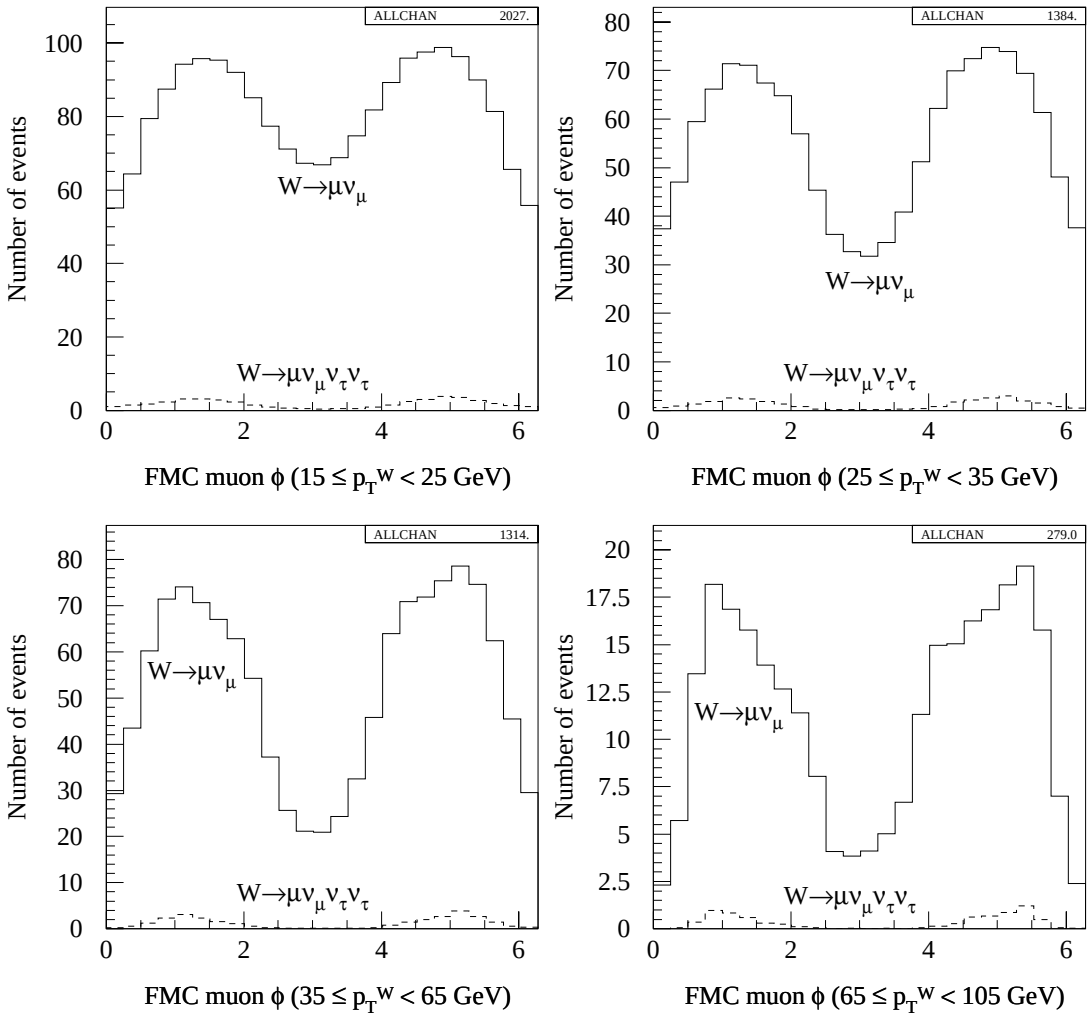

Figure 6.11 Muon ϕ distributions for the four p_T^W bins for muon W+jet FMC events (solid histogram) and for tau W+jet FMC events, where the tau decays to a muon (dashed histogram). All other experimental cuts are applied. The histograms are normalized to the FMC yields.

$(W \to \tau\ \bar{\nu}_\tau \to \bar{\nu}_\tau\ \nu_\tau\ \bar{\nu}_{e/\mu}\ e/\mu)$+jet background				
p_T^W (GeV)	N_e	Fraction	N_μ	Fraction
15-25	86 ± 3	2.22 ± 0.11 %	45 ± 2	2.22 ± 0.15 %
25-35	57 ± 2	2.16 ± 0.10 %	30 ± 2	2.17 ± 0.18 %
35-65	56 ± 2	2.26 ± 0.11 %	30 ± 2	2.28 ± 0.19 %
65-105	15 ± 1	2.89 ± 0.22 %	8 ± 0	2.87 ± 0.14 %

Table 6.2 Monte Carlo background estimation of the number of electron and muon W+jet events, where the W decays to a tau and the electron or muon is the decay product of the tau. The fractions of the backgrounds are calculated with respect to the FMC W+jet events.

for the W+jet events, where the W first decays to a tau which then decays to an electron or muon.

To examine how this background affects the W+jet lepton ϕ distribution, we plot the ϕ distribution for the leptons resulting from tau decays in W+jet events for the four p_T^W bins (Figures 6.8 and 6.10). Figures 6.9 and 6.11 show the tau background overimposed on the FMC signal, for electrons and muons respectively. We observe that the same pattern of two maxima at $\frac{\pi}{2}$ and $\frac{3\pi}{2}$ is again present. The plots are normalized to the actual expected yields from FMC. We will include the τ-background FMC ϕ distribution files into the theoretical prediction of the ϕ distributions, in order to correctly extract the angular coefficients.

6.3 The QCD Background

The QCD background in the inclusive W production and decay consists of dijet events, where one of the jets is misidentified as lepton and the other one is not measured, resulting to the creation of missing E_T. In the W+jet case, the QCD background is rather trijet events, where the highest E_T jet is the one detected, one jet is lost (resulting to missing E_T), and the other one misidentified as lepton to erroneously reconstruct a W. The studies of the QCD background of our W+jet analysis comprise the estimation of the number of the background events for the four p_T^W bins as well as the shape of the background for these bins.

To measure the expected number of QCD events in the lepton data samples we

p_T^W (GeV)	Parameterization of $ISO > 0.1$ W+jet events	$ISO > 0.1$ and $\Delta\phi_{l-j} > 2.5$ W+jet events	$ISO > 0.1$ and $\Delta\phi_{l-j} > 2.5$ (W+jet)+QCD events	Fraction of true QCD events
15-25	$5.86 \times \Delta\phi_{l-j} + 2.52$	117	420	0.4378=(420-117)/692
25-35	$3.22 \times \Delta\phi_{l-j} + 1.37$	64	190	0.3695=(190-64)/341
35-65	$2.39 \times \Delta\phi_{l-j} + 2.55$	57	100	0.1814=(100-57)/237
65-105	$0.24 \times \Delta\phi_{l-j} + 1.09$	11	15	0.0975=(15-11)/41

Table 6.3 The parameterization of the $\Delta\phi_{l-j}$ distribution for $ISO > 0.1$ electron W+events allows us to estimate the number of $ISO > 0.1$ W+jet events in the $\Delta\phi_{l-j} \geq 2.5$ region. By subtracting these events from the combined W+jet and QCD yield, and by subsequently dividing by the total number of events with $ISO > 0.1$, we estimate the fraction of true QCD events. We assume the same fraction is true in the signal ($ISO < 0.1$) region.

look at the electrons with Isolation ($ISO^\dagger$) greater than 0.1. Our signal is in the $ISO < 0.1$ region and most of the events with lepton $ISO \geq 0.1$, but not all of them, are QCD background events. The upper histograms of Figures 6.12 to 6.15 show the isolation distribution of the electrons from W+jet events, for the four p_T^W bins. In the semilog plots, the $ISO < 0.1$ region and the $ISO \geq 0.1$ can be approximated with two straight lines. The basic technique is to extrapolate the $ISO \geq 0.1$ line into the signal region and calculate its integral in that region, assuming that the QCD background is not altered at the $ISO < 0.1$ region. This integral would give us the number of QCD events, if the $ISO \geq 0.1$ region was filled exclusively with QCD events. In reality, only a fraction of the $ISO \geq 0.1$ events are true QCD background events, the rest of them being true W+jet events. We actually expect to have some signal in the region of isolation from 0.1 to 0.2, so we actually fit the area above 0.2 with a straight line (in the semilog histogram), which describes the QCD background. We also fit five continuous regions of isolation, around the central region of $ISO = 0.20$ to $ISO = 0.65$ (namely 0.15–0.65, 0.25–0.65, 0.15–0.60, 0.20–0.65, and 0.25–0.70) to get a systematic uncertainty of this procedure. We are careful not use the empty bins when we fit.

We can actually measure the percentage of the true QCD background above isolation of 0.1, by making the histogram of $\Delta\phi_{l-j}$ for the events with $ISO \geq 0.1$, where $\Delta\phi_{l-j}$ is the difference in the ϕ angle between the lepton and the highest-E_T jet, with no additional requirements for the jet. We expect the distribution to be almost flat

†The Isolation in a cone of 0.4 is defined in Section 4.1.4 for electrons, and Section 4.6.4 for muons

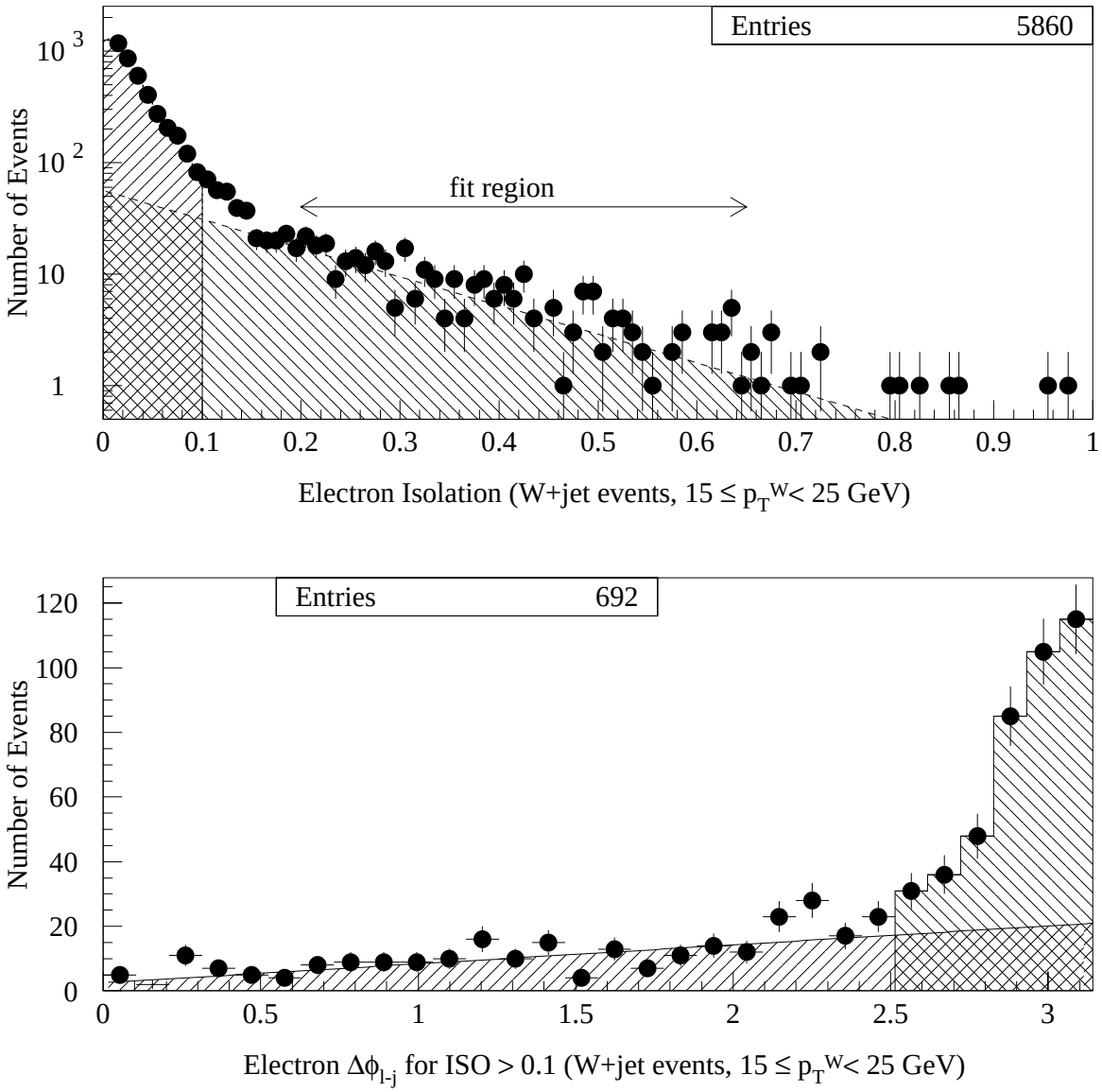

Figure 6.12 Isolation of the electron in W+jet events (upper histogram). We fit the region from 0.2 to 0.65 to straight line and extrapolate into the signal region (isolation less than 0.1) to estimate the QCD background. Not all of this extrapolated region is QCD background. This is apparent at the lower plot where most of the events with $\Delta\phi_{l-j} \geq 2.5$ are actually QCD events, while the W+jet events are described by an linear region. At low $\Delta\phi_{l-j}$ we expect the distribution to fall, due to the application of the isolation cut. (First p_T^W bin).

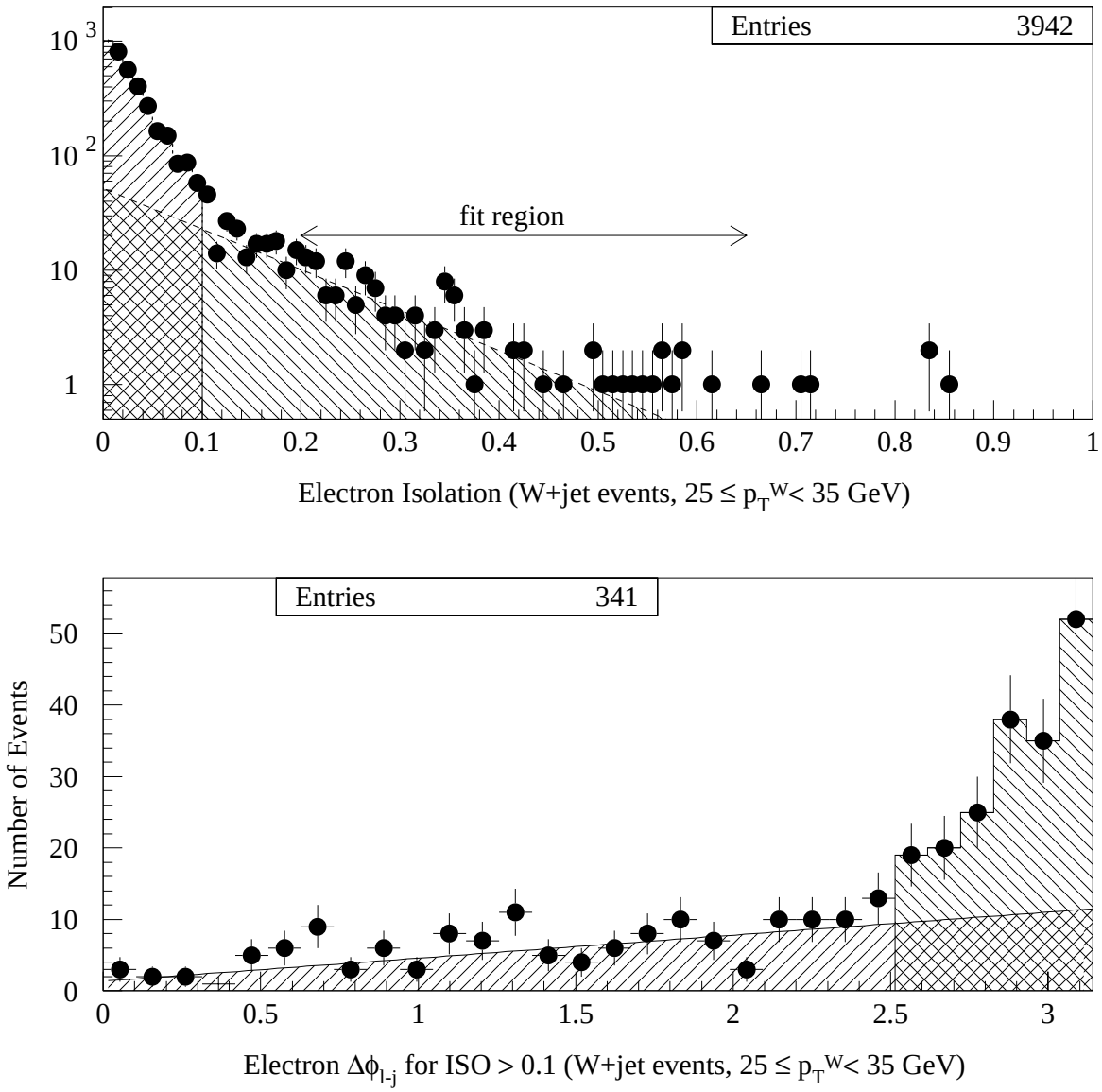

Figure 6.13 Isolation of the electron in W+jet events (upper histogram). We fit the region from 0.2 to 0.65 to straight line and extrapolate into the signal region (isolation less than 0.1) to estimate the QCD background. Not all of this extrapolated region is QCD background. This is apparent at the lower plot where most of the events with $\Delta\phi_{l-j} \geq 2.5$ are actually QCD events, while the W+jet events are described by an linear region. At low $\Delta\phi_{l-j}$ we expect the distribution to fall, due to the application of the isolation cut. (Second p_T^W bin).

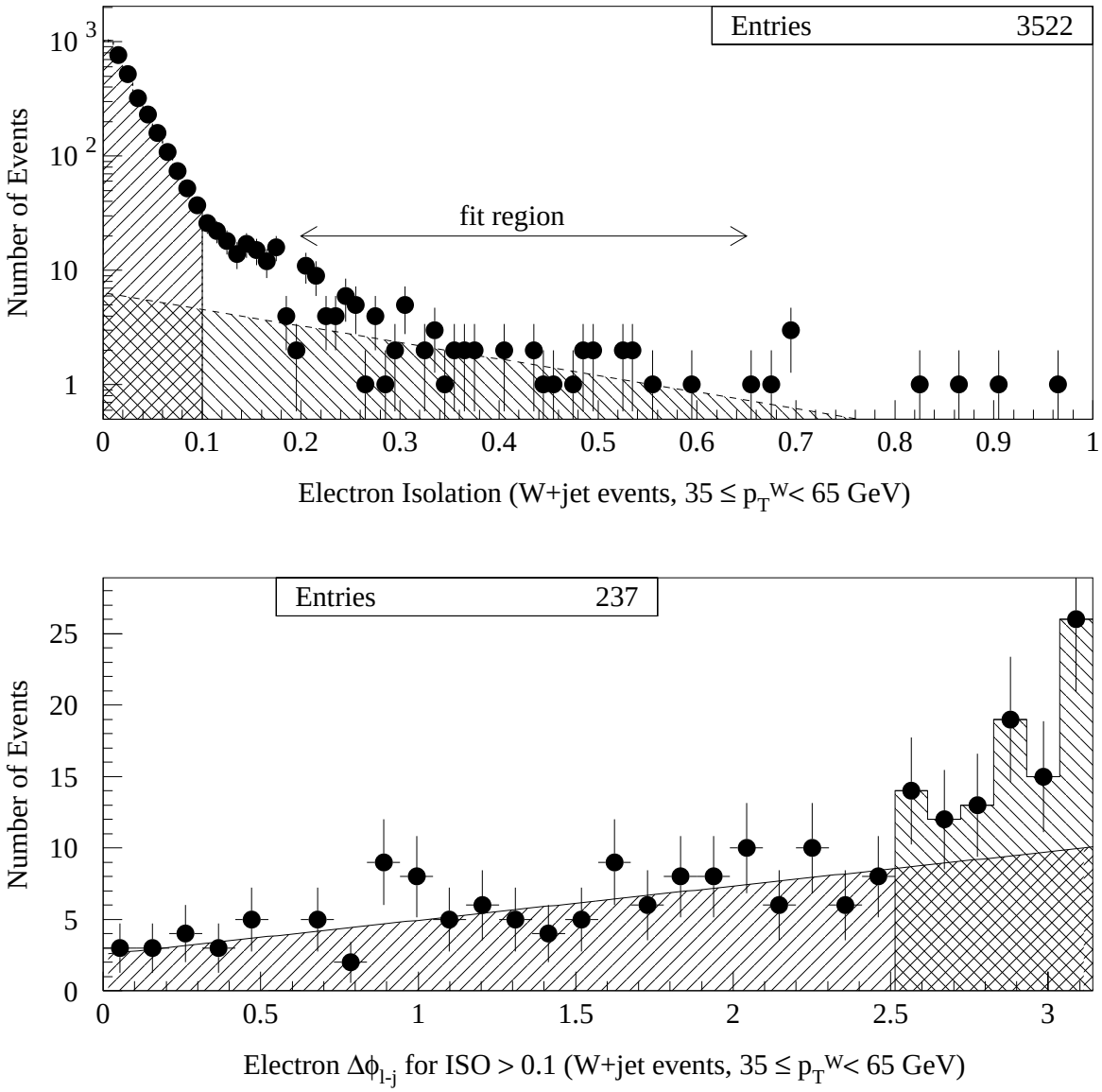

Figure 6.14 Isolation of the electron in W+jet events (upper histogram). We fit the region from 0.2 to 0.65 to straight line and extrapolate into the signal region (isolation less than 0.1) to estimate the QCD background. Not all of this extrapolated region is QCD background. This is apparent at the lower plot where most of the events with $\Delta\phi_{l-j} \geq 2.5$ are actually QCD events, while the W+jet events are described by an linear region. At low $\Delta\phi_{l-j}$ we expect the distribution to fall, due to the application of the isolation cut. (Third p_T^W bin).

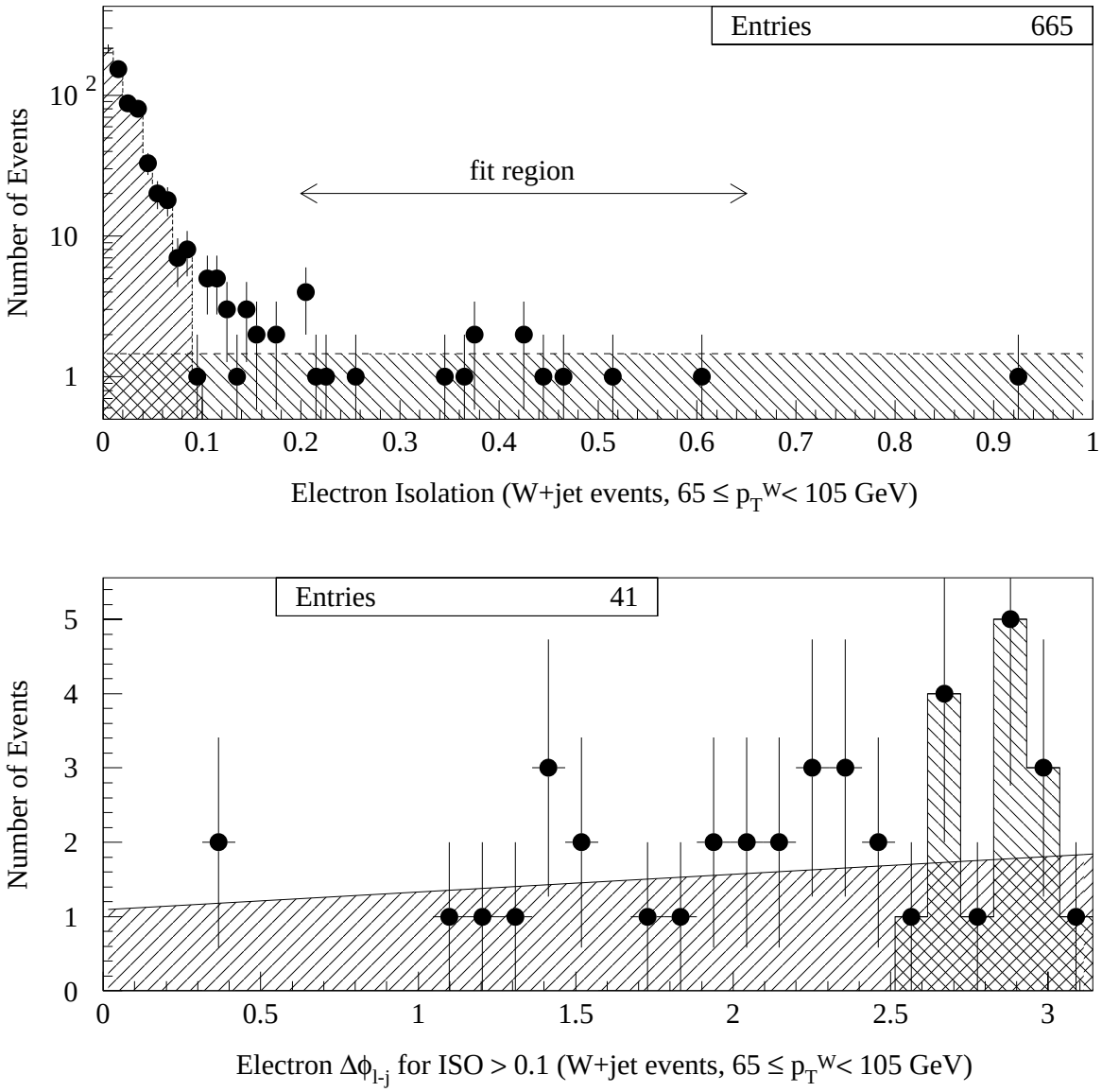

Figure 6.15 Isolation of the electron in W+jet events (upper histogram). We fit the region from 0.2 to 0.65 to straight line and extrapolate into the signal region (isolation less than 0.1) to estimate the QCD background. Not all of this extrapolated region is QCD background. This is apparent at the lower plot where most of the events with $\Delta\phi_{l-j} \geq 2.5$ are actually QCD events, while the W+jet events are described by an linear region. At low $\Delta\phi_{l-j}$ we expect the distribution to fall, due to the application of the isolation cut. (Fourth p_T^W bin).

p_T^W (GeV)	Number of electron W+jet events	Number of QCD events before correction	Percentage of QCD events before correction	Fraction of true QCD events	Percentage of QCD background
15-25	5166	423^{+77}_{-42}	$8.18^{+1.11}_{-0.81}$%	0.4378	$3.58^{+0.49}_{-0.35}$%
25-35	3601	353^{+26}_{-148}	$9.80^{+0.74}_{-4.1}$%	0.3695	$3.62^{+0.27}_{-1.51}$%
35-65	3285	54^{+151}_{-25}	$1.64^{+4.60}_{-0.75}$%	0.1814	$0.30^{+0.83}_{-0.14}$%
65-105	624	14^{+8}_{-3}	$2.24^{+1.24}_{-0.27}$%	0.0975	$0.22^{+0.12}_{-0.03}$%

Table 6.4 We fit the region from $ISO = 0.20$ to $ISO = 0.65$ to an exponential (straight line in the semilog plot). By extrapolating this line to the signal region ($ISO < 0.1$) we get the first estimation of the QCD background in the electron W+jet sample, before correction. The uncertainties are systematic and are calculated by fitting five different continuous regions from $ISO = 0.15$ to $ISO = 0.70$, ignoring the empty bins. Only a fraction of these events are true QCD background, the rest being W+jet events. Using the fractions depicted in Table 6.3, we calculate the number of QCD background events.

for the W+jet events, because there is no correlation between the jet and the lepton ϕ directions. In reality, the distribution falls at low $\Delta\phi_{l-j}$, due to the application of the isolation cut in our data. In the case of the QCD background, we expect the $\Delta\phi_{l-j}$ between the highest E_T jet and the jet resembling the lepton to peak at π. This is true, because the two lower E_T jets are balancing the jet with the highest E_T in the transverse plane. We fit the W+jet part ($\Delta\phi_{l-j} \leq 2.5$) with a straight line and the part of the histogram with $\Delta\phi_{l-j} > 2.5$ above that line corresponds to true QCD background. By dividing this part of the histogram by the total number of events with $ISO \geq 0.1$, we obtain the fraction of the true QCD background. We expect the same fraction to be valid in the signal region, so we get the right number of QCD background events by multiplying the number of $ISO \geq 0.1$ events extrapolated into the signal $ISO < 1$ region (isolation plot) with this fraction we get from the $\Delta\phi_{l-j}$ plot. We repeat for the four p_T^W bins. The lower histograms of Figures 6.12 to 6.15 show the $\Delta\phi_{l-j}$ for the events with isolation greater than 0.1 for electron W+jet events and for the four p_T^W bins. The parameterized function of W+jet events with $ISO \geq 0.1$ (straight line from fit) has to be integrated from $\Delta\phi_{l-j} = 2.5$ to $\Delta\phi_{l-j} = \pi$ and then multiplied by $30/\pi$ (because we use 30 bins) to get the total number of expected W+jet events with isolation greater than 0.1. Table 6.3 shows the extracted fraction of QCD background in the $ISO \geq 0.1$ region for the four p_T^W bins. The electron W+jet QCD background results can be seen in Table 6.4.

In the study of the QCD background in the muon sample we face a new problem. There is a cut applied to data (`zmuo_veto`) that removes events with extra activity which could be consistent with the production of a Z boson. This cut searches for a second muon in the event, which does not pass one (and only one) of the following cuts:

- The isolation cut $ISO < 0.1$
- The electromagnetic calorimeter cut $E^{\mathrm{EM}} < 2$ GeV
- The hadron calorimeter cut $E^{\mathrm{HAD}} < 6$ GeV

These events are real Z bosons that look like W bosons since their second muon does not pass one of the above cuts because of bremsstrahlung (internal or external, depending on the failing cut). The `zmuo_veto` cut mainly affects the tail of the isolation distribution ($ISO \geq 0.1$) and causes us to underestimate the QCD background, since we use that tail to estimate it. For that reason, we neglect this cut, in order to remove this bias at high isolation (ISO > 0.1) and make the transition from the low to high isolation smooth. Of course some of the Z background is included this way, but we do not expect it to radically affect our QCD background estimation. Using the isolation method for muons we fit the background starting from $ISO = 0.17$ to $ISO = 0.40$, to increase the statistical significance of our estimation. We also fit five continuous regions of isolation, around the central region of $ISO = 0.17$ to $ISO = 0.40$ (namely 0.16–0.40, 0.18–0.40, 0.16–0.35, 0.17–0.40, and 0.18–0.45) to get a systematic uncertainty of this procedure. We are careful not use the empty bins when we fit. The upper histograms of Figures 6.16 to 6.19 show the isolation distribution and fits of for the muon W+jet events and for the four p_T^W bins.

Next, we measure the percentage of the true QCD events using again the histogram of $\Delta\phi_{l-j}$ for the events with $ISO \geq 0.1$, where $\Delta\phi_{l-j}$ is the difference in the ϕ angle between the lepton and the highest-E_T jet, with no additional requirements for the jet. In the case of the muons, there is also a peak at $\Delta\phi_{l-j} = 0$, due to the electromagnetic bremsstrahlung processes that are not suppressed after we relax the `zmuo_veto` cut. For the highest muon p_T^W bin the predicted number of true W+jet events is greater than the total number of events with $ISO \geq 0.1$ and $\Delta\phi_{l-j} \geq 2.5$, which results in a

p_T^W (GeV)	Parameterization of $ISO > 0.1$ W+jet events	$ISO > 0.1$ and $\Delta\phi_{l-j} > 2.5$ W+jet events	$ISO > 0.1$ and $\Delta\phi_{l-j} > 2.5$ (W+jet)+QCD events	Fraction of true QCD events
15-25	$1.44 \times \Delta\phi_{l-j} + 3.23$	45	256	0.4414=(256-45)/478
25-35	$2.56 \times \Delta\phi_{l-j} + 0.36$	46	98	0.2131=(98-46)/244
35-65	$0.23 \times \Delta\phi_{l-j} + 3.07$	23	45	0.1419=(45-23)/155
65-105	$0 \times \Delta\phi_{l-j} + 1$	9	4	0

Table 6.5 The parameterization of the $\Delta\phi_{l-j}$ distribution for $ISO > 0.1$ muon W+events allows us to estimate the number of $ISO > 0.1$ W+jet events in the $\Delta\phi_{l-j} \geq 2.5$ region. By subtracting these events from the combined W+jet and QCD yield, and by subsequently dividing by the total number of events with $ISO > 0.1$, we estimate the fraction of true QCD events. We assume the same fraction is true in the signal ($ISO < 0.1$) region.

fraction of true QCD events above $ISO \geq 0.1$ equal to zero. The lower histograms of Figures 6.16 to 6.19 show the $\Delta\phi_{l-j}$ for the events with isolation greater than 0.1 for muon W+jet events and for the four p_T^W bins. The parameterized function of W+jet events with $ISO \geq 0.1$ (straight line from fit) has to be integrated from $\Delta\phi_{l-j} = 2.5$ to $\Delta\phi_{l-j} = \pi$ and then multiplied by $30/\pi$ (because we use 30 bins) to get the total number of expected W+jet events with isolation greater than 0.1. Table 6.5 shows the extracted fraction of QCD background in the $ISO \geq 0.1$ region for the four p_T^W bins. The muon W+jet QCD background results can be seen in Table 6.6.

After we calculate the fraction of the QCD background in the signal region, we multiply it to the actual CDF yields to get the absolute prediction of the number of QCD events in the four p_T^W bins, for electrons and muons. The results can be seen in Table 6.7.

To complete the study of the QCD background we need to estimate its shape to properly include this background in the Standard Model prediction of the lepton Collins-Soper ϕ distribution for the four p_T^W bins. For this reason we plot ϕ for the events with $ISO \geq 0.1$ and $\Delta\phi_{l-j} > 2.5$ for the electrons (Figures 6.20 and 6.21 and muons (Figures 6.22 and 6.23). We fit the distributions to the sum of two Gaussians and two straight lines. For the last p_T^W bin of the electrons and the last two p_T^W bins of the muons, there is not enough statistics for the fit, so we use the total distributions (Figures 6.20 and 6.22) normalized to the actual number of events for those high p_T^W bins. We do not expect the shape of the QCD background to considerably change with the p_T^W. We use these distributions to add the QCD background to the Standard

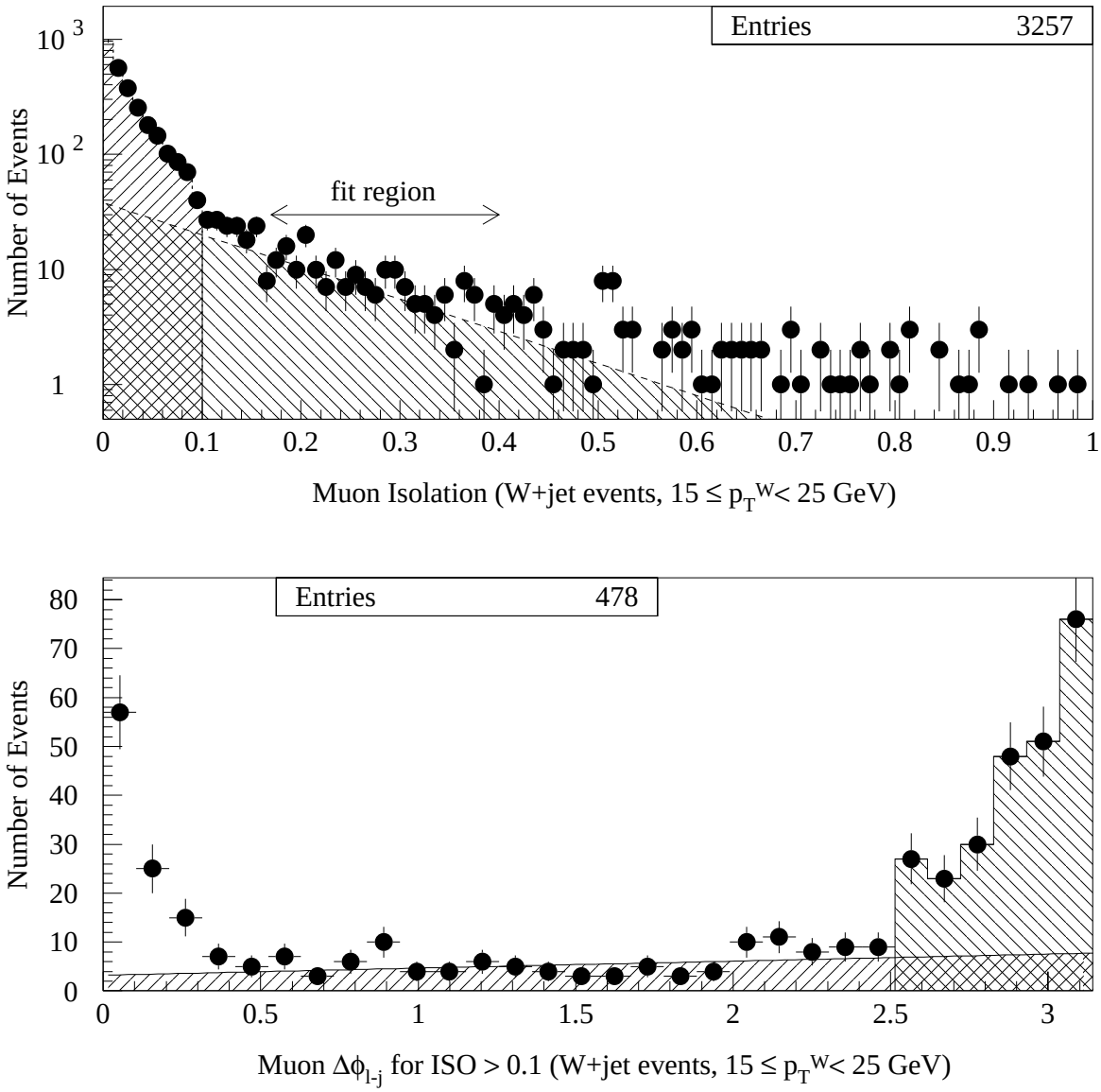

Figure 6.16 Isolation of the muon in W+jet events (upper histogram). We fit the region from 0.17 to 0.4 to straight line and extrapolate into the signal region (isolation less than 0.1) to estimate the QCD background. Not all of this extrapolated region is QCD background. This is apparent at the lower plot where most of the events with $\Delta\phi_{l-j} \geq 2.5$ are actually QCD events, while the W+jet events are described by an linear region. At low $\Delta\phi_{l-j}$ the distribution increases, due to bremsstrahlung processes, which go away if we apply the `zmuo_veto` cut. (First p_T^W bin).

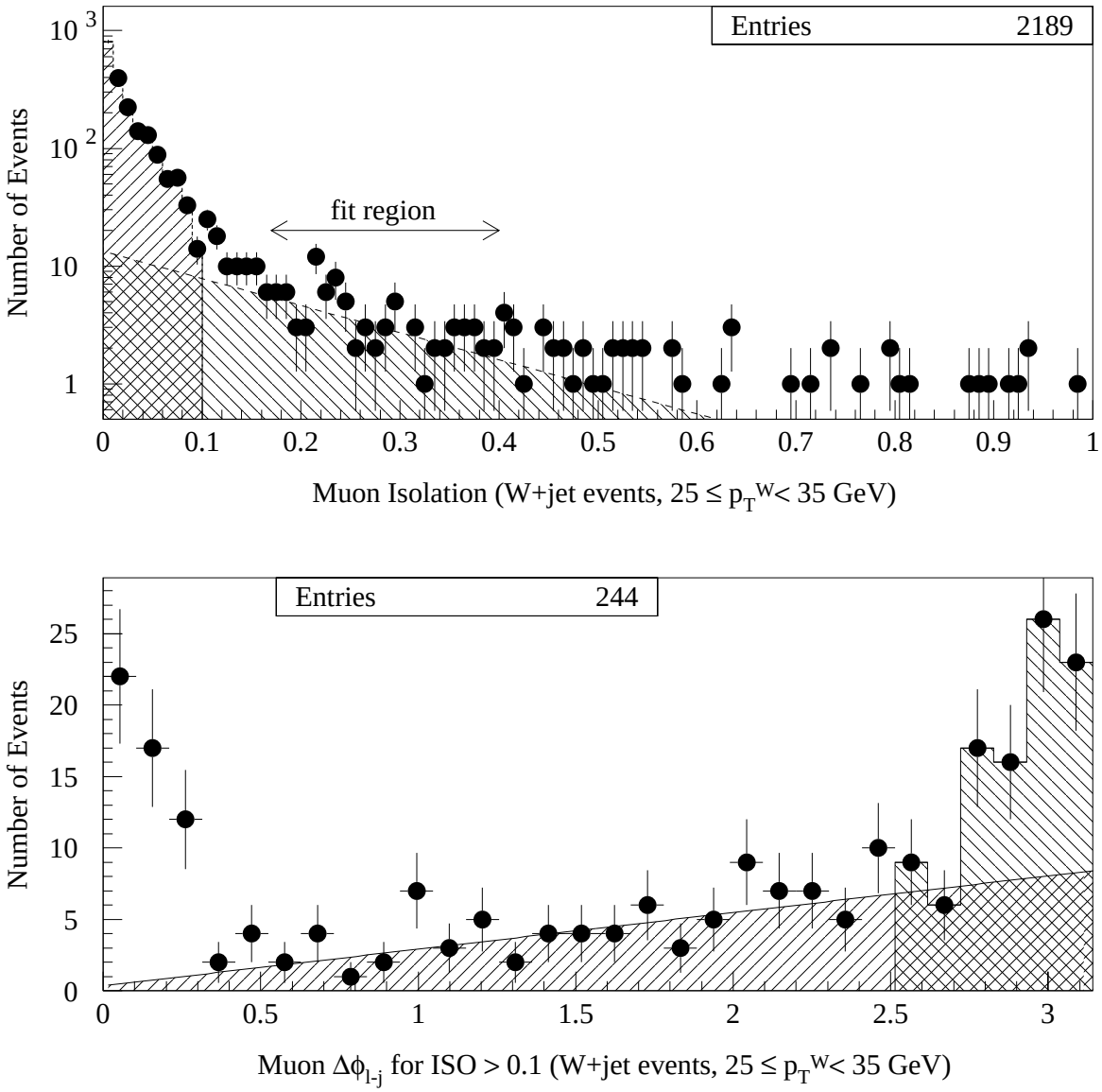

Figure 6.17 Isolation of the muon in W+jet events (upper histogram). We fit the region from 0.17 to 0.4 to straight line and extrapolate into the signal region (isolation less than 0.1) to estimate the QCD background. Not all of this extrapolated region is QCD background. This is apparent at the lower plot where most of the events with $\Delta\phi_{l-j} \geq 2.5$ are actually QCD events, while the W+jet events are described by an linear region. At low $\Delta\phi_{l-j}$ the distribution increases, due to bremsstrahlung processes, which go away if we apply the `zmuo_veto` cut. (Second p_T^W bin).

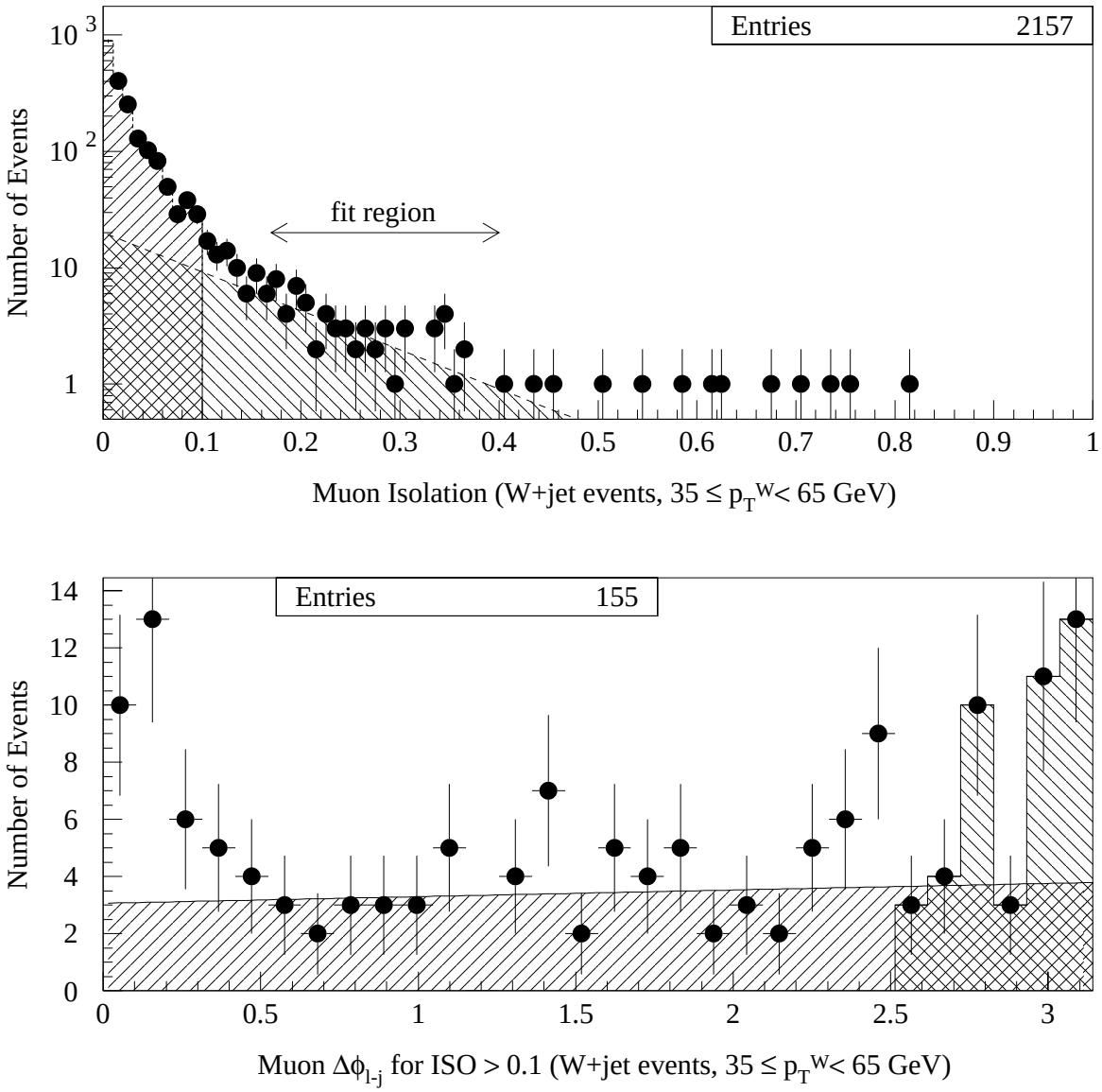

Figure 6.18 Isolation of the muon in W+jet events (upper histogram). We fit the region from 0.17 to 0.4 to straight line and extrapolate into the signal region (isolation less than 0.1) to estimate the QCD background. Not all of this extrapolated region is QCD background. This is apparent at the lower plot where most of the events with $\Delta\phi_{l-j} \geq 2.5$ are actually QCD events, while the W+jet events are described by an linear region. At low $\Delta\phi_{l-j}$ the distribution increases, due to bremsstrahlung processes, which go away if we apply the `zmuo_veto` cut. (Third p_T^W bin).

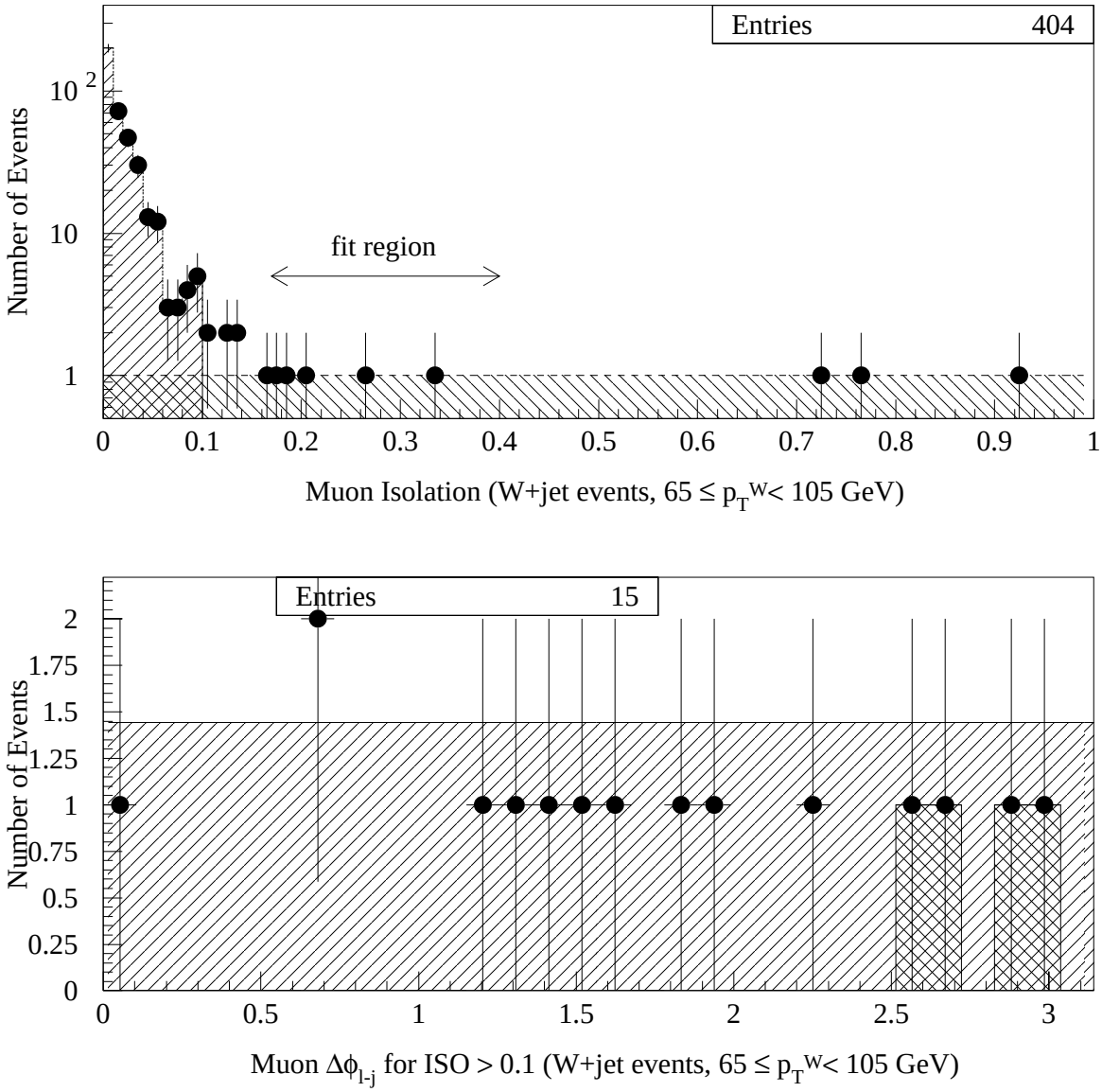

Figure 6.19 Isolation of the muon in W+jet events (upper histogram). We fit the region from 0.17 to 0.4 to straight line and extrapolate into the signal region (isolation less than 0.1) to estimate the QCD background. All of this extrapolated region is not QCD background, as it can be seen in the lower histogram. (Fourth p_T^W bin).

p_T^W (GeV)	Number of muon W+jet events	Number of QCD events before correction	Percentage of QCD events before correction	Fraction of true QCD events	Percentage of QCD background
15-25	2779	280^{+102}_{-25}	$10.07^{+3.68}_{-0.90}\%$	0.4414	$4.45^{+1.62}_{-0.40}\%$
25-35	1943	103^{+129}_{-4}	$5.30^{+6.64}_{-0.21}\%$	0.2131	$1.13^{+1.41}_{-0.04}\%$
35-65	2002	139^{+50}_{-21}	$6.94^{+2.50}_{-1.05}\%$	0.1419	$0.98^{+0.35}_{-0.15}\%$
65-105	389	11^{+0}_{-0}	$2.70^{+0.00}_{-0.00}\%$	0	0%

Table 6.6 We fit the region from $ISO = 0.17$ to $ISO = 0.40$ to an exponential (straight line in the semilog plot). By extrapolating this line to the signal region ($ISO < 0.1$) we get the first estimation of the QCD background in the muon W+jet sample, before correction. The uncertainties are systematic and are calculated by fitting five different continuous regions from $ISO = 0.16$ to $ISO = 0.45$, ignoring the empty bins. Only a fraction of these events are true QCD background, the rest being W+jet events. Using the fractions depicted in Table 6.5, we calculate the number of QCD background events.

QCD background				
p_T^W (GeV)	N_e	Fraction	N_μ	Fraction
15-25	$185\ ^{+25}_{-18}$	$3.58\ ^{+0.49}_{-0.35}$ %	$126\ ^{+46}_{-11}$	$4.45\ ^{+1.62}_{-0.40}$ %
25-35	$130\ ^{+10}_{-54}$	$3.62\ ^{+0.27}_{-1.51}$ %	$21\ ^{+26}_{-1}$	$1.13\ ^{+1.41}_{-0.04}$ %
35-65	$10\ ^{+27}_{-5}$	$0.30\ ^{+0.83}_{-0.14}$ %	$18\ ^{+7}_{-3}$	$0.98\ ^{+0.35}_{-0.15}$ %
65-105	$1\ ^{+1}_{-0}$	$0.22\ ^{+0.12}_{-0.03}$ %	0	0 %

Table 6.7 QCD background estimation for the electron and muon W+jet events. The fractions of the backgrounds are calculated with respect to the CDF Data W+jet events.

Electron W+jet Backgrounds				
Background	p_T^W=15-25 GeV	p_T^W=25-35 GeV	p_T^W=35-65 GeV	p_T^W=65-105 GeV
$W \to \tau\nu_\tau$	86 ± 3 (2.22 %)	57 ± 2 (2.16 %)	56 ± 2 (2.26 %)	15 ± 1 (2.89%)
$Z \to e^+e^-$	47 ± 2 (1.22 %)	30 ± 1 (1.14 %)	25 ± 1 (1.01 %)	5 ± 0 (0.96 %)
QCD	185^{+25}_{-18} (3.58 %)	130^{+10}_{-54} (3.62 %)	10^{+27}_{-5} (0.30 %)	1^{+1}_{-0} (0.22 %)

Table 6.8 Summary of electron W+jet backgrounds.

Muon W+jet Backgrounds				
Background	p_T^W=15-25 GeV	p_T^W=25-35 GeV	p_T^W=35-65 GeV	p_T^W=65-105 GeV
$W \to \tau\nu_\tau$	45 ± 2 (2.22 %)	30 ± 2 (2.17 %)	30 ± 2 (2.28 %)	8 ± 0 (2.87%)
$Z \to \mu^+\mu^-$	127 ± 7 (6.26 %)	82 ± 4 (5.92 %)	72 ± 4 (5.48 %)	12 ± 1 (4.30 %)
QCD	126^{+46}_{-11} (4.45 %)	21^{+26}_{-1} (1.13 %)	18^{+7}_{-3} (0.98 %)	0 (0 %)

Table 6.9 Summary of muon W+jet backgrounds.

Model prediction, after we normalize it to the expected number of QCD events, given by Table 6.7.

6.4 Summary of Backgrounds and Standard Model Yield Prediction

The summary of backgrounds for electrons and muons for the four p_T^W bins are shown in Tables 6.8 and 6.9 respectively. To construct them we used Tables 6.1, 6.2 and 6.7. We get the total FMC prediction by adding the backgrounds of Tables 6.8 and 6.9 to the FMC signal prediction from Table 5.1. To get the right errors, we add the signal and electroweak errors linearly and add the result to the QCD errors in quadrature. The results are shown in Tables 6.10 and 6.11.

FMC+backgrounds electron yields for inclusive W+jet			
p_T^W (GeV)	N_e(FMC)	N_e(Backgrounds)	N_e(Total prediction)
15-25	3867 ± 137	318^{+25}_{-19}	4185^{+144}_{-143}
25-35	2632 ± 93	217^{+10}_{-54}	2849^{+97}_{-110}
35-65	2474 ± 87	91^{+27}_{-6}	2565^{+94}_{-90}
65-105	518 ± 18	21^{+1}_{-1}	539^{+19}_{-19}

Table 6.10 The electron total yields for inclusive W+jet up to order α_s^2. The PDF and Q^2 systematics have not been included yet.

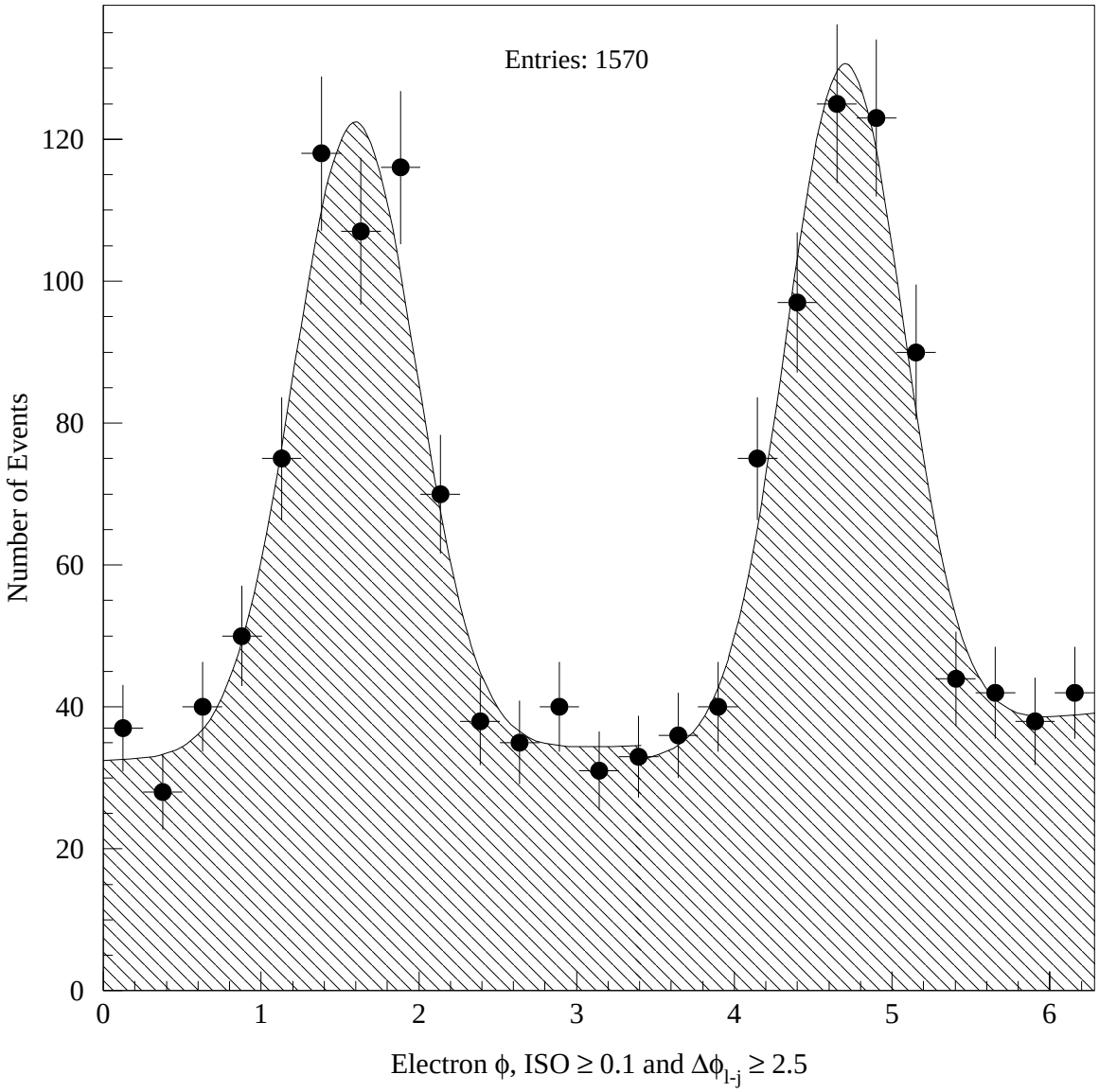

Figure 6.20 The ϕ distribution of electrons from W+jet events with $ISO \geq 0.1$ and $\Delta\phi_{l-j} \geq 2.5$. These events are more than likely QCD events. We fit them with two Gaussians on top of two straight lines. We assume that this distribution is going to be the same as the one in the signal region ($ISO < 0.1$) after it is properly normalized.

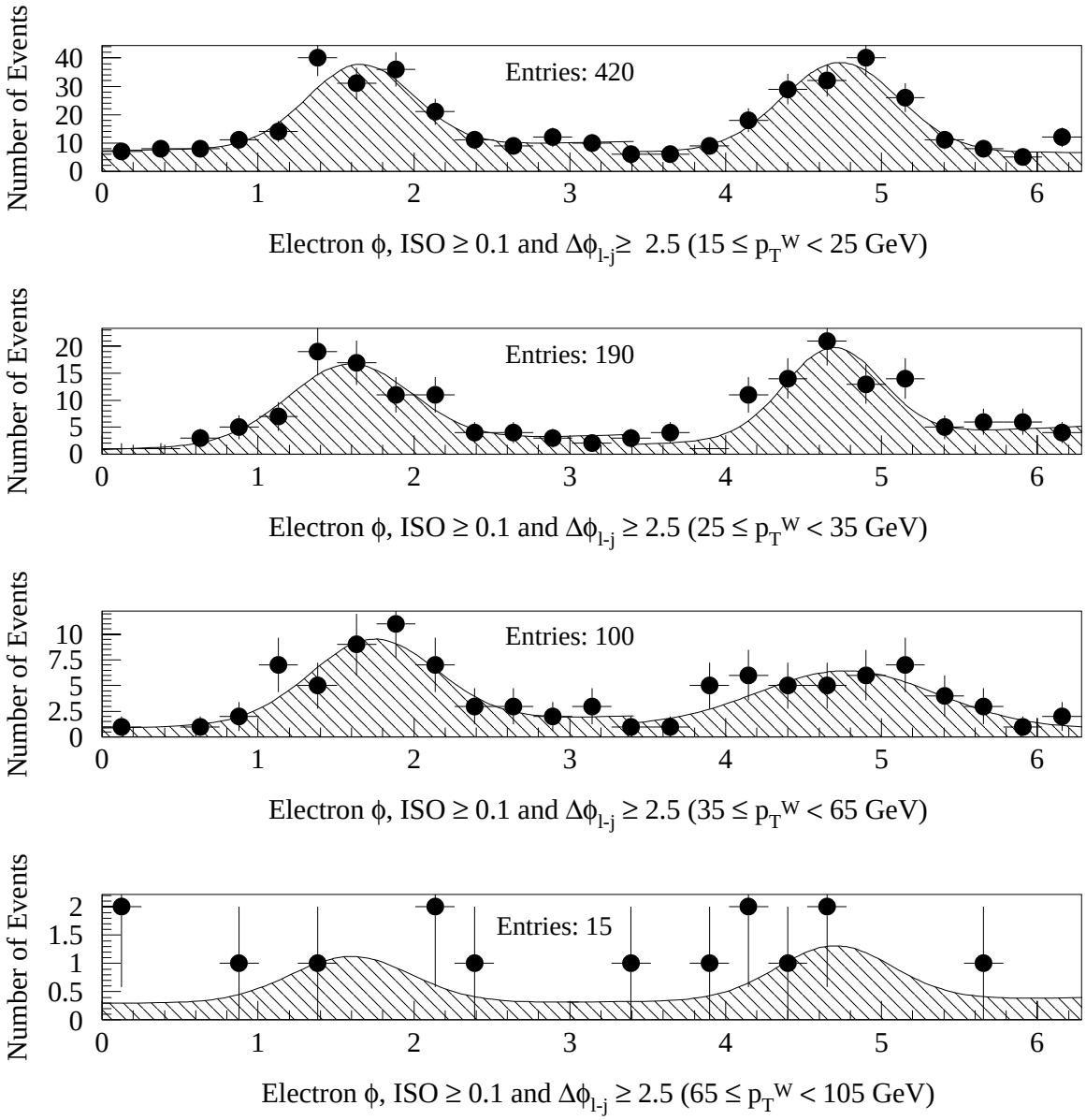

Figure 6.21 The ϕ distribution of electrons from W+jet events with $ISO \geq 0.1$ and $\Delta\phi_{l-j} \geq 2.5$ for the four p_T^W bins. These events are more than likely QCD events. We fit the distribution of the first p_T^W bin with two Gaussians on top of two straight lines. For the higher p_T^W bins we use the distribution of the total background, shown in Figure 6.20, normalized to the number of the QCD events in those bins. We assume that these distributions are going to be the same as the ones in the signal region ($ISO < 0.1$) after they are properly normalized.

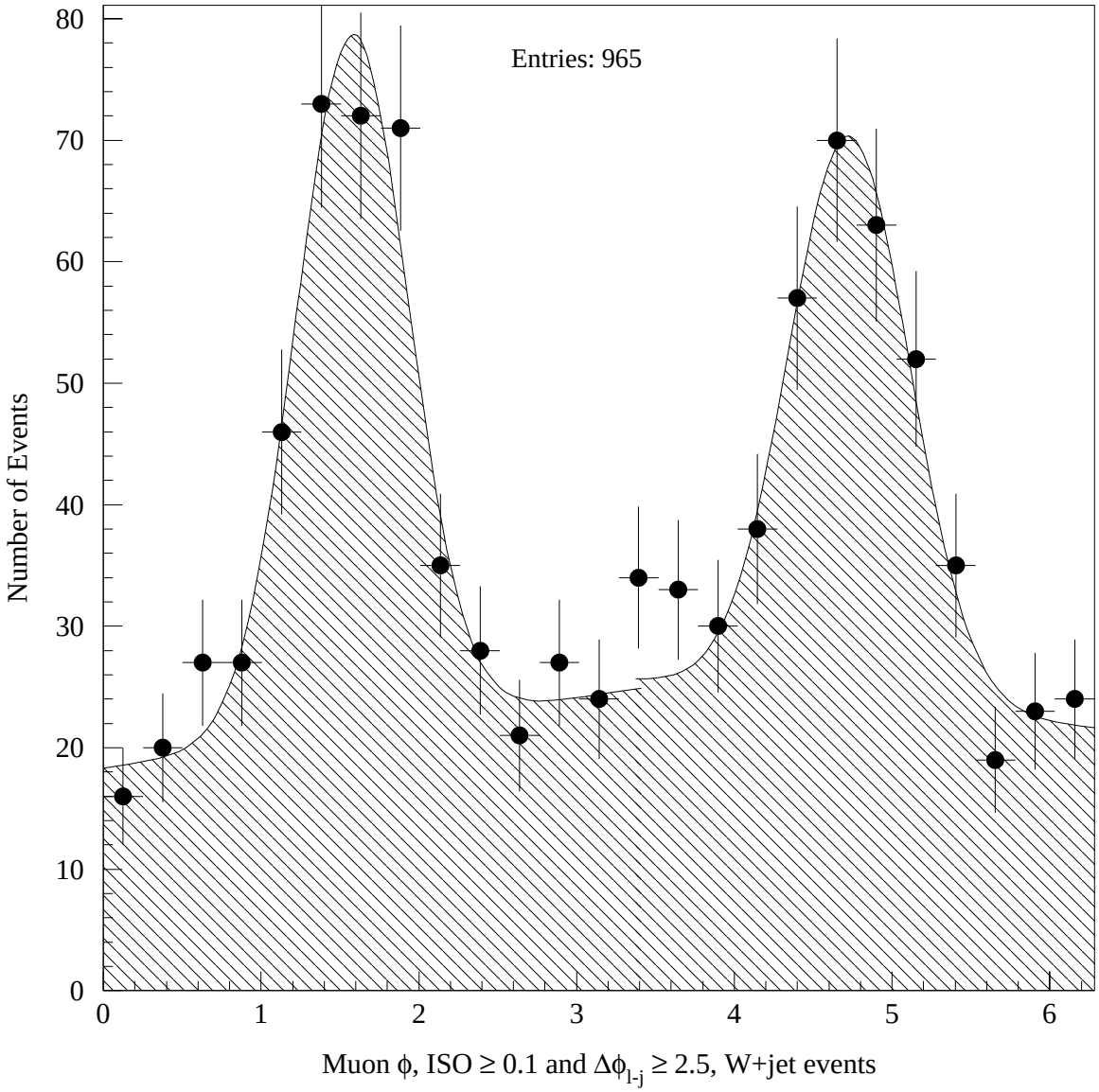

Figure 6.22 The ϕ distribution of muons from W+jet events with $ISO \geq 0.1$ and $\Delta\phi_{l-j} \geq 2.5$. These events are more than likely QCD events. We fit them with two Gaussians on top of two straight lines. We assume that this distribution is going to be the same as the one in the signal region ($ISO < 0.1$) after it is properly normalized.

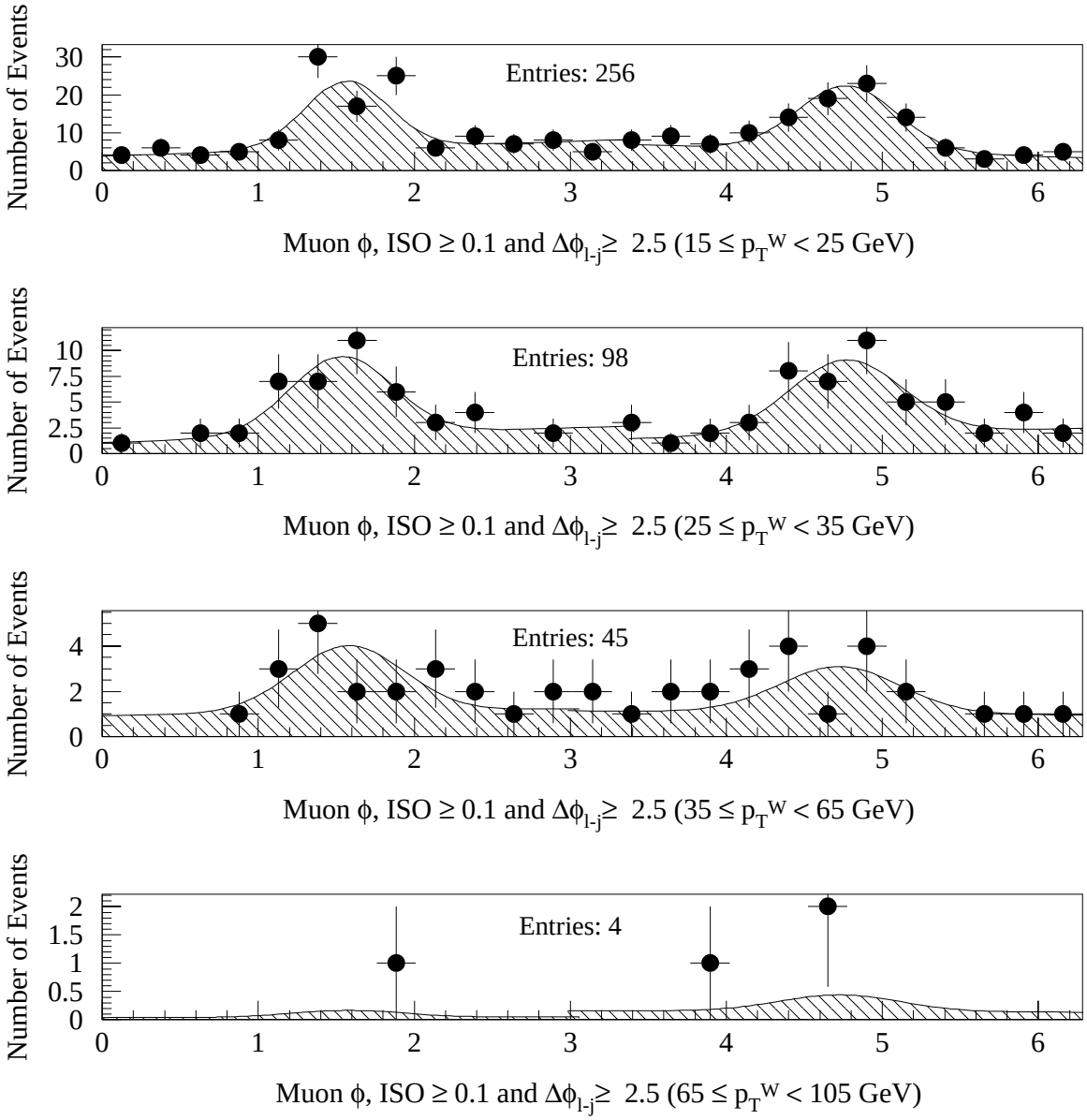

Figure 6.23 The ϕ distribution of muons from W+jet events with $ISO \geq 0.1$ and $\Delta\phi_{l-j} \geq 2.5$ for the four p_T^W bins. We fit the distribution of the first two p_T^W bins with two Gaussians on top of two straight lines. For the two highest p_T^W bins we use the distribution of the total background, shown in Figure , 6.22 normalized to the number of the QCD events in the respective bins. We assume that these distributions are going to be the same as the ones in the signal region ($ISO < 0.1$) after they are properly normalized.

FMC+backgrounds muon yields for inclusive W+jet			
p_T^W (GeV)	N_μ(FMC)	N_μ(Backgrounds)	N_μ(Total prediction)
15-25	2027 ± 102	298^{+47}_{-14}	2325^{+120}_{-112}
25-35	1384 ± 66	133^{+27}_{-6}	1517^{+77}_{-72}
35-65	1314 ± 67	120^{+9}_{-7}	1434^{+73}_{-73}
65-105	279 ± 14	20^{+1}_{-1}	299^{+15}_{-15}

Table 6.11 The muon total yields for inclusive W+jet up to order α_s^2. The PDF and Q^2 systematics have not been included yet.

Chapter 7

Measurement of the W Angular Coefficients

7.1 A Method for the Extraction of the W Angular Coefficients

It has been suggested that the experimental angular distributions of the charged lepton from the W decay in W+jet events should be divided by the Monte Carlo distributions obtained using isotropic W decays [19]. This division results in distributions similar to the theoretical ones shown in Figures 2.5 and 2.6, which makes the extraction of the angular coefficients is easier. The problem is that dividing the experimental data by the Monte Carlo distributions does not allow us to perform a model-independent unbiased measurement. We present a method that does not bias the experimental data with Monte Carlo data. Instead, our method uses the knowledge of the acceptances and efficiencies of the detector and their effect on the theoretical distributions. In this section we demonstrate the method for the ϕ analysis of FMC data. The azimuthal angle ϕ in the Collins-Soper frame is experimentally exactly measurable with negligible systematic error, so this method can be used in our experimental analysis.

Based on Equation (2.18), the assumption that only the A_2 and A_3 leading order coefficients are measurable with the ϕ analysis could be made, because the other coefficients are integrated out. In reality, the observed ϕ distribution would be given by Equation (2.18) if we had a 100% efficient detector with full acceptance and if there was no need for kinematic cuts to reduce the backgrounds. In any other case, the

acceptance and efficiency function $ae(p_T^W, \cos\theta, \phi)$ multiplies Equation (2.15) before it is integrated over $\cos\theta$ and, as a result, no angular coefficient is completely integrated out. In the actual experiment, what we measure is the number of events as a function of the transverse momentum of the W and the azimuthal angle of the charged lepton

$$N(p_T^W, \phi) = \int \frac{d\sigma}{dp_T^W d\phi d\cos\theta} ae(p_T^W, \cos\theta, \phi) d\cos\theta \int \mathcal{L} dt + N_{bg}(p_T^W, \phi), \quad (7.1)$$

where $\mathcal{L}$ is the instantaneous luminosity and $ae(p_T^W, \cos\theta, \phi)$ is the acceptances and efficiencies for the particular W transverse momentum and pixel in the $(\cos\theta, \phi)$ phase space, and $N_{bg}(p_T^W, \phi)$ is the background for the given ϕ bin and p_T^W.

If we combine Equations (7.1) and (2.15), the measured distribution becomes

$$N(p_T^W, \phi) = C'(f_{-1} + \sum_{i=0}^{7} A_i f_i) + N_{bg}(p_T^W, \phi), \quad (7.2)$$

where $C' = C \int \mathcal{L} dt$, and f_i are the fitting functions, which are integrals of the product of the explicit functions of $\cos\theta$ and ϕ and the $ae(\cos\theta, \phi)$ and are given by

$$f_i(p_T^W, \phi) = \int_{-1}^{1} \mathcal{G}_i(\theta, \phi) ae(p_T^W, \cos\theta, \phi) d\cos\theta, \quad (7.3)$$

$$i = -1, \ldots, 7 \quad (7.4)$$

where

$$\begin{aligned}
\mathcal{G}_{-1}(\theta, \phi) &= 1 + \cos^2\theta \\
\mathcal{G}_0(\theta, \phi) &= \frac{1}{2}(1 - 3\cos^2\theta) \\
\mathcal{G}_1(\theta, \phi) &= \sin 2\theta \cos\phi \\
\mathcal{G}_2(\theta, \phi) &= \frac{1}{2}\sin^2\theta \cos 2\phi \\
\mathcal{G}_3(\theta, \phi) &= \sin\theta \cos\phi \\
\mathcal{G}_4(\theta, \phi) &= \cos\theta \\
\mathcal{G}_5(\theta, \phi) &= \sin^2\theta \sin 2\phi \\
\mathcal{G}_6(\theta, \phi) &= \sin 2\theta \sin\phi
\end{aligned}$$

$$\mathcal{G}_7(\theta,\phi) \;=\; \sin\theta\sin\phi \tag{7.5}$$

The functions $f_i(p_T^W,\phi)$ can be calculated explicitly, if we know the acceptance and the efficiency of the detector. Because we multiply by $ae(p_T^W,\cos\theta,\phi)$ before integrating over $\cos\theta$, no f_i is exactly zero. Therefore, all coefficients are in principle measurable using the ϕ analysis, and not only A_2 and A_3, as Equation (2.18) suggests. In practice, the A_2 and A_3 are measurable with a greater statistical significance, because the $f_{i\neq 2,3}$ are too small or because the coefficients themselves are small. As it was shown in Chapter 2, the angular coefficients A_1, A_5, A_6 and A_7 are very small compared to the rest of the coefficients. For the precision of CDF Run I data, they can be ignored. In the following we only consider the leading order angular coefficients A_0–A_4 and the leading order functions f_{-1}–f_4

For perfect acceptance and no kinematic cuts ($ae=1$), the only surviving leading order f_i functions would be f_{-1}, f_2, f_3 and they would be equal to $\frac{8}{3}$, $\frac{2}{3}\cos 2\phi$, and $\frac{\pi}{2}\cos\phi$, in accordance to Equation (2.18). They are independent of the transverse momentum of the W, because the p_T^W dependence enters only through the ae. Figure 7.1 shows the leading order f_i functions (f_{-1}–f_4) for perfect acceptance and no experimental cuts applied on the data.

If we use the acceptances and efficiencies of the detector, and apply the experimental cuts, the f_i functions become distorted. The degree of distortion increases with the transverse momentum of the W. Figures 7.2 and 7.3 show the f_i functions for the electron and muon acceptances and efficiencies respectively and for the four p_T^W bins. As discussed in Chapter 5, the $ae(\cos\theta,\phi)$ functions depend on the p_T^W, so do the f_i functions. Again, the f_{-1}, f_2 and f_3 functions are the predominant ones. We use Simpson integration for the calculation of the f_i given by Equation (7.4). We use 100 point integration and for each value of $\cos\theta$ and ϕ we get the acceptance and efficiency given by Figures 5.8 and 5.9. In order to have smoother integrals, the value of the acceptance which corresponds to a pixel of the 50×50 scattered plot of Figures 5.8 and 5.9, is average between that pixel and its first neighbors.

The azimuthal angle distributions of the charged lepton are invariant under large variations of the $A_{i\neq 2,3}$ coefficients. Figures 7.4 to 7.8 show how the expected muon

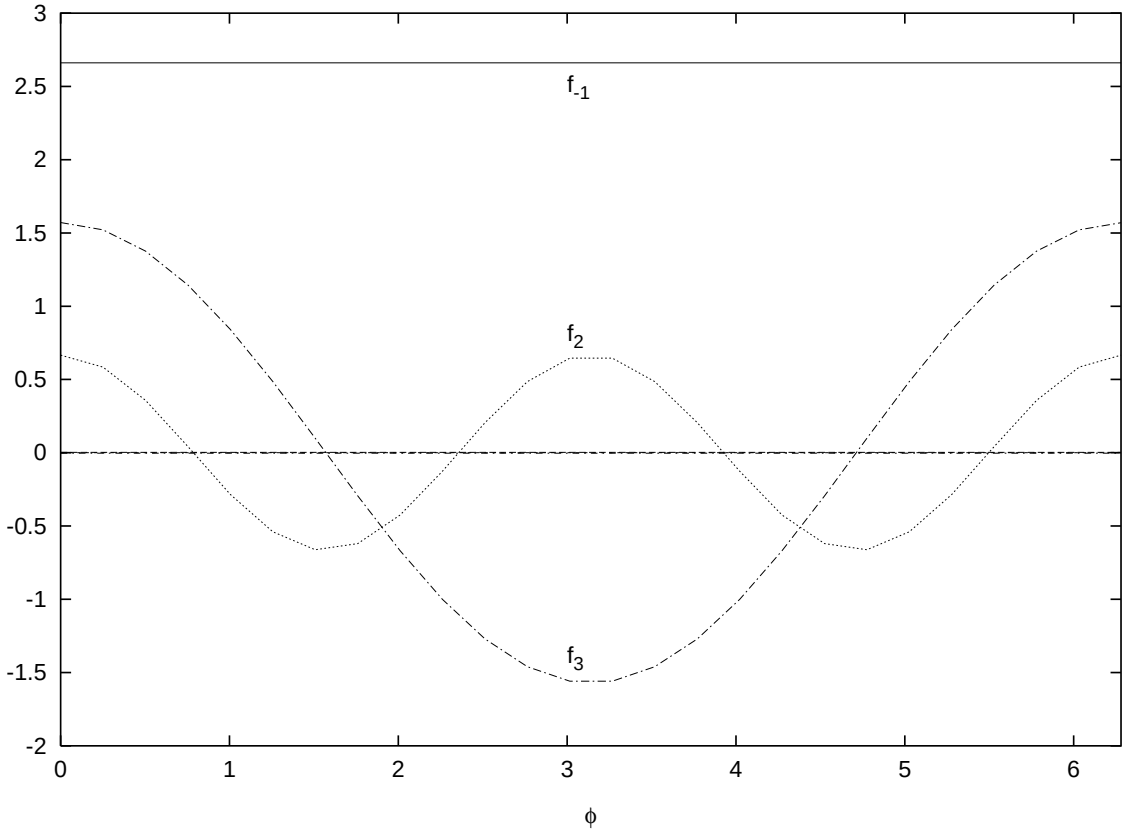

Figure 7.1 Functions f_i for perfect acceptance and efficiency.

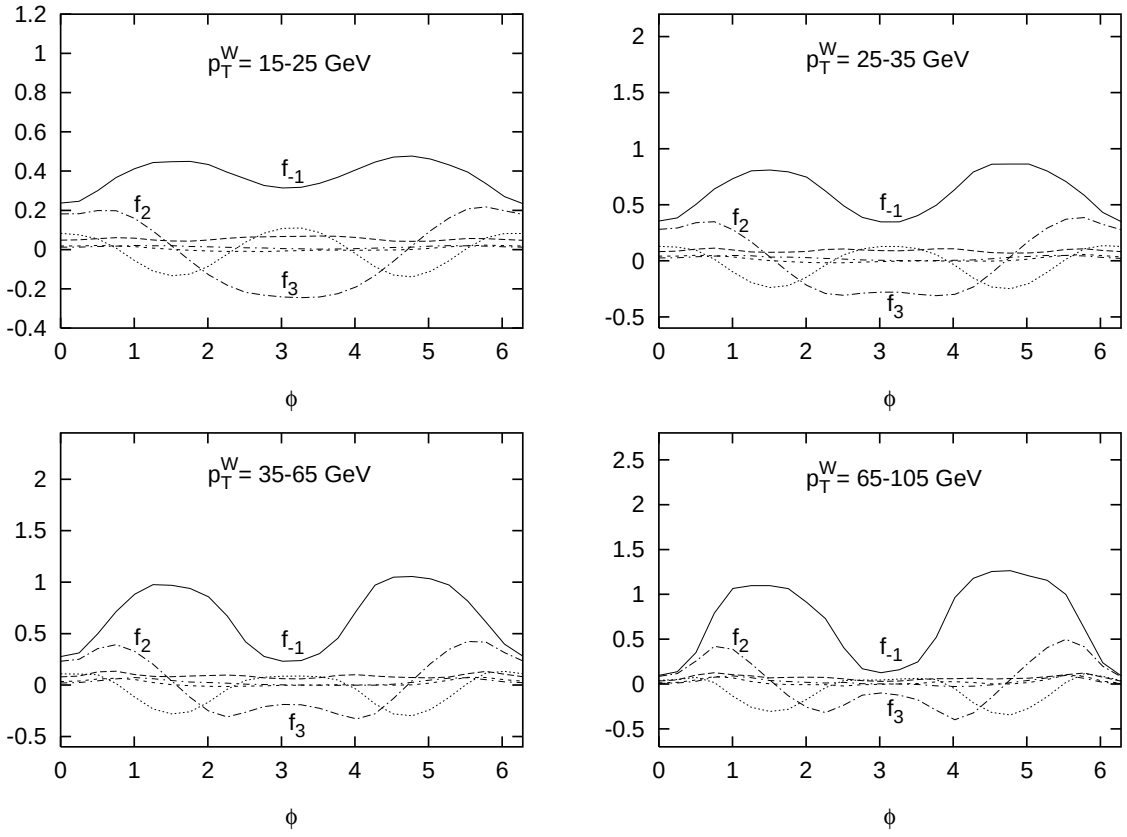

Figure 7.2 Functions f_i for the CDF electron acceptance and efficiency.

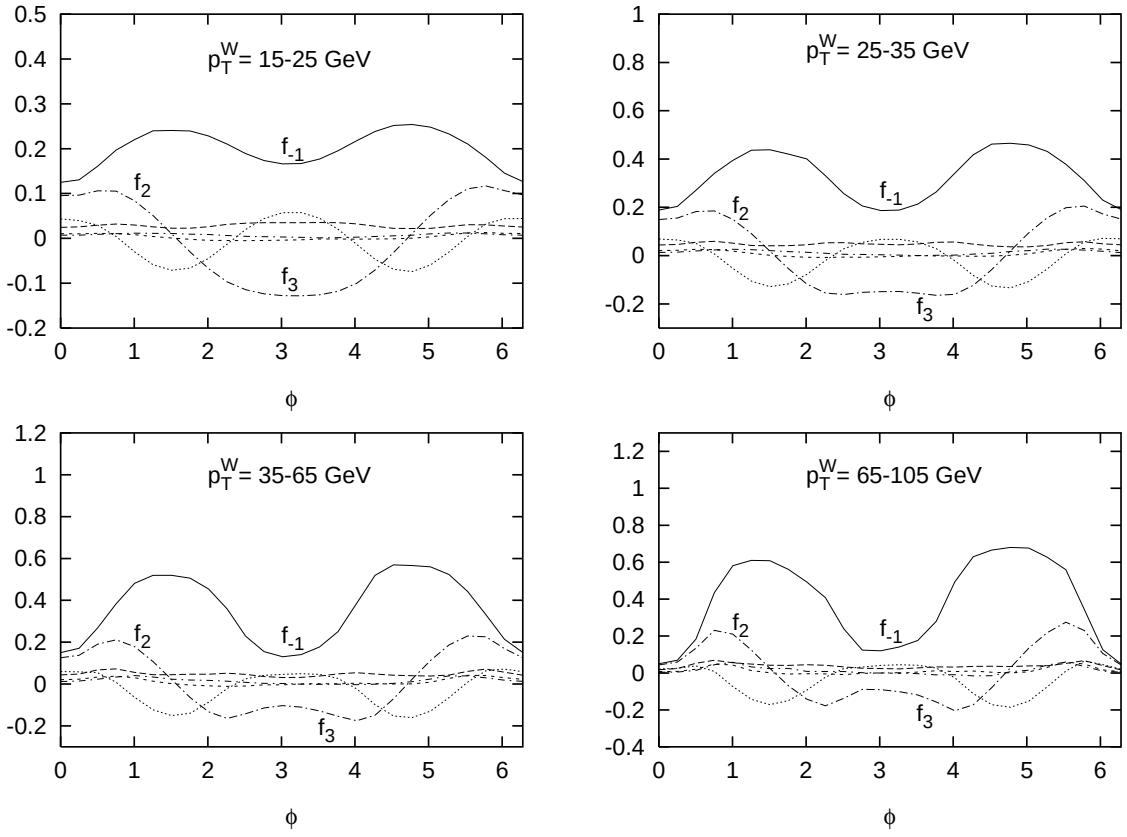

Figure 7.3 Functions f_i for the CDF muon acceptance and efficiency.

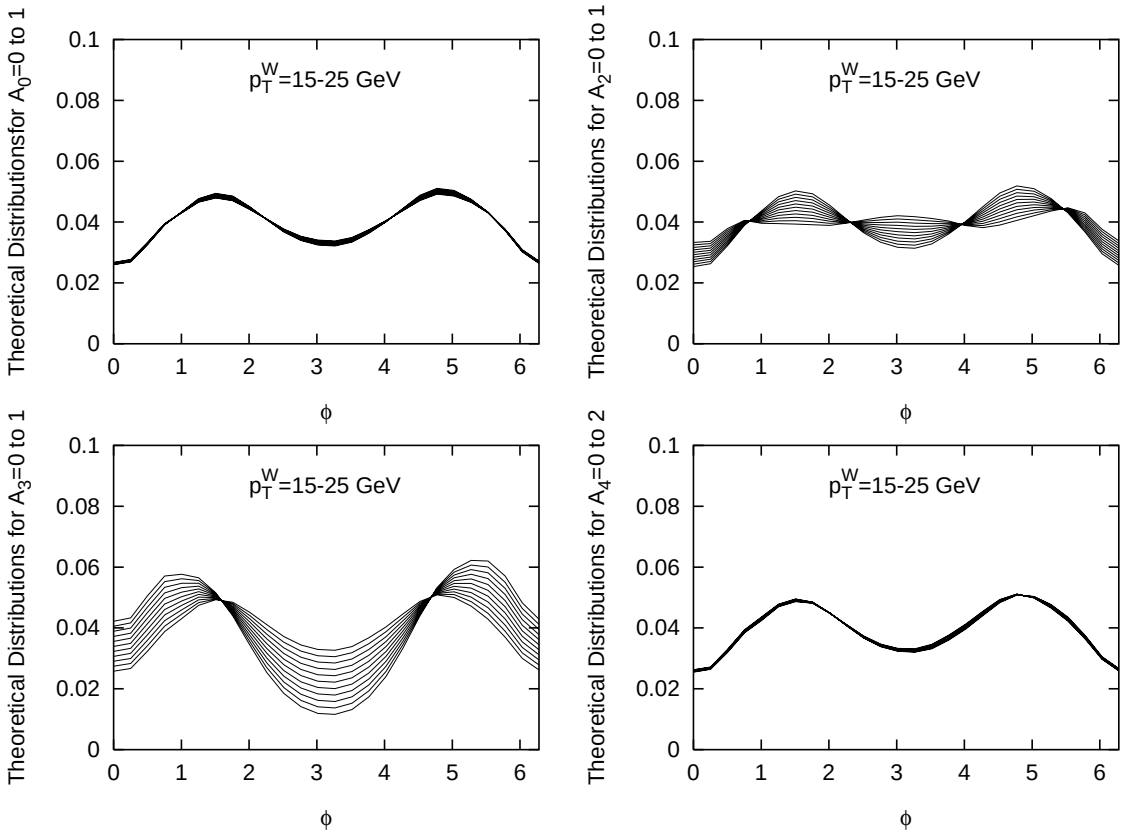

Figure 7.4 Theoretical azimuthal angle distributions for muon W+jet events, as we vary $A_{0,2,3,4}$, if we take the detector acceptance and efficiency into account, for transverse momentum of the W between 15 and 25 GeV. The backgrounds have been added and the distributions are normalized.

distributions (according to Equation (7.2)) are modified as we vary the A_i, one coefficient at a time (the electron distributions are almost identical). We vary A_0, A_1, A_2 and A_3 from 0 to 1 with a step of 0.1 and A_4 from 0 to 2 with a step of 0.2. We realize that only A_2 and A_3 affect strongly the azimuthal distributions, so only these are measurable with the ϕ analysis. Large variations of A_0 and A_4 result into small effects in the ϕ-distributions, so the error bars of the measurement of A_0 and A_4 are going to be very large, thus these coefficients cannot be measured in a statistically significant manner. The A_1 coefficient is also very small to be even considered.

To demonstrate the consistency of our method of extracting the A_2 and A_3 angular coefficients, we analyze the FMC angular distributions of Figures 5.2 and 5.3. The plots are normalized to the FMC expected experimental yields. We keep the $A_{i\neq 2, i\neq 3}$

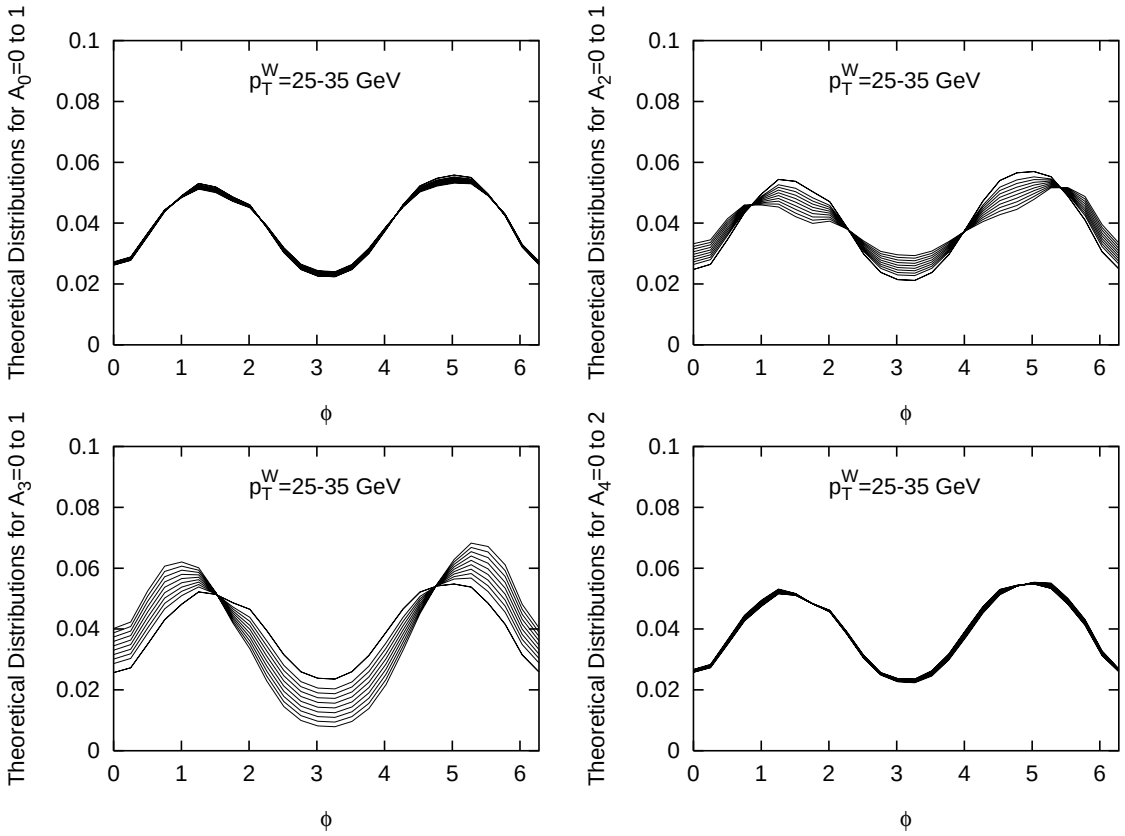

Figure 7.5 Theoretical azimuthal angle distributions for muon W+jet events, as we vary $A_{0,2,3,4}$, if we take the detector acceptance and efficiency into account, for transverse momentum of the W between 25 and 35 GeV. The backgrounds have been added and the distributions are normalized.

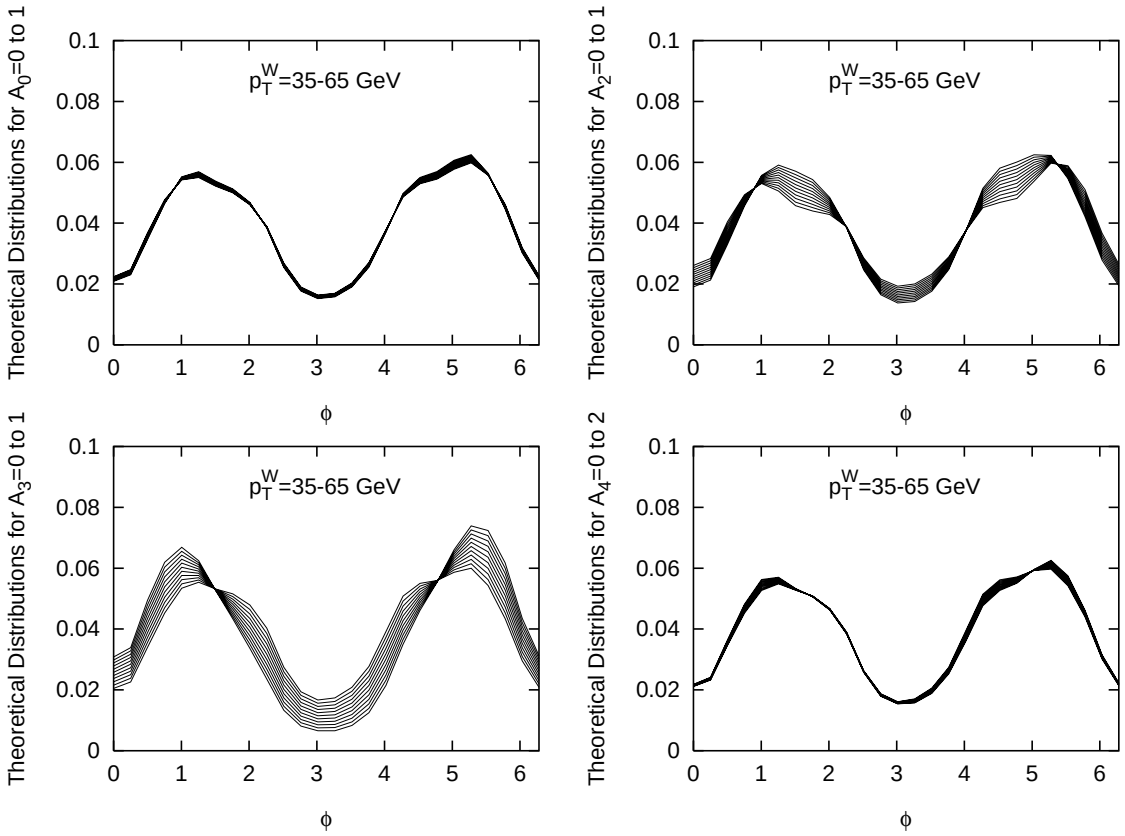

Figure 7.6 Theoretical azimuthal angle distributions for muon W+jet events, as we vary $A_{0,2,3,4}$, if we take the detector acceptance and efficiency into account, for transverse momentum of the W between 35 and 65 GeV. The backgrounds have been added and the distributions are normalized.

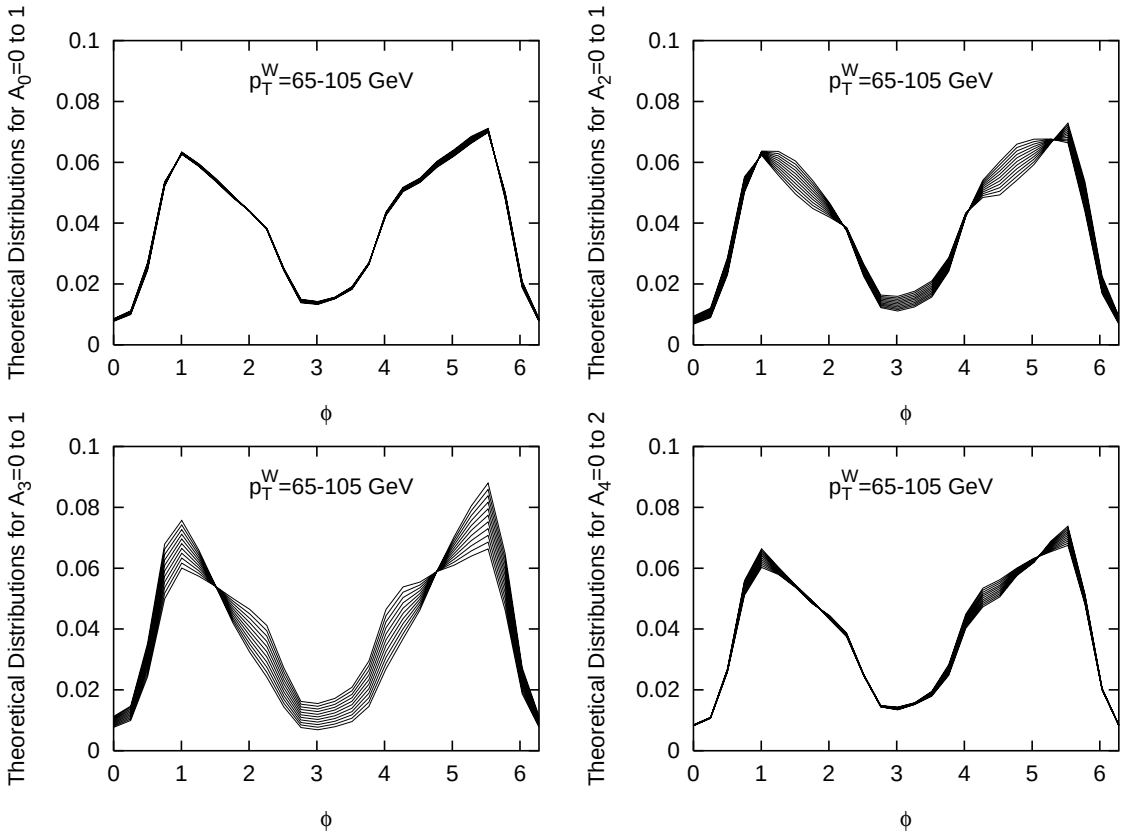

Figure 7.7 Theoretical azimuthal angle distributions for muon W+jet events, as we vary $A_{0,2,3,4}$, if we take the detector acceptance and efficiency into account, for transverse momentum of the W between 65 and 105 GeV. The backgrounds have been added and the distributions are normalized.

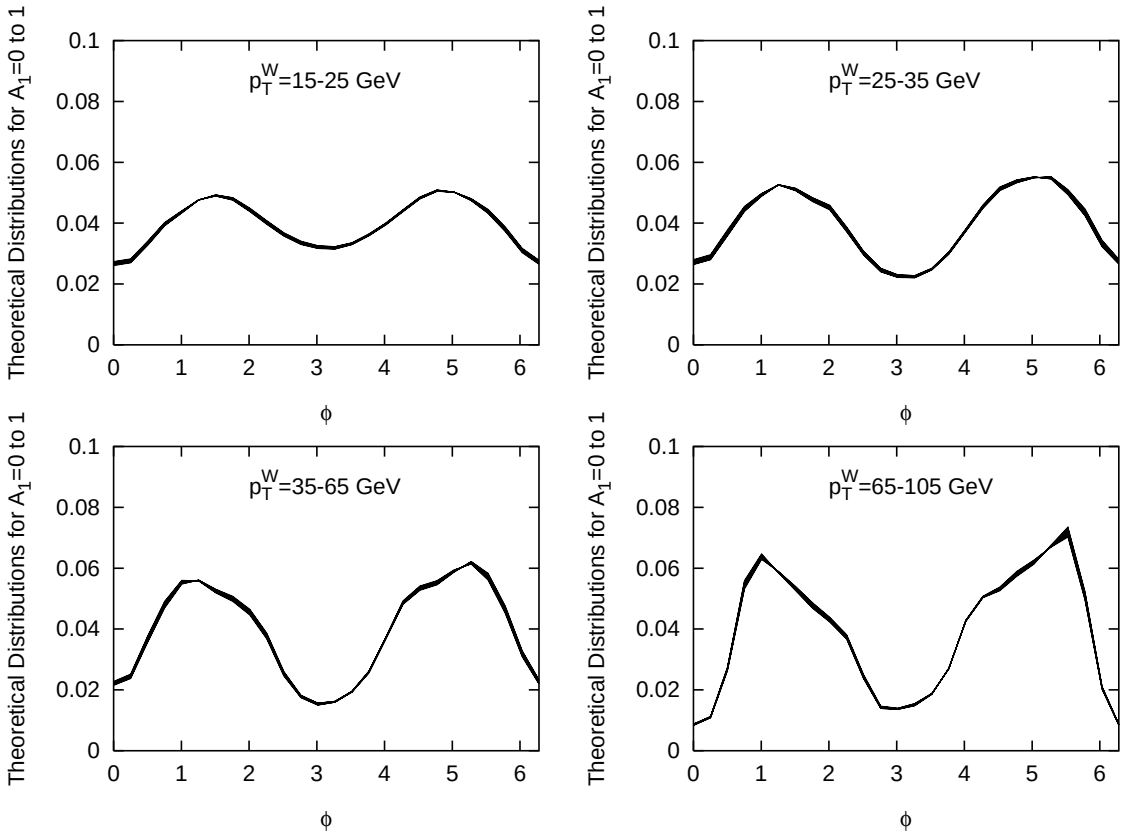

Figure 7.8 Theoretical azimuthal angle distributions for muon W+jet events, as we vary A_1, if we take the detector acceptance and efficiency into account, for the four p_T^W bins. The backgrounds have been added and the distributions are normalized.

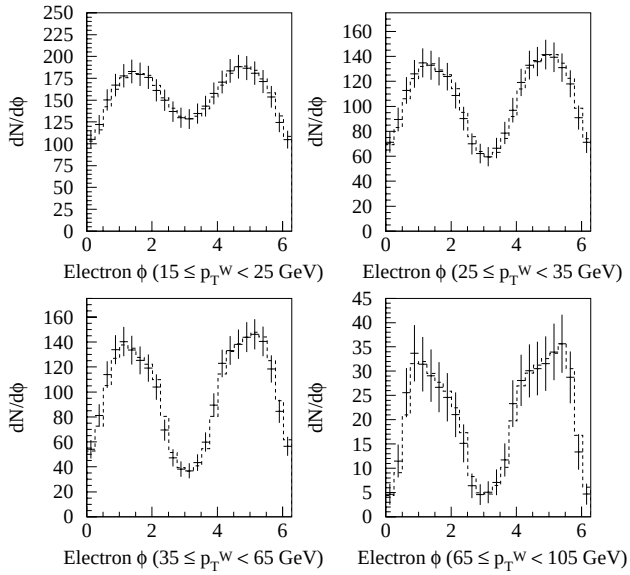

Figure 7.9 The FMC ϕ distribution (size of sample and error bars correspond to expected yields at the Run I of the Tevatron at $\sqrt{s} = 1.8$ TeV) and the result of the fit (dashed line) using the theoretical prediction of Equation (7.2) and varying A_2 and A_3 simultaneously. The backgrounds are ignored, only W events are considered.

coefficients frozen at their Standard Model values we determined in Chapter 2 and we fit the distributions to the f_i varying A_2 and A_3 simultaneously. We do not include the backgrounds in the theoretical prediction for consistency, because the FMC distribution we use does not include the background. The result of the fit can be seen in Figure 7.9 for the electrons. The extracted coefficients for the electrons and muons are presented in Figure 7.10. We conclude that the measured angular coefficients are close to the theoretical values we extracted in Chapter 2, using the DYRAD generator data. Since the FMC data are DYRAD data passed through the CDF detector simulator, the fact that we got values close to the expected ones verifies that the method is self-consistent and could be used for an experimental measurement.

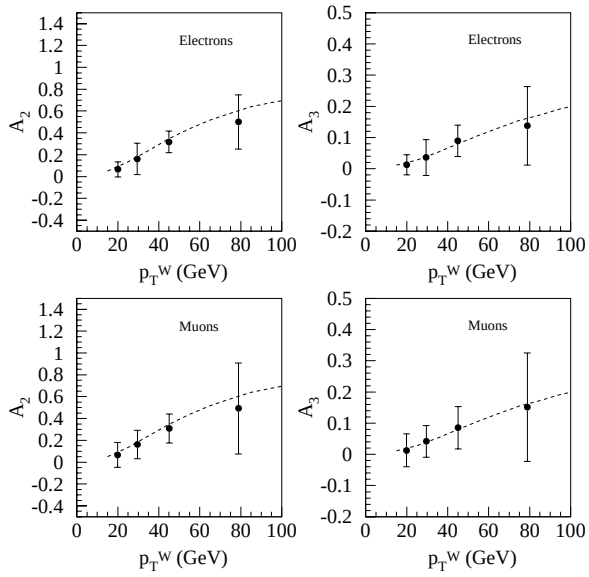

Figure 7.10 The extracted angular coefficients, using the Monte Carlo data of Figure 7.9 and fitting using the f_i functions. The angular coefficients that do not affect the shape of the ϕ distribution are fixed at their Standard Model values.

7.2 Measurement of the W Angular Coefficients

The analysis of real CDF data introduces some fundamental problems. For each W+jet event in our data sample, we need to boost to the W rest frame to calculate the polar and azimuthal angles of the charged lepton. The longitudinal momentum of the W (p_z^W) is not known, because the longitudinal momentum of the neutrino is not measurable. This does not allow us to fully reconstruct the W in three-dimensional space and does not permit us to boost to its rest frame. To attack this problem, we use the mass of the W to constrain the longitudinal momentum of the neutrino.

For a particular event, the longitudinal momentum of the neutrino is constrained by the mass of the W, according to the Equation

$$p_z^\nu = \frac{1}{(2p_T^l)^2}\left(Ap_z^l \pm E^l\sqrt{A^2 - 4(p_T^l)^2(p_T^\nu)^2}\right) \tag{7.6}$$

where

$$A^2 = M_W^2 + (p_T^W)^2 - (p_T^l)^2 - (p_T^\nu)^2, \tag{7.7}$$

E^l is the energy of the charged lepton, p_T^l is its transverse momentum, p_T^ν is the neutrino transverse momentum and and p_T^W is the transverse momentum of the W. This Equation is unique for every event, since the kinematics of the lepton and neutrino as well as the mass of the W contribute to the shape of the curve. If the mass of the W was known on an event by event basis, there would be a two-fold ambiguity in the value of the p_z^ν of the neutrino in the lab frame. Because the W has a finite width given by the Breit-Wigner distribution $BW(M)$, we practically have two distributions of possible values of the p_z of the neutrino $BW(M(p_z^\nu))$, where $M(p_z^\nu)$ is the mass of the W as a function of the neutrino longitudinal momentum for the particular kinematics of the event.

The choice of one of the two neutrino longitudinal momentum does not affect the ϕ analysis, since both solutions result in the same charged lepton ϕ (and opposite values of $\cos\theta$) in the CS frame. Only the choice of the W mass is of interest. It is made based on the DYRAD M_W vs M_T^W scattered plot constructed with DYRAD events, as discussed in Appendix B. For a specific M_T^W we get a probability distribution of W masses and we select one for each event, randomly, based on that distribution. This complicated method was devised to better reconstruct the $|\cos(\theta)|$. In our analysis of the ϕ angle, the azimuthal angle is not affected by the choice of mass, so the answer is almost the same even if we choose a mass based on the Breit-Wigner distribution and the requirement that the mass is greater than the transverse mass.

After getting a ϕ for every event, we proceed to analyze our sample, using the ϕ analysis. We have verified that the FMC data fitted with the linear combination of f_i give us the expected angular coefficients. The expected experimental measurements of the ϕ distributions can be seen in Figure 7.11 for the electrons and Figure 7.12 for the muons (we used the f_i and the SM values of the A_i). To produce this plots we used Equation (7.2) and the A_i extracted from the analysis of DYRAD events with the method of moments. We used the background ϕ shapes given by Figures 6.2, 6.8, 6.21 for electrons and 6.4, 6.10, 6.23 for muons, normalized to the yields of Tables 6.8 and 6.9 respectively. The theoretical signal is normalized to the FMC yields of Tables 6.10 and 6.11 and the whole prediction $N(p_T^W, \phi)$ is normalized to one after the inclusion of the backgrounds.

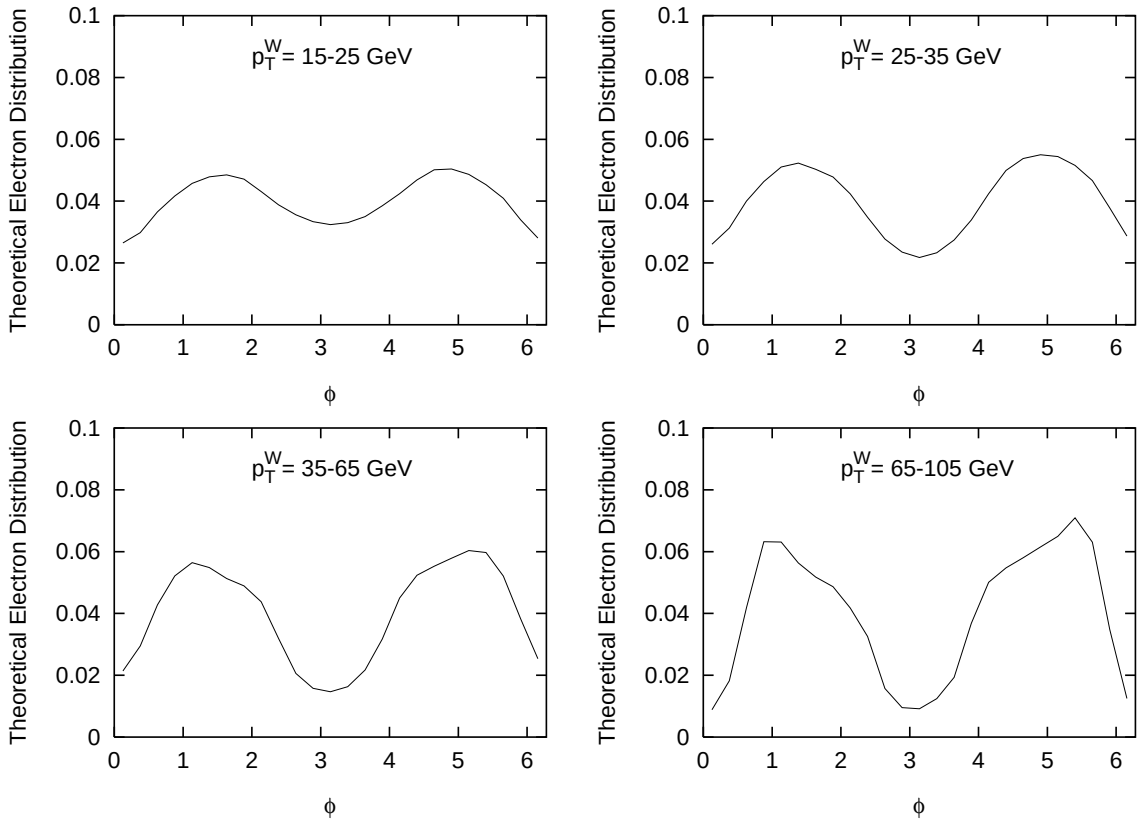

Figure 7.11 Theoretical prediction for the normalized ϕ distributions for the electron W+jet events, taking into account the CDF detector acceptances and efficiencies. The functions f_i and the SM values of A_i have been used and the backgrounds have been included.

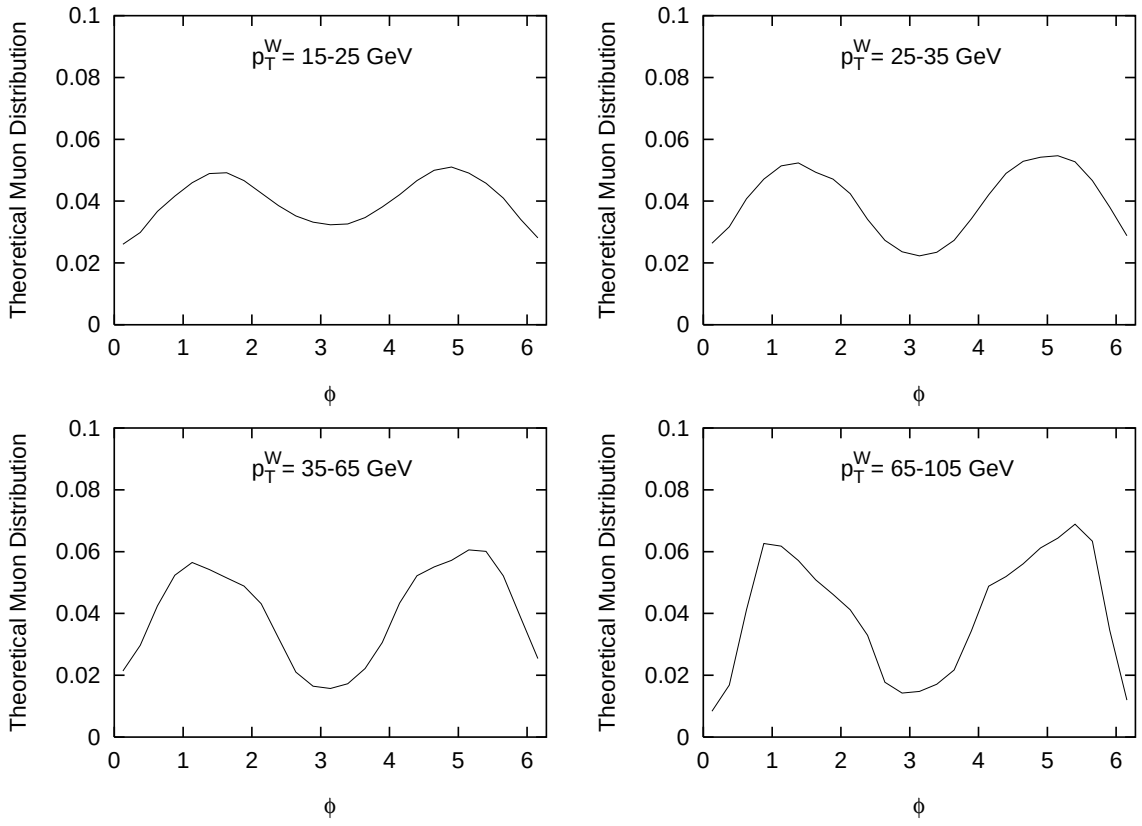

Figure 7.12 Theoretical prediction for the ϕ normalized distributions for the muon W+jet events, taking into account the CDF detector acceptances and efficiencies. The functions f_i and the SM values of A_i have been used and the backgrounds have been included.

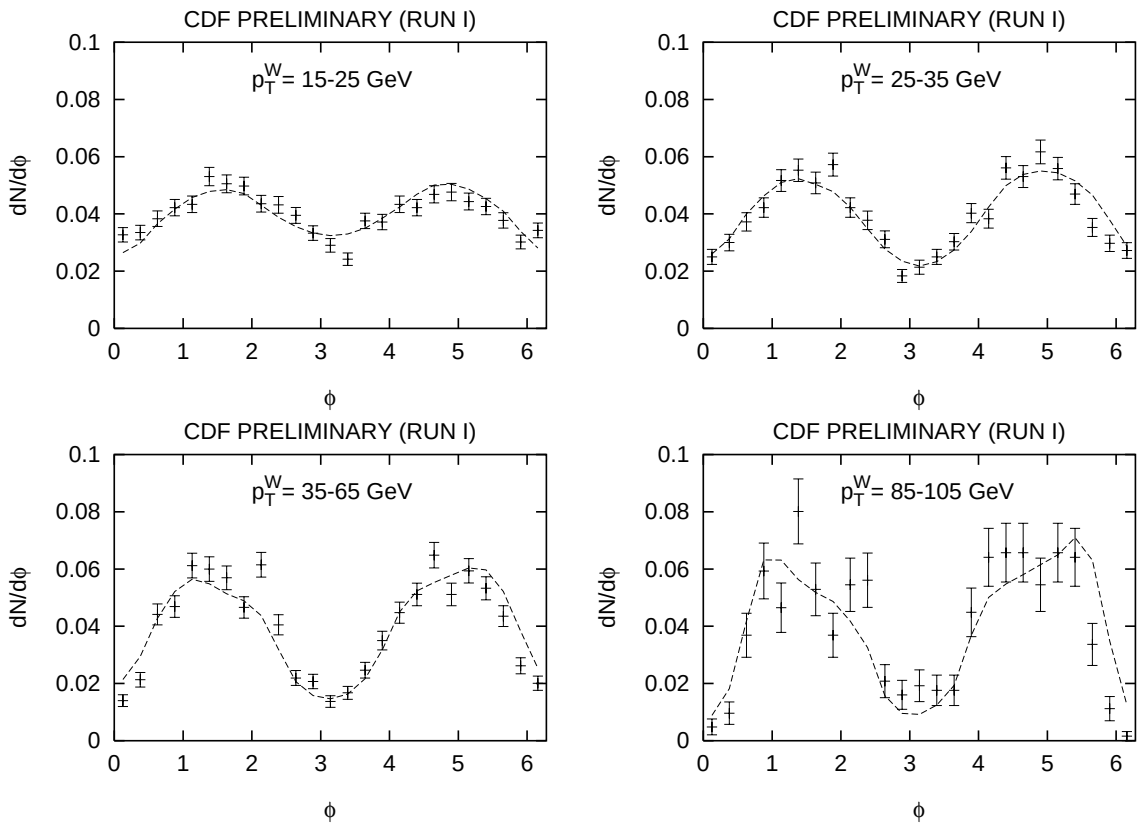

Figure 7.13 The ϕ distributions for the electron data (points) and the SM (line) for the four bins of W boson p_T^W. The error bars are only statistical. Both data and SM are normalized to one.

Figure 7.13 shows the ϕ distribution of the CDF electrons in W+jet events in the CS frame for the four p_T^W bins. Figure 7.14 shows the ϕ distribution of the CDF muons. The dashed distributions are the expectation from the SM for the CDF detector (using Equation (7.2)) and the points correspond to the CDF data (the error bars are the statistical ones). Both theoretical and experimental plots are normalized to one. These results, show that there is agreement between the CDF distributions and the expected ones according to the SM. The effects of W polarization and the QCD processes in the W angular distribution is close to the one predicted by the Standard Model.

Our next natural step is to try to extract a measurement of A_2 and A_3 using the fitting method. We use MINUIT and vary both coefficients freely. Since the

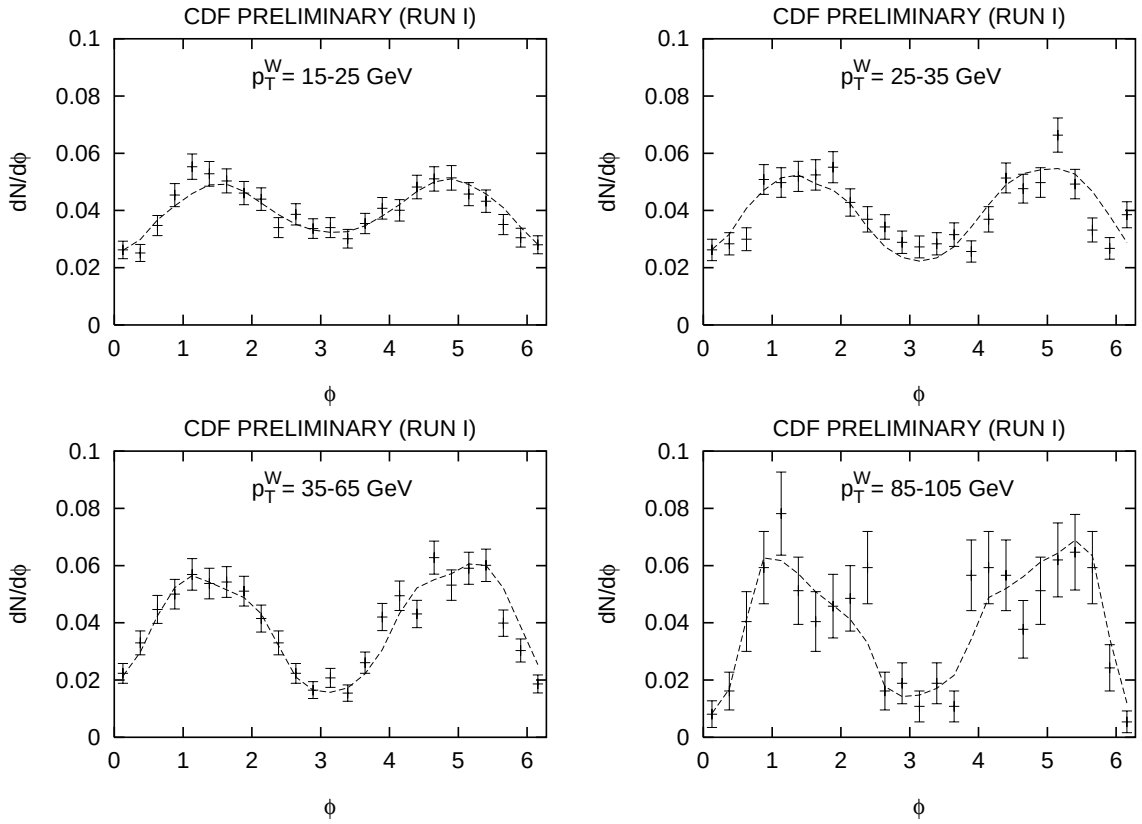

Figure 7.14 The ϕ distributions for the muon data (points) and the MC (line) for the four bins of W boson p_T^W. The error bars are only statistical. Both data and SM are normalized to one.

f_i functions we use for fitting are not linearly independent, we cannot fit having all parameters free. For this reason we keep the A_0, A_4 coefficients constant and vary the A_2, A_3 coefficients, which are the parameters which mainly affect the ϕ distribution. After performing the χ^2 fit, we fix A_2 and A_3 at the measured values, and we fit again varying only A_0 and A_4 this time. We expect large error bars for the A_0 and A_4, since they do not seriously affect the ϕ distribution and big variations in their values slightly alters the ϕ angular distribution. We always keep A_1, A_5, A_6, and A_7 fixed to the SM values, since the theoretical prediction for these coefficient is very close to zero and the variation for the first 100 GeV of p_T^W is negligible and much smaller than our experimental precision.

We perform our fit in the negative-x $x-y$ half-plane ($\pi/2 \leq \phi \leq 3\pi/2$), because of the following considerations:

- If the jet perfectly balances the W, its momentum will be placed on the z-x plane and actually on the positive x axis. In reality, the jet lies close to that position. This can be seen in Figure 7.15 for the electron and muon data. The jet's ϕ in the Collins-Soper frame is always less than $\pi/2$ or greater of $3\pi/2$ (Figure 7.16). Thus, there is a correlation between the distance ΔR between the jet and the lepton in the $\phi - \eta$ space, as can be seen in Figure 7.16 . The situation is similar for the extra jets (Figures 7.17 and 7.18), which are not modeled in our Monte Carlo and may cause an extra problem in the region. Because we have a lepton-jet separation requirement and since our sample is biased in this respect (there is a default isolation requirement between the lepton and all jets), we are more accurate in the measurement of small and sensitive variables, such as the A_3, if we completely avoid the positive-x $x-y$ half-plane.

- The A_3 variable multiplies the f_3 function to contribute to the total ϕ distribution of the charged lepton. The term $A_3 f_3(\phi)$ is the smallest measurable term (A_1 is practically zero so are the next-to-leading order ones). Its measurement is more realistic in the region where the rest of the terms (and mainly the $A_4 f_4(\phi)$, which is the biggest in most of the ϕ range) are smaller. Figure 7.19 shows the ratio $A_3 f_3(\phi)$ / $A_4 f_4(\phi)$ for all ϕ bins. It is obvious that the term $A_3 f_3(\phi)$ be-

comes significantly larger than the $A_4 f_4(\phi)$ one in the region between $\pi/2$ and $3\pi/2$.

Noting that there is a bias if we try to fit the ϕ distribution over the whole x-y plane, we fit it in the negative-x $x - y$ half-plane. We normalize the theory to data from $\pi/2$ to $3\pi/2$ before we start the fitting procedure.

The result of the fits are shown in Figure 7.20 for the electrons and Figure 7.21 for the muons. The MC prediction along with the ϕ distribution corresponding to the parameters extracted with the fit are presented. Both the Standard Model prediction and the fit is normalized to the data from $\pi/2$ to $3\pi/2$. In Figures 7.22 and 7.23 we compare the ϕ distributions that correspond to the extracted values of the A_2 and A_3 angular coefficients to the Standard Model distribution and CDF data, for the electrons and muons respectively. In these plots, the data and the theory (for the extracted and the Standard Model A_2 and A_3) are normalized to unity, from 0 to 2π.

Our measurement of the angular coefficients for the electrons can be seen in Figure 7.24, while the result for muons in Figure 7.25. The centers of the bins are determined using the average value of p_T^W for the range of our four p_T^W bins. The electrons and muons agree with the SM prediction and the measurement is self-consistent and monotonic. We emphasize that the SM prediction is only up to order α_s^2 in QCD. Note that the systematic uncertainties have not been presented yet. The statistical uncertainties slightly depend on the initial MINUIT step. For this reason, we run the χ^2 minimization routine for 10 different values of the initial step and we choose the highest value of the parabolic error to be our acceptable statistical uncertainty for each bin. The statistical uncertainties for A_0 and A_4 are very large, as we expected, making the measurement of these coefficients unrealistic. Figure 7.26 shows the electron and muon results overimposed.

Now, we proceed to combine the electron and muon measurements since there is no theoretical reason for the angular coefficients to be different for the two leptons. We combine the electron and muon results treating them as the measurements of two separate experiments. For the combination we use the statistical uncertainties for the electron and muon measurements for each bin. If A_e is the electron measurement, A_μ is the muon measurement, and σ_e, σ_μ are the respective statistical uncertainties,

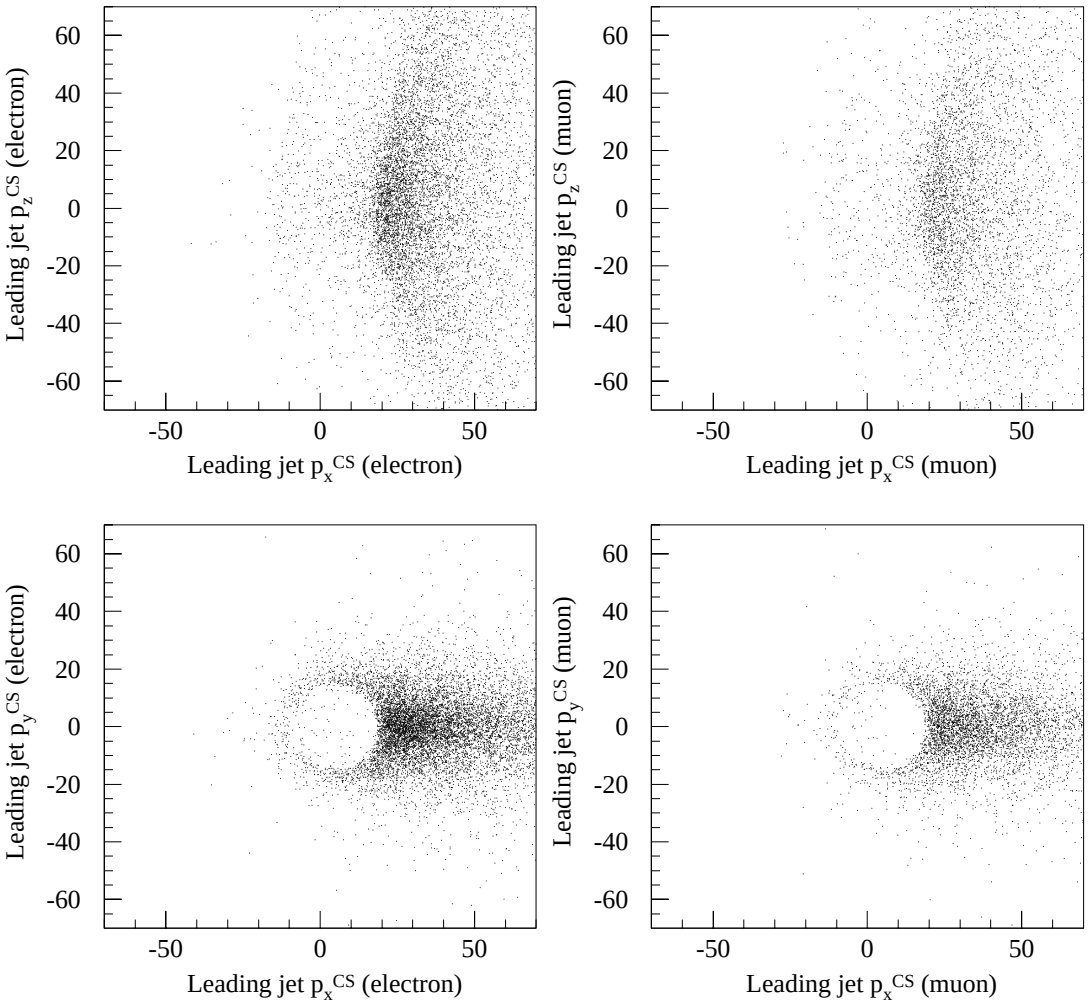

Figure 7.15 The p_z versus p_x and p_y versus p_x for the leading jet in the Collins-Soper frame, for electron (left) and muon (right) events.

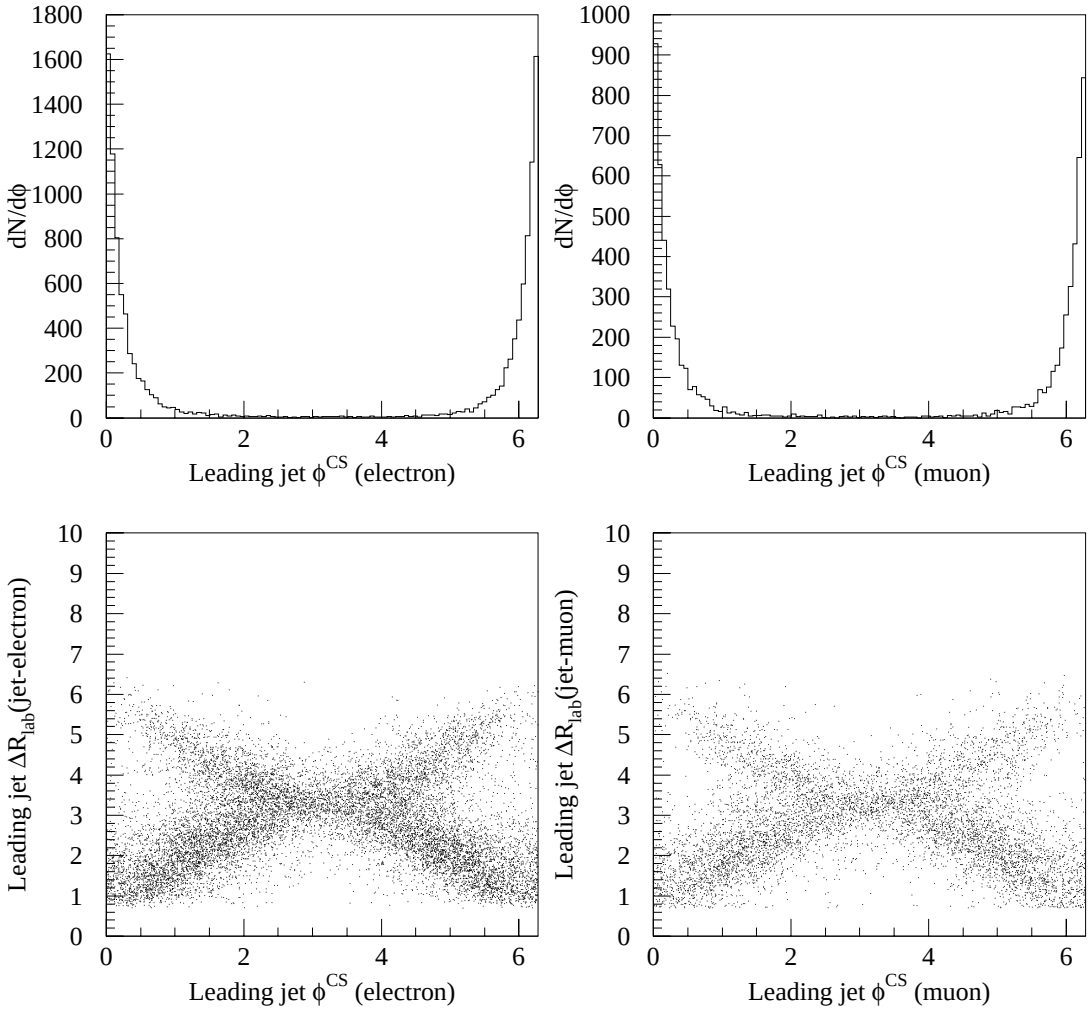

Figure 7.16 The ϕ of the leading jet in the Collins-Soper frame and the ΔR between the jet and the lepton in the lab frame, for electron (left) and muon (right) events.

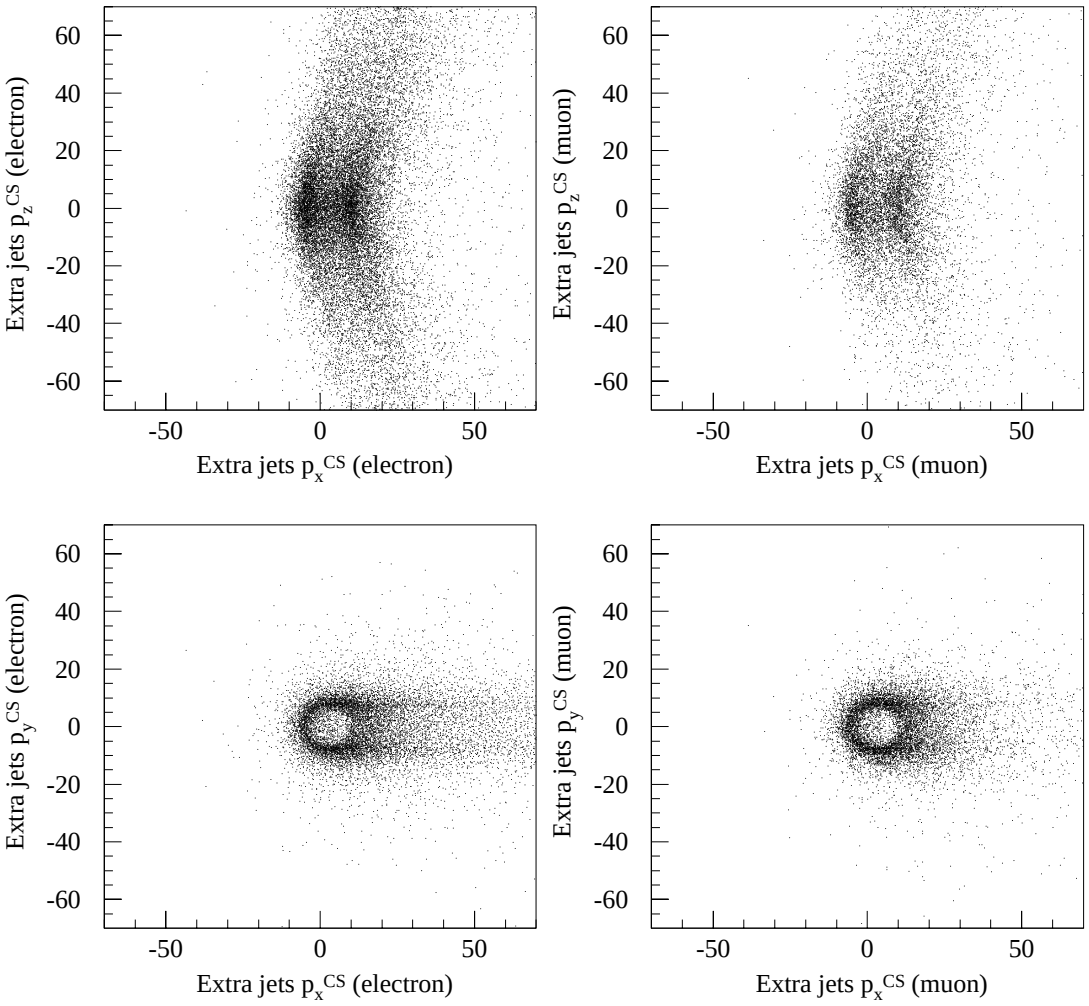

Figure 7.17 The p_z versus p_x and p_y versus p_x for the extra jets in the Collins-Soper frame, for electron (left) and muon (right) events.

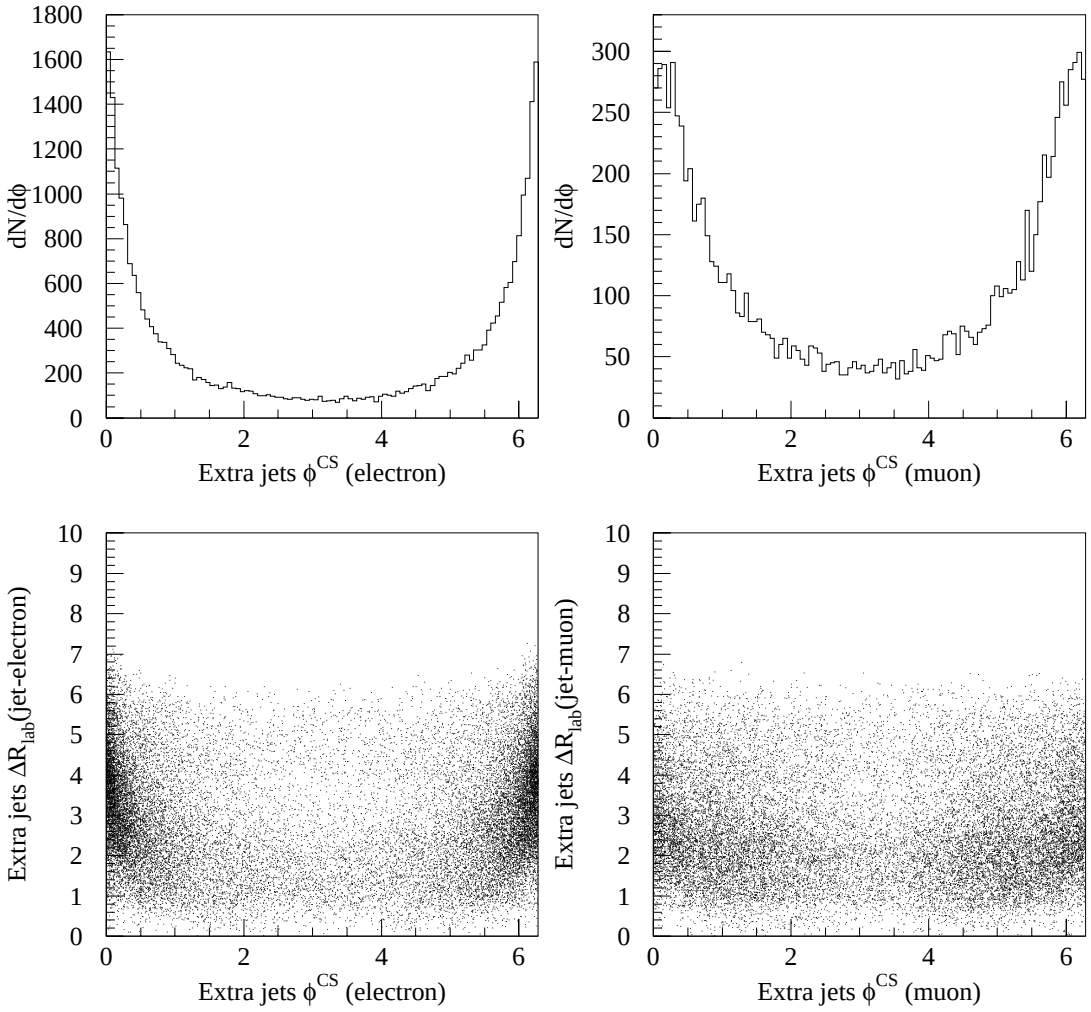

Figure 7.18 The ϕ of the extra jets in the Collins-Soper frame and the ΔR between the jets and the lepton in the lab frame, for electron (left) and muon (right) events.

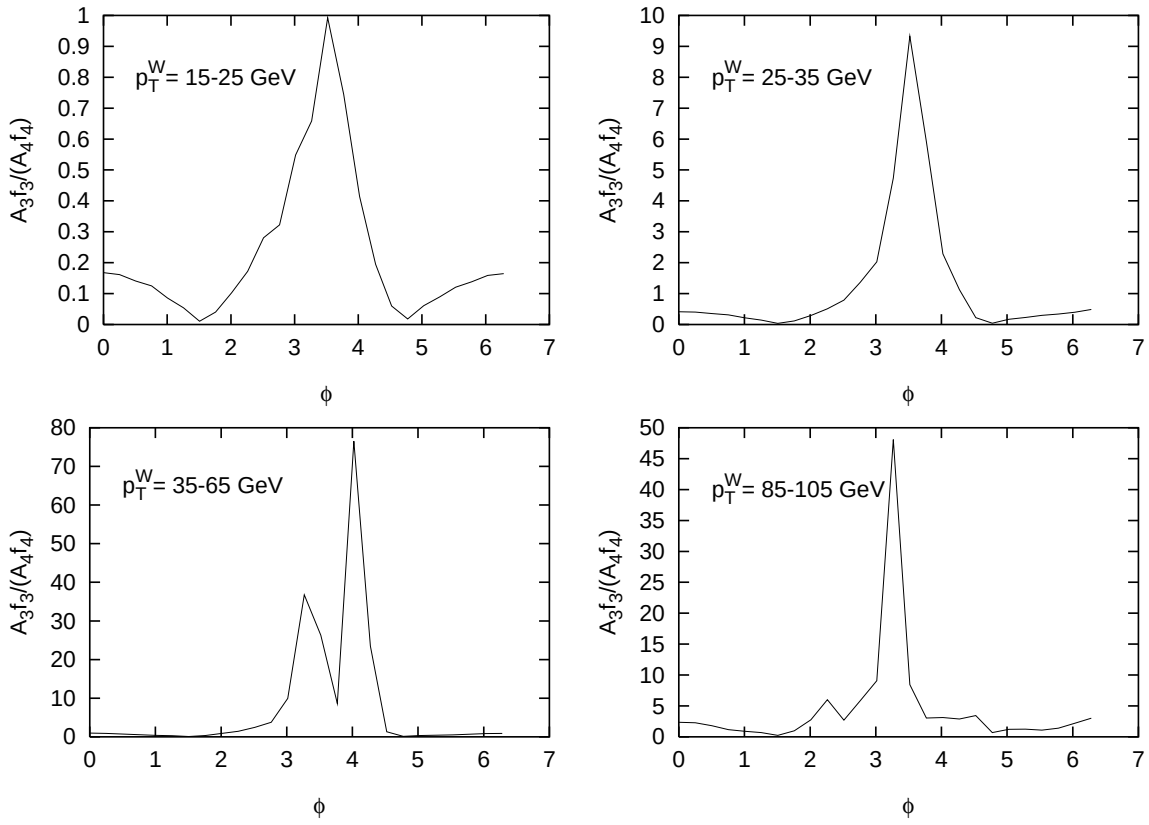

Figure 7.19 The $A_3 f_3(\phi)$ / $A_4 f_4(\phi)$ ratio for the electron events.

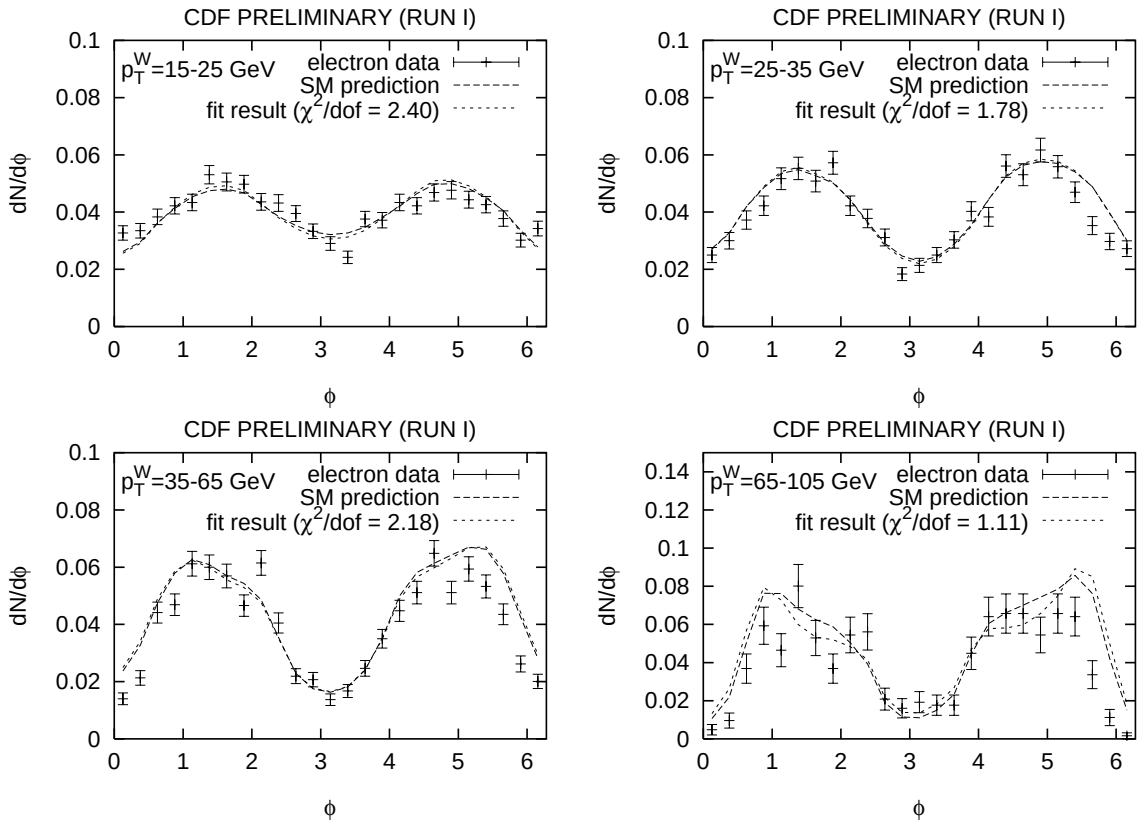

Figure 7.20 The ϕ distributions for the electron data (points) along with the result of the fit (short-dashed line) and the MC prediction (long-dashed line). The data is normalized to one and the theory is normalized to the data from $\pi/2$ to $3\pi/2$. The error bars are only statistical.

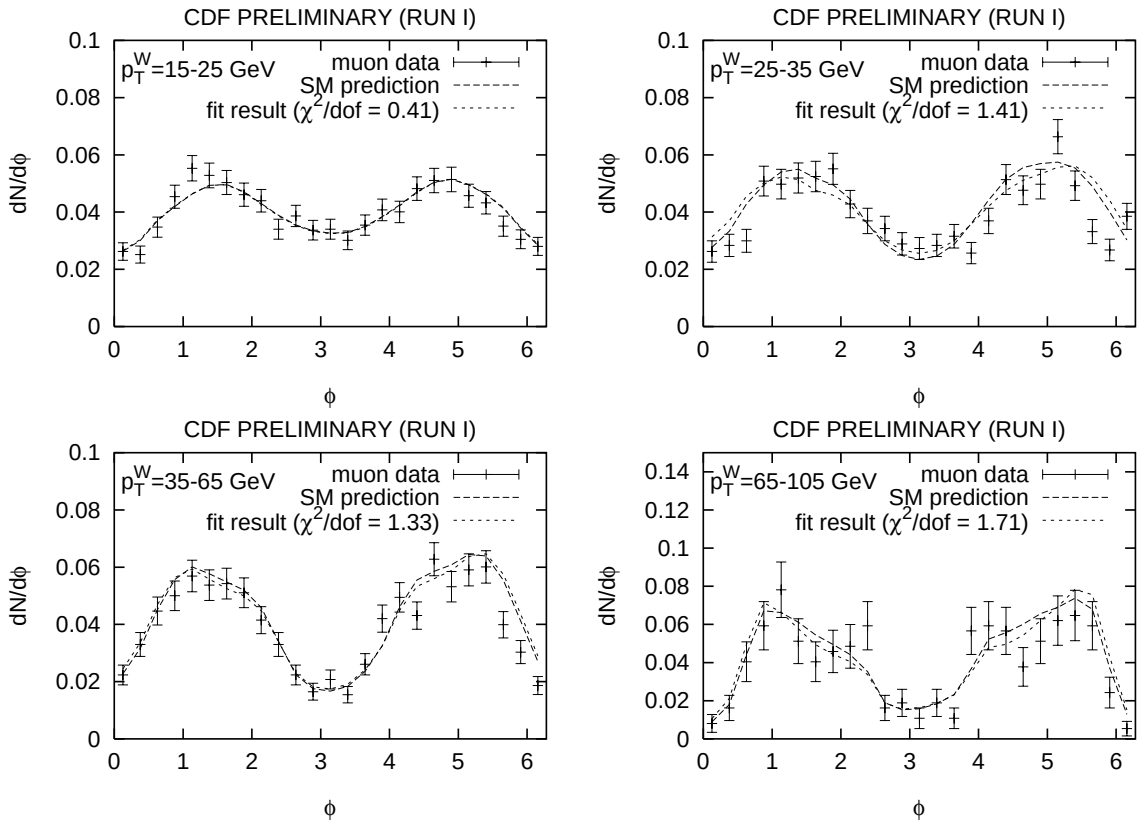

Figure 7.21 The ϕ distributions for the muon data (points) along with the result of the fit (short-dashed line) and the MC prediction (long-dashed line). The data is normalized to one and the theory is normalized to the data from $\pi/2$ to $3\pi/2$. The error bars are only statistical.

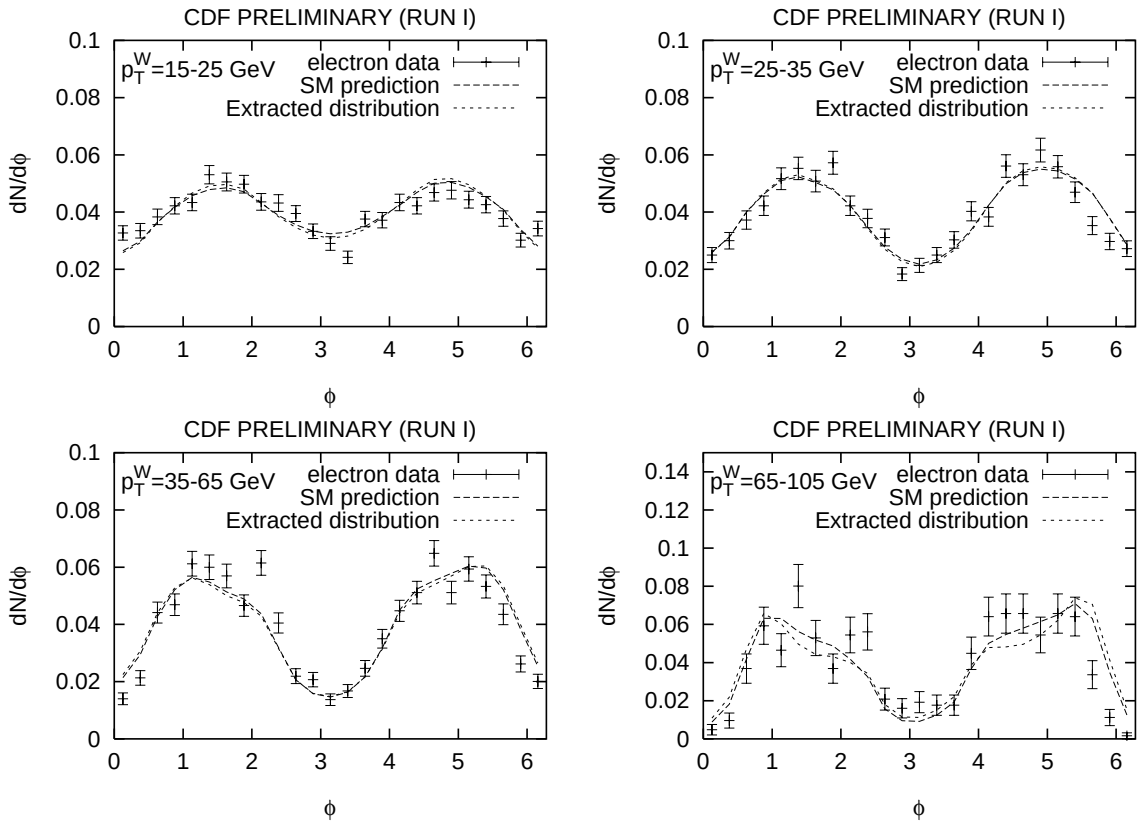

Figure 7.22 The ϕ distributions for the electron data (points) along with the MC predictions using the Standard Model $A_{2,3}$ (long-dashed line) and the experimentally extracted $A_{2,3}$ (short-dashed line) The data and MC is normalized to one. The error bars are only statistical.

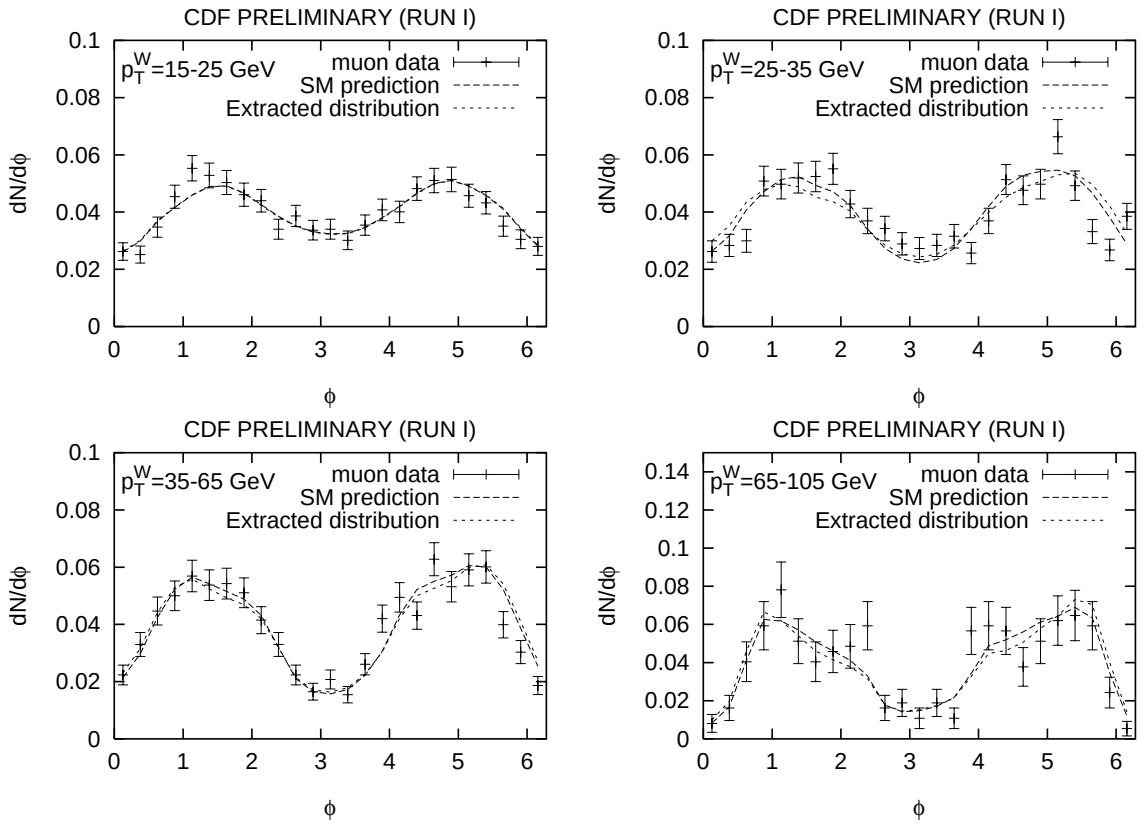

Figure 7.23 The ϕ distributions for the electron data (points) along with the MC predictions using the Standard Model $A_{2,3}$ (long-dashed line) and the experimentally extracted $A_{2,3}$ (short-dashed line) The data and MC is normalized to one. The error bars are only statistical.

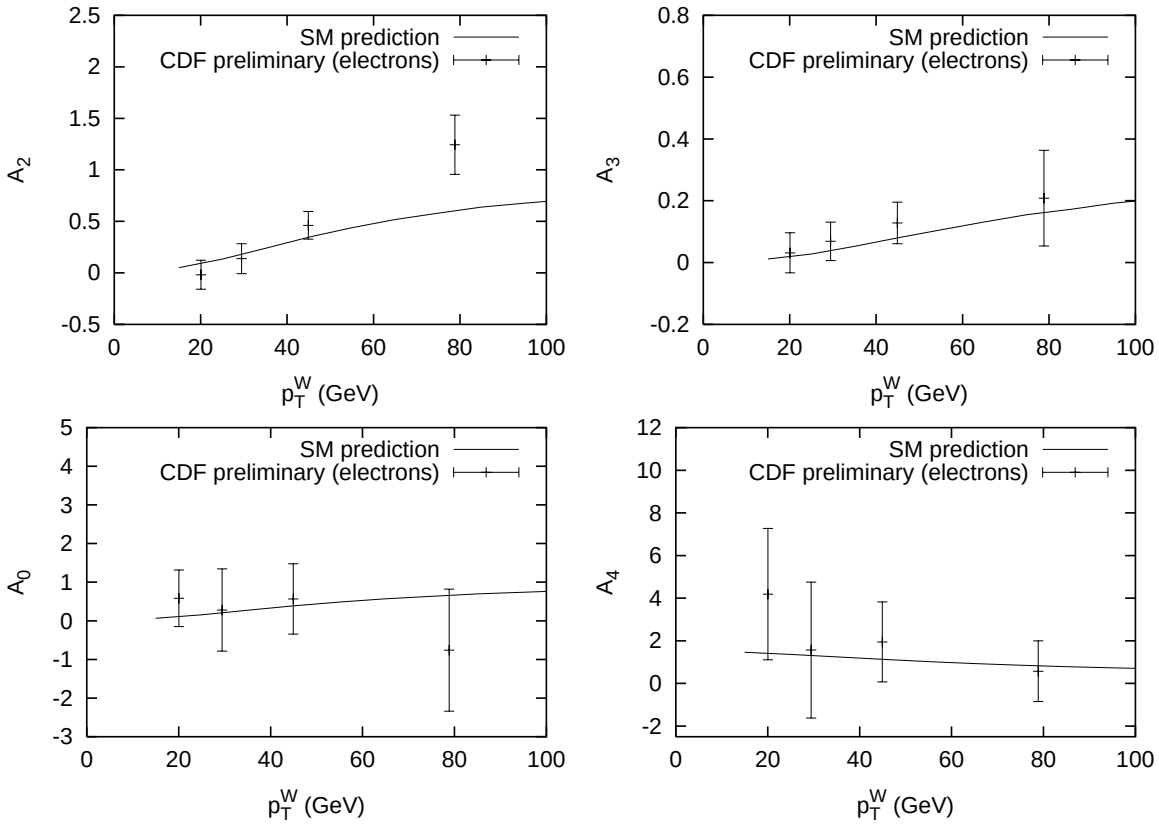

Figure 7.24 The measurement of the Angular Coefficients for the electron data (points) and the SM prediction up to order α_s^2 (line). The error bars are only statistical.

then the combined measurement is:

$$A_{\rm comb} = \frac{\frac{A_e}{\sigma_e^2} + \frac{A_\mu}{\sigma_\mu^2}}{\frac{1}{\sigma_e^2} + \frac{1}{\sigma_\mu^2}}, \tag{7.8}$$

and the uncertainty for the combined measurement is

$$\frac{1}{\sigma_{\rm comb}^2} = \frac{1}{\sigma_e^2} + \frac{1}{\sigma_\mu^2}. \tag{7.9}$$

The result of this statistical combination, along with the SM prediction, are presented in Figure 7.27. This procedure will be repeated after the systematic uncertainties are established, in order to reach our final measurement.

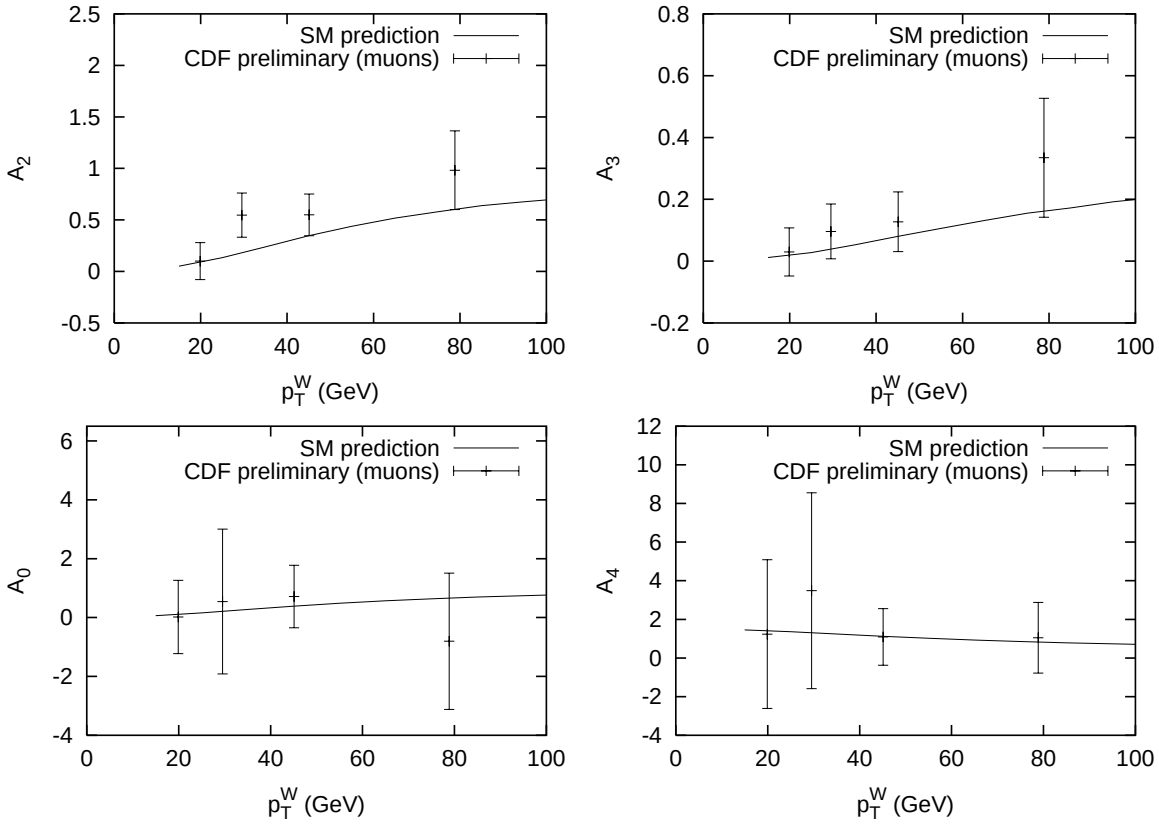

Figure 7.25 The measurement of the Angular Coefficients for the muon data (points) and the SM prediction up to order α_s^2 (line).The error bars are only statistical.

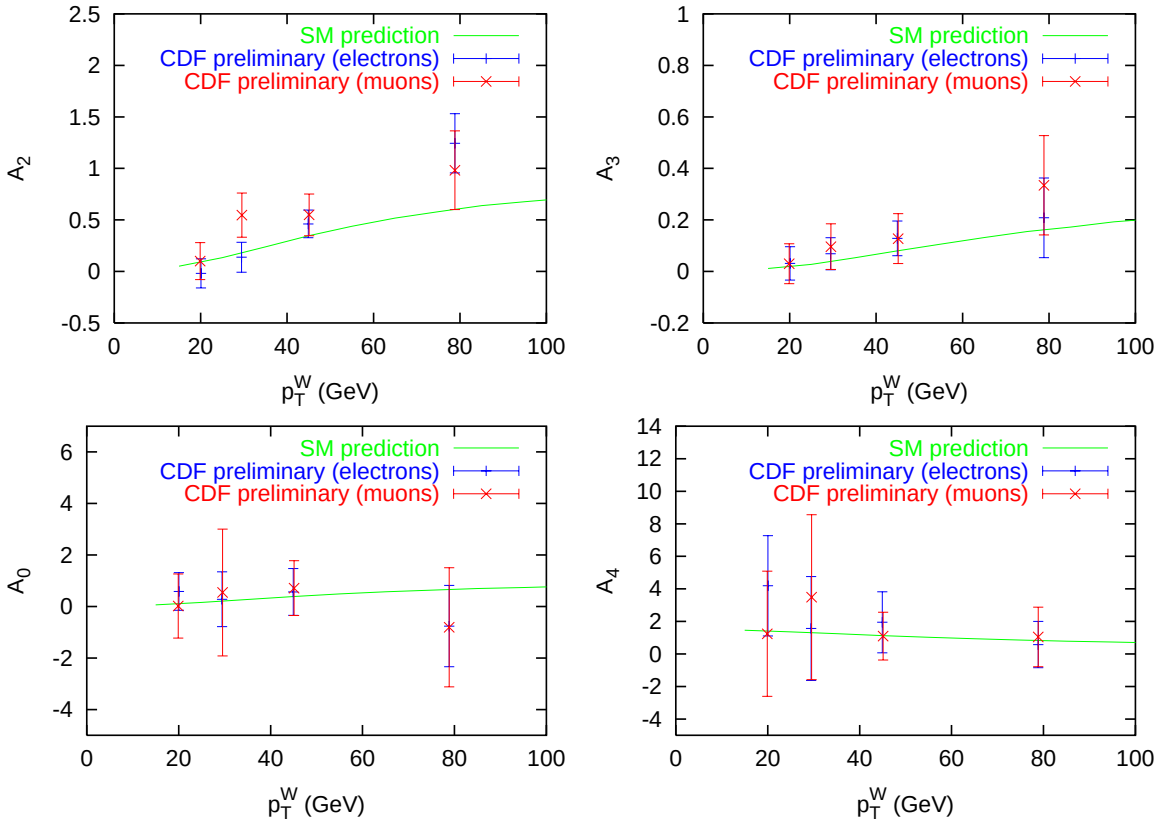

Figure 7.26 The measurement of the Angular Coefficients for the electron and muon data (points) and the SM prediction up to order α_s^2 (line). The error bars are only statistical.

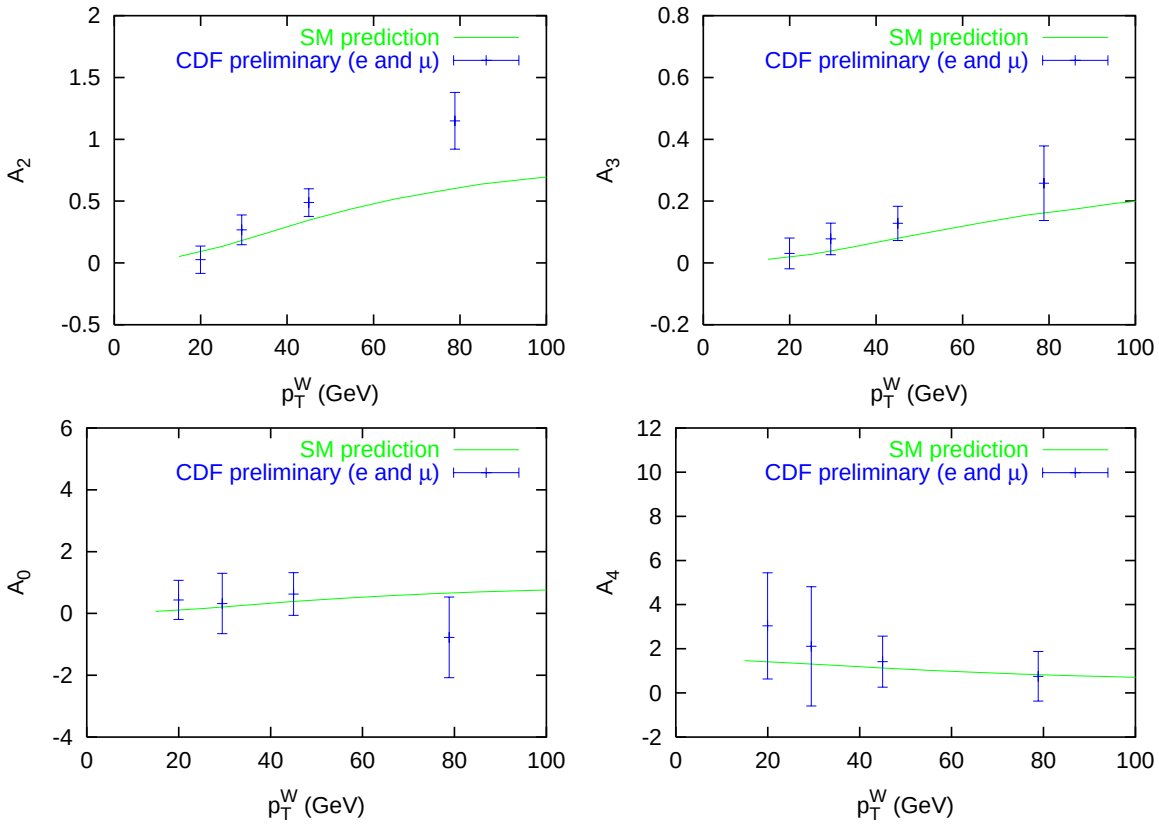

Figure 7.27 The measurement of the Angular Coefficients for the combination of electrons and muons (points) and the SM prediction up to order α_s^2 (line). The error bars are only statistical.

7.3 Systematic Uncertainties

7.3.1 Jet Systematic Uncertainties

The number of data events passing the jet cuts is affected by the systematic uncertainties associated with the jet E_T scale and the rapidity requirement. The same systematic uncertainty has an effect on the measurement of the angular coefficients and helicity cross sections.

The uncertainty on jet E_T scale depends on the calorimeter stability, relative corrections, extra interactions, and absolute underlying event corrections. The total uncertainty is a quadratic sum of these effects

$$(\delta E_T) = \sqrt{((\delta E_T)_{\rm cal})^2 + ((\delta E_T)_{\rm rel})^2 + ((\delta E_T)_{\rm EI})^2 + ((\delta E_T)_{\rm UE})^2} \tag{7.10}$$

The systematic uncertainty in the jet energy scale affects the reconstruction of the missing E_T and the W. For every FMC event, we shift the energy of the jet by $+\sigma = 85\%\sqrt{E^{\rm jet}}$, where $E^{\rm jet}$ is the energy of the jet in GeV, without changing its direction. We then properly correct the $\not\!\!E_T$ value and recalculate all the W, jet and $\not\!\!E_T$ kinematic variables. We subsequently calculate the new acceptance times efficiency $ae(\cos\theta, \phi)$ and analyze the data. We repeat for the energy shifted by $-\sigma = -85\%\sqrt{E^{\rm jet}}$ and calculate the systematic effect of the jet energy scale on the measurement of the angular coefficients, presented in Tables 7.4, 7.6 and 7.8 for the electron, muon, and combined results respectively.

We subsequently vary the jet E_T cut by $(\delta E_T) = 850$ MeV in 10 steps. Figure 7.28 shows how our yield changes as a function of the jet E_T cut. Table 7.1 shows the systematic uncertainty in the measurement of the yields of the W+jet events due to the jet E_T cut variation, for 15 GeV $\leq p_T^W <$ 105 GeV. The uncertainty on the rapidity η of the jet is $\delta\eta = \pm 0.2$. We vary the jet η cut from 2.2 to 2.6 and we get the variation in the data yields presented in Table 7.2, for 15 GeV $\leq p_T^W <$ 105 GeV. Table 7.3 shows the yield systematic uncertainties due to $E_T^{\rm jet}$ and $\eta^{\rm jet}$ cuts and the overall systematic uncertainty for the four p_T^W bins and for 15 GeV $\leq p_T^W <$ 105 GeV.

The systematic uncertainties for the angular coefficients due to the $E_T^{\rm jet}$ cut vari-

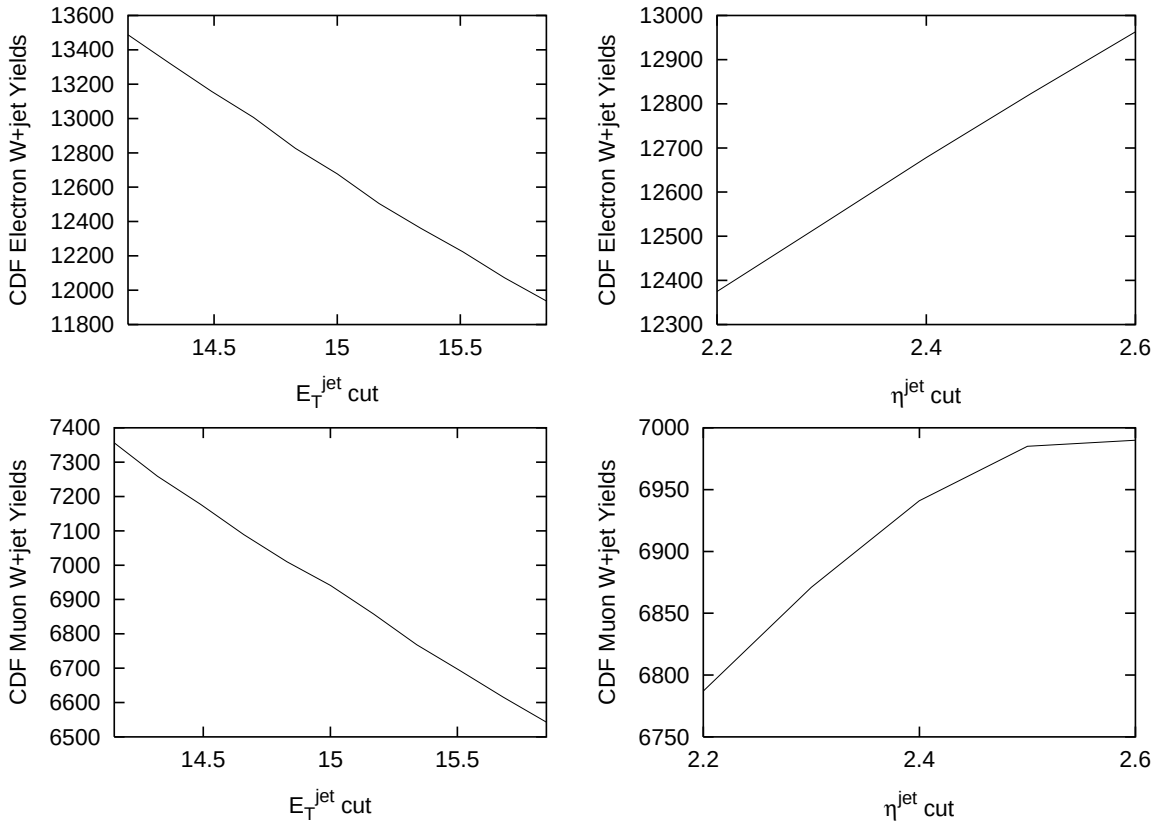

Figure 7.28 CDF W+jet yields as a function of the $E_T^{\rm jet}$ cut (left plots) and the $\eta^{\rm jet}$ cut (right plots) for electrons (upper plots) and muons (lower plots). The solid lines are for the total yields and the dashed for the yields in the 15 GeV $\leq p_T^W <$ 105 GeV region.

$E_T^{\rm jet}$ cut (GeV)	Number of electrons	Difference	Number of muons	Difference
14.15	13488	6.4 %	7356	6.0 %
14.32	13321	5.1 %	7259	4.6 %
14.49	13158	3.8 %	7177	3.4 %
14.66	13006	2.6 %	7089	2.1 %
14.83	12826	1.2 %	7010	1.0 %
15.00	12678	0.0 %	6941	0.0 %
15.17	12505	-1.4 %	6858	-1.2 %
15.34	12360	-2.5 %	6768	-2.5 %
15.51	12224	-3.6 %	6693	-3.6 %
15.68	12073	-4.8 %	6616	-4.7 %
15.85	11937	-5.8 %	6543	-5.7 %

Table 7.1 Variation of data yields due to $E_T^{\rm jet}$ cut uncertainty for W+jet events and for 15 GeV $\leq p_T^W <$ 105 GeV.

$\eta^{\rm jet}$ cut	Number of electrons	Difference	Number of muons	Difference
2.2	12375	-2.4 %	6787	-2.2 %
2.3	12526	-1.2%	6871	-1.0 %
2.4	12678	0.0 %	6941	0.0 %
2.5	12823	1.1 %	6985	0.6 %
2.6	12963	2.2 %	6990	0.7%

Table 7.2 Variation of data yields due to $\eta^{\rm jet}$ cut uncertainty for W+jet events and for 15 GeV $\leq p_T^W <$ 105 GeV.

ation are presented in Tables 7.4, 7.6 and 7.8 for the electron, muon and combined results respectively. To obtain the combined results we combine the electron and muon measurements for each bin and for each value of the $E_T^{\rm jet}$ choice using the statistical uncertainties of the central measurements as described in Section 7.2. The same method is used for all the combined systematic uncertainties estimation.

We also run our analysis program for all different values of the jet rapidity cut and we study the variation of the measured angular coefficients. The systematic uncertainty in the measurement of the angular coefficients due the jet rapidity measurement uncertainty is shown in Tables 7.4, 7.6 and 7.8 for the electron, muon and combination results.

W+jet yield systematic uncertainties due to the $E_T^{\rm jet}$ and $\eta^{\rm jet}$ cuts				
p_T^W (GeV)	Charged Lepton	δN due to $E_T^{\rm jet}$	δN due to $\eta^{\rm jet}$	Total systematic uncertainty
15–25	electron	$^{+593}_{-515}$	$^{+156}_{-154}$	$^{+613}_{-538}$
	muon	$^{+308}_{-290}$	$^{+34}_{-81}$	$^{+310}_{-301}$
25–35	electron	$^{+179}_{-175}$	$^{+78}_{-104}$	$^{+195}_{-204}$
	muon	$^{+95}_{-79}$	$^{+12}_{-44}$	$^{+96}_{-90}$
35–65	electron	$^{+38}_{-50}$	$^{+50}_{-43}$	$^{+63}_{-66}$
	muon	$^{+12}_{-29}$	$^{+3}_{-29}$	$^{+12}_{-41}$
65–105	electron	$^{+0}_{-1}$	$^{+1}_{-2}$	$^{+1}_{-2}$
	muon	$^{+0}_{-0}$	$^{+0}_{-0}$	$^{+0}_{-0}$

Table 7.3 Systematic uncertainties on W+jet yields to due the $E_T^{\rm jet}$ cut, $\eta^{\rm jet}$ cut and total systematic uncertainty, for the four p_T^W bins.

7.3.2 Selection of W mass Systematic Uncertainties

As we previously discussed, in order to boost to the W rest frame, we have to select a mass for the W boson. We have four different method for selecting the mass and we study how the application of each method affects our angular coefficients measurement. The first method selects a Breit-Wigner mass which is greater than the measured transverse mass of the W. The second method selects the pole mass, if it is greater than the transverse mass or selects the transverse mass, if the pole mass is less than the transverse mass. In the third method we select the pole mass or, in case it is less than the transverse mass, we select a Breit-Wigner mass which is greater then the transverse mass. Finally the fourth method (default) selects a mass based on the modified Breit-Wigner distribution which results from the slice of the theoretical (DYRAD) M_W versus M_T^W scattered plot (for W+jet events) at the measured transverse mass of the W (Figure B.5). This last method was preferred because it removed some biases in the measurement of the polar angle θ. In the ϕ analysis, the systematic uncertainty caused on the azimuthal angle ϕ by the selection of the mass of the W, is minimal. All methods give almost identical measurements of ϕ. The systematic uncertainties for the three cases are presented in 7.4, 7.6 and 7.8.

7.3.3 Backgrounds Estimation Systematic Uncertainties

There is an uncertainty in the estimation of the backgrounds, given by the uncertainties shown in Tables 6.8 and 6.9. We vary our prediction from the highest value to the

lowest possible value for every background as well as the FMC yields. These uncertainties do not include the PDF/Q^2-scale systematics. For each variation, we rerun our analysis programs for electron and muon and we also combine the measurements. The systematic uncertainties are shown in Tables 7.4 – 7.9.

7.3.4 $W + \gamma$ Systematic Uncertainty

The W+jet angular distribution can be affected by $W+\gamma$ production, for hard γ well-separated from the decay charged lepton. Some of the events in our data-sets are consistent with $W + \gamma$ production, according to [67]. We remove those events and remeasure A_2 and A_3. The new measurement is treated as a systematic uncertainty. The systematic uncertainty is presented in Tables 7.5, 7.7 and 7.9 for the electron, muon, and combined measurement respectively.

7.3.5 A_0 and A_4 Variation Systematic Uncertainty

In our analysis, we keep A_0 and A_2 fixed at their SM values. To check how this affects our measurement, we set $A_{0,2}$ at a minimum and a maximum value in all possible combinations and repeat the analysis (A_0(min)=0, A_0(max)=1, A_4(min)=0 and A_4(max)=2). The systematic uncertainties are presented in Tables 7.5, 7.7 and 7.9 for the electron, muon, and combined measurement respectively.

7.3.6 PDF Systematic Uncertainty

We change the Parton Distribution Functions to the MRSA$'$ [$\alpha_s(M_Z) = 0.105$ and $\Lambda = 0.150$] and repeat the analysis. The systematic uncertainties are presented in Tables 7.5, 7.7 and 7.9 for the electron, muon, and combined measurement respectively. If we try all PDFs of the MRSA and CTEQ families, we end up with a systematic uncertainty of $\pm 11\%$ on the DYRAD cross section which affects both the central FMC yields and the electroweak backgrounds. These will be used for the estimation of the FMC total systematic uncertainties.

7.3.7 Q^2-Scale Systematic Uncertainty

Finally, we change the renormalization and factorization scale (Q^2) so that it is equal to the square of the transverse momentum of the W. The systematic uncertainties are presented in Tables 7.5, 7.7 and 7.9 for the electron, muon, and combined measurement respectively. If we try all Q^2 choices provided by DYRAD, we end up with a systematic uncertainty of $(+19\% \ / \ -10\%)$ on the DYRAD cross section which affects both the central FMC yields and the electroweak backgrounds. These will be used for the estimation of the FMC total systematic uncertainties.

7.3.8 Overall Analysis Systematic Uncertainties

Tables 7.10, 7.11, 7.12 summarize the total systematic uncertainties for the A_2 and A_3 measurement, for the four p_T^W bins and for the electron, muon, and combined results respectively.

Combining the $E_T^{\rm jet}$ and $\eta^{\rm jet}$ systematic uncertainties in quadrature, we get the final CDF yields presented in Table 7.13. Comparing with the FMC yields of Tables 7.14 and 7.15, we see that there is a reasonable agreement with the SM prediction. We have also included the PDF and Q^2 FMC systematic uncertainties described in sections 10.6 and 10.7, combined in quadrature to give a systematic uncertainty of $(+22\%/-15\%)$ on the FMC yields and electroweak background.

The observed deviation of the FMC yields (Tables 7.14 and 7.15) from the data yields (Table 7.13) could be explained based on the fact that the Monte Carlo Feynman diagrams include only one outgoing parton if there is no gluon loop and up to two outgoing partons if there is one gluon loop. This results in the production of a jet with $E_T^{\rm jet} > 15$ GeV and $|\eta^{\rm jet}| < 2.4$ and (sometimes) the production of a second jet with $E_T^{\rm jet} > 10$ GeV (the tighter cuts on the leading jet are the same with the ones imposed by CDF). On the other hand, in the experimental data we do not have any limitation in the number of jets. As a result, we expect the experimental yields to be higher than the FMC ones. When we performed our analysis of CDF data requiring only 1 jet with the tight cuts ($E_T^{\rm jet} > 15$ GeV and $|\eta^{\rm jet}| < 2.4$) and accepting only one additional jet with with the softer cut of $E_T^{\rm jet} > 10$ GeV (to imitate what the

DYRAD generator is producing) there was a better agreement between the experimental data and the FMC prediction. Moreover, to count correctly the number of W+jet events, we have to remove the out of cone correction [69]. This reduces the jet energy scale and reduces the experimental data yields, improving the agreement between data and Monte Carlo. In our analysis, we are not interested in jet counting, since we are not trying to measure the W+jet cross section. We concentrate on the W angular distribution and the jet is there just to balance the W transverse momentum. Because we normalize both CDF and FMC data, and study only the shapes of the distributions, the actual yields determination does not affect the measurement of the angular coefficients. After the inclusion of the PDF/Q^2 systematic uncertainties in the FMC prediction and the jet E_T and jet η systematic uncertainties in the CDF data measurement, the disagreement became less significant.

Source of systematic error	p_T^W (GeV)	δA_2	δA_3
Jet E_T cut	15–25	$^{+0.0266}_{-0.0529}$	$^{+0.0000}_{-0.0066}$
	25–35	$^{+0.0380}_{-0.0103}$	$^{+0.0045}_{-0.0039}$
	35–65	$^{+0.0432}_{-0.0000}$	$^{+0.0031}_{-0.0034}$
	65–105	$^{+0.0005}_{-0.0615}$	$^{+0.0170}_{-0.0151}$
Jet η cut	15–25	$^{+0.0039}_{-0.0319}$	$^{+0.0000}_{-0.0037}$
	25–35	$^{+0.0007}_{-0.0336}$	$^{+0.0013}_{-0.0020}$
	35–65	$^{+0.0092}_{-0.0050}$	$^{+0.0023}_{-0.0004}$
	65–105	$^{+0.0000}_{-0.0614}$	$^{+0.0023}_{-0.0051}$
Jet energy scale	15–25	$^{+0.0607}_{-0.0606}$	$^{+0.0045}_{-0.0017}$
	25–35	$^{+0.0842}_{-0.1101}$	$^{+0.0092}_{-0.0015}$
	35–65	$^{+0.0017}_{-0.0510}$	$^{+0.0208}_{-0.0070}$
	65–105	$^{+0.2469}_{-0.3818}$	$^{+0.0841}_{-0.0487}$
M_W selection	15–25	$^{+0.0028}_{-0.0001}$	$^{+0.0000}_{-0.0011}$
	25–35	$^{+0.0018}_{-0.0000}$	$^{+0.0010}_{-0.0000}$
	35–65	$^{+0.0068}_{-0.0045}$	$^{+0.0033}_{-0.0001}$
	65–105	$^{+0.0001}_{-0.0559}$	$^{+0.0034}_{-0.0001}$
τ background	15–25	$^{+0.0008}_{-0.0010}$	$^{+0.0000}_{-0.0000}$
	25–35	$^{+0.0010}_{-0.0011}$	$^{+0.0001}_{-0.0001}$
	35–65	$^{+0.0009}_{-0.0011}$	$^{+0.0001}_{-0.0002}$
	65–105	$^{+0.0025}_{-0.0025}$	$^{+0.0002}_{-0.0003}$
Z background	15–25	$^{+0.0000}_{-0.0010}$	$^{+0.0000}_{-0.0000}$
	25–35	$^{+0.0000}_{-0.0011}$	$^{+0.0001}_{-0.0000}$
	35–65	$^{+0.0000}_{-0.0012}$	$^{+0.0001}_{-0.0000}$
	65–105	$^{+0.0000}_{-0.0025}$	$^{+0.0002}_{-0.0000}$

Table 7.4 Systematic errors in the measurement of A_2 and A_3, and their sources, for electron W+jet events.

Source of systematic error	p_T^W (GeV)	δA_2	δA_3
QCD background	15–25	$^{+0.0080}_{-0.0074}$	$^{+0.0003}_{-0.0004}$
	25–35	$^{+0.0043}_{-0.0311}$	$^{+0.0027}_{-0.0004}$
	35–65	$^{+0.0069}_{-0.0025}$	$^{+0.0003}_{-0.0007}$
	65–105	$^{+0.0000}_{-0.0026}$	$^{+0.0003}_{-0.0000}$
FMC yield	15–25	$^{+0.0031}_{-0.0067}$	$^{+0.0000}_{-0.0023}$
	25–35	$^{+0.0181}_{-0.0000}$	$^{+0.0003}_{-0.0016}$
	35–65	$^{+0.0173}_{-0.0000}$	$^{+0.0023}_{-0.0034}$
	65–105	$^{+0.0000}_{-0.0538}$	$^{+0.0011}_{-0.0051}$
W+γ	15–25	$^{+0.0000}_{-0.0064}$	$^{+0.0000}_{-0.0032}$
	25–35	$^{+0.0000}_{-0.0063}$	$^{+0.0019}_{-0.0000}$
	35–65	$^{+0.0102}_{-0.0000}$	$^{+0.0023}_{-0.0000}$
	65–105	$^{+0.0000}_{-0.0702}$	$^{+0.0028}_{-0.0000}$
A_0/A_4 variation	15–25	$^{+0.0295}_{-0.2055}$	$^{+0.0076}_{-0.0015}$
	25–35	$^{+0.0690}_{-0.2328}$	$^{+0.0153}_{-0.0050}$
	35–65	$^{+0.1051}_{-0.1605}$	$^{+0.0219}_{-0.0158}$
	65–105	$^{+0.1190}_{-0.0707}$	$^{+0.0152}_{-0.0275}$
PDF variation	15–25	$^{+0.0000}_{-0.0160}$	$^{+0.0013}_{-0.0000}$
	25–35	$^{+0.0149}_{-0.0000}$	$^{+0.0000}_{-0.0034}$
	35–65	$^{+0.0000}_{-0.0070}$	$^{+0.0011}_{-0.0000}$
	65–105	$^{+0.0024}_{-0.0000}$	$^{+0.0137}_{-0.0000}$
Q^2 variation	15–25	$^{+0.1019}_{-0.0000}$	$^{+0.0032}_{-0.0000}$
	25–35	$^{+0.1323}_{-0.0000}$	$^{+0.0000}_{-0.0102}$
	35–65	$^{+0.1352}_{-0.0000}$	$^{+0.0000}_{-0.0258}$
	65–105	$^{+0.0000}_{-0.0960}$	$^{+0.0107}_{-0.0000}$

Table 7.5 Systematic errors in the measurement of A_2 and A_3, and their sources, for electron W+jet events (continued).

Source of systematic error	p_T^W (GeV)	δA_2	δA_3
Jet E_T cut	15–25	$^{+0.0147}_{-0.0498}$	$^{+0.0037}_{-0.0032}$
	25–35	$^{+0.0672}_{-0.0554}$	$^{+0.0073}_{-0.0016}$
	35–65	$^{+0.0178}_{-0.0128}$	$^{+0.0042}_{-0.0011}$
	65–105	$^{+0.1519}_{-0.0000}$	$^{+0.0055}_{-0.0808}$
Jet η cut	15–25	$^{+0.0099}_{-0.0371}$	$^{+0.0045}_{-0.0000}$
	25–35	$^{+0.0291}_{-0.0219}$	$^{+0.0000}_{-0.0085}$
	35–65	$^{+0.0071}_{-0.0076}$	$^{+0.0039}_{-0.0028}$
	65–105	$^{+0.1021}_{-0.0000}$	$^{+0.0000}_{-0.0557}$
Jet energy scale	15–25	$^{+0.0511}_{-0.0703}$	$^{+0.0075}_{-0.0044}$
	25–35	$^{+0.0859}_{-0.0996}$	$^{+0.0262}_{-0.0142}$
	35–65	$^{+0.0147}_{-0.0848}$	$^{+0.0183}_{-0.0101}$
	65–105	$^{+0.2989}_{-0.3186}$	$^{+0.0382}_{-0.0176}$
M_W selection	15–25	$^{+0.0001}_{-0.0016}$	$^{+0.0000}_{-0.0001}$
	25–35	$^{+0.0030}_{-0.0002}$	$^{+0.0008}_{-0.0000}$
	35–65	$^{+0.0001}_{-0.0119}$	$^{+0.0038}_{-0.0000}$
	65–105	$^{+0.0560}_{-0.0000}$	$^{+0.0000}_{-0.0598}$
τ background	15–25	$^{+0.0014}_{-0.0014}$	$^{+0.0000}_{-0.0001}$
	25–35	$^{+0.0022}_{-0.0018}$	$^{+0.0002}_{-0.0002}$
	35–65	$^{+0.0018}_{-0.0017}$	$^{+0.0002}_{-0.0002}$
	65–105	$^{+0.0000}_{-0.0000}$	$^{+0.0000}_{-0.0000}$
Z background	15–25	$^{+0.0000}_{-0.0017}$	$^{+0.0001}_{-0.0000}$
	25–35	$^{+0.0000}_{-0.0036}$	$^{+0.0002}_{-0.0000}$
	35–65	$^{+0.0000}_{-0.0029}$	$^{+0.0002}_{-0.0000}$
	65–105	$^{+0.0001}_{-0.0000}$	$^{+0.0006}_{-0.0007}$

Table 7.6 Systematic errors in the measurement of A_2 and A_3, and their sources, for muon W+jet events.

Source of systematic error	p_T^W (GeV)	δA_2	δA_3
QCD background	15–25	$^{+0.0162}_{-0.0059}$	$^{+0.0006}_{-0.0022}$
	25–35	$^{+0.0202}_{-0.0044}$	$^{+0.0003}_{-0.0023}$
	35–65	$^{+0.0000}_{-0.0032}$	$^{+0.0003}_{-0.0000}$
	65–105	$^{+0.0001}_{-0.0000}$	$^{+0.0000}_{-0.0007}$
FMC yield	15–25	$^{+0.0000}_{-0.0002}$	$^{+0.0013}_{-0.0032}$
	25–35	$^{+0.0350}_{-0.0000}$	$^{+0.0021}_{-0.0016}$
	35–65	$^{+0.0031}_{-0.0020}$	$^{+0.0039}_{-0.0000}$
	65–105	$^{+0.0830}_{-0.0000}$	$^{+0.0000}_{-0.0557}$
W+γ	15–25	$^{+0.0023}_{-0.0000}$	$^{+0.0022}_{-0.0000}$
	25–35	$^{+0.0049}_{-0.0000}$	$^{+0.0000}_{-0.0039}$
	35–65	$^{+0.0028}_{-0.0000}$	$^{+0.0015}_{-0.0000}$
	65–105	$^{+0.0000}_{-0.0060}$	$^{+0.0000}_{-0.0166}$
A_0/A_4 variation	15–25	$^{+0.0320}_{-0.1997}$	$^{+0.0081}_{-0.0016}$
	25–35	$^{+0.0551}_{-0.1747}$	$^{+0.0240}_{-0.0081}$
	35–65	$^{+0.0917}_{-0.1392}$	$^{+0.0169}_{-0.0121}$
	65–105	$^{+0.0963}_{-0.0553}$	$^{+0.0167}_{-0.0312}$
PDF variation	15–25	$^{+0.0000}_{-0.0415}$	$^{+0.0016}_{-0.0000}$
	25–35	$^{+0.0000}_{-0.0014}$	$^{+0.0000}_{-0.0003}$
	35–65	$^{+0.0761}_{-0.0000}$	$^{+0.0000}_{-0.0003}$
	65–105	$^{+0.4001}_{-0.0000}$	$^{+0.0000}_{-0.0931}$
Q^2 variation	15–25	$^{+0.1186}_{-0.0000}$	$^{+0.0000}_{-0.0114}$
	25–35	$^{+0.0662}_{-0.0000}$	$^{+0.0000}_{-0.0075}$
	35–65	$^{+0.0386}_{-0.0000}$	$^{+0.0000}_{-0.0180}$
	65–105	$^{+0.0000}_{-0.2251}$	$^{+0.0162}_{-0.0000}$

Table 7.7 Systematic errors in the measurement of A_2 and A_3, and their sources, for muon W+jet events (continued).

Source of systematic error	p_T^W (GeV)	δA_2	δA_3
Jet E_T cut	15–25	$^{+0.0221}_{-0.0517}$	$^{+0.0000}_{-0.0037}$
	25–35	$^{+0.0472}_{-0.0246}$	$^{+0.0049}_{-0.0027}$
	35–65	$^{+0.0354}_{-0.0000}$	$^{+0.0032}_{-0.0022}$
	65–105	$^{+0.0546}_{-0.0302}$	$^{+0.0026}_{-0.0378}$
Jet η cut	15–25	$^{+0.0008}_{-0.0160}$	$^{+0.0000}_{-0.0013}$
	25–35	$^{+0.0097}_{-0.0299}$	$^{+0.0000}_{-0.0032}$
	35–65	$^{+0.0069}_{-0.0032}$	$^{+0.0013}_{-0.0000}$
	65–105	$^{+0.0107}_{-0.0261}$	$^{+0.0000}_{-0.0207}$
Jet energy scale	15–25	$^{+0.0570}_{-0.0643}$	$^{+0.0057}_{-0.0028}$
	25–35	$^{+0.0847}_{-0.1068}$	$^{+0.0148}_{-0.0057}$
	35–65	$^{+0.0057}_{-0.0614}$	$^{+0.0200}_{-0.0080}$
	65–105	$^{+0.2658}_{-0.3589}$	$^{+0.0661}_{-0.0365}$
M_W selection	15–25	$^{+0.0018}_{-0.0000}$	$^{+0.0000}_{-0.0007}$
	25–35	$^{+0.0022}_{-0.0001}$	$^{+0.0007}_{-0.0000}$
	35–65	$^{+0.0010}_{-0.0038}$	$^{+0.0035}_{-0.0000}$
	65–105	$^{+0.0000}_{-0.0154}$	$^{+0.0013}_{-0.0214}$
τ background	15–25	$^{+0.0010}_{-0.0011}$	$^{+0.0000}_{-0.0001}$
	25–35	$^{+0.0014}_{-0.0013}$	$^{+0.0001}_{-0.0002}$
	35–65	$^{+0.0012}_{-0.0013}$	$^{+0.0002}_{-0.0002}$
	65–105	$^{+0.0016}_{-0.0016}$	$^{+0.0001}_{-0.0002}$
Z background	15–25	$^{+0.0000}_{-0.0012}$	$^{+0.0000}_{-0.0000}$
	25–35	$^{+0.0000}_{-0.0019}$	$^{+0.0001}_{-0.0000}$
	35–65	$^{+0.0000}_{-0.0017}$	$^{+0.0002}_{-0.0000}$
	65–105	$^{+0.0000}_{-0.0016}$	$^{+0.0004}_{-0.0001}$

Table 7.8 Systematic errors in the measurement of A_2 and A_3, and their sources, for the combined results of electron and muon W+jet events.

Source of systematic error	p_T^W (GeV)	δA_2	δA_3
QCD background	15–25	$^{+0.0111}_{-0.0069}$	$^{+0.0004}_{-0.0011}$
	25–35	$^{+0.0093}_{-0.0226}$	$^{+0.0019}_{-0.0011}$
	35–65	$^{+0.0040}_{-0.0027}$	$^{+0.0003}_{-0.0004}$
	65–105	$^{+0.0000}_{-0.0016}$	$^{+0.0000}_{-0.0002}$
FMC yield	15–25	$^{+0.0018}_{-0.0042}$	$^{+0.0000}_{-0.0018}$
	25–35	$^{+0.0234}_{-0.0000}$	$^{+0.0009}_{-0.0016}$
	35–65	$^{+0.0114}_{-0.0000}$	$^{+0.0028}_{-0.0022}$
	65–105	$^{+0.0104}_{-0.0270}$	$^{+0.0000}_{-0.0250}$
W+γ	15–25	$^{+0.0000}_{-0.0031}$	$^{+0.0000}_{-0.0010}$
	25–35	$^{+0.0000}_{-0.0027}$	$^{+0.0000}_{-0.0000}$
	35–65	$^{+0.0079}_{-0.0000}$	$^{+0.0020}_{-0.0000}$
	65–105	$^{+0.0000}_{-0.0470}$	$^{+0.0000}_{-0.0048}$
A_0/A_4 variation	15–25	$^{+0.0305}_{-0.2033}$	$^{+0.0078}_{-0.0016}$
	25–35	$^{+0.0646}_{-0.2145}$	$^{+0.0182}_{-0.0061}$
	35–65	$^{+0.1010}_{-0.1539}$	$^{+0.0203}_{-0.0146}$
	65–105	$^{+0.1108}_{-0.0652}$	$^{+0.0158}_{-0.0290}$
PDF variation	15–25	$^{+0.0000}_{-0.0257}$	$^{+0.0014}_{-0.0000}$
	25–35	$^{+0.0098}_{-0.0000}$	$^{+0.0000}_{-0.0024}$
	35–65	$^{+0.0185}_{-0.0000}$	$^{+0.0007}_{-0.0000}$
	65–105	$^{+0.1463}_{-0.0000}$	$^{+0.0000}_{-0.0282}$
Q^2 variation	15–25	$^{+0.1082}_{-0.0000}$	$^{+0.0000}_{-0.0028}$
	25–35	$^{+0.1114}_{-0.0000}$	$^{+0.0000}_{-0.0093}$
	35–65	$^{+0.1055}_{-0.0000}$	$^{+0.0000}_{-0.0233}$
	65–105	$^{+0.0000}_{-0.1427}$	$^{+0.0129}_{-0.0000}$

Table 7.9 Systematic errors in the measurement of A_2 and A_3, and their sources, for the combined results of electron and muon W+jet events (continued).

p_T^W (GeV)	Total Systematics δA_2	Total Systematics δA_3
15–25	$^{+0.1255}_{-0.2239}$	$^{+0.0095}_{-0.0089}$
25–35	$^{+0.1771}_{-0.2619}$	$^{+0.0187}_{-0.0129}$
35–65	$^{+0.1782}_{-0.1687}$	$^{+0.0308}_{-0.0315}$
65–105	$^{+0.2742}_{-0.4225}$	$^{+0.0890}_{-0.0584}$

Table 7.10 Total systematic errors in the measurement of A_2 and A_3, for electron W+jet events.

p_T^W (GeV)	Total Systematics δA_2	Total Systematics δA_3
15–25	$^{+0.1352}_{-0.2246}$	$^{+0.0129}_{-0.0133}$
25–35	$^{+0.1478}_{-0.2098}$	$^{+0.0364}_{-0.0205}$
35–65	$^{+0.1276}_{-0.1642}$	$^{+0.0262}_{-0.0241}$
65–105	$^{+0.5497}_{-0.3941}$	$^{+0.0451}_{-0.1629}$

Table 7.11 Total systematic errors in the measurement of A_2 and A_3, for muon W+jet events.

p_T^W (GeV)	Total Systematics δA_2	Total Systematics δA_3
15–25	$^{+0.1285}_{-0.2217}$	$^{+0.0098}_{-0.0063}$
25–35	$^{+0.1638}_{-0.2438}$	$^{+0.0240}_{-0.0135}$
35–65	$^{+0.1524}_{-0.1658}$	$^{+0.0291}_{-0.0288}$
65–105	$^{+0.3279}_{-0.3978}$	$^{+0.0692}_{-0.0770}$

Table 7.12 Total systematic errors in the measurement of A_2 and A_3, for the combined results of electron and muon W+jet events (continued).

Data yields for inclusive W+jet		
p_T^W (GeV)	N_e	N_μ
15–25	5166 ± 72 +613/−538	2821 ± 53 +310/−301
25–35	3601 ± 60 +195/−204	1869 ± 43 +96/−90
35–65	3285 ± 57 +63/−66	1880 ± 43 +12/−41
65–105	624 ± 25 +1/−2	371 ± 19 +0/−0

Table 7.13 The electron and muon CDF data yields for inclusive W+jet up to order α_s^2, with statistical and systematic errors. The systematic errors are due to $E_T^{\rm jet}$ and $\eta^{\rm jet}$ scale uncertainties.

FMC+backgrounds electron yields for inclusive W+jet				
p_T^W (GeV)	N_e(FMC)	N_e(Backgrounds)	N_e(Total prediction)	PDF/Q^2 systematic
15–25	3867 ± 137	318^{+25}_{-19}	4185^{+144}_{-143}	+880/−660
25–35	2632 ± 93	217^{+10}_{-54}	2849^{+97}_{-110}	+598/−408
35–65	2474 ± 87	91^{+27}_{-6}	2565^{+94}_{-90}	+562/−383
65–105	518 ± 18	21^{+1}_{-1}	539^{+19}_{-19}	+118/−81

Table 7.14 Total electron FMC yields for inclusive W+jet up to order α_s^2, with statistical and systematic errors. The backgrounds are included. The systematic errors are due to PDF and Q^2 uncertainties.

FMC+backgrounds muon yields for inclusive W+jet				
p_T^W (GeV)	N_μ(FMC)	N_μ(Backgrounds)	N_μ(Total prediction)	PDF/Q^2 systematic
15–25	2027 ± 102	298^{+47}_{-14}	2325^{+120}_{-112}	+484/−330
25–35	1384 ± 66	133^{+27}_{-6}	1517^{+77}_{-72}	+329/−224
35–65	1314 ± 67	120^{+9}_{-7}	1434^{+73}_{-73}	+312/−212
65–105	279 ± 14	20^{+1}_{-1}	299^{+15}_{-15}	+66/−45

Table 7.15 Total muon FMC yields for inclusive W+jet up to order α_s^2, with statistical and systematic errors. The backgrounds are included. The systematic errors are due to PDF and Q^2 uncertainties.

Chapter 8

Results and Conclusions

8.1 Inclusion of Systematics and Final Results

Combining our statistical and systematic errors for the A_2 and A_3 measurement, we obtain our final result, presented in Tables 8.1, 8.2, and 8.3. Figures 8.1, 8.2 and 8.3 show the measurement of A_2 for the electron data, muon data, and the combination of the two results respectively. Figures 8.4, 8.5 and 8.6 show the measurement of A_3. The centers of the bins are determined from the p_T^W distribution within the bin and they are determined to be 20, 29, 45 and 79 GeV.

8.2 Conclusions

The eight angular coefficients of the W fully describe its differential cross section and angular distributions, according to Equation (2.15). The coefficients are related to the hadronic tensor of the cross section, whereas the leptonic part is described by explicit functions of the polar and azimuthal angles of the charged lepton from the W decay.

We extracted the Standard Model prediction for these angular coefficients up to second order in perturbative Quantum Chromodynamics. The inclusion of a jet is important for balancing the transverse momentum of the W and also introduces most of the leading-order angular coefficients. The consideration of a gluon loop is important for the study of the last three P-odd and T-odd coefficients, which appear only at next-to-leading order QCD calculations. We established that the leading

Measurement of A_2 and A_3 angular coefficients (electrons)				
p_T^W (GeV)	A_2	A_2(SM)	A_3	A_3(SM)
15–25	-0.02 $\pm$ 0.14 $^{+0.13}_{-0.22}$	0.08639	0.03 $\pm$ 0.06 $^{+0.009}_{-0.010}$	0.01801
25–35	0.14 $\pm$ 0.15 $^{+0.18}_{-0.26}$	0.18629	0.07 $\pm$ 0.06 $^{+0.019}_{-0.013}$	0.03989
35–65	0.46 $\pm$ 0.13 $^{+0.18}_{-0.17}$	0.35196	0.13 $\pm$ 0.07 $^{+0.031}_{-0.032}$	0.08239
65–105	1.24 $\pm$ 0.29 $^{+0.27}_{-0.42}$	0.59764	0.21 $\pm$ 0.15 $^{+0.089}_{-0.058}$	0.16071

Table 8.1 Our measurement of the A_2 and A_3 coefficients along with the statistical and systematic errors (electrons). The SM values up to order α_s^2 are also included.

Measurement of A_2 and A_3 angular coefficients (muons)				
p_T^W (GeV)	A_2	A_2(SM)	A_3	A_3(SM)
15–25	0.10 $\pm$ 0.18$^{+0.14}_{-0.22}$	0.08639	0.03 $\pm$ 0.08$^{+0.013}_{-0.013}$	0.01801
25–35	0.55 $\pm$ 0.21 $^{+0.15}_{-0.21}$	0.18629	0.10 $\pm$ 0.09$^{+0.036}_{-0.021}$	0.03989
35–65	0.55 $\pm$ 0.20 $^{+0.13}_{-0.16}$	0.35196	0.13 $\pm$ 0.10$^{+0.026}_{-0.024}$	0.08239
65–105	0.98 $\pm$ 0.38$^{+0.55}_{-0.39}$	0.59764	0.33 $\pm$ 0.19 $^{+0.045}_{-0.163}$	0.16071

Table 8.2 Our measurement of the A_2 and A_3 coefficients along with the statistical and systematic errors (muons). The SM values up to order α_s^2 are also included.

Measurement of A_2 and A_3 angular coefficients (combined results)				
p_T^W (GeV)	A_2	A_2(SM)	A_3	A_3(SM)
15–25	0.03 $\pm$ 0.11$^{+0.13}_{-0.22}$	0.08639	0.03 $\pm$ 0.05 $^{+0.010}_{-0.006}$	0.01801
25–35	0.27 $\pm$ 0.12$^{+0.16}_{-0.24}$	0.18629	0.08 $\pm$ 0.05$^{+0.024}_{-0.014}$	0.03989
35–65	0.49 $\pm$ 0.11 $^{+0.15}_{-0.16}$	0.35196	0.13 $\pm$ 0.06 $^{+0.029}_{-0.029}$	0.08239
65–105	1.15 $\pm$ 0.23$^{+0.33}_{-0.40}$	0.59764	0.26 $\pm$ 0.12 $^{+0.069}_{-0.077}$	0.16071

Table 8.3 Our measurement of the A_2 and A_3 coefficients along with the statistical and systematic errors (combination of electron and muon results). The SM values up to order α_s^2 are also included.

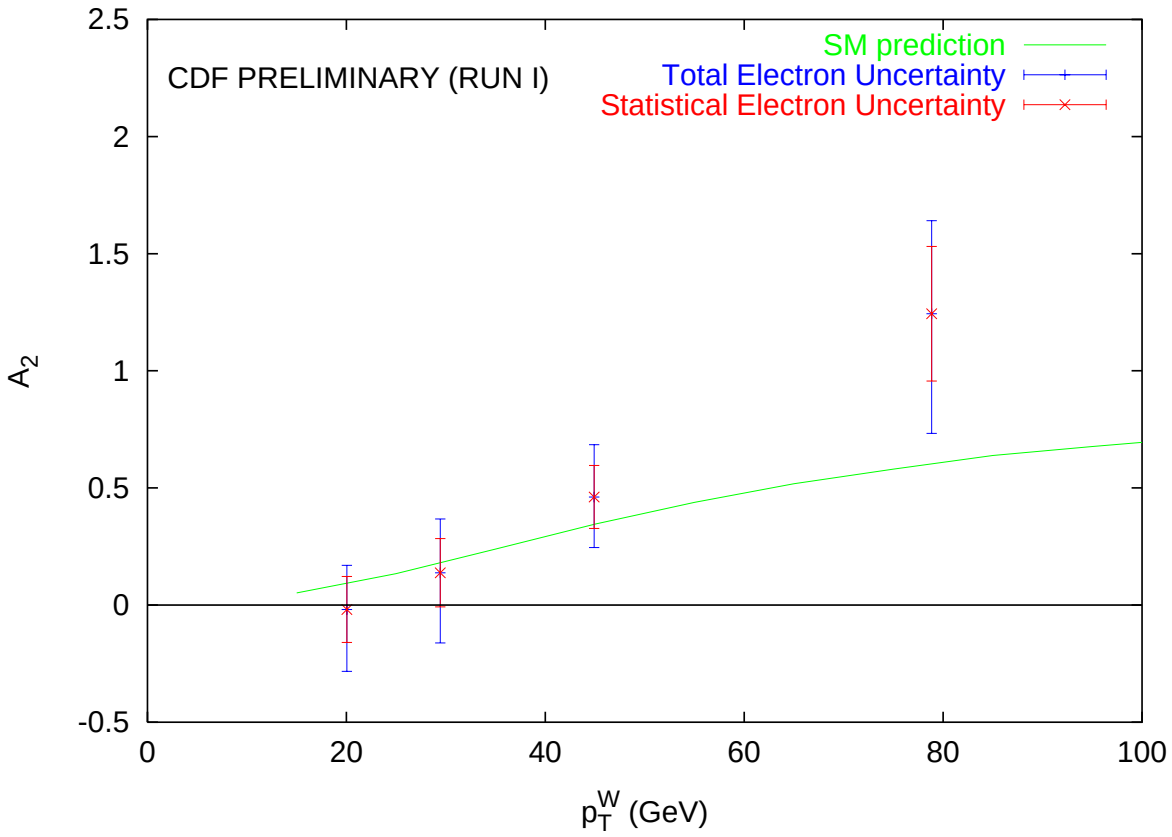

Figure 8.1 Measurement of A_2 (stars) using electron W+jet. The total (outer) and statistical (inner) errors are shown along with the Standard Model 1-loop prediction up to order α_s^2 (line).

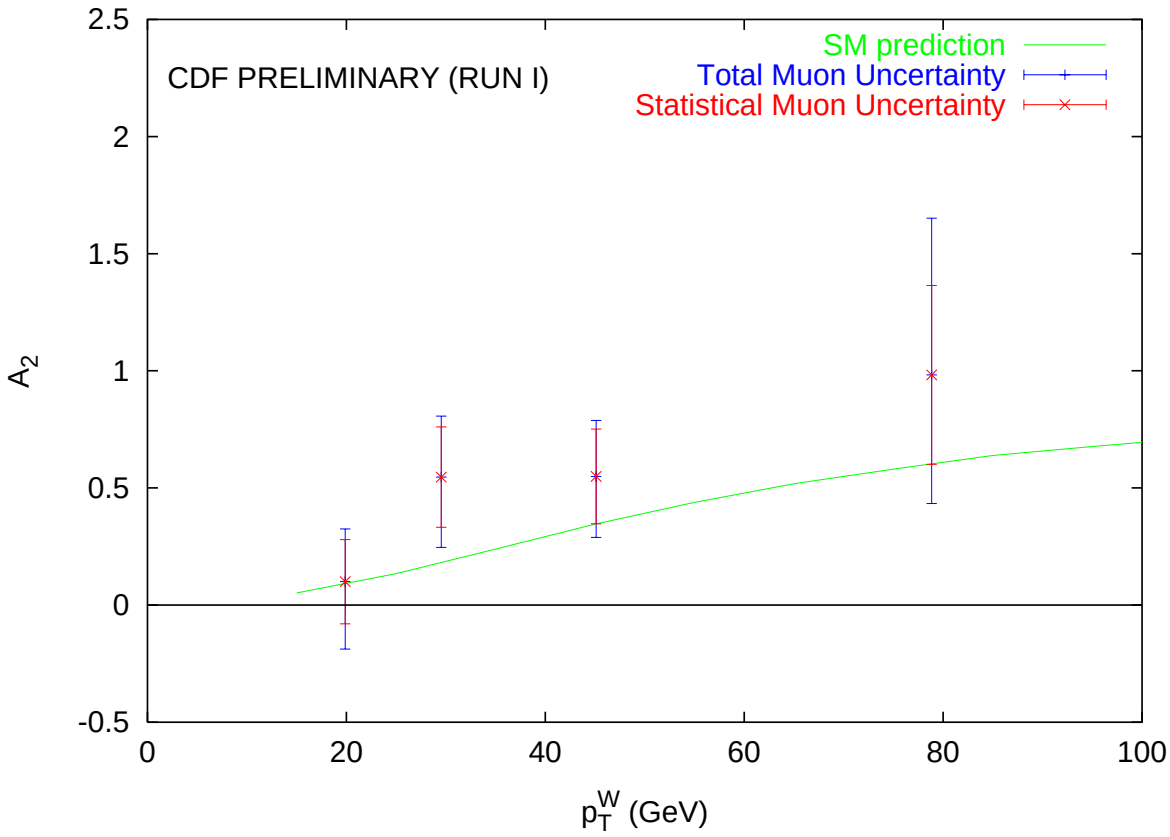

Figure 8.2 Measurement of A_2 (stars) using muon W+jet. The total (outer) and statistical (inner) errors are shown along with the Standard Model 1-loop prediction up to order α_s^2 (line).

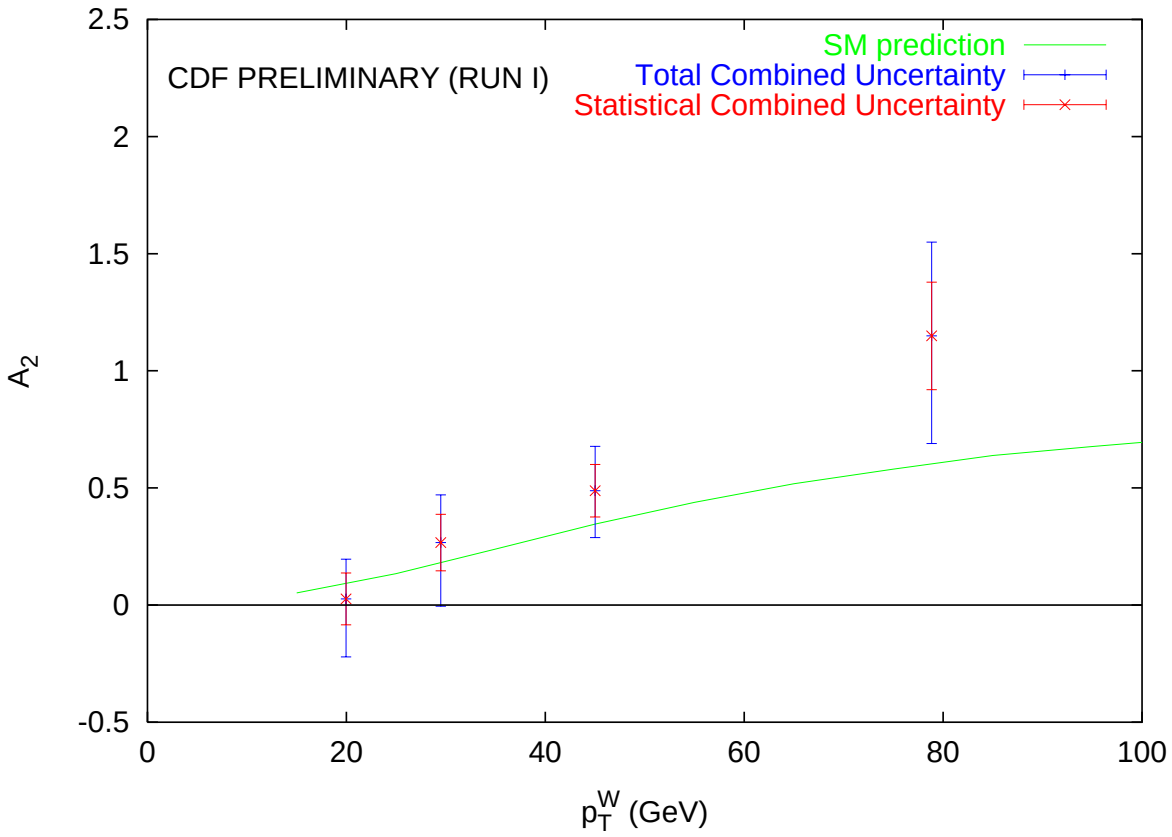

Figure 8.3 Measurement of A_2 (stars) using the combination of electron and muon A_2 measurements. The total (outer) and statistical (inner) errors are shown along with the Standard Model 1-loop prediction up to order α_s^2 (line).

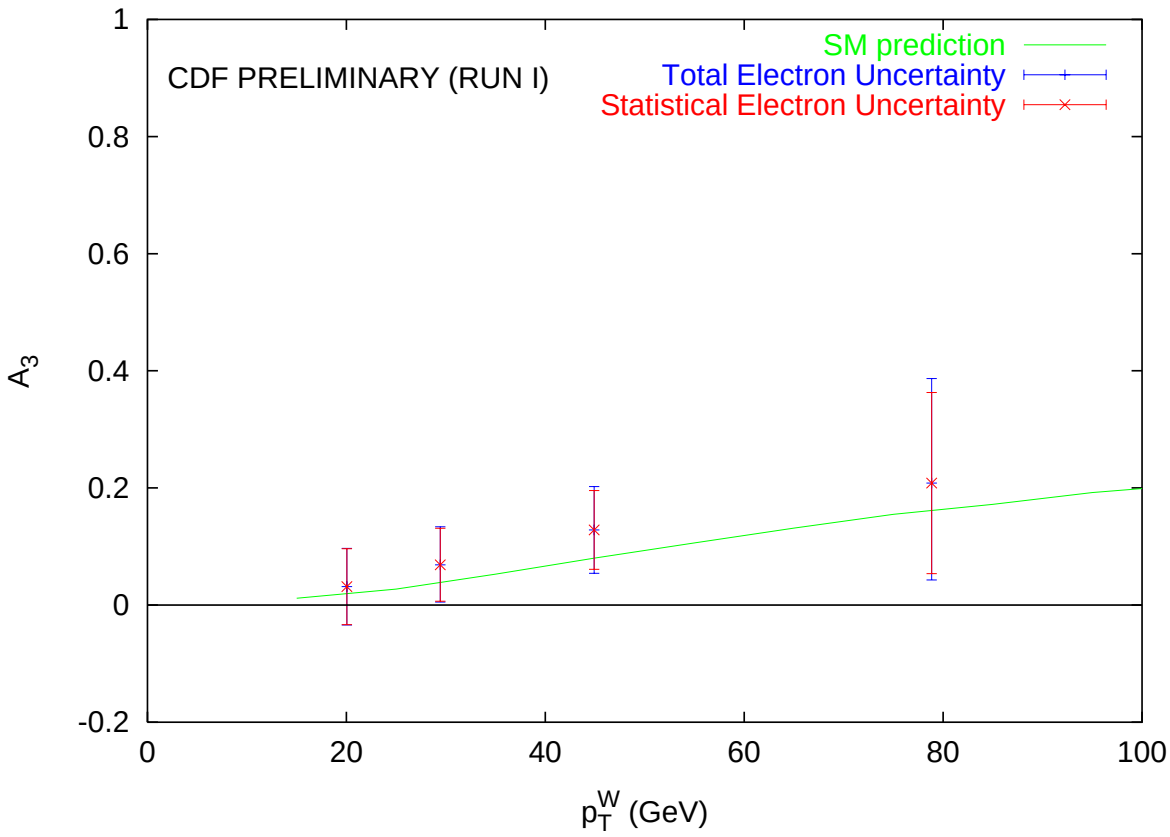

Figure 8.4 Measurement of A_3 (stars) using electron W+jet. The total (outer) and statistical (inner) errors are shown along with the Standard Model 1-loop prediction up to order α_s^2 (line).

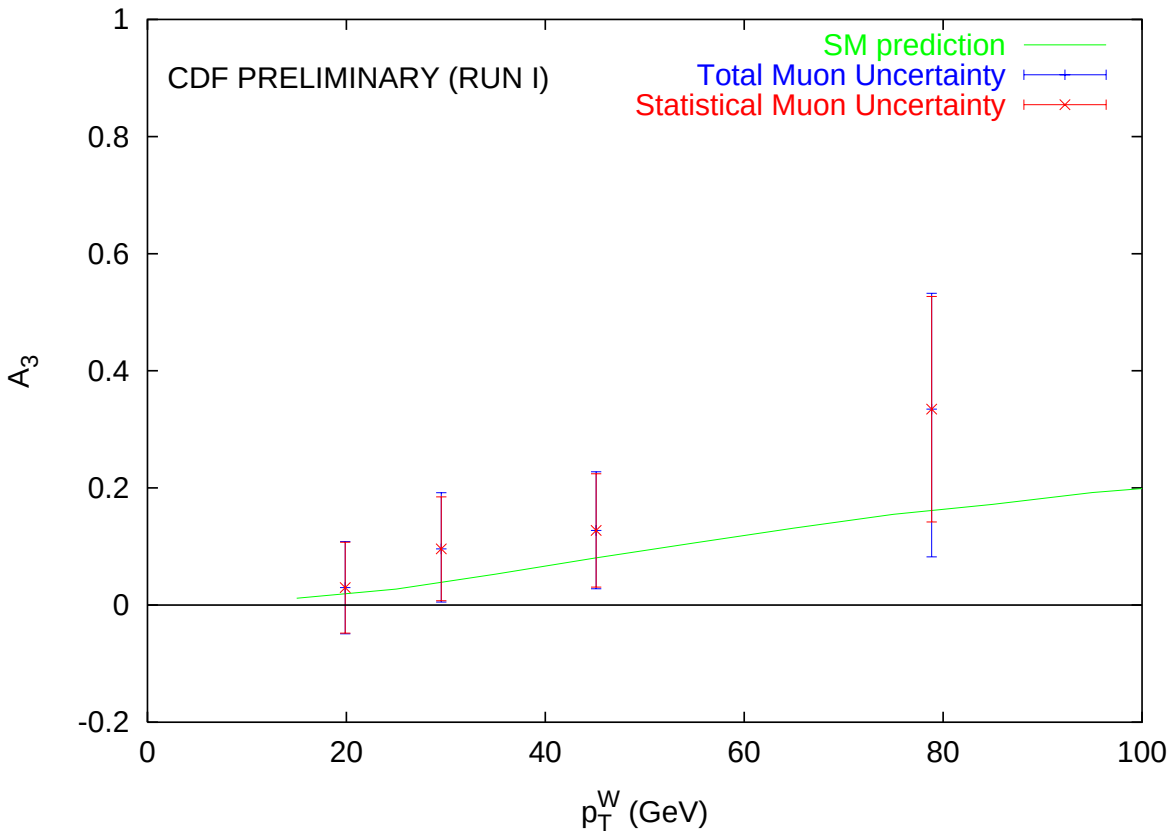

Figure 8.5 Measurement of A_3 (stars) using muon W+jet. The total (outer) and statistical (inner) errors are shown along with the Standard Model 1-loop prediction up to order α_s^2 (line).

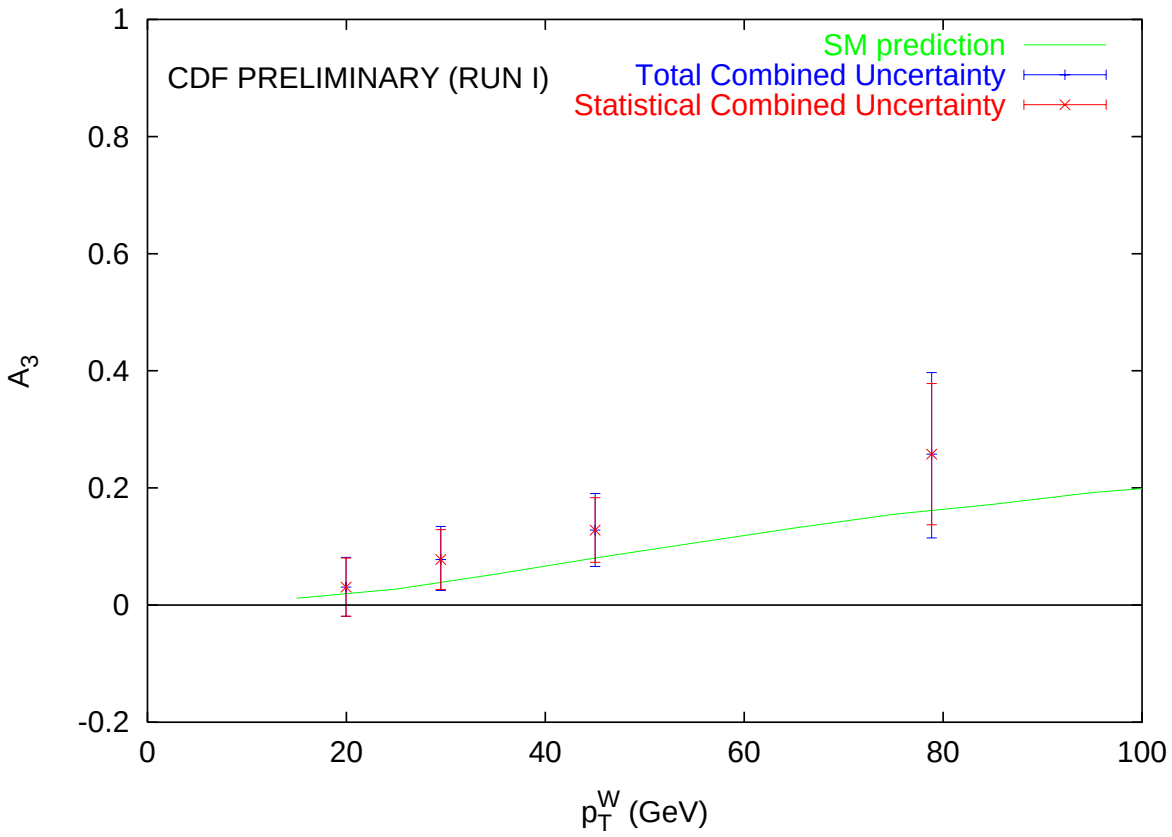

Figure 8.6 Measurement of A_3 (stars) using the combination of electron and muon A_3 measurements. The total (outer) and statistical (inner) errors are shown along with the Standard Model 1-loop prediction up to order α_s^2 (line).

order coefficient A_1 and the next-to-leading order coefficients A_5, A_6, A_7 are negligible, given the statistical significance of our data sample. The direct measurement of the polar angle θ of the charged lepton in the rest frame of the W produced in a hadron collider is seriously limited due to the two-fold ambiguity in the longitudinal direction of the neutrino, the large systematic uncertainty related to the choice of the mass of the W on an event-by-event basis, and the poor acceptance of the detector at high values of $\cos\theta$.

On the other hand, the direct measurement of the azimuthal angle ϕ of the charged lepton is possible with minimal systematic uncertainties. As explicitly shown in this dissertation, only the A_2 and A_3 angular coefficients affect the shape of the ϕ distribution. Large variations in the values of A_0 and A_4 do not affect the azimuthal distributions. This fact does not allow us to measure A_0 and A_4 with statistical significance, but it nevertheless gives us the opportunity to measure A_2 and A_3; with the current size of our data sample it would have been very difficult to simultaneously extract the four angular coefficients.

We performed the analysis of the azimuthal angle of electrons and muons from the Run Ia and Run Ib of the CDF experiment using four regions of the transverse momentum of the W. We constructed the theoretical prediction for the observed ϕ distributions, taking into account the detector effects, before integrating Equation (2.15) with respect to $\cos\theta$. We also included all relevant backgrounds. By fitting the data to this prediction, we extracted the angular coefficients A_2 and A_3 for the four p_T^W regions for electrons and muons and their statistical combination (Tables 8.1, 8.2, and 8.3, and Figures 8.1 to 8.6). These results are consistent with the Standard Model prediction of Chapter 2. There exists some tendency of the measurements to be higher than the Standard Model predictions, especially in the last p_T^W bin of the A_2 coefficient. This could be due to the fact that our data sample contains all orders of QCD, unlike our theory prediction which contains only the first two orders. No significant discrepancy is observed. The values we extracted for the A_0 and A_4 coefficients are not inconsistent with the Standard Model prediction, however the large uncertainties do not allow us to extract a statistically significant measurement.

Appendix A

The Standard Model

The Standard Model is the dominant theory that describes the microcosm today. It is based on field theory, which combines quantum mechanics and special relativity in a Hamilton-Lagrange formalism. The Standard Model describes the electromagnetic, weak, and strong interactions in a consistent way [74, 75, 76, 77], whereas gravity is not yet part of it; because the particles are so light, the gravitational interaction between them are very weak compared to the other interactions and its experimental study is not easy. From the theoretical point of view, there are models that describe gravity in a gauge fashion, with gravitons, gauge bosons of spin 2, carrying the interactions. Gravity is important mainly in the macrocosm; Newton's laws are routinely used on terrestrial problems, while General Relativity is the main tool of astrophysicists and astronomers.

A.1 Quantum Electrodynamics

Particle physicists aspire to explain everything using as few axioms as possible. One of the starting points is always symmetry. The world is undeniably symmetric and we have to construct our theories respecting this reality. Maybe in the future we understand why this is the case. We use global and local (*gauge*) symmetries to construct our theory and explain the conservation of basic physical quantities.

In field theory we start from a Lagrangian $\mathcal{L}$ and subsequently the Euler-Lagrange equation gives us the equation of motion for the particles. This is similar to the classical mechanics approach, with the main difference being that we substitute space

position by fields and time by the space-time vector (4-space). In quantum field theory the fields operate on the vacuum and they produce the particles at a specific space and time.

Quantum Electrodynamics (QED) is the field theory that describes the electromagnetic interactions between spin-$\frac{1}{2}$ particles (elementary particles with spin equal to 1/2 i.e., leptons and quarks). The QED Lagrangian is

$$\mathcal{L} = -\frac{1}{4}F_{\mu\nu}F^{\mu\nu} + \bar{\psi}(i\gamma^{\mu}D_{\mu} - m)\psi. \tag{A.1}$$

The first term of Equation (A.1) is the kinetic energy part of a massless electromagnetic field A_{μ}, which describes the photon that transfers the interaction. The quantity $F_{\mu\nu}$ is the *electromagnetic field tensor* (or *field strength*), defined as

$$F_{\mu\nu} = \partial_{\mu}A_{\nu} - \partial_{\nu}A_{\mu}. \tag{A.2}$$

The second term describes the kinetic energy and mass of the fermionic field ψ of mass m where D_{μ} is the covariant derivative, defined as

$$D_{\mu} = \partial_{\mu} + ieA_{\mu}Q, \tag{A.3}$$

where e is the unit of electric charge and Q is the charge operator ($Q\psi = q\psi$, where q is the charge of the particle). The field ψ is a 4-spinor, since we could have a particle or an antiparticle and there is also a spin up and spin down probability. The Dirac γ-matrices also have dimension four.

This Lagrangian is invariant under local (gauge) transformation of the form

$$\psi \to U(x)\psi(x), \qquad A_{\mu}(x) \to A_{\mu}(x) + \partial_{\mu}\alpha(x), \tag{A.4}$$

where

$$U(x) = e^{-ieQ\alpha(x)}, \tag{A.5}$$

and $\alpha(x)$ is an arbitrary function of the 4-space. For infinitesimal gauge transforma-

tion, equation (A.4) becomes

$$\psi \rightarrow (1 - ieQ\alpha(x))\psi(x). \tag{A.6}$$

Actually, the reason we replaced the derivative ∂_μ of the fermion kinetic part of the Lagrangian by the covariant one given by equation (A.3) was to make the Lagrangian gauge invariant. According to the Noether's theorem, this gauge invariance leads to the conservation of a quantity, which in our case is the electric charge. We realize that starting from the QED Lagrangian, we can prove the conservation of charge, an axiom of the past. Applying the Euler-Lagrange equations, we arrive at the Maxwell equation describing the photon

$$\partial_\nu F^{\mu\nu} = \bar{\psi}\gamma^\mu Q\psi, \tag{A.7}$$

and the Dirac equation describing the spin-$\frac{1}{2}$ fermion

$$(i\gamma^\mu D_\mu - m)\psi = 0, \tag{A.8}$$

which are both well established equations. The coupling of the fermion field to the photon, which transfers the electromagnetic interaction and is given by the covariant derivative, is again governed by the Lagrangian gauge symmetry requirement. Other forms of couplings do not give us a gauge invariant Lagrangian.

This important symmetry, out of which we extract so much physical information, belongs to the unitary group $U(1)$, since the matrix U is unitary and of dimension one. It is denoted $U(1)_Q$ in our case, since the charge is the generator of the transformations.

QED is the most successful physical theory. Its predictions have been experimentally verified up to few parts in a million.

A.2 The Weak Interactions

In quantum mechanics we often group spin-$\frac{1}{2}$ particles in doublets (2-spinors), since we have two possible third-projections of the spin. We then apply the spin operator to move from one entry of the doublet to the other. These rotations in the spin space, generated by the spin, are similar to the space rotations generated by the angular momentum. In QED, we used 4-spinors instead, to include the antiparticles. After the discovery of the fact that the neutron can decay to a proton through the weak nuclear interaction, and since the neutron and the proton are not different from the weak interactions point of view, it was natural to try to repeat the same grouping of particles in isospin doublets ψ.[‡] The proton and the neutron are assinged isospin equal to 1/2 and opposite third-projections. This isospin is the generator of rotations that trasform a neutron to a proton. As a result, theorists tried to introduce a Lagrangian and a gauge symmetry similar to the one described in the previous section.

The weak Lagrangian is

$$\mathcal{L} = -\frac{1}{4}\boldsymbol{W}_{\mu\nu}\boldsymbol{W}^{\mu\nu} + \bar{\psi}(i\gamma^{\mu}D_{\mu} - m)\psi, \tag{A.9}$$

which is invariant under the infinitesimal gauge transformation

$$\psi \to (1 - ig\boldsymbol{\alpha}(x)\cdot\boldsymbol{T})\psi(x), \tag{A.10}$$

where $\boldsymbol{\alpha}$ is an infinitesimal vector in isospin space and $\boldsymbol{T}$ is the isospin operator whose components T_i are the generators of the isospin rotations. The isospin components T_i are given by

$$T_i = \frac{1}{2}\tau_i, \tag{A.11}$$

where τ_i are the Pauli matrices. Since the generated matrices are unitary, their determinant is one, and their dimension is two, the T_i are generators of the SU(2) symmetry transformations. Just like the angular momentum, the T_i do not commute

[‡]Of course, each entry of the isospin doublet is a 4-spinor, describing the corresponding fermion.

and they follow the Lie Algebra

$$[T_i, T_j] = i\epsilon_{ijk} T_k. \tag{A.12}$$

The covariant derivative is given by

$$D_\mu = \partial_\mu + ig\boldsymbol{W}_\mu \cdot \boldsymbol{T}. \tag{A.13}$$

The $\boldsymbol{W}_\mu$ fields transfer the weak interactions and transform as

$$\boldsymbol{W}_\mu(x) \to \boldsymbol{W}_\mu(x) + \partial_\mu \boldsymbol{\alpha}(x) + g\boldsymbol{\alpha}(x) \times \boldsymbol{W}_\mu(x). \tag{A.14}$$

The field strength $W_{\mu\nu}$ is

$$\boldsymbol{W}_{\mu\nu} = \partial_\mu \boldsymbol{W}_\nu - \partial_\nu \boldsymbol{W}_\mu - g\boldsymbol{W}_\mu \times \boldsymbol{W}_\nu. \tag{A.15}$$

The last term in equations (A.14) and (A.15) appears because of the non-abelian nature of the group. It tells us that the weak bosons interact with each other, unlike the photons. It is important to notice that the weak fields and the weak strength are vectors, because the isospin is a vector operator and the covariant derivative of equation (A.13) would have no sense for a scalar weak field. This way, the need for three gauge bosons to transfer the weak interactions arises naturally.

Although the theory presented above is consistent with the QED formalism, it does not describe reality. We can construct two positive and a neutral gauge bosons out of this theory, by proper linear combinations of the fields W_μ^i $(i = 1, 2, 3)$, but they have to be massless. If we include a mass term in the Lagrangian, it will not be gauge invariant anymore. This contradicts the experimental observations, according to which the weak gauge bosons are massive. Another serious problem with the theory is that the left-handed nature of the charge-current couplings is not included, although in nature only the left-handed fermions and right-handed anti-fermions participate in weak interactions. These problems are solved with the introduction of the Electroweak Unification.

A.3 The Unified Electroweak Model

A.3.1 The Unbroken $SU(2)_L \times U(1)_Y$

We define the massless left-handed and right-handed fermion fields

$$\psi_L = \frac{1}{2}(1-\gamma_5)\psi, \qquad \psi_R = \frac{1}{2}(1+\gamma_5)\psi. \tag{A.16}$$

The helicity operator (that gives us the projection of the spin in the direction of motion of the particle) is the same as the chirality operator for massless fermions (or high energies). Therefore, the left-handed fermions correspond to negative helicity and the right-handed fermions correspond to positive helicity.

We would like to have the $SU(2)$ symmetry applied only to the left-handed fermion field ψ_L, to be consistent with observation, so we call the new symmetry $SU(2)_L$. The mass term $m\bar{\psi}\psi = m(\bar{\psi_L}\psi_R + \bar{\psi_R}\psi_L)$ is not invariant under the $SU(2)_L$, so at this point we consider massless fermions. This problem will be solved later. The conserved quantum number is T_L or *weak isospin*. As we will see in section A.5, any charged-current weak interaction will include terms of the form $\bar{\psi_1}\gamma^\mu\frac{1}{2}(1-\gamma_5)\psi_2$. The bilinear quantities of the form $\bar{\psi_1}\gamma^\mu\psi_2$ are *vectors* (they transform as vectors under Lorentz boosts, rotations and Parity transformation) while the bilinear quantities of the form $\bar{\psi_1}\gamma^\mu\gamma_5\psi_2$ are axial vectors (they transform as vectors under Lorentz boosts and rotations, but they are Parity-even). That is why we refer to the unified theory involving only left-handed fermions and right-handed antifermions as the $V-A$ (Vector minus Axial Vector) theory.

Now, in order to unify the electromagnetic and weak interactions, we introduce the weak hypercharge Y, so that the charge operator is given by

$$Q = T_{L3} + \frac{1}{2}Y. \tag{A.17}$$

The Lagrangian will be invariant under the new $U(1)_Y$ symmetry and the conserved quantum number is Y. The overall symmetry is denoted $SU(2)_L \times U(1)_Y$.

We can now write the Lagrangian for the unified electroweak model

$$\mathcal{L} = -\frac{1}{4}\boldsymbol{W}_{\mu\nu}\boldsymbol{W}^{\mu\nu} + -\frac{1}{4}B_{\mu\nu}B^{\mu\nu} + \bar{\psi}i\gamma^{\mu}D_{\mu}\psi. \tag{A.18}$$

The massless gauge fields are now the isotriplet $\boldsymbol{W}_{\mu}$ for $SU(2)_L$ and the hypersinglet B_{μ} for $U(1)_Y$. The field strength $\boldsymbol{W}_{\mu\nu}$ is defined in (A.15), while

$$B_{\mu\nu} = \partial_{\mu}B_{\nu} - \partial_{\nu}B_{\mu}, \tag{A.19}$$

and the covariant derivative becomes

$$D_{\mu} = \partial_{\mu} + ig\boldsymbol{W}_{\mu} \cdot \boldsymbol{T_L} + ig'\frac{1}{2}B_{\mu}Y. \tag{A.20}$$

The Lagrangian (A.18) is invariant under $SU(2)_L$ and $U(1)_Y$ separately. To have a unified theory, the neutral term $i(gW_{3\mu}T_{L3} + g'\frac{1}{2}B_{\mu}Y)$ of (A.20) has to contain the term $ieA_{\mu}Q$ of (A.3). For this to happen, the W_3 and B_{μ} fields have to be linear combinations of A_{μ} and another neutral field Z_{μ}. The coefficients of the linear combination can be expressed as sines and cosines, because the normalization of all the vector boson fields is the same. So we can write

$$\begin{pmatrix} W_{3\mu} \\ B_{\mu} \end{pmatrix} = \begin{pmatrix} \cos\theta_W & \sin\theta_W \\ -\sin\theta_W & \cos\theta_W \end{pmatrix} \begin{pmatrix} Z_{\mu} \\ A_{\mu} \end{pmatrix}, \tag{A.21}$$

where θ_W is the electroweak mixing angle, a parameter of the Standard Model. The neutral part of (A.20) now becomes

$$i(gW_{3\mu}T_{L3} + g'\frac{1}{2}B_{\mu}Y) = D_{\mu}^{A} + D_{\mu}^{Z}, \tag{A.22}$$

where

$$D_{\mu}^{A} = ieA_{\mu}Q, \tag{A.23}$$

$$D_{\mu}^{Z} = ig_Z Z_{\mu}(T_L 3 - x_W Q), \tag{A.24}$$

and

$$g = \frac{e}{\sin\theta_W}, \qquad g' = \frac{e}{\cos\theta_W}$$
$$g_Z = \frac{e}{\sin\theta_W \cos\theta_W}, \qquad x_W = \sin^2\theta_W. \tag{A.25}$$

If we define

$$W_\mu^\pm = \frac{1}{\sqrt{2}}(W_{1\mu} \mp iW_{2\mu}) \quad \text{and} \quad T_L^\pm = \frac{1}{\sqrt{2}}(T_{L1} \mp iT_{L2}), \tag{A.26}$$

then the charge parts of (A.20) become

$$D_\mu^{W^\pm} = igW_\mu^\pm T_L^\pm, \tag{A.27}$$

and we can write the covariant derivative (A.20) as

$$D_\mu = \partial_\mu + D_\mu^{W^+} + D_\mu^{W^-} + D_\mu^A + D_\mu^Z. \tag{A.28}$$

Because the interaction part of the Lagrangian is given by the $\bar{\psi}i\gamma^\mu D_\mu\psi$, we realize that equation (A.28) explicitly describes the interaction of the fermion with four gauge bosons which correspond to the $W^\pm$ and Z particles and the photon γ. The electromagnetic and weak interactions are unified.

We have solved the problem of the $V-A$ nature of the interactions by the unified $SU(2)_L \times U(1)_Y$ theory but, at the same time we have not solved the problem of the massive weak gauge bosons. Actually we introduced an extra problem: we assumed that fermions are massless as well. Both these problems are solved with the spontaneous symmetry breaking mechanism or Higgs Mechanism.

A.3.2 The Higgs Mechanism

We introduce a scalar field Φ which is described by the isodoublet of a positive and neutral field.

$$\Phi(x) = \begin{pmatrix} \phi^+(x) \\ \phi^0(x) \end{pmatrix}. \tag{A.29}$$

We add to our Lagrangian (A.18) a kinetic part and a self-interaction part corresponding to the new field

$$\mathcal{L}_\Phi = |D_\mu \Phi| - V(|\Phi|^2), \tag{A.30}$$

where $|\Phi| = \Phi^\dagger \Phi$ and V is a scalar potential, the most general renormalizable form of which is

$$V = \mu^2 |\Phi|^2 + \lambda |\Phi|^4, \tag{A.31}$$

where $\mu^2 < 0$. From $\mathcal{L}_\Phi$ we will get a mass for the weak gauge bosons and we will introduce a new massive particle, the Higgs boson. The masses for the fermions will come from explicit Yukawa couplings.

The minimum of V occurs at $|\Phi|^2 = -\frac{1}{2}\mu^2/\lambda \equiv \upsilon^2/2$, also known as the vacuum expectation value of Φ. This vacuum expectation value defines a preferred direction in the hypercharge plus weak isospin space and spontaneous breaks $SU(2)_L \times U(1)_Y$. It is common to redefine the scalar Φ as

$$\Phi(x) = \exp\left(\frac{i\boldsymbol{\xi}(x)\cdot\boldsymbol{\tau}}{2\upsilon}\right)\begin{pmatrix} 0 \\ (\upsilon + H(x)) \end{pmatrix}, \tag{A.32}$$

were $\boldsymbol{\xi}$ are real scalar fields, the Goldstone bosons, that appear whenever a continuous symmetry is spontaneously broken and $H(x)$ is a massive Higgs scalar with zero expectation value. Finally we perform a finite $SU(2)_L$ gauge transformation with $\boldsymbol{a}(x) = \boldsymbol{\xi}(x)$ and we eliminate the exponential. In this *unitary gauge* the $W^\pm$ and Z acquire their mass. Using equation (A.32) – without the exponential –, equation (A.28), and equation (A.30), we arrive to explicit mass terms for the gauge bosons. The Higgs related part of the Lagrangian becomes:

$$\mathcal{L} = \frac{1}{2}(\partial_\mu H)^2 + \frac{1}{4}g^2 W^+W^-(\upsilon + H)^2 + \frac{1}{8}ZZ(\upsilon + H)^2 - V\frac{1}{2}(\upsilon + H)^2. \tag{A.33}$$

From the equation above, we realize that the masses of the W and Z are

$$M_W = \frac{1}{2}g\upsilon \quad \text{and} \quad M_Z = \frac{1}{2}g_Z\upsilon = \frac{M_W}{\cos\theta_W}. \tag{A.34}$$

After some manipulation, equation (A.33) describes a scalar boson H with cubic

and quartic self-interactions, which couples to the weak gauge bosons with cubic and quartic interactions and does not interact electromagnetically. Its mass is

$$M_H = \sqrt{-2\mu^2}. \tag{A.35}$$

There are two kinds of spin-$\frac{1}{2}$ fermions, the leptons and the quarks. The charged leptons interact electromagnetically and weakly, while the neutral leptons (neutrinos) interact only weakly. The quarks are all charged, so they interact electromagnetically and weakly. The basic difference is that they also interact strongly. The leptons and quarks acquire their masses through their Yukawa couplings to the Higgs doublet.

A.3.3 Lepton Masses

In the weak isospin formalism, the left-handed leptons are written in doublets (their weak isospin is $\frac{1}{2}$) and the right-handed charged leptons are singlets (their weak isospin is zero). There are no right-handed neutrinos in the Standard Model. The Lagrangian that corresponds to the Yukawa coupling between the Higgs doublet Φ and the lepton doublet ℓ_L is

$$\mathcal{L}_{\text{Yukawa}} = -G_l \left[\bar{\ell}_R(\Phi^\dagger \ell_L) + (\bar{\ell}_L \Phi)\ell_R\right], \tag{A.36}$$

where

$$\ell_L = \begin{pmatrix} \nu_l \\ l \end{pmatrix}_L, \tag{A.37}$$

and l is the charged lepton (electron, muon or tau) and ν_l is the corresponding neutrino. We understand that there are 3 terms of the form (A.36) in the total Lagrangian. Notice that couplings between different lepton flavors are not allowed, due to lepton number conservation. Using the unitary form of $\Phi(x)$, we get

$$\mathcal{L}_{\text{Yukawa}} = -\frac{G_l \upsilon}{\sqrt{2}}\bar{l}l - \frac{G_l}{\sqrt{2}}H\bar{l}l. \tag{A.38}$$

This equations tells us that the mass of the charged lepton l is

$$M_l = \frac{G_l \upsilon}{\sqrt{2}}, \tag{A.39}$$

and its coupling to the Higgs is $\frac{G_l}{\sqrt{2}}$. We realize that we do not really answer the question why the masses of the charged leptons are the ones we observe. We have to understand why the charged leptons couplings to the Higgs are the ones we observe to answer this question. Also note that the neutrinos do not have mass or couplings to the Higgs, since there are no right-handed neutrinos.

A.3.4 Quark Masses

The quarks come in three generations just like the leptons. If we forget about Quantum Chromodynamics, the main difference is that they all come in left-handed and right-handed versions (whereas neutrinos are only left-handed). For each generation we have a weak isospin doublet and two isospin singlets

$$\mathcal{Q}_{iL} = \begin{pmatrix} q_i \\ q_i' \end{pmatrix}_L, \quad q_{iR}, \quad q'_{iR}, \tag{A.40}$$

where (q_i, q_i') are the weak eigenstates of the quarks and $i = 1, .., 3$ for three quark generations. The most general Yukawa interaction is

$$\mathcal{L}_{\text{Yukawa}} = -\sum_{i=1}^{3}\sum_{j=1}^{3}\left[\tilde{G}_{ij}\bar{q}_{iR}(i\tau_2\Phi^*)^\dagger D_{iL} + G_{ij}\bar{q'}_{iR}\Phi^\dagger D_{iL}\right] + \text{h.c.}, \tag{A.41}$$

where G_{ij} and $\tilde{G}_{ij}$ are coupling constants, and "h.c." means hermitian conjugate. When Φ and its conjugate acquire a vacuum expectation value, the mass terms become

$$\overline{(q_1, q_2, q_3)_R}\mathcal{M}^q \begin{pmatrix} q_1 \\ q_2 \\ q_3 \end{pmatrix}_L + \text{h.c.}, \tag{A.42}$$

and

$$\overline{(q_1', q_2', q_3')_R}\mathcal{M}^{q'}\begin{pmatrix} q_1' \\ q_2' \\ q_3' \end{pmatrix}_L + \text{h.c.}, \tag{A.43}$$

where $\mathcal{M}^q_{ij} = \frac{v}{\sqrt{2}}\tilde{G}_{ij}$ and $\mathcal{M}^{q'}_{ij} = \frac{v}{\sqrt{2}}G_{ij}$ are quark mass matrices. These mass matrices are not diagonal, so the weak eigenstates of the quarks are not the mass eigenstates. For this reason, we define the following unitary transformations

$$\begin{pmatrix} q_1 \\ q_2 \\ q_3 \end{pmatrix}_{L,R} = U_{L,R}\begin{pmatrix} u \\ c \\ t \end{pmatrix}_{L,R} \quad \text{and} \quad \begin{pmatrix} q_1' \\ q_2' \\ q_3' \end{pmatrix}_{L,R} = D_{L,R}\begin{pmatrix} d \\ s \\ b \end{pmatrix}_{L,R} \tag{A.44}$$

which diagonalize the M matrices

$$\begin{aligned} U_R^{-1}\mathcal{M}^q U_L &= \begin{pmatrix} m_u & 0 & 0 \\ 0 & m_c & 0 \\ 0 & 0 & m_t \end{pmatrix} \\ D_R^{-1}\mathcal{M}^{q'} D_L &= \begin{pmatrix} m_d & 0 & 0 \\ 0 & m_s & 0 \\ 0 & 0 & m_b \end{pmatrix}, \end{aligned} \tag{A.45}$$

where the diagonal elements are the quark masses. The quark mass eigenstates u, c, t are linear combinations of the weak eigenstates q_1, q_2, q_3 and the quark mass eigenstates d, s, b are linear combinations of the weak eigenstates q_1', q_2', q_3'. The bilinear terms of the charged-current weak interactions are

$$\overline{(q_1, q_2, q_3)_L}\gamma_\mu\begin{pmatrix} q_1' \\ q_2' \\ q_3' \end{pmatrix}_L = \overline{(u, c, t)_L}U_L^\dagger D_L\gamma_\mu\begin{pmatrix} d \\ s \\ b \end{pmatrix}_L, \tag{A.46}$$

where $V \equiv U_L^\dagger D_L$ is the generation mixing matrix, the most common form of which is the one constructed by Cabbibo-Kobayashi-Maskawa (CKM). There is no similar

matrix for the neutral-current weak interactions, since the bilinears have the form

$$\overline{(q_1, q_2, q_3)_L}\gamma_\mu \begin{pmatrix} q_1 \\ q_2 \\ q_3 \end{pmatrix}_L = \overline{(u, c, t)_L} U_L^\dagger U_L \gamma_\mu \begin{pmatrix} u \\ c \\ t \end{pmatrix}_L , \tag{A.47}$$

and $U_L^\dagger U_L = 1$. In other words there are no flavor-changing neutral currents, in accordance with the experimental observation; only flavor-conserving weak neutral currents have been observed [23]. Finally, since we observe flavor-changing charged-currents, the matrix $V \neq 1$, so $U_L \neq D_L$. Since these matrices diagonalize $\mathcal{M}_{ij}^q$ and $\mathcal{M}_{ij}^{q'}$, we conclude that $\mathcal{M}_{ij}^q \neq \mathcal{M}_{ij}^{q'}$ and consequently $\tilde{G}_{ij} \neq G_{ij}$, which means that the right-handed weak quark singlets are coupled to the left-handed weak quark doublet and the right-handed weak quark with different strengths and this is true for all 9 flavor combinations.

A.4 Quantum Chromodynamics

The final piece of the Standard Model is the Quantum Chromodynamics (QCD) that describes the strong interactions transmitted by the gluons. The quarks and gluons are the only particles that interact strongly. It is an experimental fact that there the quarks come in three colors (strong charges). The first proof was the discovery of the Δ^{++} baryon, that has three identical quarks (uuu). The only way for three fermions to be in the same state is to have three different quantum numbers, which in our case is color. Because of the three colors, the non-abelian symmetry of the QCD Lagrangian is $SU(3)$. Following the established procedure, the QCD Lagrangian is

$$\mathcal{L} = -\frac{1}{4} F_{a\mu\nu} F_a^{\mu\nu} + \bar{\psi}_j (i\gamma^\mu D_{\mu jk} - m_j \delta_{jk}) \psi_k, \tag{A.48}$$

where the covariant derivative is

$$D_{\mu jk} = \delta_{jk}\partial_\mu + i g_s T_{ajk} G_{a\mu}, \tag{A.49}$$

where G_a^μ are the gluon fields, T_a are the $SU(3)$ generators, g_s is the strong coupling and m_j are the masses of the quarks. To generate $SU(3)$ we need 8 generators, so the index a takes the values $1, ..., 8$ while the indices j and k take the values $1, ..., 3$, since they are related to color. The delta functions make sure that the mass terms and the kinetic terms are properly included (they should involve one quark and not two quarks at a time) The gluon field tensor is

$$F_{a\mu\nu} = \partial_\mu G_{a\nu} - \partial_{a\nu} G_\mu - g_s f_{abc} G_{b\mu} G_{c\nu}, \tag{A.50}$$

where f_{abc} are the structure constants of SU(3) defining the Lie Algebra

$$[T_a, T_b] = i f_{abc} T_c. \tag{A.51}$$

The Lagrangian (A.48) includes a gluon self-interaction, characteristic of the non-abelian nature of the $SU(3)$ symmetry. It is also invariant under the infinitesimal local gauge transformations

$$\begin{aligned} \psi(x) &\to [1 - i g_s \alpha_a(x) T_a] \psi(x) \\ G_{a\mu}(x) &\to G_{a\mu}(x) + \partial_\mu \alpha_a(x) + g_s f_{abc} \alpha_b(x) G_{c\mu}(x). \end{aligned} \tag{A.52}$$

One of the characteristics of the QCD is the appearance of divergencies in calculations such as infrared divergencies (appearing at low energies), ultraviolet divergencies (appearing at high energies) or colinear (appearing when the angle between two momenta is almost zero). The way to solve these problems is to introduce new parameters (propagator mass, momentum cut-off Λ in integration or decreased space-time dimensions $D - 2\epsilon$), redo the calculations and then absorb the parameters in the existing physical quantities by redefining them. This process is called "renormalization".

The other peculiarity of QCD is the asymptotic freedom and infrared slavery. The strong coupling constant α_s goes to zero at high momenta transfers (or low distances) between the strongly interacting particles. This means that we can use perturbation for particles that are very close to each other, like the valence quarks in a hadron. They behave like almost free particles, hence the term "asymptotic freedom". At

the same time the quarks inside a hadron are "infrared slaves" as at low energies (or long distances) the strong coupling becomes so big, that they can never escape their hadron without producing more hadrons in the process. If the potential energy of the "bond" that connects the outgoing quark with the rest of the valence and sea quarks becomes higher than the energy of a quark-antiquark pair produced out of vacuum, a *jet* of hadrons is created. These jets are an the evidence for the existence of quarks, since there is no way to separate the quarks from their hadrons and directly observe them [24].

A.5 Feynman Diagrams and Practical Calculations

In the previous sections we summarized the Standard Model theoretical framework. A complete theory should describe all physical processes observed in nature or in the laboratory. In this section we will describe the connection between the abstract theoretical formulas and practical physical quantities that are experimentally measured. We will concentrate on the cross sections predictions of the theory, because the subject of this thesis is the differential cross section of the W production in a collider.

A common collision experiment involves two initial particles that interact with each other and produce a number of other particles. We can write the total Hamiltonian of the system, as a sum of the free Hamiltonian H_0 and the interaction Hamiltonian H_I

$$H = H_0 + H_I. \tag{A.53}$$

Suppose we have some wavepackets that are initially (at time $-T$) free, they interact through H_I for some time $2T$ and at time T we have the creation of some new wavepackets that are also free. We define a wavepacket in space as

$$|\phi\rangle = \int \frac{d^3k}{(2\pi)^3} \frac{1}{\sqrt{2E_{\boldsymbol{k}}}} \phi(\boldsymbol{k})|\boldsymbol{k}\rangle, \tag{A.54}$$

where $\phi(\boldsymbol{k})$ is the Fourier transformation of the spatial wavefunction and $|\boldsymbol{k}\rangle$ is a one-particle state of momentum $\boldsymbol{k}$ in the interacting theory.

Suppose we initially have two fields ϕ_A and ϕ_B that interact with each other through H_I to give us n fields ϕ_1, ϕ_2, ... ϕ_n. The probability for this to happen is

$$\mathcal{P} = |\langle \phi_1 \phi_2 \cdots \phi_n | \phi_A \phi_B \rangle|^2. \tag{A.55}$$

The cross section is defined to be

$$\sigma = \int d^2 b \mathcal{P}(\boldsymbol{b}), \tag{A.56}$$

where $\boldsymbol{b}$ are the possible impact parameters in the colliding beams. Using (A.54) the cross section is written in terms of the interacting-theory states of definite momentum, as follows:

$$d\sigma = dF |\langle \boldsymbol{p}_1 \boldsymbol{p}_2 \cdots | \boldsymbol{k}_A \boldsymbol{k}_B \rangle|^2, \tag{A.57}$$

where F is the factor that contains the product of the factors in front of the momentum states of the form (A.54). The final states are calculated at time T, whereas the initial states are calculated at time $-T$. We can use the time-evolution operator, to shift the states to define them at a common reference time

$$d\sigma = dF | \lim_{T\to\infty} \langle \boldsymbol{p}_1 \boldsymbol{p}_2 \cdots | e^{-iH(2T)} | \boldsymbol{k}_A \boldsymbol{k}_B \rangle|^2 \equiv dF |\langle \boldsymbol{p}_1 \boldsymbol{p}_2 \cdots | \mathcal{S} | \boldsymbol{k}_A \boldsymbol{k}_B \rangle|^2, \tag{A.58}$$

We just defined the unitary operator called the $\mathcal{S}$-matrix. If we want to separate only the part of the $\mathcal{S}$-matrix that is causing the interaction, we define the $\mathcal{T}$-matrix as

$$\mathcal{S} = \mathbf{1} + i\mathcal{T}. \tag{A.59}$$

We can also define the invariant amplitude $\mathcal{M}$, in order to separate kinematics (phase factors) from dynamics

$$\langle \boldsymbol{p}_1 \boldsymbol{p}_2 \cdots | i\mathcal{T} | \boldsymbol{k}_A \boldsymbol{k}_B \rangle = (2\pi)^4 \delta^{(4)}(k_A + k_B - \sum_f p_f) \cdot i\mathcal{M}(k_A + k_B \to p_1 p_2 \cdots). \tag{A.60}$$

Using (A.57) and (A.60) and summing over all final states and averaging over all initial states, we get the cross section for the interacting transition from the initial to

the final states

$$d\sigma = dJ \sum |\mathcal{M}(k_A + k_B \to p_1 p_2 \cdots)|^2, \tag{A.61}$$

where the variable dJ includes the infinitesimal phase space factors, the initial flux factors and the normalization factors. The states of equation (A.60) are states of the interacting theory. In a perturbative picture we would like to express everything in terms of the free theory states. We use the relation

$$|\boldsymbol{k}_A \boldsymbol{k}_B\rangle \sim \lim_{T\to\infty(1-i\epsilon)} e^{-iHT} |\boldsymbol{k}_A \boldsymbol{k}_B\rangle_0, \tag{A.62}$$

where $|\boldsymbol{k}_A \boldsymbol{k}_B\rangle_0$ are the free theory states, the ones we would like to use to estimate the interaction theory solutions. Finally, we use the two-point correlation function to write

$$\begin{aligned}
\langle \boldsymbol{p}_1 \boldsymbol{p}_2 \cdots |\mathcal{S}| \boldsymbol{k}_A \boldsymbol{k}_B\rangle &= \lim_{T\to\infty(1-i\epsilon)} {}_0\langle \boldsymbol{p}_1 \boldsymbol{p}_2 \cdots | e^{-iH(2T)} |\boldsymbol{k}_A \boldsymbol{k}_B\rangle_0 \\
&= \lim_{T\to\infty(1-i\epsilon)} {}_0\langle \boldsymbol{p}_1 \boldsymbol{p}_2 \cdots | T(\exp[-i\int_{-T}^{T} dt H_I(t)]) |\boldsymbol{k}_A \boldsymbol{k}_B\rangle_0 \\
&= \lim_{T\to\infty(1-i\epsilon)} {}_0\langle \boldsymbol{p}_1 \boldsymbol{p}_2 \cdots | T(\exp[-i\int d^4x \mathcal{L}_I(x)]) |\boldsymbol{k}_A \boldsymbol{k}_B\rangle_0
\end{aligned} \tag{A.63}$$

where T denotes time-order. If the coupling of the interacting Lagrangian $\mathcal{L}_I$ is small enough, we can Taylor-expand the exponential, keep only the few first terms of the expansion and still get a good prediction of the cross-section. This is the main idea of the perturbation theory. Expression (A.63) becomes

$$\begin{aligned}
\langle \boldsymbol{p}_1 \boldsymbol{p}_2 \cdots |\mathcal{S}| \boldsymbol{k}_1 \boldsymbol{k}_2\rangle &= {}_0\langle \boldsymbol{p}_1 \boldsymbol{p}_2 \cdots |\boldsymbol{k}_1 \boldsymbol{k}_2\rangle_0 + {}_0\langle \boldsymbol{p}_1 \boldsymbol{p}_2 \cdots | T(-i\int d^4x \mathcal{L}_I(x)) |\boldsymbol{k}_1 \boldsymbol{k}_2\rangle_0 + \\
&\quad {}_0\langle \boldsymbol{p}_1 \boldsymbol{p}_2 \cdots | \frac{1}{2!} T(\int d^4x \mathcal{L}_I(x) \int d^4y \mathcal{L}_I(y)) |\boldsymbol{k}_1 \boldsymbol{k}_2\rangle_0 + \cdots
\end{aligned} \tag{A.64}$$

The first term contains no interactions (the particles do not "see" each other). The second term contains one interaction, the third term contains two interactions and so on. Using Wick's theorem, we can write the time-ordered sum of the product of the fields that appear in the $\mathcal{L}_I$ as a normal order (*creation* operators are to the left of *annihilation* operators) of the sum of all possible contractions of the fields. By

contraction of two fields we mean the Feynman propagator, which is the commutation (bosons) or anticommutation (fermions) of the two fields, respecting causality. After contracting the fields and producing the propagators, we contract any remaining fields with the initial and final states of definite momentum.

In the unbroken Electroweak and the QCD theory we can have three kinds of interaction Lagrangians:

$$\begin{aligned}
\mathcal{L}_I^{(1)} &= \bar{\psi}\gamma^\mu B_\mu c O \psi \\
\mathcal{L}_I^{(2)} &= -c f^{abc}(\partial_\kappa B^a_\lambda B^{\kappa b} B^{\lambda c}) \text{ and} \\
\mathcal{L}_I^{(3)} &= -c^2(f^{eab}B^a_\kappa B^b_\lambda)(f^{ecd}B^{\kappa c}B^{\lambda d}),
\end{aligned} \tag{A.65}$$

where $\mathcal{L}_I^{(1)}$ describes the interaction of two fermions with a gauge boson (for interaction with a photon it is $B_\mu = A_\mu$, $c = e$ and $\mathcal{O} = Q$, for interaction with a Z it is $B_\mu = Z_\mu$, $c = g_Z$ and $\mathcal{O} = (T_{L3} - x_W Q)$, for interaction with a $W^\pm$ it is $B_\mu = W^\pm_\mu$, $c = g$ and $\mathcal{O} = T^\pm_L$ and for interaction with a gluon it is $B_\mu = G_\mu$, $c = g_s$ and $\mathcal{O} = T^\pm_L$), $\mathcal{L}_I^{(2)}$ describes a cubic interaction of gauge bosons (the coupling is $c = g\sin\theta_W$ for W^+W^-Z interaction and $c = g\cos\theta_W$ for $W^+W^-\gamma$ interaction and g_s for ggg interaction.) $\mathcal{L}_I^{(3)}$ describes a quartic interaction of gauge bosons (the coupling is $c = g^2$ for $W^+W^-W^+W^-$ interaction, $c = g^2\cos^2\theta_W$ for W^+W^-ZZ interaction, $c = e^2$ for $W^+W^-\gamma\gamma$ interaction, $c = eg\cos\theta_W$ for $W^+W^-Z\gamma$ interaction and $c = g_s^2$ for $gggg$ interaction). In the broken Electroweak theory we have in addition interactions of the fermions with the Higgs field, cubic interactions involving the Higgs field (HHH, W^+W^-H and ZZH) and quartic interactions involving the Higgs field ($HHHH$, W^+W^-HH, $ZZHH$). The interactions above are the only ones allowed in the theory.

In our theory the free fermions fields are given by

$$\psi(x) = \int \frac{d^3p}{(2\pi)^3}\frac{1}{\sqrt{2E_{\boldsymbol{p}}}}\sum_s (a^s_{\boldsymbol{p}} u^s(p)e^{-ip\cdot x} + b^{s\dagger}_{\boldsymbol{p}} v^s(p)e^{ip\cdot x}), \tag{A.66}$$

where $u^s(p)$ and $u^s(p)$ are 4-spinors which correspond to the fermion and antifermion 4-spinors, $a^s_{\boldsymbol{p}}$ is the annihilation operator of a particle with spin s and momentum $\boldsymbol{p}$,

and $b^{s\dagger}_{\boldsymbol{p}}$ is the creation operator of an antiparticle.

The free vector boson fields are given by

$$B_\mu(x) = \int \frac{d^3p}{(2\pi)^3}\frac{1}{\sqrt{2E_{\boldsymbol{p}}}}\sum_{r=0}^{3}(a^r_{\boldsymbol{p}}\epsilon^r_\mu(p)e^{-ip\cdot x} + a^{r\dagger}_{\boldsymbol{p}}\epsilon^{r*}_\mu(p)e^{ip\cdot x}e^{ip\cdot x}), \tag{A.67}$$

where $\epsilon^r_\mu(p)$ are the polarization vectors. The only scalar boson of the theory (the Higgs boson) is

$$h(x) = \int \frac{d^3p}{(2\pi)^3}\frac{1}{\sqrt{2E_{\boldsymbol{p}}}}(a_{\boldsymbol{p}}e^{-ip\cdot x} + a^\dagger_{\boldsymbol{p}}e^{ip\cdot x}). \tag{A.68}$$

Using equations (A.64), (A.65), (A.66), (A.67) and (A.68) we can arrive to expressions for any physical process.

We will continue for a $2 \to 2$ process of two particles colliding and producing two particles. For a $2 \to 2$ process the leading-order term contains two interactions, so the interacting part of (A.64) becomes

$$\langle \boldsymbol{p}_1\boldsymbol{p}_2|i\mathcal{T}|\boldsymbol{k}_1\boldsymbol{k}_2\rangle = {}_0\langle \boldsymbol{p}_1\boldsymbol{p}_2|\frac{1}{2!}T(\int d^4x\mathcal{L}_I(x)\int d^4y\mathcal{L}_I(y))|\boldsymbol{k}_1\boldsymbol{k}_2\rangle_0 \tag{A.69}$$

For the simplest interaction of two fermions through only one gauge boson (tree level) the interaction Lagrangian is $\mathcal{L}^{(1)}$. After substituting the time-order with the normal order and keeping only one contraction (one gauge boson interaction) we have

$$\begin{aligned}&\langle \boldsymbol{p}_1\boldsymbol{p}_2|i\mathcal{T}|\boldsymbol{k}_1\boldsymbol{k}_2\rangle \sim \\ &{}_0\langle \boldsymbol{p}_1\boldsymbol{p}_2|\frac{1}{2!}N(\int d^4x\bar{\psi}(x)\gamma^\mu B_\mu(x)\mathcal{O}\psi(x)\int d^4y\bar{\psi}(y)\gamma^\mu B_\mu(y)\mathcal{O}\psi(y))|\boldsymbol{k}_1\boldsymbol{k}_2\rangle_0.\end{aligned} \tag{A.70}$$

We contract the boson fields B_μ with each other to produce the gauge boson propagator term and contract the remaining fermion fields with the initial and final state particles to produce the charge currents. Using equations (A.60), (A.66), (A.67) (A.70) and performing the contractions as described, the result is

$$i\mathcal{M} = (-ic)^2\bar{u}(k_1)\gamma^\mu\mathcal{O}u(k_2)\cdot\ [\text{Propagator}]\ \cdot\bar{u}(p_1)\gamma^\nu\mathcal{O}u(p_2). \tag{A.71}$$

Similarly we calculate higher order terms of the expansion.

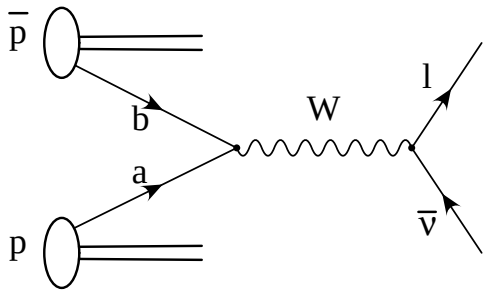

Figure A.1 W production at tree level and low p_T at a $p\bar{p}$ collider.

Practical rules (the Feynman rules) can be defined, based on Equation (A.64) and the form of the interacting Hamiltonian to calculate the invariant amplitude $\mathcal{M}$. We start from a Feynman diagram and assign a value for every propagator (intermediate fermion or boson), external lines (interacting fermions or bosons) and vertices (couplings). For the tree-level W production from the collision of two quarks, we start with the Feynman Diagram shown in Figure A.1.

We assign $-i\frac{g}{\sqrt{2}}\gamma^\mu\frac{1}{2}(1-\gamma^5)$ to the vertices, u_{q_1} and v_{q_2} to the quark external lines, u_ν and v_l to the neutrino and lepton external lines and $\frac{-ig_{\mu\nu}}{p^2-M_W^2+iM_W\Gamma_W}$ to the W propagator. We use the u and v to denote incoming fermion and antifermion and $\bar{u}$ and $\bar{v}$ to denote outgoing fermion and antifermion. The invariant amplitude is then constructed out of these quantities. The expressions "outgoing" and "incoming" refer to the charge flow of the external lines. For an antifermion, the momentum direction is opposite to the direction of the external lines. The Feynman rules directly give us the expression of Equation (A.71) for the W production:

$$\begin{aligned} i\mathcal{M} &= (\frac{-ig}{\sqrt{2}})^2 V_{q_1q_2}\bar{v}_{q_2}\gamma^\mu\frac{1}{2}(1-\gamma^5)u_{q_1}\frac{-ig_{\mu\nu}}{p^2-M_W^2+iM_W\Gamma_W}\bar{u}_\nu\gamma^\mu\frac{1}{2}(1-\gamma^5)v_l \\ &= i(\frac{g^2}{8})V_{q_1q_2}\bar{v}_{q_2}\gamma^\mu(1-\gamma^5)u_{q_1}\frac{1}{p^2-M_W^2+iM_W\Gamma_W}\bar{u}_\nu\gamma_\mu(1-\gamma^5)v_l \quad \text{(A.72)} \end{aligned}$$

where q_2 is the quark with the lower charge, p is the momentum of the W and $V_{q_1q_2}$ is the element of the CKM matrix (quark mixing). Using Equation (A.72), averaging over the initial spins and summing over the final spins, the cross section (A.61),

becomes

$$d\sigma = dJ \sum_{\text{spins}} |\mathcal{M}|^2 = dJ(\frac{g^4}{16})\frac{|V_{q_1 q_2}|^2}{(p^2 - M_W^2)^2 + (M_W \Gamma_W)^2} L_{\mu\nu} H^{\mu\nu}, \tag{A.73}$$

were we defined the lepton tensor as

$$L_{\mu\nu} = \sum_{spins} [\bar{u}_\nu \gamma_\mu (1 - \gamma^5) \upsilon_l][\bar{u}_\nu \gamma_\nu (1 - \gamma^5) \upsilon_l]^*, \tag{A.74}$$

and the quark tensor as

$$H^{\mu\nu} = \sum_{spins} [\bar{\upsilon}_{q_2} \gamma^\mu (1 - \gamma^5) u_{q_1}][\bar{\upsilon}_{q_2} \gamma^\nu (1 - \gamma^5) u_{q_1}]^*. \tag{A.75}$$

The formalism of Equation (A.73) is used in Chapter 2, when we study the general production of the W in a hadron collider with a considerable transverse momentum, taking into account next-to-leading order Feynman diagrams as well.

Appendix B

Polar Angle Studies

B.1 Introduction

The study of the angular distribution of the W boson is done through the analysis of the azimuthal (ϕ) and polar (θ) angles of the decay charged lepton in the rest frame of the W. To get these angles, we have to boost to the W rest frame. However, this is not possible, because of our ignorance of the longitudinal momentum of the W, due to our inability to measure or estimate the longitudinal missing energy corresponding to the longitudinal neutrino momentum p_z^ν. Nevertheless, we can constrain p_z^ν using Equations (7.6) and (7.7). An important point is that the mass of the W (M_W) is not known on an event-by-event basis. However, we know that it follows the Breit-Wigner distribution and has to be greater than its transverse mass (which is measured in the laboratory). If we assign a mass to the W boson , there are two possible solutions for p_z^ν leading to two possible momenta for the W and two possible values of $\cos\theta$ and ϕ. If we choose to work on the Collins-Soper frame, both choices of p_z^ν, for a specific M_W, lead to the same ϕ and opposite $\cos\theta$. Consequently, the selection of the value of M_W for a particular event uniquely determines $|\cos\theta|$. The angle ϕ is better measured because the choice of M_W only causes a negligible systematic error in the measurement of ϕ. In this Appendix we discuss the problems in the reconstruction of $\cos\theta$.

B.2 Reconstruction of $\cos\theta$ Using DYRAD Events

The first natural step is to try to reconstruct the $\cos\theta$ using events from the DYRAD Monte Carlo generator. Since we know the true value of $\cos\theta$ for each generated event, we are able to compare it to the reconstructed value of $\cos\theta$. We run DYRAD at leading order in QCD (no gluon loops), to avoid the negative weights.

There are two issues pertinent to the reconstruction of the $\cos\theta$: the choice of the mass of the W and the choice of the right sign of $\cos\theta$. We will first use our knowledge of the W mass for each generated event, to try to correctly guess the sign of $\cos\theta$, without seriously distorting its distribution. In [78] the shape of the $\cos\theta$ is not important, so always the positive value of $\cos\theta$ was chosen. The $\cos\theta$ distributions of Figure 2.6, tells us that this method gives a successful reconstruction about 70% of the times. It cannot be used in our case, because the shape of the $\cos\theta$ carries the information we need.

Our method consists of constructing a multidimensional phase space filled with kinematic variables from DYRAD events. The two p_z^ν choices result in two different locations in our phase space. We choose the value of p_z^ν that falls to the location more heavily populated by the DYRAD events used to fill the phase space. This is the most probable phase space location leading to the most probable choice for the longitudinal momentum of the neutrino and the corresponding $\cos\theta$ sign.

We tried different variables and concluded that the most effective phase space is the four-dimensional space of the rapidities of the W, charged lepton, neutrino, and jet. Using this phase space (of 40 bins for each dimension) we arrive at $\sim$80% success in reconstructing the $\cos\theta$ and, more importantly, the shape of the $\cos\theta$ is preserved. This can be seen if Figure B.1. This approach capitalized on the kinematic correlations of the W boson, the charged lepton, and the neutrino, similar to those assosiated with the $W+\gamma$ production [79]. To demonstrate the correlations for the W^-+jet case, we show the scatter plots of the rapidity y_l of the charged lepton versus the rapidity y_W of the W^-, the rapidity y_ν of the neutrino versus the rapidity of the W^-, the rapidity $y_{\rm jet}$ of the jet versus the rapidity of the W^-, and the rapidity of the neutrino versus the rapidity of the charged lepton (Figure B.2). Figure B.3 shows the histograms of the corresponding rapidity differences $(y_l - y_W)$, $(y_\nu - y_W)$, $(y_{\rm jet} - y_W)$,

and $(y_\nu - y_l)$. These differences of rapidities are invariant under longitudinal Lorentz boosts.

The next step is to try to select a mass for the W, instead of using the actual one. This introduces a serious systematic uncertainty at the region around $\cos\theta = 0$. This is because the curve $M_W = f(p_z^\nu)$ given by Equations (7.6) and (7.7) is usually flat close to its minimum (depending on the kinematics of the particular event). This minimum corresponds to $M_W = M_T^W$ and $\cos\theta = 0$. Small variations in the selected mass lead to big variations in the resulting value of $|\cos\theta|$, if $M_T^W \sim M_W$. This correlation between $\cos\theta$ and M_T^W can be seen in Figure B.4, which depicts the scatter plot of M_T^W versus the $\cos\theta$, for DYRAD W+jet events up to order α_s^2. If the transverse mass of the W is close to the pole mass of the W, the uncertainty in the reconstruction of $|\cos\theta|$ is increased.

We use four methods for selecting a mass for the W:

1. We select the Breit-Wigner mass above the transverse mass of the W.

2. We select the pole mass or, if it is less than the transverse mass, select the transverse mass instead.

3. We select the pole mass or, if it is less than the transverse mass, select the Breit-Wigner mass above the transverse mass of the W.

4. We use the mass versus transverse mass DYRAD scatter plot to select a mass for the W.

The fourth method uses the M_W-versus-M_T^W scatter plot and our knowledge of M_T^W, to select a mass for the W. This scatter plot can be seen in Figure B.5. We used eight different scatter plots, depending on the transverse momentum of the W. Figures B.6 to B.9 show the $\cos\theta$ reconstructed and actual distributions for the four p_T^W regions. The $\cos\theta$ is reconstructed using the four methods of choosing the M_W (for the selection of a $|\cos\theta|$) and the four-dimensional phase-space (for the selection of the sign of $\cos\theta$). We conclude that the fourth method for selecting the mass, is the most effective one. Finally, to demonstrate how the ϕ angle is not affected at all by the selection of the M_W or the selection of the direction of the neutrino,

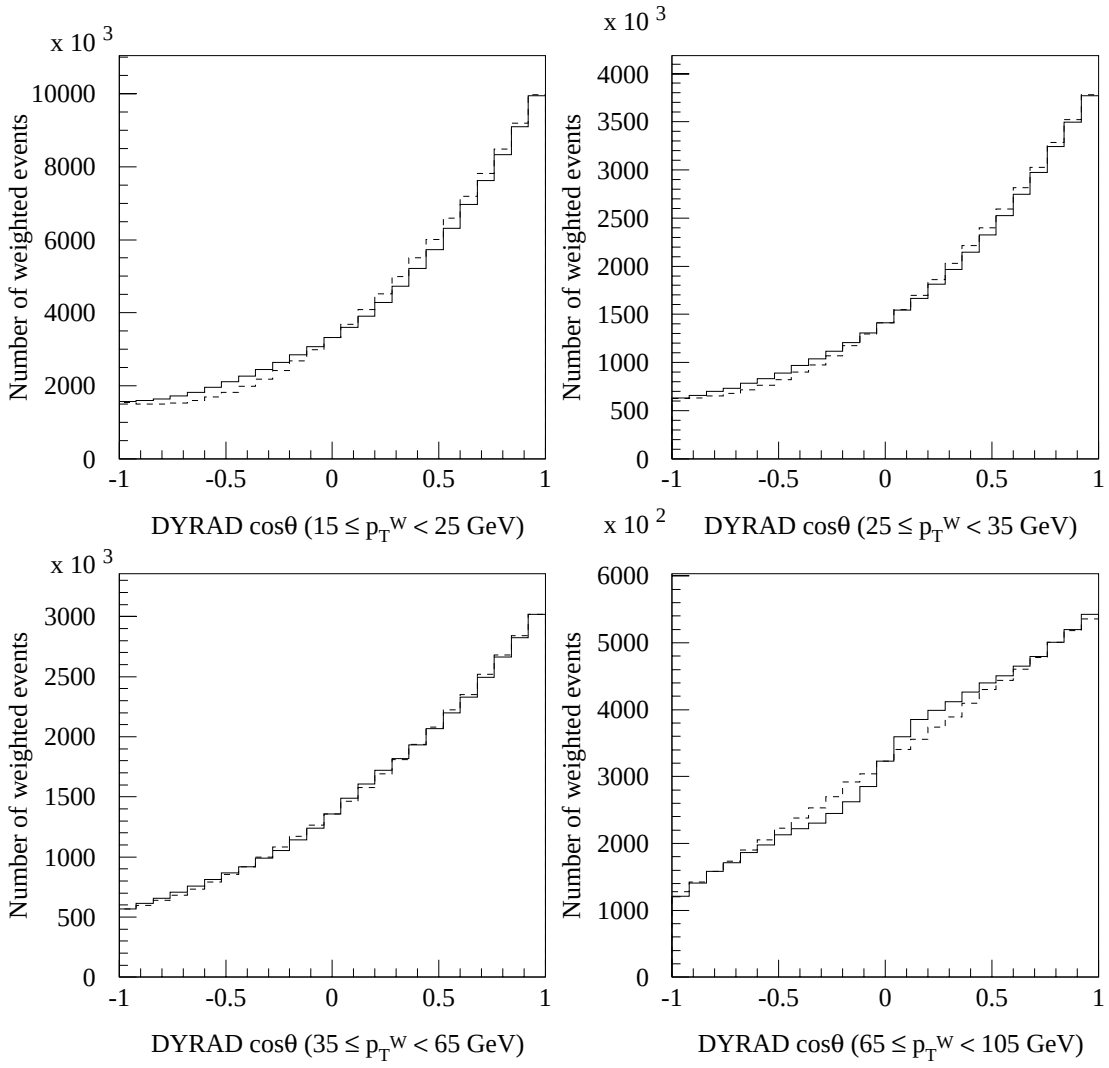

Figure B.1 The $\cos\theta$ reconstructed distributions (solid histograms) and actual distributions (dashed histograms), for leading-order (no gluon loops) DYRAD events, for four p_T^W regions. We use our knowledge of the mass of the W on an event-by-event basis to determine $|\cos\theta|$. We choose the sign of $\cos\theta$ using the four-dimensional phase-space of the rapidities of the charged lepton, neutrino, W boson, and jet at the generator level.

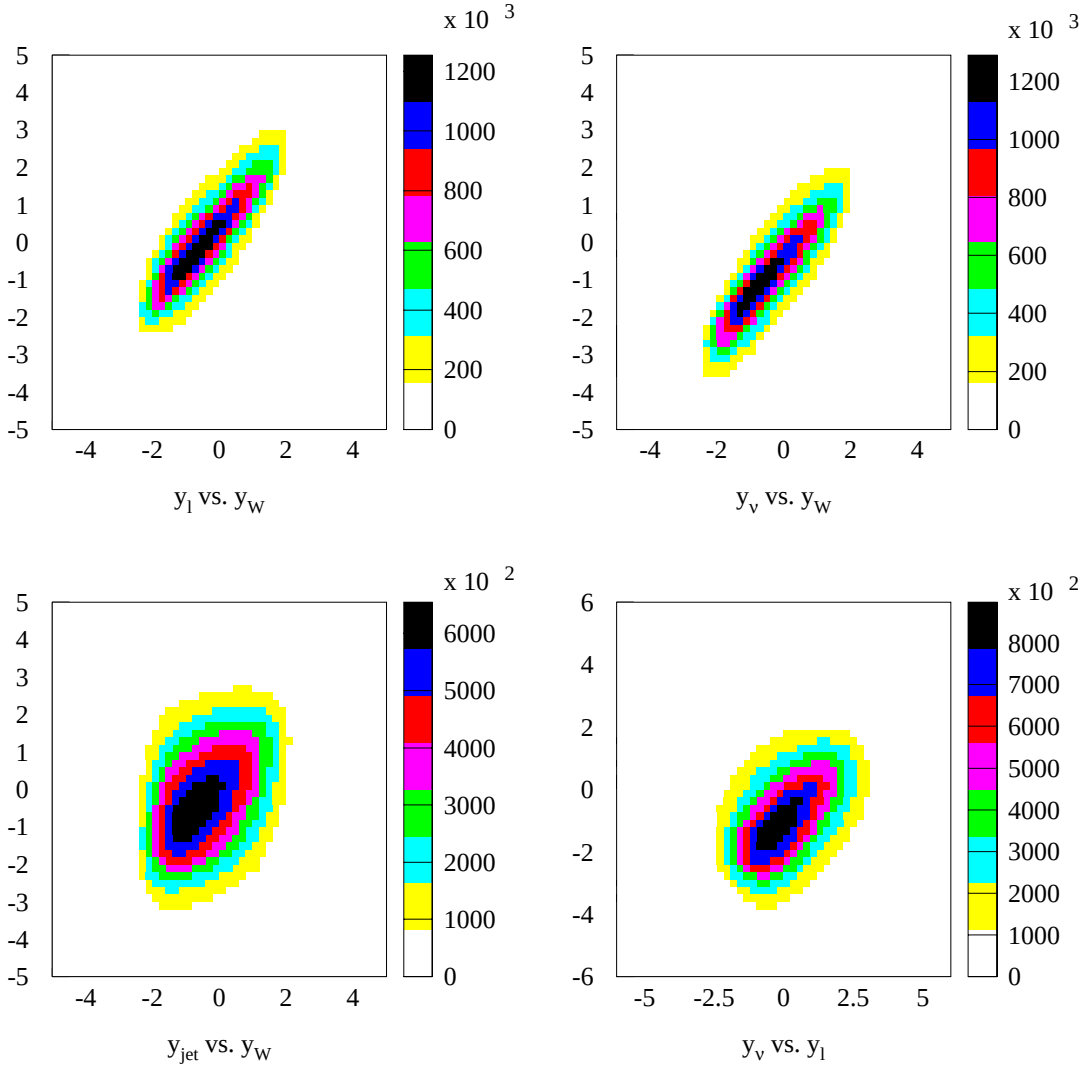

Figure B.2 The scatter plots of the rapidity y_l of the charged lepton versus the rapidity y_W of the W^- (upper left), the rapidity y_ν of the neutrino versus the rapidity of the W^- (upper right), the rapidity y_{jet} of the jet versus the rapidity of the W^- (lower left), and the rapidity of the neutrino versus the rapidity of the charged lepton (lower right).

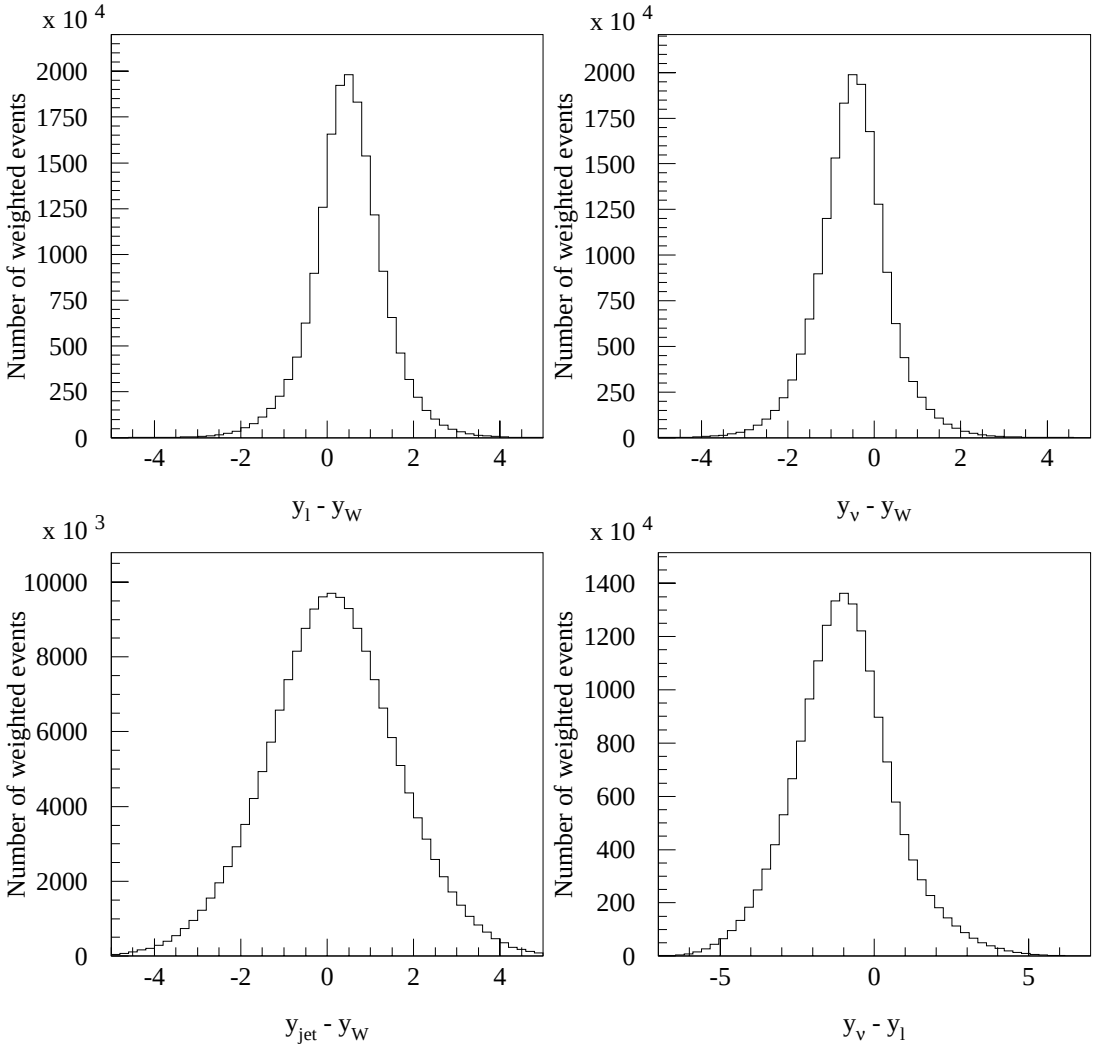

Figure B.3 The histograms of the corresponding rapidity differences $(y_l - y_W)$ (upper left plot), $(y_\nu - y_W)$ (upper right), $(y_{\rm jet} - y_W)$ (lower left plot), and $(y_\nu - y_l)$ (lower right). These differences of rapidities are invariant under longitudinal Lorentz boosts.

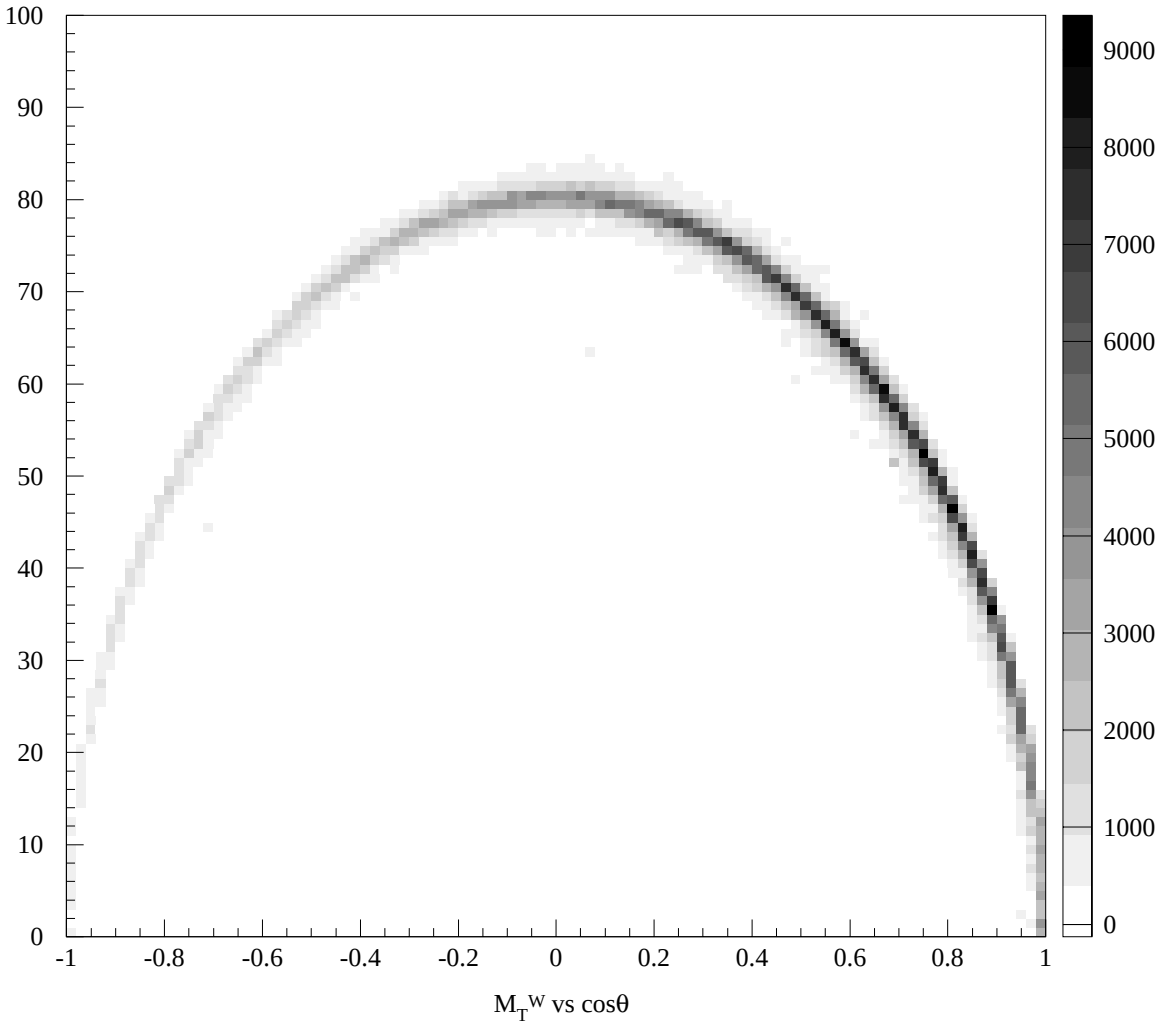

Figure B.4 The transverse mass of the W versus the $cos\theta$ of the charged lepton in the Collins-Soper frame, for DYRAD W+jet events up to order α_s^2. We see that the greatest uncertainty in the selection of a value for the polar angle θ is when $\cos\theta \sim 0$, which corresponds to transverse mass close to the pole mass of the W.

we show its true and reconstructed distributions overimposed for the four regions of the p_T^W (Figure B.10). We observe a perfect reconstruction of the ϕ angle. Figure B.11 shows the error in ϕ and $\cos\theta$ reconstruction as a function of transverse mass of the W and the scatter plots of reconstructed versus true ϕ and $|\cos\theta|$, for DYRAD data. We realize that the $\cos\theta$ reconstruction is difficult at high values of M_T^W, which correspond to low values of $|\cos\theta|$.

B.3 Reconstruction of $\cos\theta$ Using FMC Events

The situation is different, if we use FMC events instead of DYRAD events. Using the same phase-space filled with FMC events and the four methods of choosing a mass for the W, we arrive at plots shown in Figures B.12 to B.15 for electrons (the plots for the muons are similar). The reconstruction is not satisfactory, due to the smearing caused by the detector resolution and the effects of the acceptances and efficiencies, that affect our choice of the longitudinal direction of the neutrino and sign of $\cos\theta$. If we plot the $|\cos\theta|$ (Figures B.16 to B.19) in order to be insensitive to the choice of the sign of $\cos\theta$, we realize that the problem still exists and it is caused by the selection of the W mass. The situation is not different for data, so we conclude that the effects of the detector, as well as the systematic uncertainties caused by the choice of the mass of the W on an event-by-event basis, bias the shape of the $\cos\theta$ distribution and do not allow us to directly measure it. Again, the reconstruction of ϕ at the FMC level is not a problem at all, as shown in Figure B.20.

Future progress in the direct measurement of the polar angle θ could be achieved, if the bias of the W mass selection is resolved. Alternatively, a parameterization of this bias, for a specific mass selection technique, could be used, for the extraction of the true polar angle distribution. A better understanding of our detector acceptances and efficiencies is crucial for the application of this parameterization to experimental data and for the correct selection of the sign of $\cos\theta$. The determination of this sign leads to the complete reconstruction of the charged lepton polar angle distribution, that is necessary for the measurement of the A_4 and A_6 angular coefficients and the full understanding of the W differential cross section.

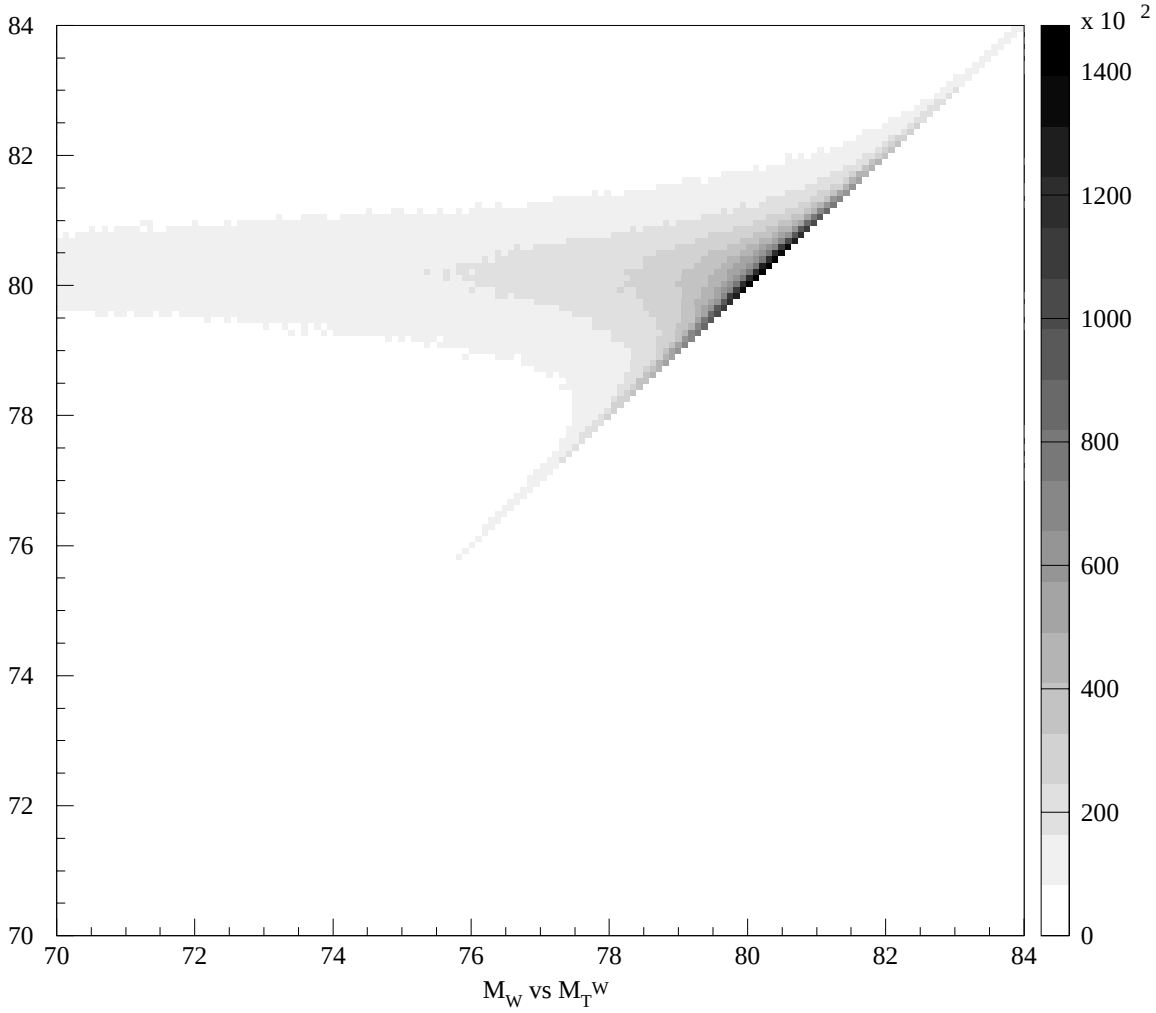

Figure B.5 The scatter plot of actual mass versus the transverse mass for DYRAD leading order (no gluon loops) events.

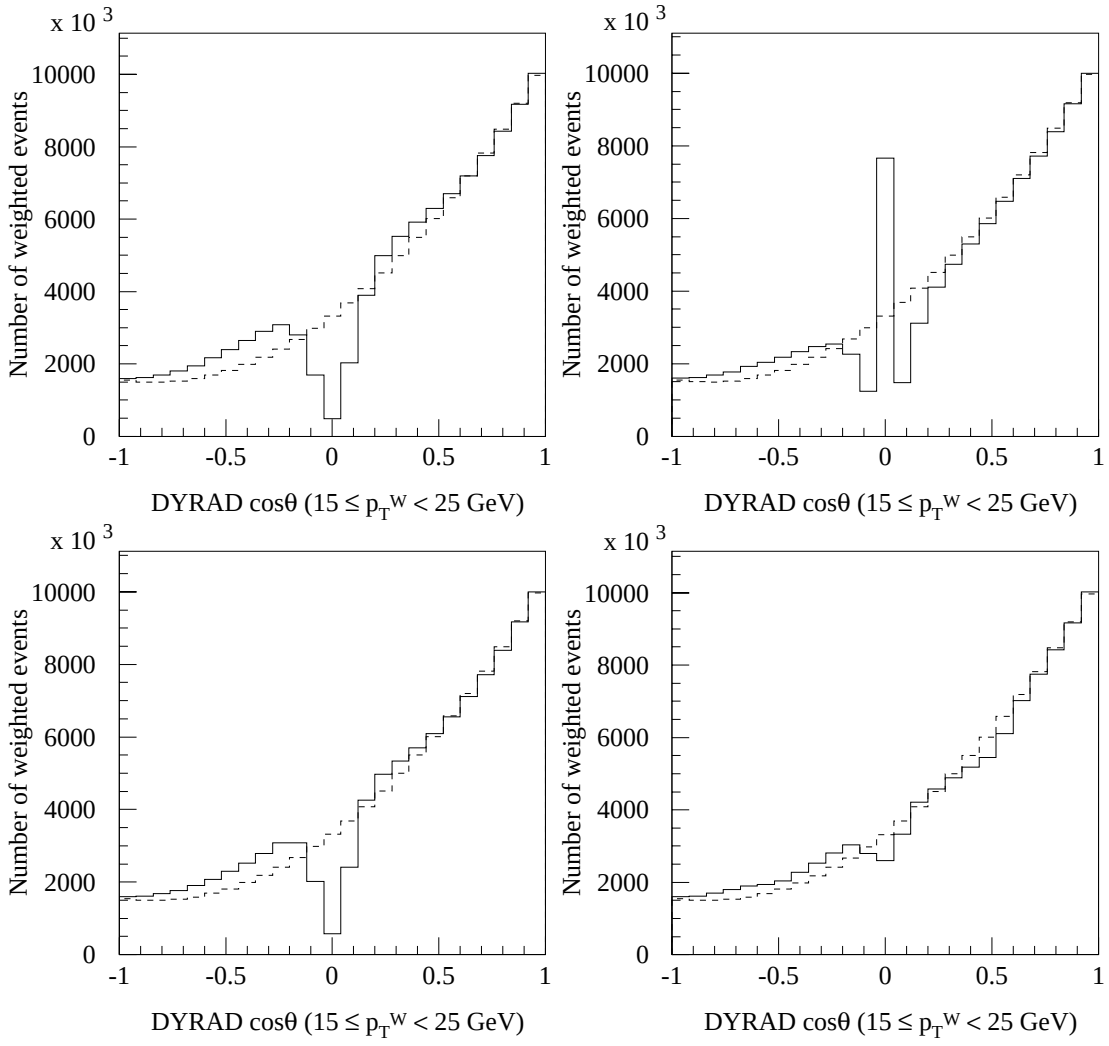

Figure B.6 The $\cos\theta$ reconstructed distributions (solid histograms) and actual distributions (dashed histograms), for leading-order (no gluon loops) DYRAD events with $15 \leq p_T^W < 25$ GeV, and for the four methods of selecting the mass for the W (method 1 is used in the upper left plot, method 2 in the upper right plot, method 3 in the lower left plot and method 4 in the lower right plot).

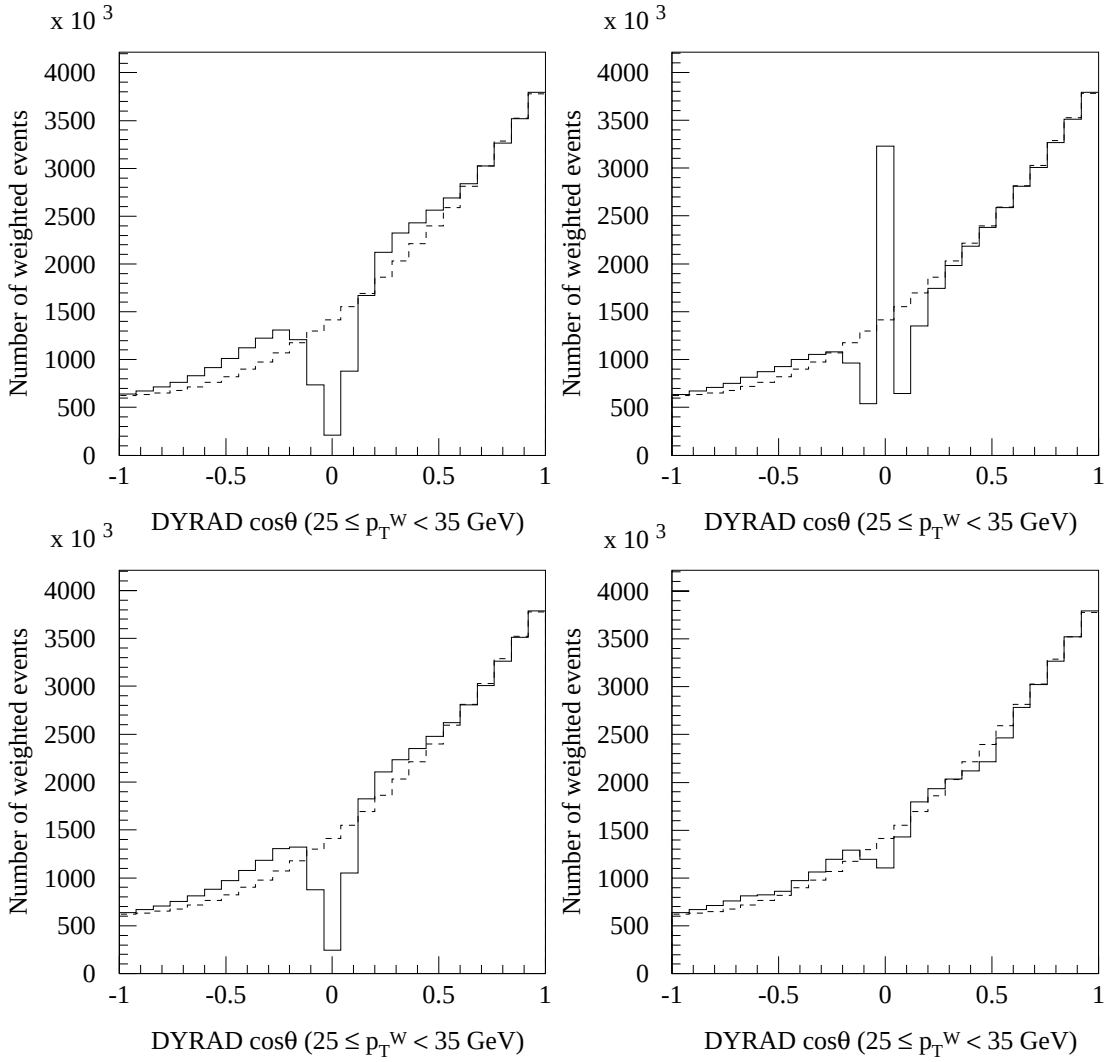

Figure B.7 The $\cos\theta$ reconstructed distributions (solid histograms) and actual distributions (dashed histograms), for leading-order (no gluon loops) DYRAD events with $25 \leq p_T^W < 35$ GeV, and for the four methods of selecting the mass for the W (method 1 is used in the upper left plot, method 2 in the upper right plot, method 3 in the lower left plot and method 4 in the lower right plot).

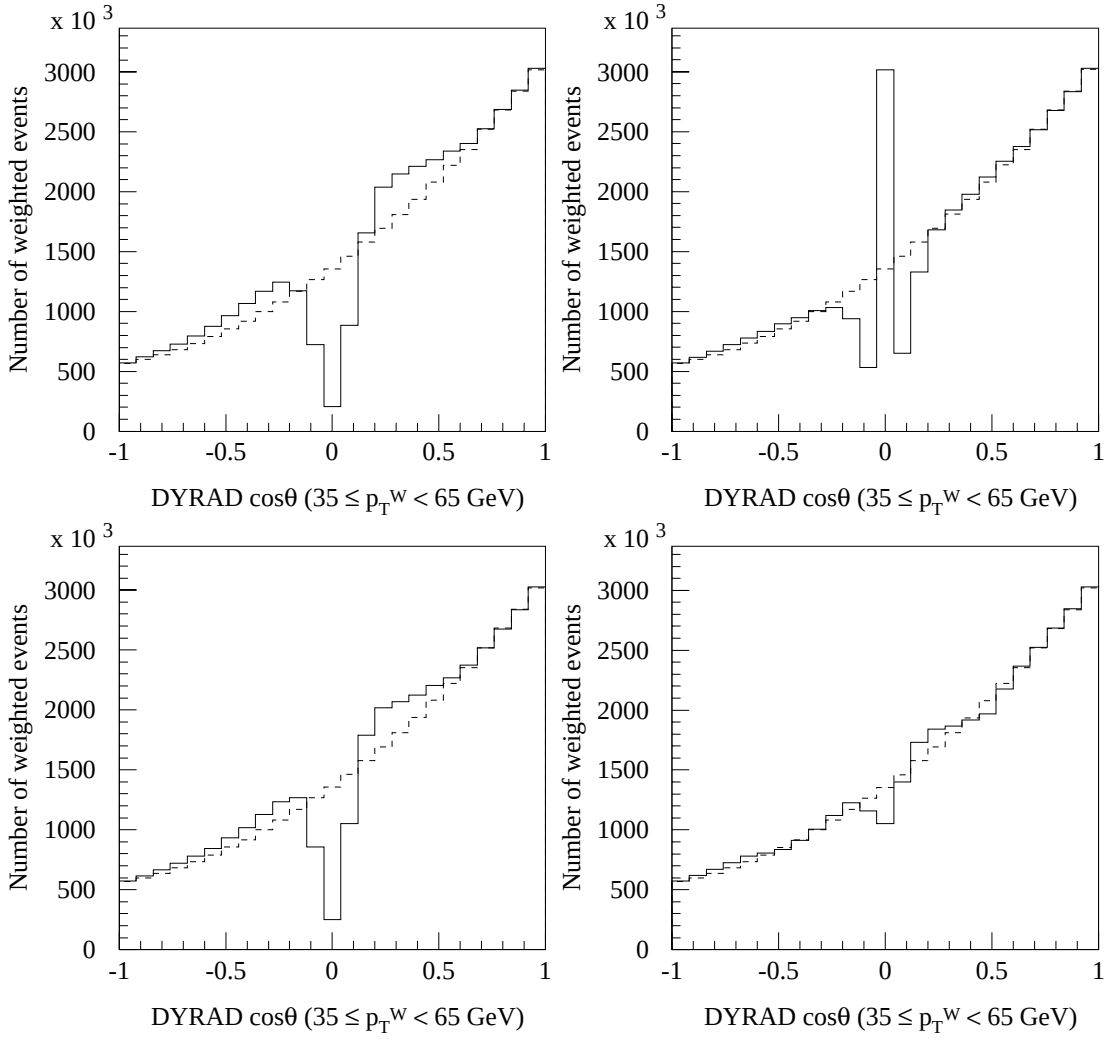

Figure B.8 The $\cos\theta$ reconstructed distributions (solid histograms) and actual distributions (dashed histograms), for leading-order (no gluon loops) DYRAD events with $35 \leq p_T^W < 65$ GeV, and for the four methods of selecting the mass for the W (method 1 is used in the upper left plot, method 2 in the upper right plot, method 3 in the lower left plot and method 4 in the lower right plot).

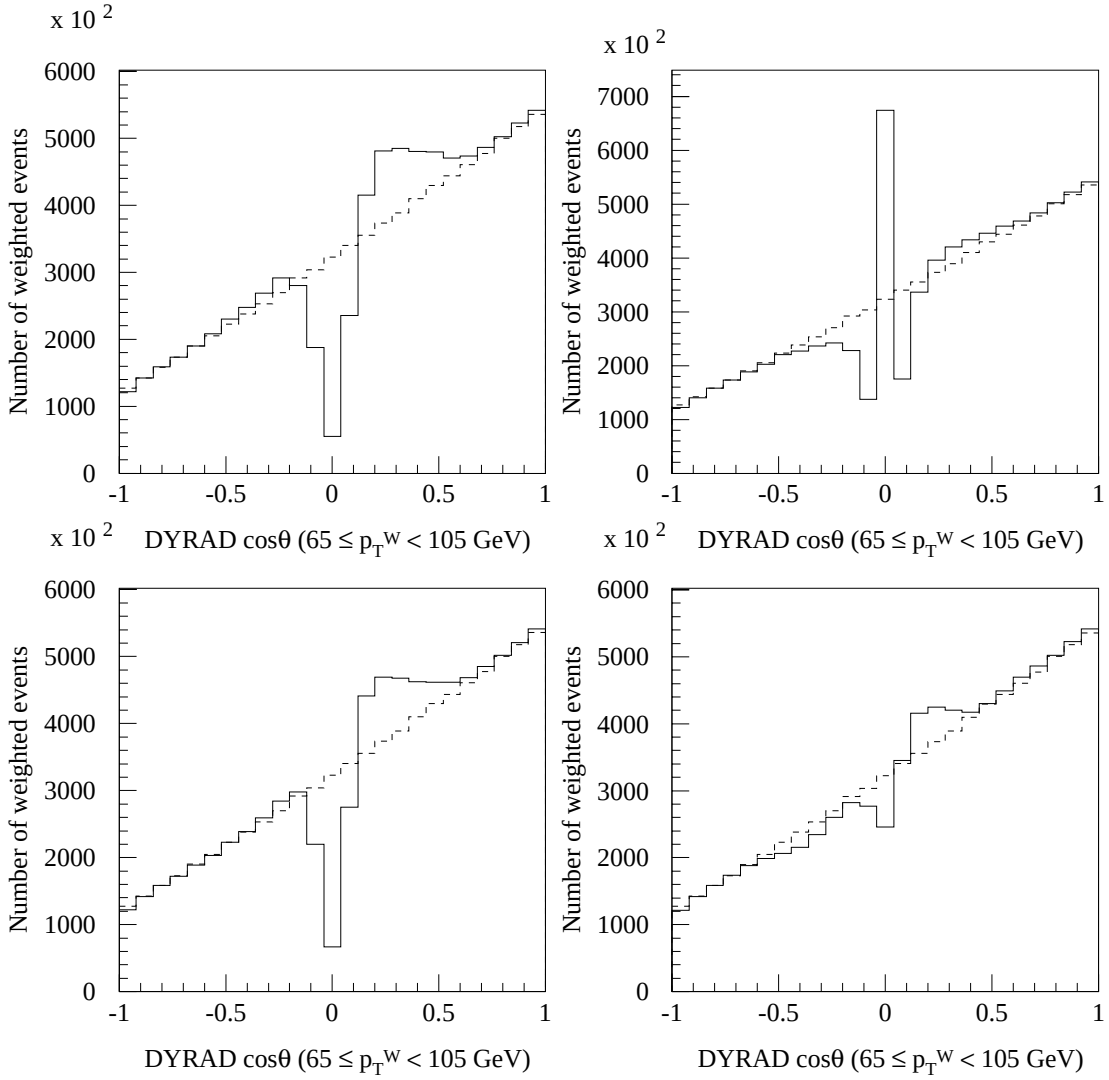

Figure B.9 The $\cos\theta$ reconstructed distributions (solid histograms) and actual distributions (dashed histograms), for leading-order (no gluon loops) DYRAD events with $65 \leq p_T^W < 105$ GeV, and for the four methods of selecting the mass for the W (method 1 is used in the upper left plot, method 2 in the upper right plot, method 3 in the lower left plot and method 4 in the lower right plot).

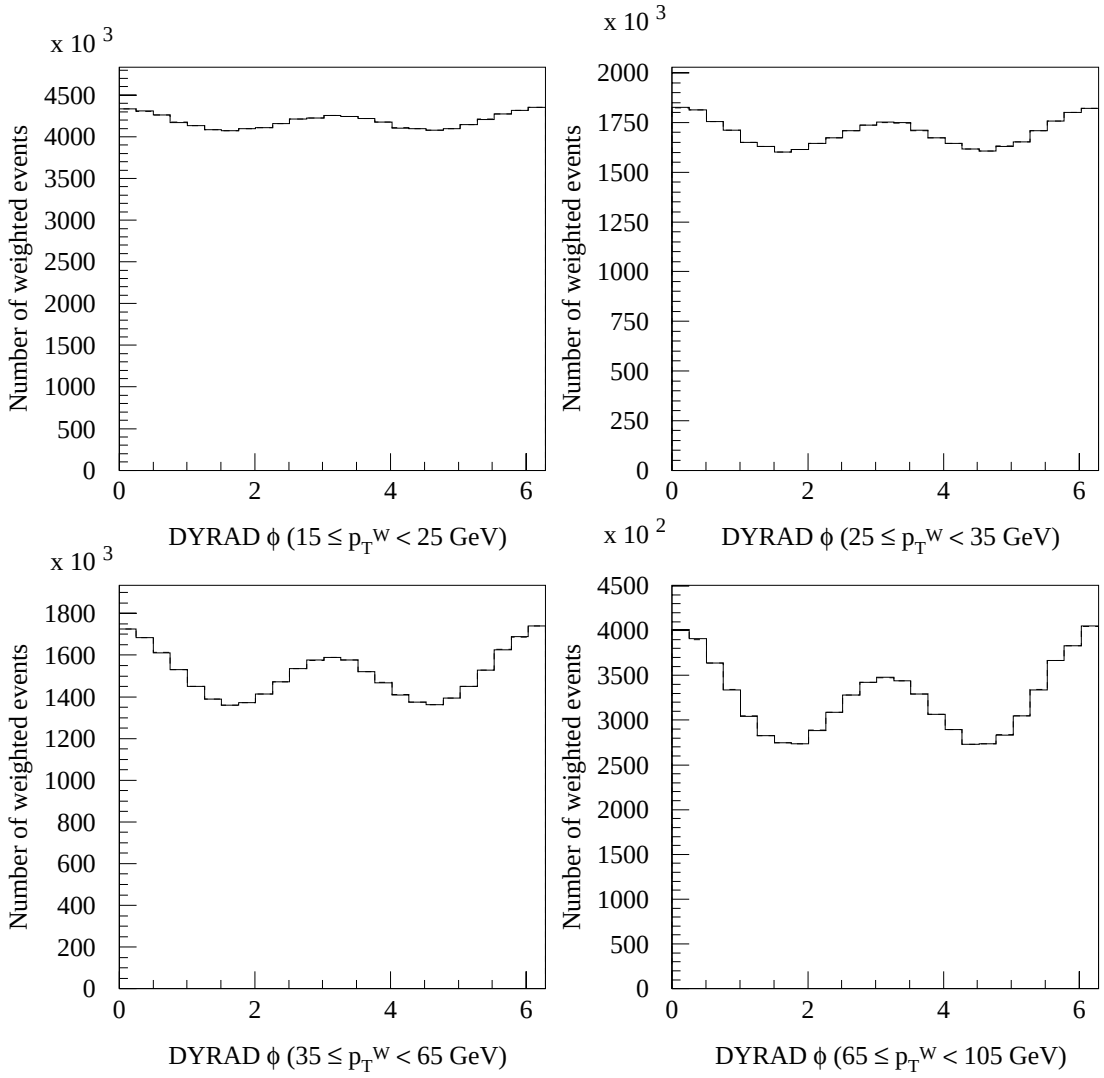

Figure B.10 The ϕ reconstructed distributions (solid histograms) and actual distributions (dashed histograms), for leading-order (no gluon loops) DYRAD events, and for four p_T^W regions. The result does not depend on the method of selecting the mass of the W.

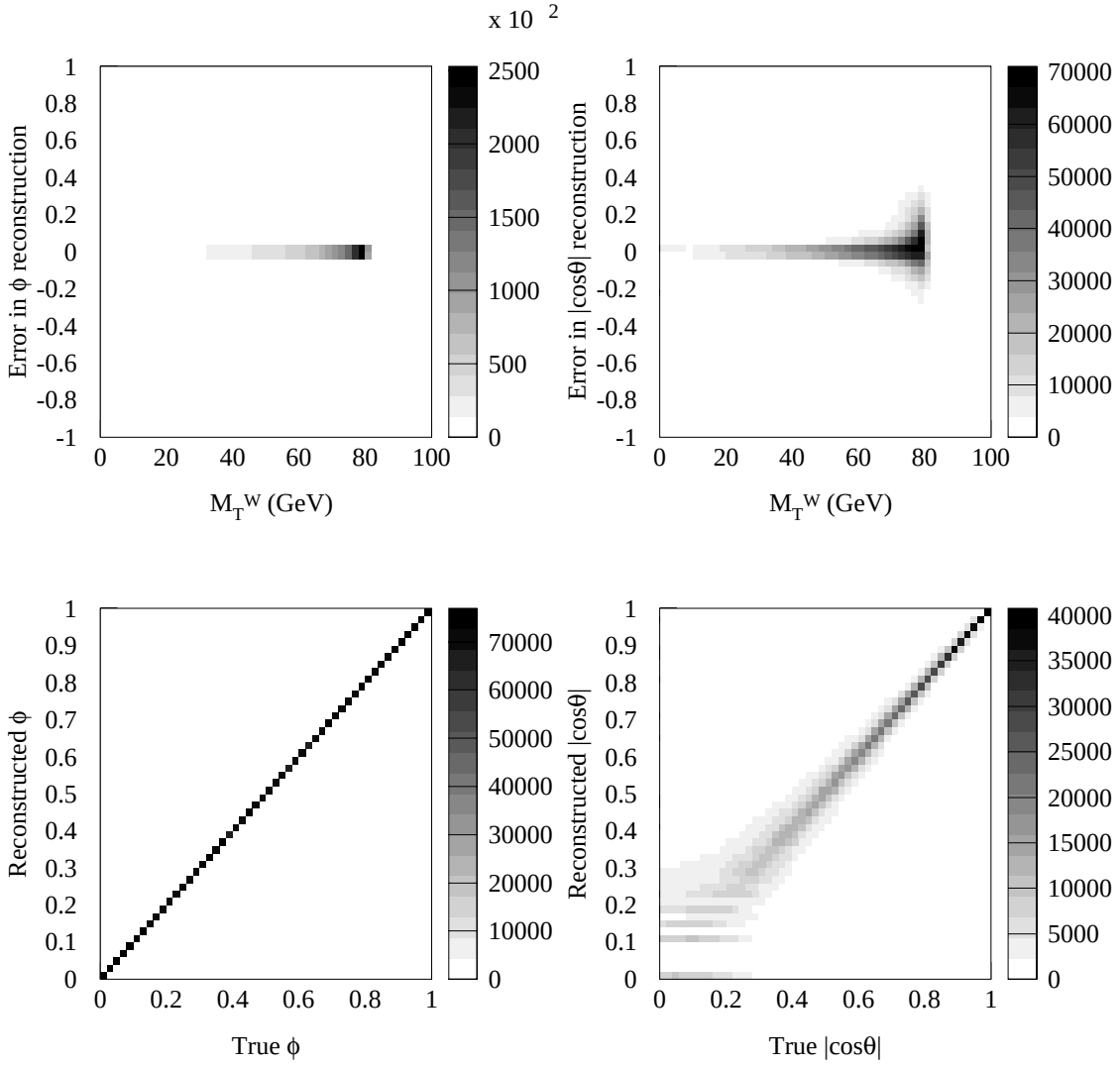

Figure B.11 The error in ϕ and $\cos\theta$ reconstruction as a function of the transverse mass of the W (upper plots) and the reconstructed versus the actual ϕ and $|\cos\theta|$ (lower plots), for DYRAD data. The errors in ϕ reconstruction are negligible (the thickness of the scatter plots equals the width of the bins), whereas the reconstruction of the $|\cos\theta|$ is problematic at high values of M_T^W, which correspond to low values of $|\cos\theta|$.

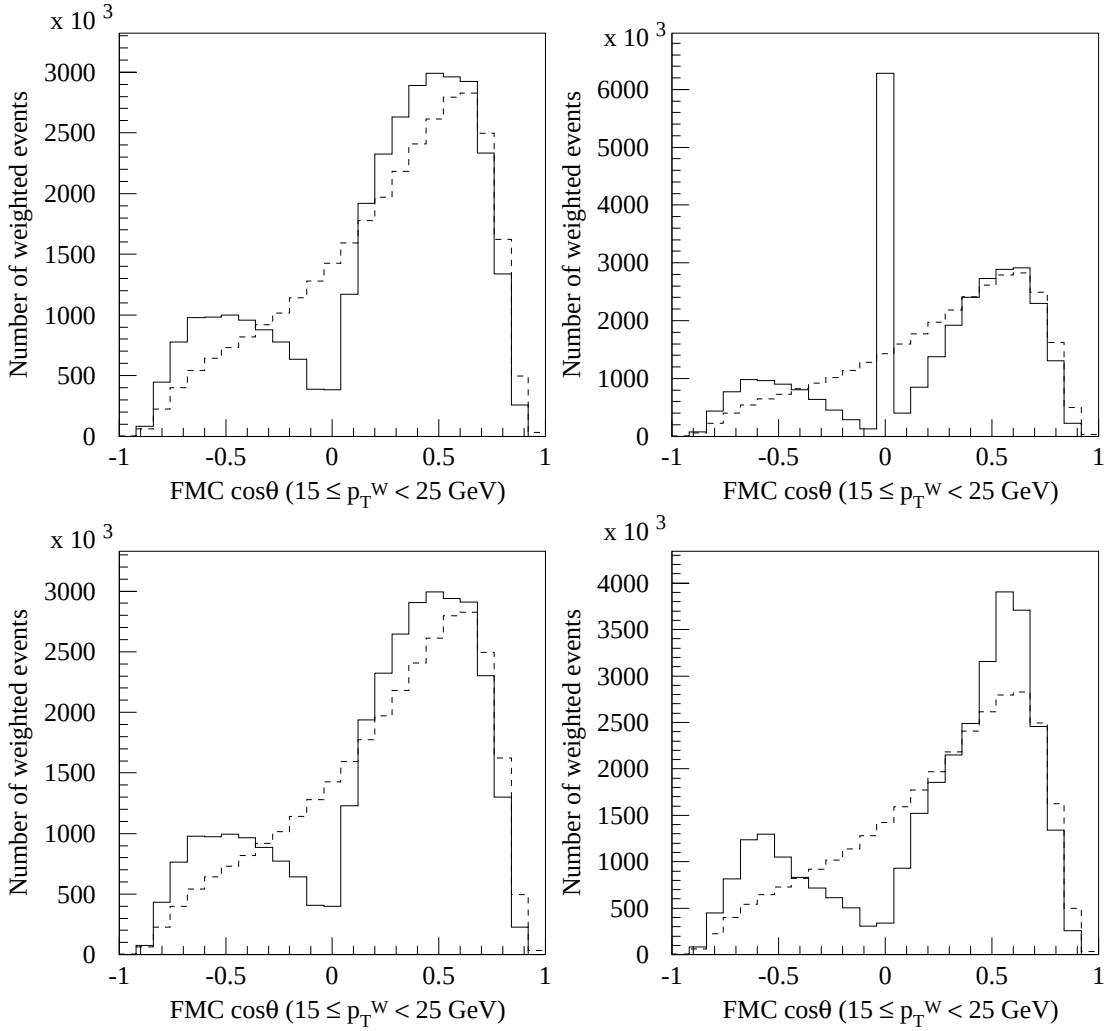

Figure B.12 The $\cos\theta$ reconstructed distributions (solid histograms) and actual distributions (dashed histograms), for leading-order (no gluon loops) FMC electron events with $15 \leq p_T^W < 25$ GeV, and for the four methods of selecting the mass for the W (method 1 is used in the upper left plot, method 2 in the upper right plot, method 3 in the lower left plot and method 4 in the lower right plot).

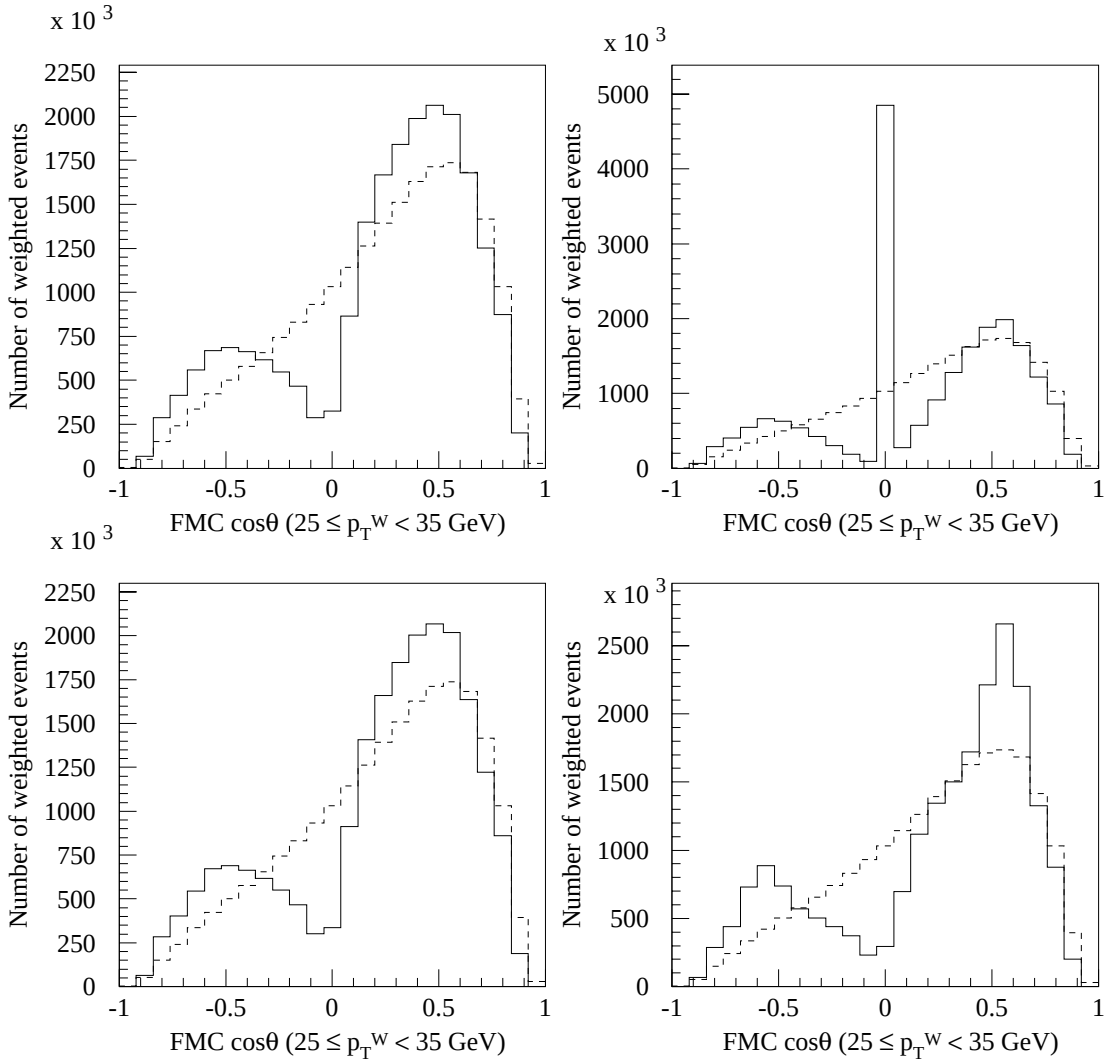

Figure B.13 The $\cos\theta$ reconstructed distributions (solid histograms) and actual distributions (dashed histograms), for leading-order (no gluon loops) FMC electron events with $25 \leq p_T^W < 35$ GeV, and for the four methods of selecting the mass for the W (method 1 is used in the upper left plot, method 2 in the upper right plot, method 3 in the lower left plot and method 4 in the lower right plot).

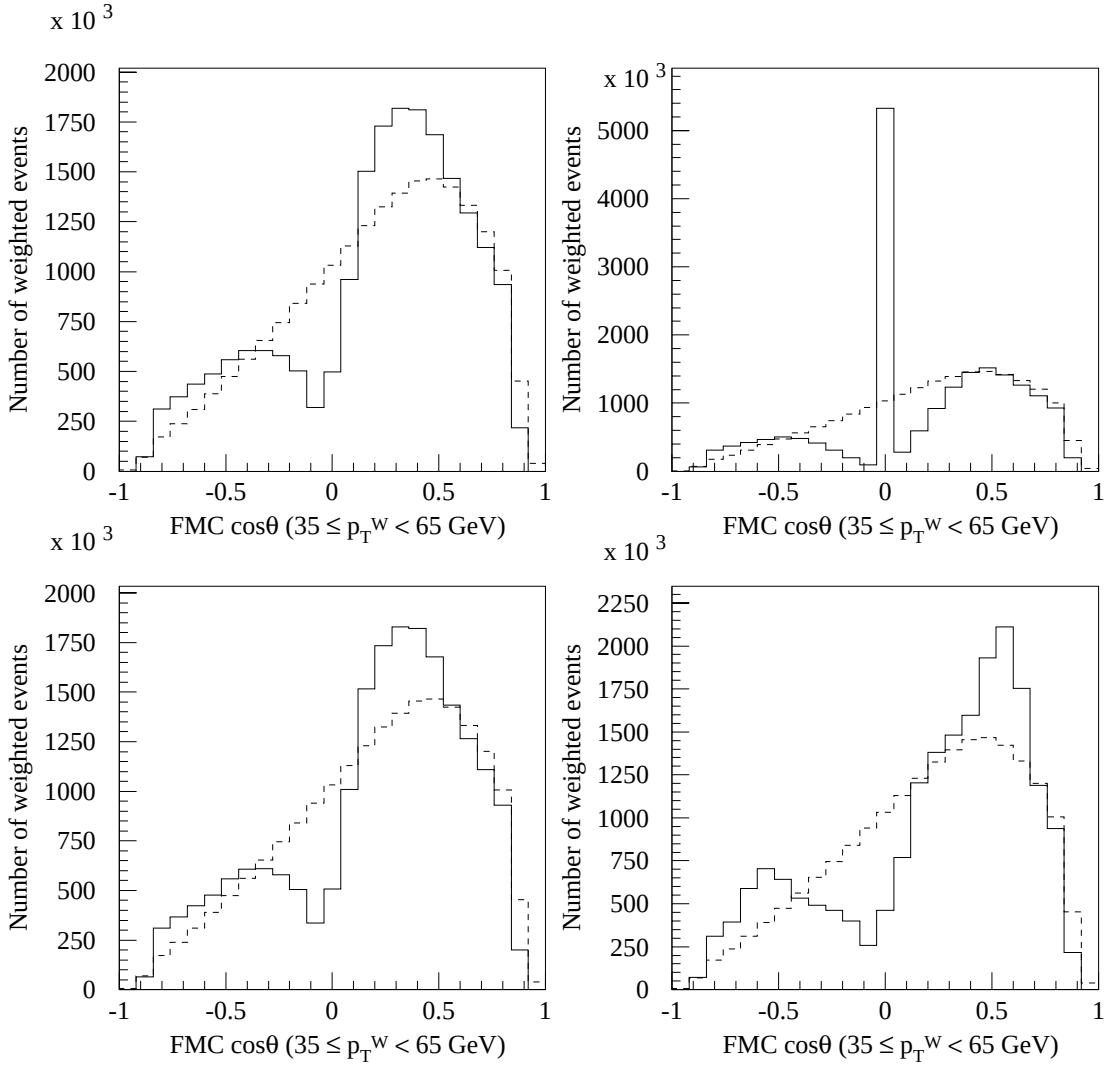

Figure B.14 The $\cos\theta$ reconstructed distributions (solid histograms) and actual distributions (dashed histograms), for leading-order (no gluon loops) FMC electron events with $35 \leq p_T^W < 65$ GeV, and for the four methods of selecting the mass for the W (method 1 is used in the upper left plot, method 2 in the upper right plot, method 3 in the lower left plot and method 4 in the lower right plot).

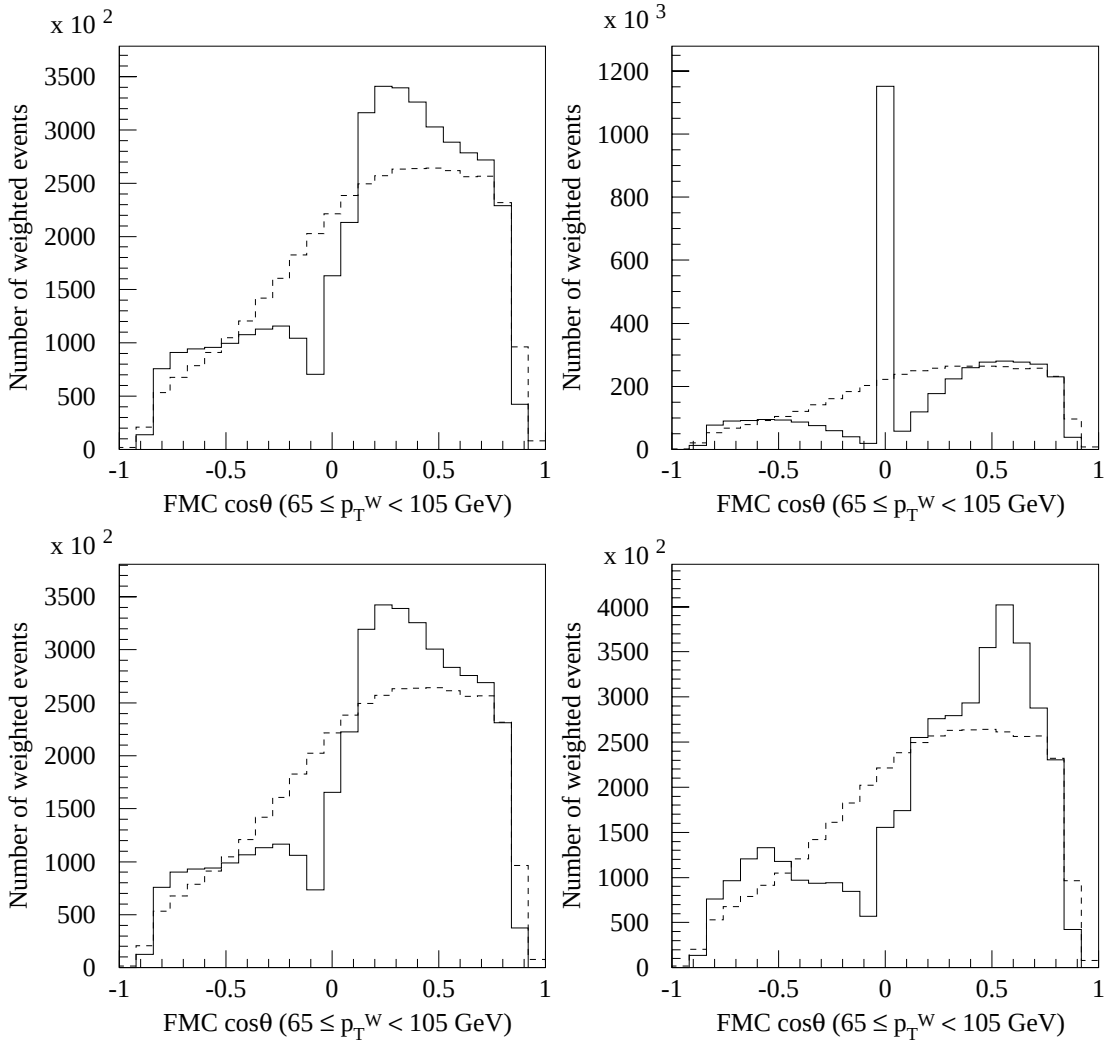

Figure B.15 The $\cos\theta$ reconstructed distributions (solid histograms) and actual distributions (dashed histograms), for leading-order (no gluon loops) FMC electron events with $65 \leq p_T^W < 105$ GeV, and for the four methods of selecting the mass for the W (method 1 is used in the upper left plot, method 2 in the upper right plot, method 3 in the lower left plot and method 4 in the lower right plot).

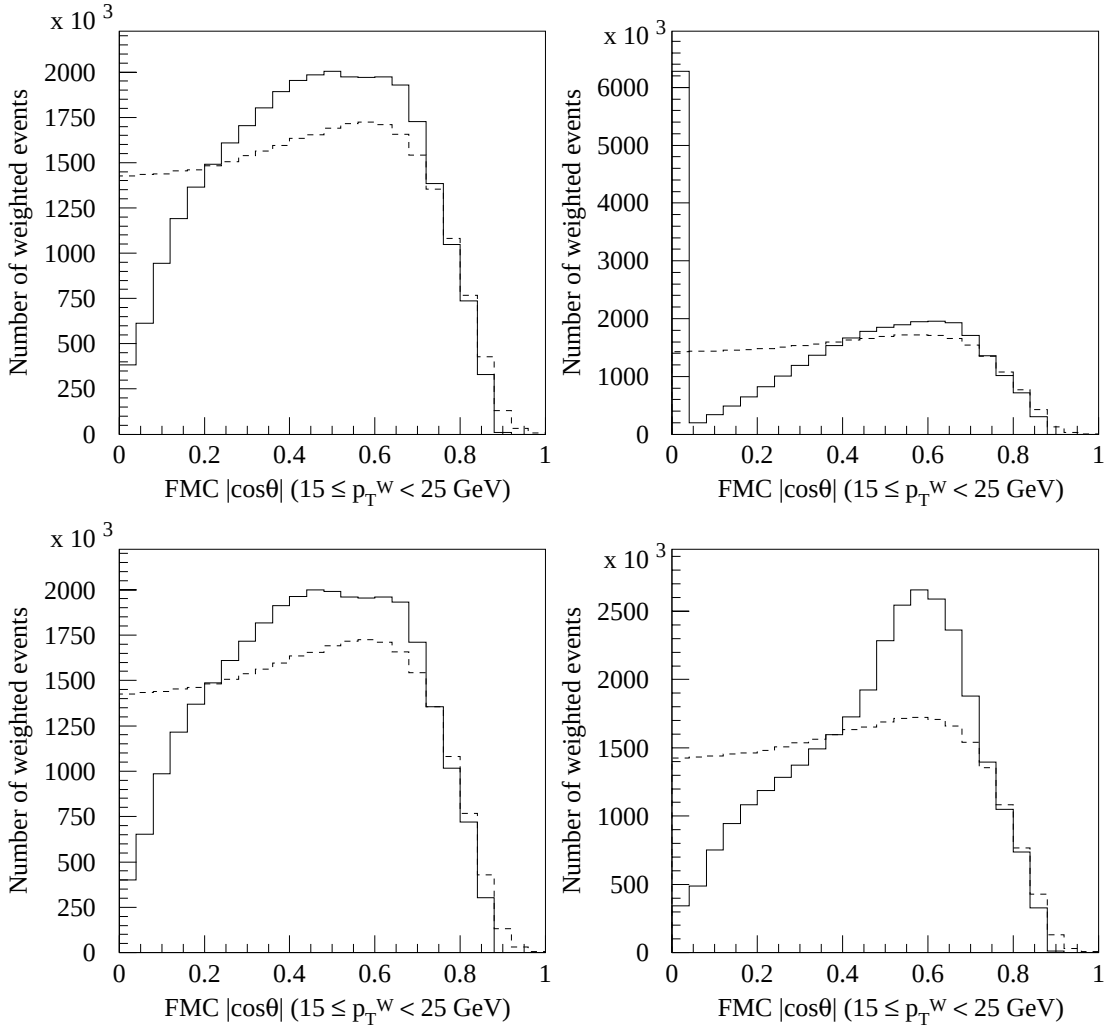

Figure B.16 The $|\cos\theta|$ reconstructed distributions (solid histograms) and actual distributions (dashed histograms), for leading-order (no gluon loops) FMC electron events with $15 \leq p_T^W < 25$ GeV, and for the four methods of selecting the mass for the W (method 1 is used in the upper left plot, method 2 in the upper right plot, method 3 in the lower left plot and method 4 in the lower right plot).

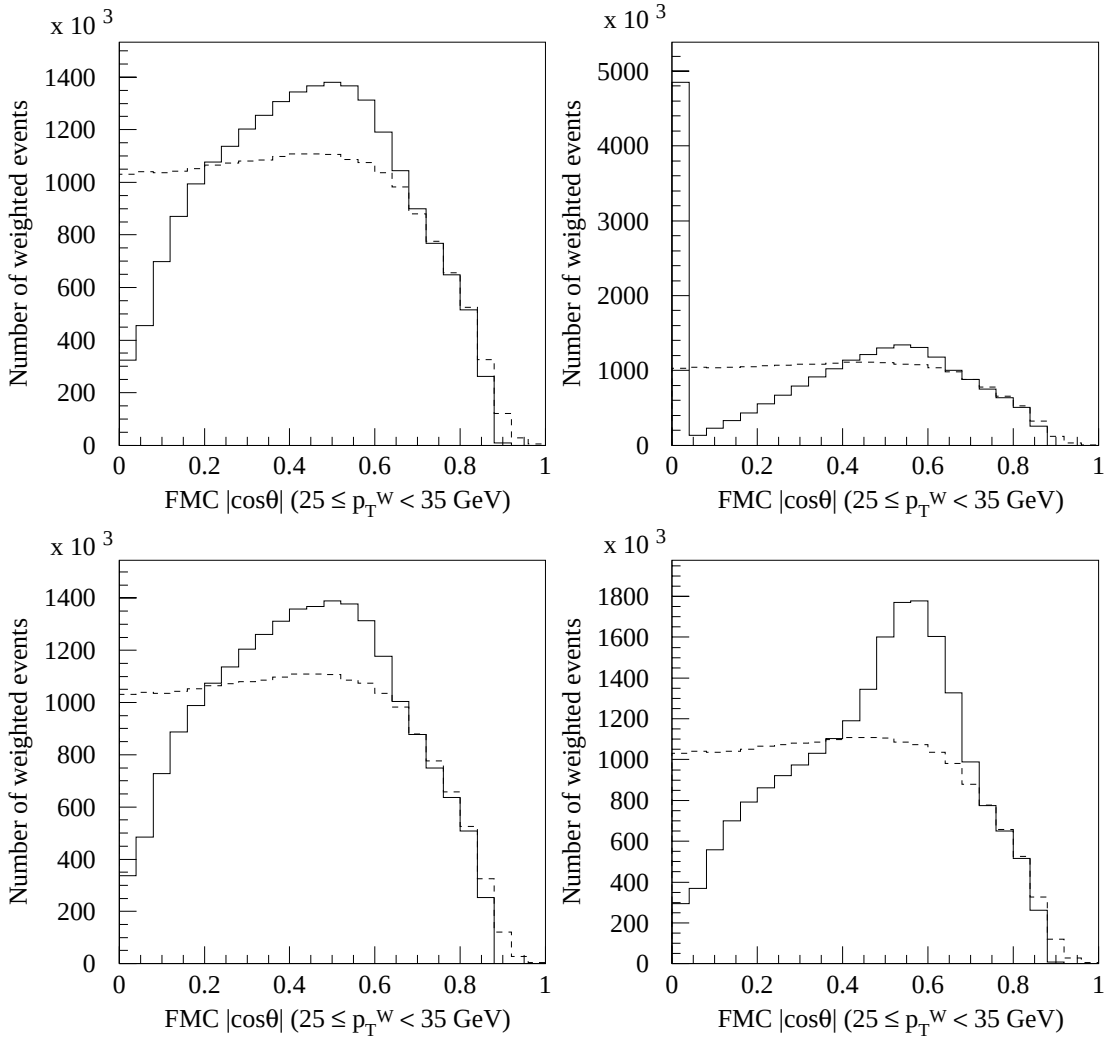

Figure B.17 The $|\cos\theta|$ reconstructed distributions (solid histograms) and actual distributions (dashed histograms), for leading-order (no gluon loops) FMC electron events with $25 \leq p_T^W < 35$ GeV, and for the four methods of selecting the mass for the W (method 1 is used in the upper left plot, method 2 in the upper right plot, method 3 in the lower left plot and method 4 in the lower right plot).

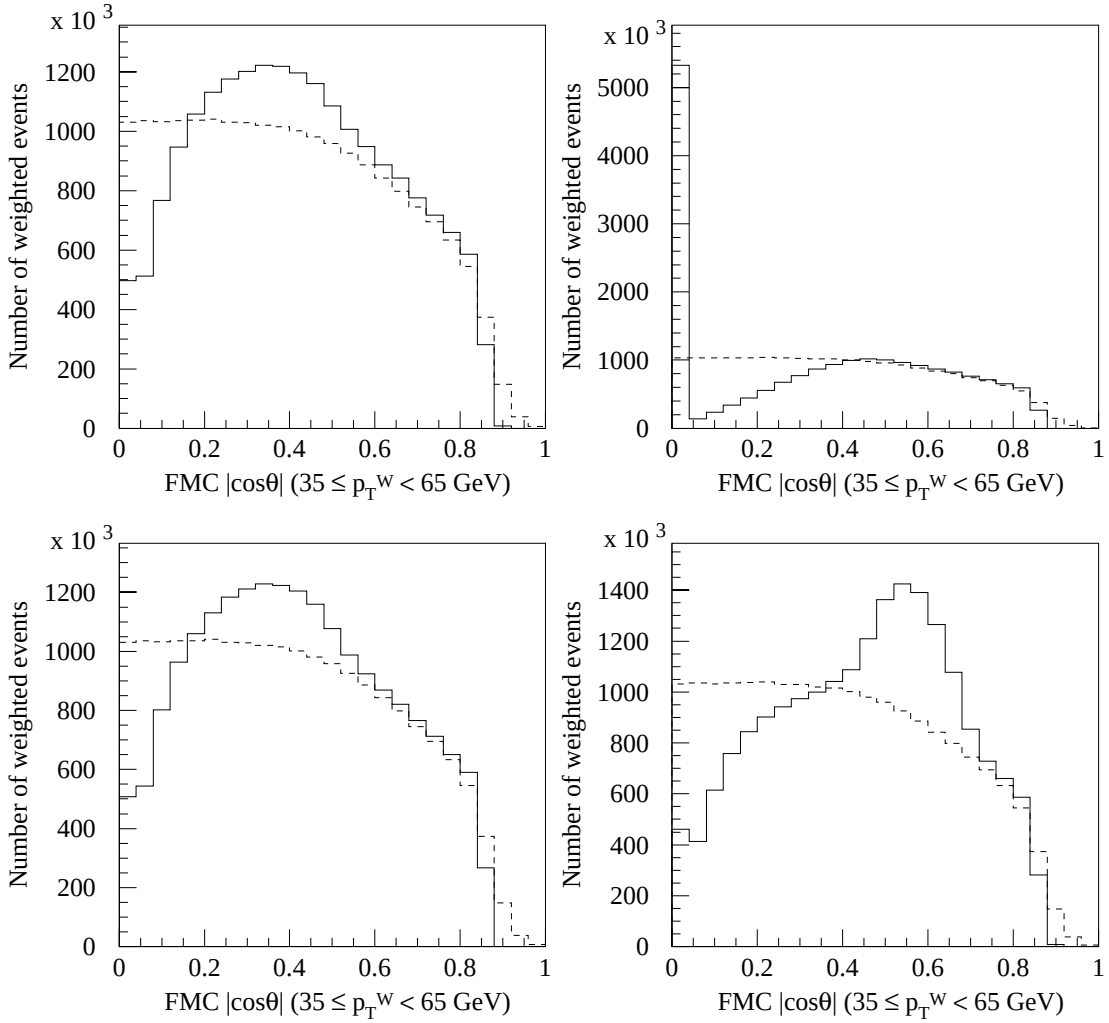

Figure B.18 The $|\cos\theta|$ reconstructed distributions (solid histograms) and actual distributions (dashed histograms), for leading-order (no gluon loops) FMC electron events with $35 \leq p_T^W < 65$ GeV, and for the four methods of selecting the mass for the W (method 1 is used in the upper left plot, method 2 in the upper right plot, method 3 in the lower left plot and method 4 in the lower right plot).

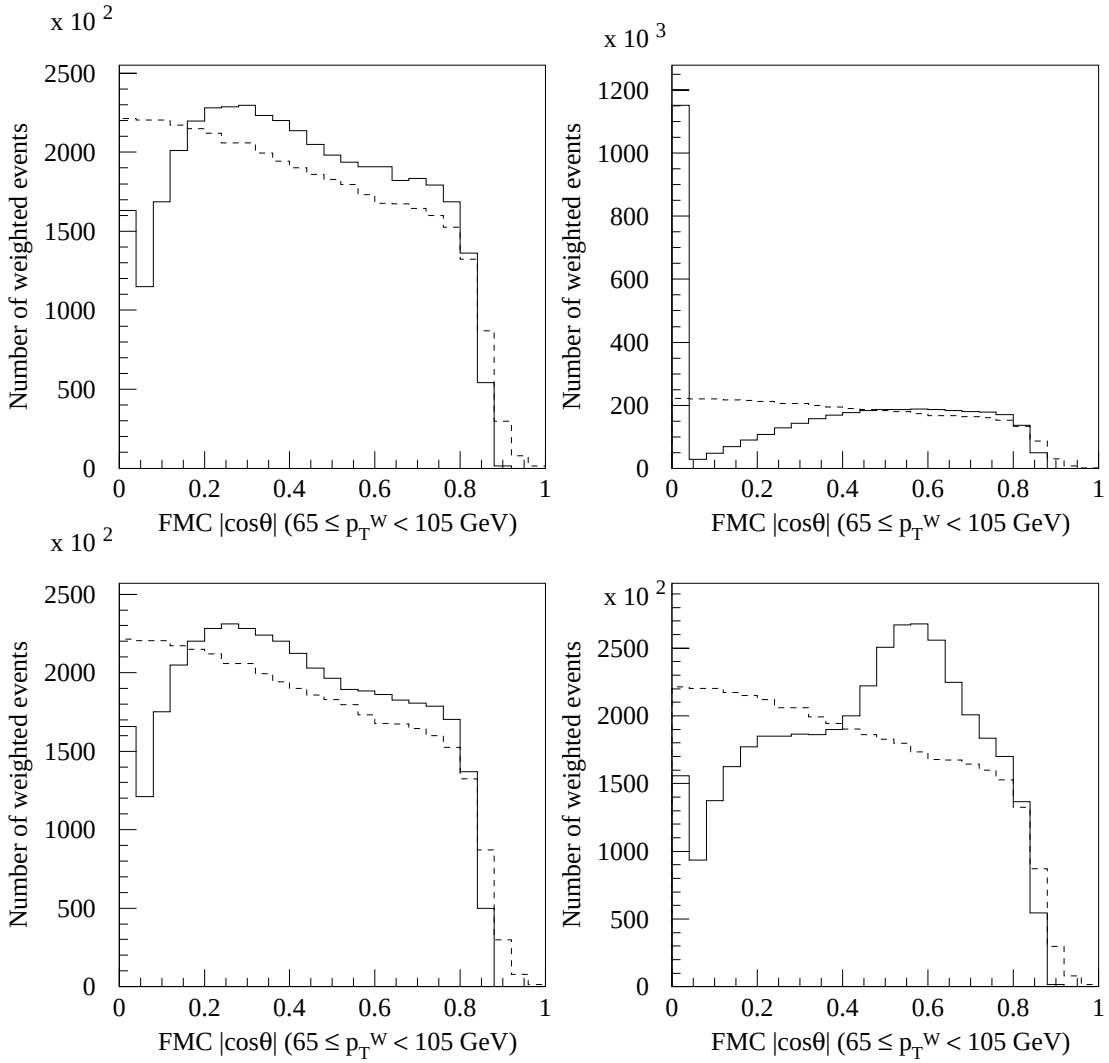

Figure B.19 The $|\cos\theta|$ reconstructed distributions (solid histograms) and actual distributions (dashed histograms), for leading-order (no gluon loops) FMC electron events with $65 \leq p_T^W < 105$ GeV, and for the four methods of selecting the mass for the W (method 1 is used in the upper left plot, method 2 in the upper right plot, method 3 in the lower left plot and method 4 in the lower right plot).

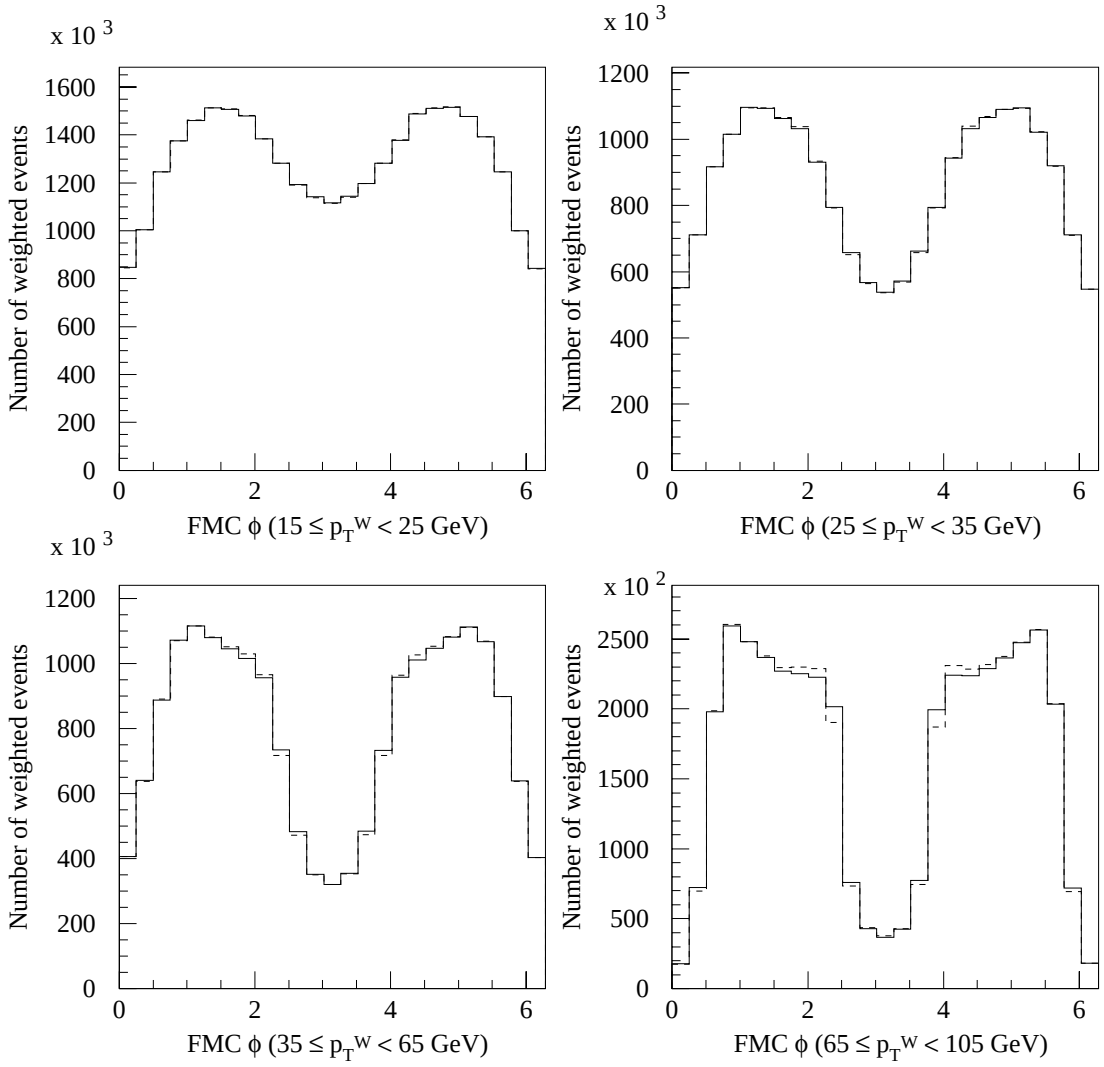

Figure B.20 The ϕ reconstructed distributions (solid histograms) and actual distributions (dashed histograms), for leading-order (no gluon loops) FMC electron events, and for four p_T^W regions. The result does not depend on the method of selecting the mass of the W.

Bibliography

[1] J. Barnes, *The Presocratic Philosophers*, Rootledge and Kegan Paul, Boston, 1982.

[2] R. C. James and G. James", *Mathematics Dictionary*, Chapman and Hall, 1992.

[3] C. D. Anderson, "The Positive Electron", Phys. Rev. **43**, 491 (1933).

[4] S. H. Neddermeyer and C. D. Anderson, "Note on the Nature of Cosmic Ray Particles", Phys. Rev. **51**, 884 (1937).

[5] O. Chamberlain, E. Segrè, C. Wiegand and T. Ypsilantis, "Observation of Antiprotons", Phys. Rev. **100**, 947 (1955).

[6] J. J. Aubert *et al.*, "Experimental Observation of a Heavy Particle J", Phys. Rev. Lett. **33**, 1404 (1974).

[7] J.E. Augustin *et al.*, "Discovery of a Narrow Resonance in e^+e^- Annihilation", Phys. Rev. Lett. **33**, 1406 (1974).

[8] M. L. Perl *et al.*, "Evidence for Anomalous Lepton Production in $e^+ - e^-$ Annihilation", Phys. Rev. Lett. **35**, 1489 (1975).

[9] S. W. Herb *et al.*, "Observation of a Dimuon Resonance at 9.5 GeV in 400-GeV Proton-Nucleus Collisions", Phys. Rev. Lett. **39**, 252 (1977).

[10] UA1 Collaboration, G. Arnison *et al.*, "Experimental Observation of Isolated Large Transverse Energy Electrons with Associated Missing Energy at $\sqrt{s} = 540$ GeV", Phys. Lett. B **122**, 103 (1983).

[11] UA1 Collaboration, C. Albajar *et. al.*, "Studies of Intermediate Vector Boson Production and Decay in UA1 at the CERN proton-antiproton collider", Z. Phys. C **44**, 15 (1989).

[12] CDF Collaboration, F. Abe *et al.*, "Observation of Top Quark Production in $\bar{p}p$ Collisions with the Collider Detector at Fermilab", Phys. Rev. Lett. **74**, 2626 (1995).

[13] D0 Collaboration, S. Abachi *et al.*, "Observation of the Top Quark", Phys. Rev. Lett. **74**, 2632 (1995).

[14] DONUT Collaboration, K. Kodama *et al.*, "Observation of tau neutrino interactions", Phys. Lett. B **122**, 103 (1983).

[15] J. H. Christenson, J. W. Cronin, V. L. Fitch and R. Turlay, "Evidence for the 2π Decay of the K_2^0 Meson", Phys. Rev. Lett. **13**, 138 (1964).

[16] Super-Kamiokande Collaboration, Y. Fukuda *et al.*, "Evidence for Oscillations of Atmospheric Neutrinos", Phys. Rev. Lett. **81**, 1562 (1998).

[17] C. S. Wu, "Experimental Test of Parity Conservation in Beta Decay", Phys. Rev. **105**, 1413 (1957).

[18] B. Abbott *et al.*, "Measurement of the Angular Distribution of Electrons from $W \to e\nu$ Decays in $p\bar{p}$ Collisions at $\sqrt{s} = 1.8$ TeV", Phys. Rev D **63**, 072001 (2001).

[19] E. Mirkes and J. Ohnemus, "W and Z Polarization Effects in Hadronic Collisions", Phys. Rev. D **50**, 5692 (1994).

[20] K. Hagiwara, K. Hikasa and N. Kai, "Parity Odd Asymmetries in W+Jet Events at Hadron Colliders", Phys. Rev. Lett. **52**, 1076 (1984).

[21] E. Mirkes, "Angular Decay Distribution of Leptons from W-Bosons at NLO in Hadronic Collisions", Nucl. Phys. B **319**, 37 (1989).

[22] NA10 Collaboration, S. Falciano *et al.*, "Angular Distribution of Muon Pairs Produced by 194-Gev/c Negative Pions", Z. Phys. C **31**, 513 (1986).

[23] F. J. Hazert *et al.*, "Observation of Neutrino-Like Interactions without Muon or Electron in the Gargamelle Neutrino Experiment", Phys. Lett. B **46**, 138 (1973).

[24] UA2 Collaboration, M. Banner *et al.*, "Observation of very large transverse momentum jets at the CERN $\bar{p}p$ Collider", Phys. Lett. B **118**, 203 (1982).

[25] F. Halzen, A. D. Martin and D. M. Scott, "Identification of W Bosons in $\bar{p}p$ Collisions: A Detailed Study", Phys. Rev. D **25**, 754 (1982).

[26] C. S. Lam and W. K. Tung, "Systematic Approach to Inclusive Lepton Pair Production in Hadronic Collisions", Phys. Rev. D **18**, 2447 (1978).

[27] J. C. Collins and D. E. Soper, "Angular Distribution of Dileptons in High-Energy Hadron Colliders", Phys. Rev. D **16**, 2219 (1977).

[28] W. T. Giele, E. W. N. Glover and D. A. Kosower, "Higher-Order Corrections to Jet Cross Sections in Hadron Colliders", Nucl. Phys. B **403**, 633 (1993).

[29] D. A. Finley, J. Marriner and N. V. Mokhov, "Tevatron Status and Future Plans", Fermilab Technical Report, Fermilab-Conf-96/408, November 1996.

[30] S. D. Holmes *et al.*, "The Fermilab Upgrade", Proc. of IEEE Part. Accel. Conf., pp. 436–468, vol. 1, Chicago, March 1989.

[31] J. A. MacLachlan, "400 MeV Upgrade for the Fermilab Linac", Proc. of IEEE Part. Accel. Confer., pp. 950–952, vol. 2, Chicago, March 1989.

[32] D. E. Young and R. J. Noble, "400-MeV Upgrade for the Fermilab Linac", Fermilab Technical Report, Fermilab-Conf-89/198, September 1989.

[33] R. C. Webber, "Fermilab Booster Low Level RF System Upgrades", Proc. of IEEE Part. Accel. Conf., pp. 2687–2689, vol. 4, Dallas, May 1995.

[34] S. Ohnuma, "Main Ring Lattice", Fermilab Technical Report, TM-1413, July 1986.

[35] P. Martin *et al.*, "Antiproton Acceleration in the Fermilab Main Ring and Tevatron", Fermilab Technical Report, TM-1440, March 1987.

[36] R. Johnson, "Initial Operation of the Tevatron Collider", Fermilab Technical Report, TM-1449, March 1987.

[37] R. Johnson, "A new RF System for Bunch Coalescing in the Fermilab Main Ring", Proc. of IEEE Part. Accel. Conf., pp. 1672–1674, vol. 3, Dallas, May 1995.

[38] E. Hubbard *et al.*, "Booster Synchrotron", Fermilab Technical Report, TM-405, January 1973.

[39] M. Popovic and C. Akenbrandt, "Performance and Measurement of the Fermilab Booster", Fermilab Technical Report, Fermilab-Conf-98/198, June 1998.

[40] E. Holmes and j. Morgan, *The Antiproton Source Rookie Book*, Batavia, August 1999.

[41] V. Visnjic and M. Halling, "Study of Betatron Stochastic Cooling in Fermilab Antiproton Debuncher", Proc. of IEEE Part. Accel. Conf., pp. 3814–3816, vol. 5, Washington, May 1993.

[42] M. Church and S. O'Day, "Antiproton Extraction in the Fermilab Antiproton Accumulator", Proc. of IEEE Part. Accel. Conf., pp. 330–332, vol. 1, Washington, May 1993.

[43] J. Petter, D. McGinnis, J. Marriner and J. Misek, "New 4-8 GHz Core Cooling Pickups and Kickers for the Fermilab Accumulator", Proc. of IEEE Part. Accel. Conf., pp. 648–650, vol. 1, Chicago, March 1989.

[44] D. McGinnis and J. Marriner, "Design of 4–8 GHz Stochastic Cooling Equalizers for the Fermilab Accumulator", Proc. of IEEE Part. Accel. Conf., pp. 1392–1394, vol. 3, San Francisco, May 1991.

[45] D. A. Finley, "Fermilab Collider Upgrade: Recent Results and Plans", Proc. of IEEE Part. Accel. Conf., pp. 3721–3725, vol. 5, Washington, May 1993.

[46] V. Bharadwaj, J. Crawford and R. Mau, "Fermilab Collider Run IB Statistics", Proc. of IEEE Part. Accel. Conf., pp. 443–445, vol. 1, Dallas, May 1995.

[47] V. Bharadwaj, "Status and Future of the Tevatron", Proc. of IEEE Part. Accel. Conf., pp. 396–400, vol. 1, Dallas, May 1995.

[48] R. Perin, "Superconducting Magnets", Proc. of IEEE Part. Accel. Conf., pp. 1282–1287, vol. 2, Dallas, May 1995.

[49] S. D. Holmes, "Design Criteria and Performance Goals for the Fermilab Main Injector", Fermilab Technical Report, Fermilab-Conf-97/038, February 1997.

[50] I. Kourbanis and D. Wildman, "RF Manipulations in the Fermilab Main Injector", Proc. of IEEE Part. Accel. Conf., pp. 2840–2842, vol. 4, New York, May 1999.

[51] D. E. Johnson *et al.*, "Design and Simulation of the Antiproton Recycler Lattice", Proc. of IEEE Part. Accel. Conf., pp. 997–999, vol. 1, Vancouver, May 1997.

[52] N. Hu *et al.*, "The Fermilab Recycler Ring", Proc. of IEEE Part. Accel. Conf., pp. 30–32, vol. 1, Chicago, May 2001.

[53] S. O'Day and M. Church, "The Fermilab Accumulator Ring Lattice Upgrade", Proc. of IEEE Part. Accel. Conf., pp. 1006-1008, vol. 1, Vancouver, May 1997.

[54] F. Abe *et al.*, "The CDF Detector: An Overview", Nucl. Instrum. Methods Phys. Res. A **271**, p. 387 (1988).

[55] W. C. Carithers *et al.*, "The CDF SVX: A Silicon Vertex Detector for a Hadron Collider", Nucl. Instrum. Methods Phys. Res. A **271**, p. 387 (1988).

[56] P. Azzi *et al.*, "SVX′, the New CDF Silicon Vertex Detector", Nucl. Instrum. Methods Phys. Res. A **271**, p. 387 (1988).

[57] F. Snider *et al.*, "The CDF Vertex Time Projection Chamber System", Nucl. Instrum. Methods Phys. Res. A **268**, p. 75 (1988).

[58] F. Bedeschi *et al.*, "Design and Construction of the CDF Central Tracking Chamber", Nucl. Instrum. Methods Phys. Res. A **268**, p. 50 (1988).

[59] L. Balka *et al.*, "The CDF Central Electromagnetic Calorimeter", Nucl. Instrum. Methods Phys. Res. A **267**, p. 272 (1988).

[60] Y. Fukui *et al.*, "CDF End Plug Electromagnetic Calorimeter Using Conductive Plastic Proportional Tubes", Nucl. Instrum. Methods Phys. Res. A **267**, p. 280 (1988).

[61] G. Brandenburg *et al.*, "An Electromagnetic Calorimeter for the Small Angle Regions of the Collider Detector at Fermilab", Nucl. Instrum. Methods Phys. Res. A **267**, p. 257 (1988).

[62] S. Bertolucci *et al.*, "The CDF Central and Endwall Hadron Calorimeter", Nucl. Instrum. Methods Phys. Res. A **267**, p. 301 (1988).

[63] S. Cihangir *et al.*, "The CDF Forward/Backward Hadron Calorimeter", Nucl. Instrum. Methods Phys. Res. A **267**, p. 249 (1988).

[64] G. Ascoli *et al.*, "CDF Central Muon Detector", Nucl. Instrum. Methods Phys. Res. A **268**, p. 33 (1988).

[65] K. Byrum *et al.*, "The CDF Forward Muon System", Nucl. Instrum. Methods Phys. Res. A **268**, p. 46 (1988).

[66] F. Abe *et al.*, "Fastbus Data Acquisition for CDF", Nucl. Instrum. Methods Phys. Res. A **269**, p. 82 (1988).

[67] Leonard Christofek, "Analysis of the Vector Boson Self Interaction and the Search for Anomalous Couplings at $\sqrt{s} = 1.8$ TeV $p\bar{p}$ Collisions",University of Illinois, Ph.D. thesis (2001).

[68] F. Abe *et al.*, "Topology of Three-Jet Events in $\bar{p}p$ Collisions at $\sqrt{s} = 1.8$ TeV", Phys. Rev. D **45**, 1448 (1992).

[69] J. Dittmann, "Measurement of the $W+ \geq 1$ Jet Cross Section in Proton-Antiproton Collisions", Duke University, Ph.D. thesis (1998).

[70] D. Cronin-Hennessy and Thomas J. Phillips, "The Missing Transverse Energy Correction", CDF note 4085, (1997).

[71] D. Benjamin *et al.*, "The Missing E_T Correction for the Run I $W/Z+\gamma$ Analysis", CDF note 4193, (1997).

[72] D. Benjamin *et al.*, "Inclusive W and Z Selection in the CDF Run I $V + \gamma$ Analysis", CDF note 5668, (2001).

[73] G. P. Lepage, "A New Algorithm for Adaptive Multidimensional Integration", Journ. Comp. Physics **27**, 192 (1978).

[74] F. Halzen and A. D. Martin, *Quarks and Leptons*, Wiley, New York, 1984.

[75] V. D. Barger and R. J. N. Phillips, *Collider Physics*, Addison Wesley, Reading, 1997.

[76] L. H. Ryder, *Quantum Field Theory*, Cambridge University Press, Cambridge, 1988.

[77] M. E. Peskin and D. V. Schroeder, *An Introduction to Quantum Field Theory*, Addison Wesley, Reading, 1997.

[78] CDF Collaboration, F. Abe *et al.*, "W Boson + Jet Angular Distribution in $\bar{p}p$ Collisions at $\sqrt{s} = 1.8$ TeV", Phys. Rev. Lett. **73**, 2296 (1994).

[79] U. Baur, S. Errede and G. Landsberg, "Rapidity Correlations in $W\gamma$ production at Hadron Colliders", Phys. Rev. D **50**, 1917 (1994).

Vita

John Strologas [redacted]. He received his B.S. in physics from the University of Athens in 1994 and a graduate certificate from the Nuclear Physics Institute of the Demokritos National Center for Scientific Research in 1995. The same year he joined the University of Illinois, where he combined his education at the Department of Physics with research at the Fermi National Accelerator Laboratory. Later on he carried out research on semiconductor devices at the Electrical and Computer Engineering Department and the Beckman Institute for Advanced Science and Technology. He has received an M.S. degree in physics, an M.S. degree in electrical engineering and a Ph.D. degree in particle physics. Strologas is a member of the American Physical Society Divisions of Particles and Fields, Nuclear Physics and Astrophysics, the Space Physics Section of the American Geophysical Union, and the Electron Devices Society and the Nuclear and Plasma Sciences Society of the IEEE. He received the Giulio Ascoli Award for originality and excellence in high-energy physics research in 2000 and the Asketh Fellowship for the best European graduate student in 1999, both from the University of Illinois, and the Hellenic Link Midwest award in 1999. He has been a member of the Phi Kappa Phi Honorary Society since 2000.